Photoemission Studies on the Efficacy of Self-assembled Monolayers for use in Transistor Interconnect Applications

Anita Brady-Boyd
B.Sc.

A thesis presented for the degree of Doctor of Philosophy
Dublin City University
School of Physical Sciences
Supervised by Professor Greg Hughes
November 2018

Declaration

I hereby certify that this material, which I now submit for assessment on the programme of study leading to the award of doctor of philosophy is entirely my own work, and that I have exercised reasonable care to ensure that the work is original, and does not to the best of my knowledge breach any law of copyright, and has not been taken from the work of others save and to the extent that such work has been cited and acknowledged within the text of my work.

Signed:______________________________ ID No.:_________________ Date:_________

Dedication and Acknowledgements

Firstly, I would like to thank my supervisor Greg Hughes for all his help and for sharing his knowledge with me for the last 4 years. He has given me a great opportunity to travel and experience working in world class facilities which few PhD students are lucky to visit once never mind 8 times!

To all in DCU especially Tony, Justin, Venkat, Rob and Conor who are always happy to discuss results and help if a problem arises. Also, to Conor, (gone but not forgotten) who trained me to use all the systems in my first year. A special thanks to Pat Wogan, without him we would never get any work done. The past 4 years it has never felt like a chore going to work but a pleasure.

A special thanks to Aaron, Muhammad and Kate for the many lunches and cups of tea and coffee. I like to think we kept each other relatively sane over the years. To my friends in Carlow who have supported me and listened to me even when they had no clue what I was talking about.

To my parents, Tony and Pauline who taught me that doing what you love is the most important thing. I owe them so much for raising me to be who I am. To my parents in law, Tommy and Elaine thank you for the continued support. Thank you to Edna who thoroughly proof read the whole thesis.

Most importantly, I would like to thank my amazing wife Claire for all the support she has given me, so I can follow my dreams and do something that I love. Words can’t express how lucky I am to have her in my life. I would never have gotten this far without her constant encouragement and unwavering patience and I dedicate this thesis to her.

Finally, I would like to acknowledge Science Foundation Ireland for the financial support of this work.

Table of Contents

Table of Figures

Publications arising from this work

Investigation of Nitrogen Incorporation into Manganese Based Copper Diffusion Barrier Layers for Future Interconnect Applications

Selvaraju, V., Brady-Boyd, A., O'Connor, R., Hughes, G and Bogan, J.

Surfaces and Interfaces, **2018,** 13, 133 – 138.

Nucleation and Adhesion of ultra-thin Copper films on amino-terminated Self-Assembled Monolayers

Bogan, J., Brady-Boyd, A., Armini, S., Lundy, R., Selvaraju, V., O'Connor, R. and Hughes, G

Appl. Surf. Sci. **2018**, *462*, 38–47.

A Synchrotron Radiation Study of Metallic Titanium deposited on Dielectric Substrates

Bogan, J., Selvaraju, V., Brady-Boyd, A., Hughes, G. and O'Connor, R.

J. Vac. Sci. Technol. B 2018, 36 (4), 040602.

On the use of (3-trimethoxysilylpropyl) diethylenetriamine self-assembled monolayers as seed layers for the growth of Mn based copper diffusion barrier layers

Brady-Boyd, A., O'Connor, R., Armini, S., Selvaraju, V., Hughes, G. and Bogan, J.
Appl. Surf. Sci. **2018**, *427*, 260–266.

Physical, Chemical and Electrical Characterisation of the Diffusion of Copper in Silicon Dioxide and Prevention via a CuAl Alloy Barrier Layer System

Byrne, C.; Brennan, B.; Lundy, R.; Brady, A.; Hurley, P.; Hughes, G.
Mater. Sci. Semicond. Process. **2017**, *63* (February), 227–236.

In Situ XPS Chemical Analysis of $MnSiO_3$ Copper Diffusion Barrier Layer Formation and Simultaneous Fabrication of Metal Oxide Semiconductor Electrical Test MOS Structures

Byrne, C.; Brennan, B.; McCoy, A. P.; Bogan, J.; Brady, A.; Hughes, G.

ACS Appl. Mater. Interfaces **2016**, *8* (4), 2470–2477.

Chemical and electrical characterisation of the segregation of Al from a CuAl alloy (90%:10% wt) with thermal anneal

Byrne, C., Brady, A., Walsh, L., McCoy, A. P., Bogan, J., McGlynn, E., Rajani, K. V. and Hughes, G.

Thin Solid Films ***2016,*** *599, 59-63.*

Oxidation of Ruthenium Thin Films Using Atomic Oxygen

McCoy, A. P.; Bogan, J.; Brady, A.; Hughes, G.

Thin Solid Films **2015**, *597*, 112–116.

Publications in preparation

Atomic Oxygen Treatment of Self-Assembled Monolayers

Brady-Boyd, A., Selvaraju, V., Bogan, J., O'Connor, R. and Hughes, G

Conference Proceedings

Characterisation of Electroless Deposited Cobalt by Hard and Soft X-ray Photoemission Spectroscopy

Brady-Boyd, A., Selvaraju, V., Bogan, J., O'Connor, R. and Hughes, G.

Accepted to: The 18th IEEE International Conference on Nanotechnology, 23-26 July 2018, Cork.

On the use of (3-trimethoxysilylpropyl) diethylenetriamine self-assembled monolayers as seed layers for the growth of Mn based copper diffusion barrier layers

Brady-Boyd, A., O'Connor, R., Armini, S., Selvaraju, V., Hughes, G. and Bogan, J.

2017 Materials for Advanced Metallization (MAM) Conference, 26th-29th March Dresden, Germany.

&

IOP Spring Meeting 2017, March, Dublin – *Finalist for Rosse Medal*

Characterisation of CuAl alloy for future interconnect technologies

Byrne, C., Brady, A., Walsh, L., McCoy, A. P., Bogan, J., McGlynn, E., Rajani, K. V. and Hughes, G.

2015 IEEE International Interconnect Technology Conference and 2015 Materials for Advanced Metallization Conference, IITC/MAM, 18th-21th May Grenoble, France.

Abstract

Anita Brady-Boyd

Photoemission studies on the efficacy of self-assembled monolayers for use in transistor applications

The thesis explores the effectiveness of incorporating amino terminated self-assembled monolayers (SAMs) into several different aspects of the back-end-of-line (BEOL) process for integrated circuit (IC) fabrication. SAMs are essentially two-dimensional nanomolecular assemblies which can display large scale ordering via weak Van der Waals interactions, when deposited on a surface. In this study SAMs are considered for four main applications (i) as a pore sealant for porous dielectrics, (ii) as an adhesion promoter between copper and SiO_2, (iii) as a blocker for area selective atomic layer deposition (ALD) and (iv) as a means to trap a Pd catalyst for the novel electroless deposition (ELD) of cobalt. From a pore sealing perspective, in-situ x-ray photoelectron spectroscopy (XPS) studies have shown that a manganese silicate layer is formed when a thin film of manganese is deposited and annealed on SAM terminated SiO_2 and spin-on glass substrates. The presence of a silicate implies that the manganese can diffuse through the SAM and form a chemically stable barrier which could inhibit copper infiltration into the dielectric. In a separate study, XPS analysis of ultra-thin copper films (~0.5nm) deposited on three differently terminated SAMs suggests that amino terminated SAMs offer significant benefits in terms of both the nucleation and adhesion of copper over layers on dielectric surfaces. A subsequent in-situ XPS study of the effects of atomic oxygen treatments of SAM terminated dielectric substrates displayed that highly controlled stepwise removal of the SAM could be routinely achieved which has significance for the understanding the oxidation cycle in the ALD growth of metal oxides on SAM terminated substrates. Finally, the role of SAMs in cobalt interconnect electroless deposition (ELD) has been characterised by hard x-ray photoelectron spectroscopy (HAXPES) in order to understand the optimized process to fabricate these interconnect structures.

Chapter 1

1 Introduction

With the end of Moore's law almost insight the semiconductor industry must find novel ways of increasing speed and efficiency in new devices while keeping the power consumption to a minimum[1]. During the 1960's Moore was the first to observe that the number of transistors on an integrated circuit (IC) chip doubles roughly every 18 – 24 months[2]. This observation has become a self-fulfilling prophecy with companies like Intel, Global Foundries and Samsung all competing to keep Moore's law alive by aggressive scaling of feature sizes in the IC chip. The IC chip is generally split into two main parts: the front end of line (FEOL) where the transistors are patterned directly in the semiconductor and the back end of line (BEOL) where the individual transistors are wired by the interconnecting wires or interconnects. Intel's 10nm node boasts of 100 million transistors per mm^2 in the FEOL of the chip[3]. This however, requires sophisticated patterning of the interconnects in the BEOL as seen in Figure 1.1. This scaling is propelled by new advances in mobile technology of phones, tablets and laptops. The desire of consumers to always have fast powerful devices at our fingertips is ensuring that technology gets the most out of Moore's Law.

This thesis will emphasise some of the critical challenges facing the microelectronics industry today and propose possible solutions for these problems. The integration of self-assembled monolayers (SAMs) into the BEOL is investigated as a means of solving some of the main difficulties in device fabrication. In this section, the processing problems faced by industry are outlined. Self-assembled monolayers are also introduced and reasons for their interest is highlighted.

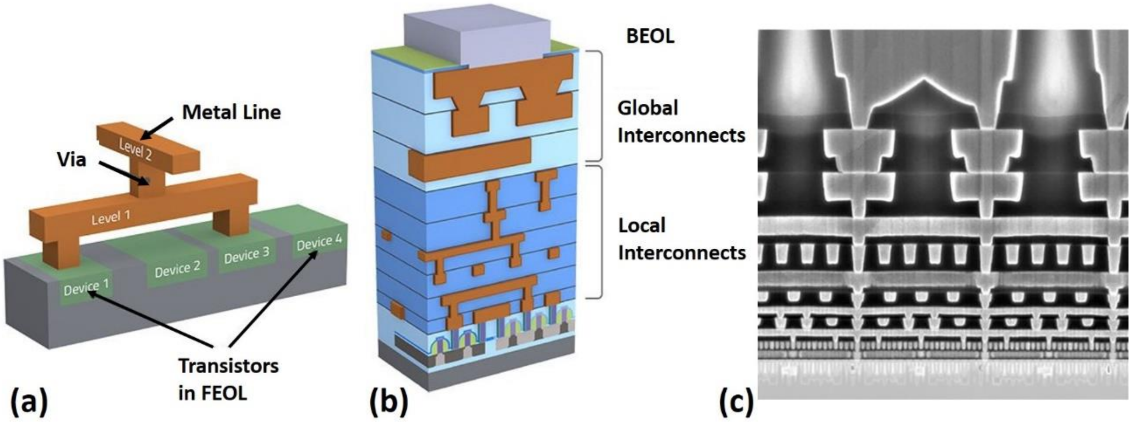

Figure 1.1 (a) basic schematic of how interconnects work [4] (b) the complete stack from the transistors right up to the solder bump [4] and (c) Scanning electron microscope (SEM) image of the actual 12 metal layer interconnect stack in Intel's 10nm node [5].

1.1 Challenges Facing the Microelectronics Industry

There are a variety of problems associated with the scaling down of features on IC's. With a pitch width of 34 nm at 10 nm node[3,5], and even 7 nm node technology[6] on the way, the problems associated with shrinkage are not easily overcome. The resistance-capacitance (RC) time delay in particular has become one of the limiting factors for ultra-large-scale integration (ULSI) of IC's. In addition to the scaling issues, choice of material can also have consequences. Copper (Cu) for example, introduces some difficulties like electromigration and diffusion into the surrounding dielectric insulating layer[7–12]. This has led to the need for barrier layers[13–17] and in the newest technology node, cobalt (Co) has been introduced to replace copper in the first three metal lines[5]. It is predicted that in subsequent technology nodes cobalt will in fact replace copper altogether as the interconnect material of choice[1,6,18].

Silicon dioxide (SiO2) also has limitations as the interlayer dielectric (ILD) material, with a dielectric constant, k, of 3.9 being considered to be too high for future back end interconnect fabrication. This has initiated the search for new lower dielectric constant materials or low-k materials in the BEOL processing.

However, there are considerable material challenges in their introduction. Problems of adhesion between the different layers in the device, in particular between metal lines and the surrounding dielectric material, have also been a hindrance. Delamination due to poor adhesion is common[19].

Finally, the ability to deposit the barriers and the copper in a conformal way that will reach to the depths of the vias and trenches is becoming increasingly difficult. In the 10 nm node the aspect ratio of the trench height to its width is 7:1 as shown in Figure 1.2. This creates a problem for traditional chemical vapour deposition (CVD) and physical vapour deposition (PVD) based techniques. Atomic layer deposition (ALD) and electroless deposition (ELD) show great promise for depositing a variety of thin films including oxides and metals due to their uniformity and control over material thickness[20,21].

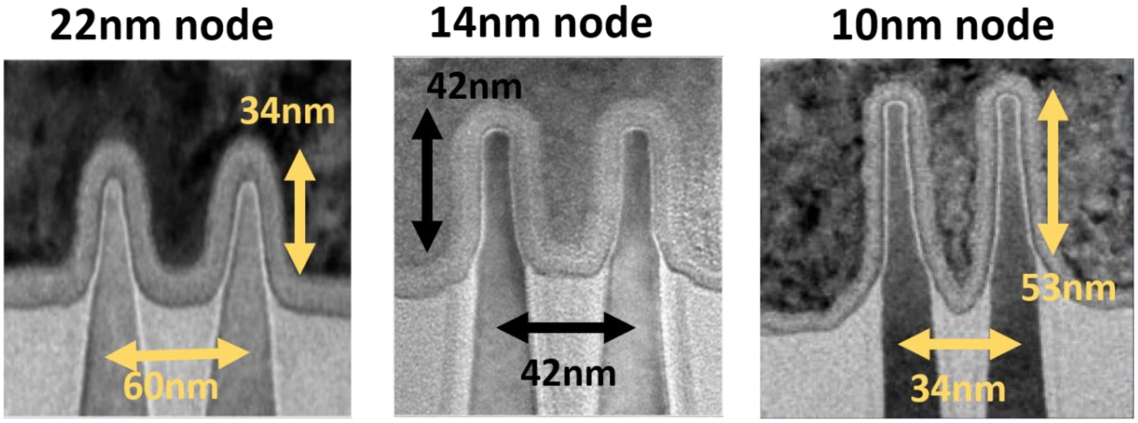

Figure 1.2 Scaling from the 22nm node to the 10nm node[3].

1.1.1 RC Time Delay

The miniaturisation of device features has greatly improved the overall chip performance due to the larger number of transistors per chip and their closer proximity to each other. This has led to a decrease in the gate switching delay but ultimately to an increase in the interconnect delay as more narrower wires are required to connect these devices. This delay is due to (i) the interconnect dimensions and (ii) the electrical resistance of the metal line and the capacitance between neighbouring lines surrounded by the dielectric and is known as the RC time delay. The RC time delay also limits the clock frequency of the chip, which determines how fast the transistors can be switched on and off.

Since the resistance, R, of the line is dependent on its geometry, if the cross-sectional area decreases the resistance will increase. This can be seen by:

$$R = \frac{\rho L}{A} \,, \tag{1.1}$$

where ρ is the intrinsic resistivity of the material in the line, L is the length of the line and A is the cross-sectional area of the interconnect.

Similarly, the capacitance, C, between two interconnecting lines is given by:

$$C = 2\kappa\varepsilon_0 \left(\frac{2LT}{P} + \frac{LP}{2T}\right) , \tag{1.2}$$

where κ is the dielectric constant of the material, ε_0 is the permittivity of free space, T is the thickness of the line and P is the minimum metal pitch. As the capacitance is directly proportional to the dielectric constant, if its value remains constant while the dimensions of the metal lines decreases, then the capacitance will increase correspondingly.

From these equations it can be deduced that if the RC time delay is to be kept to a minimum the metal of choice for interconnects must have a low resistivity and the ILD must have a low dielectric constant. All these factors led to copper replacing aluminium as the interconnect material of choice in the late 1990's with the introduction of the 180 nm node [22–25]. The introduction of copper led to a significant improvement in RC time delay due to copper's lower resistivity value meaning that the aggressive scaling trend could continue. The resistivity of bulk copper is 1.7 μΩ.cm while bulk aluminium is 2.7 μΩ.cm.

Today, it would appear that the microelectronics industry is set for another switch in metallisation scheme. From Figure 1.3 below it can be seen that cobalt interconnects on low-*k* dielectrics with air gaps, have the potential to greatly reduce the RC time delay to allow scaling to continue for several more nodes[26]. Although the resistivity of bulk cobalt is higher than copper at 6 μΩ.cm, at these length scales it surpasses copper in terms of performance. Figure 1.3 shows the time delay due to cobalt interconnects, which even integrates airgaps in the ILD (purple line), is ~67 % lower than the best performing copper interconnects.

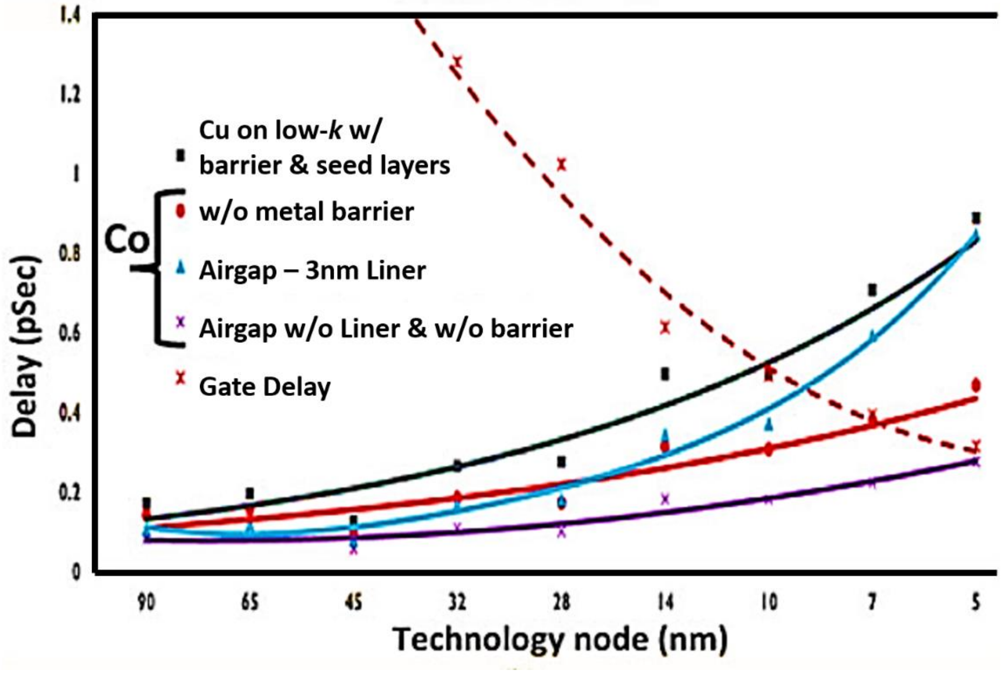

Figure 1.3 RC time delay as a function of technology node. The gate delay can be reduced by decreasing feature size. Changing to Co should decrease the interconnect delay[26].

Furthermore, the capacitance can also be reduced to keep the interconnect delay minimised. From equation 1.2 it is clear that as devices continue to shrink the capacitance will increase. The only way to keep the capacitance minimised is to lower the dielectric constant of the ILD. A low-*k* dielectric material is defined as having a dielectric constant less than the SiO_2 value of 3.9. Today's low-*k* dielectric materials average around $k = 2.5$. A lower k value is mainly achieved by two different methods. The first is to introduce carbon into the oxide. This has the effect of replacing some of the highly polarisable Si-O bonds with less polarizable $Si\text{-}CH_3$ bonds. The introduction of the C also increases the interatomic distances in the silicon and this also decreases the dielectric constant[27–29].

The second method used to reduce the k value, is to introduce voids/air gaps or pores into the dielectric material. The lowest k value that can be achieved is 1, which is that of air. Therefore, by introducing air gaps or pores into the dielectric material, the dielectric constant can be lowered. The pores are introduced by adding nanoparticles called porogens to the dielectric, which are then burned out when the dielectric is heated, leaving air gaps behind. The porogen is an organic precursor, normally a hydrocarbon, which is added during the deposition of the low-*k* material. The most common type of porogens are cyclopentane oxide (CPO) or butadiene monoxide (BMO). The "burn out" process usually involves thermally annealing the dielectric at high temperatures for several hours or by UV curing the dielectric to remove the porogen[30]. The size of the pores can be selected by choosing the size of the porogens themselves[31]. Generally, the larger the pores, the higher percentage of porosity of the film. Although new methods such as foaming have also been developed where the porosity of the films can reach 65 % [32]. Porous films are quite challenging as they offer little resistance to metals diffusing through the pores and degrading the film[33]. If the pores are connected they form large open areas that can easily hold moisture and other ambient gases, leading to contamination and increase in the dielectric constant. For example, water has a dielectric constant of 80.4 and if water vapour was to infiltrate the pores it would drastically effect device performance. The pore size and pore density can also have consequences on the mechanical properties of the dielectric, with porous dielectrics generally being easier to damage as they have a lower Young's modulus than silicon dioxide. The severity of all these problems increase as the porosity percentage increases, making highly porous films difficult to integrate into the fabrication process[34,35].

1.1.2 Electromigration, Diffusion and Adhesion

Copper diffusion and electromigration into the dielectric layer are well studied phenomena[36,37]. Electromigration is the result of momentum transfer from the electrons to the atoms which make up the interconnect metal. Electromigration can lead to several consequences which can affect device performance such as voids, hillock formation and track thinning[12,38]. An example of a void is shown in Figure 1.4. Electromigration is primarily an interface related event due to the poor adhesion between the Cu and the ILD[39].

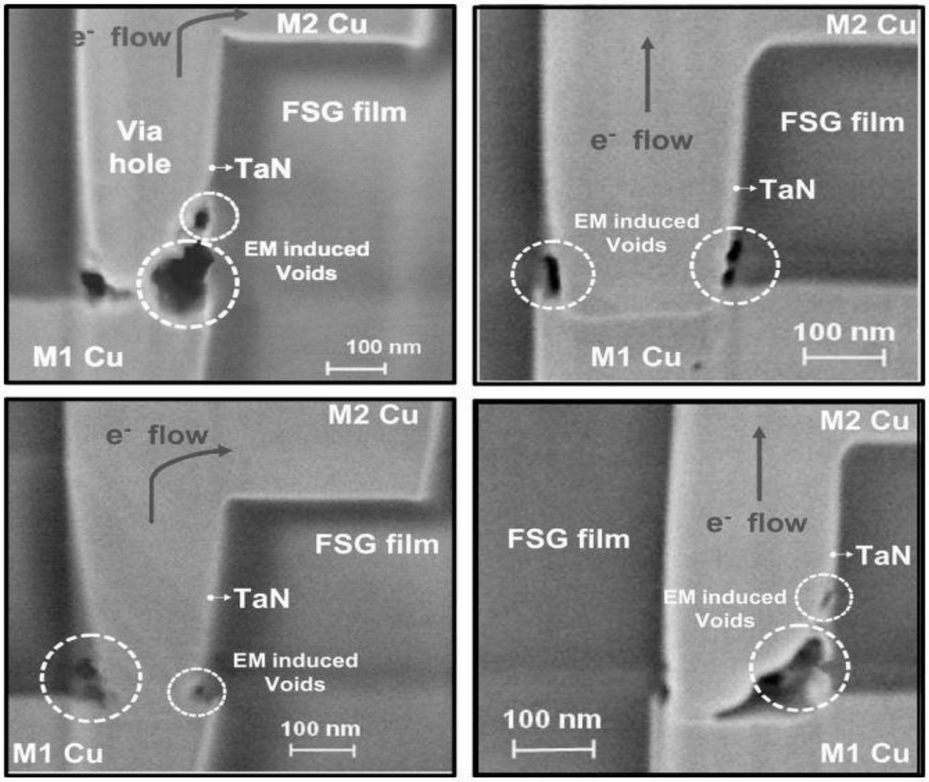

Figure 1.4 Transmission electron microscope (TEM) cross-sectional images of four failed samples after 19-50-hour electromigration testing. Voids were always found in the via sidewall and bottom corner[38].

Diffusion occurs when particles move from a region of high concentration to a region of low concentration. Copper's high mobility allows it to readily diffuse through silicon and silicon dioxide even at low temperatures. It is thought the diffusion process in copper is due to mobile copper ions[7,8]. To impede the diffusion of copper, barrier layers are inserted between the copper interconnect and the dielectric. These barriers prevent interdiffusion across the Cu-SiO_2 interface, as any copper in the silicon can produce deep electronic level traps in the silicon which will degrade device performance by permitting recombination of the minority carriers[40].

Barrier layers must meet several criteria which include, ensuring mechanical stability, demonstrating improved adhesion between the copper interconnect and ILD, be conformal on the surface, scalability, and they must also have a low resistance[25,28]. A tantalum (Ta) and tantalum nitride (TaN) stack, currently being used as the barrier layer of choice, gives a layered stack of Cu/TaN/Ta/SiO_2 [28,41]. As device miniaturisation continues, Ta/TaN can no longer meet these requirements because it demands more of the cross-sectional area of the line leaving less room for copper.

Over the last decade there has been considerable interest in the idea of a self-forming barrier which involves depositing a copper barrier metal alloy onto the dielectric surface. Following deposition of the alloy, the device is then annealed and the copper and the alloy metal separate, with the alloying metal migrating to all edges where it can chemically interact with the surface of the dielectric. The alloying metal must have a preference to chemically react with the dielectric rather than stay in its metallic form. Ideally, this reaction would be self-limiting to a few nanometres into the surface of the dielectric to ensure that the barrier layer remained thin. The alloying metals which have been considered as suitable candidates include aluminium[19,42], magnesium (Mg)[43], titanium (Ti)[44,45] and manganese (Mn)[15,46,47].

The microelectronics industry must contend with multilayer systems of dissimilar materials such as oxides, metals and dielectrics. The reliability and lifetime of the device all depend on how well these materials can bond or adhere together, making adhesion a major challenge from a fabrication viewpoint. Delamination is common in systems with poor interfacial adhesion and will ultimately lead to device failure. Poor adhesion can be related to a range of factors including deposition method, temperature, oxygen partial pressure during deposition, the type of substrate, purity of material being deposited and surface termination of the underlying substrate[48,49]. It has been revealed that copper deposited on SiO_2 and low-k dielectrics can show inferior adhesive strength and can be easily delaminated after annealing[15,50,51]. It has been proposed that this is due to the difference in thermal expansion between the copper and the underlying substrate[48].

As there is no one definitive way to measure adhesion this makes a quantitative analysis very difficult. At present there are over 200 techniques to measure adhesion of thin films such as four-point bending test, nanoindentation and scratch testing, blister test and tape testing[52–58]. These techniques can measure the modulus, hardness, interfacial strength and toughness of the thin film, and can give indications of the adhesive energy and strength. They are however, time consuming and can involve complicated microscopy analysis or modelling to yield results.

A simple peel test or tape test is one of the easiest and quickest ways to check for adhesion. Although, it is purely qualitative and gives no absolute value to the measure of adhesion it does provide a very valuable comparative method of adhesion analysis across a range of differently treated samples. The tape test has been used in industry to check the efficacy of copper adhesion to barriers. The tape is placed on a sample, normally copper deposited on a silicon substrate with or without a barrier metal, and then peeled off. If the metal remains on the substrate it is a pass, if the metal is removed from the substrate, it fails the test.

1.1.3 Atomic Layer Deposition (ALD) & Electroless Deposition (ELD)

As stated previously, with scaling the ability to deposit a uniform homogenous film is increasingly difficult with higher aspect ratios in vias and trenches. A variety of deposition techniques are used at different stages of the fabrication process such as plasma-enhanced CVD (PECVD), electron-beam (e-beam) evaporation, sputtering and electroplating just to name a few. However, these CVD and PVD techniques do not have the ability to reach the critical dimensions of the newest technology nodes with void free filling of small features increasingly becoming a significant challenge. For barrier layer formation on high aspect structures the main problem lies with coverage, thicker layers tend to form at the top, leaving the bottom of the line uncoated. This also makes it hard for the subsequently deposited copper to fill the line as displayed in Figure 1.5.

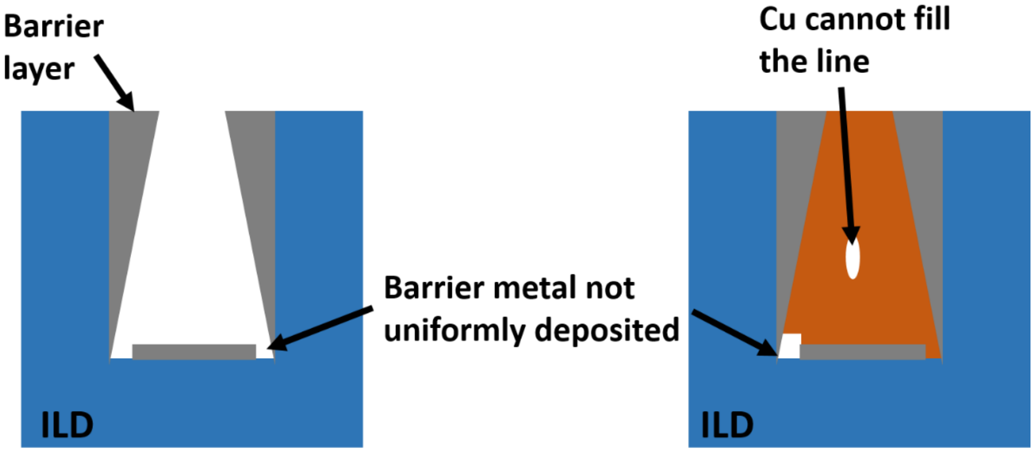

Figure 1.5 Schematic showing poor deposition of barrier metal and subsequent copper line.

ALD is a vapour phase technique that has exhibited the ability to deposit homogenous ultra-thin films of various materials. ALD was developed by Suntola in the 1970s and was originally called atomic layer epitaxy (ALE)[59]. ALD deposits a material one atomic layer at a time by using sequential, self-limiting reactions with different precursors. Many materials can be deposited via ALD such as metals, oxides and nitrides. ALD has many advantages over CVD and PVD deposition techniques such as precise thickness control at an atomic level. It is an extremely conformal and uniform deposition technique which does not require line of sight like most other techniques. Since the precursors are in a gaseous phase they can infiltrate even the smallest of spaces so high aspect ratio features or samples with 3D geometry are readily coated. The deposited film is continuous due to the self-limiting nature of the reactions and defects such as pinholes are much less likely to occur[60,61].

Figure 1.6 displays one complete cycle of the ALD process for depositing aluminium oxide, Al_2O_3. In Figure 1.6(a) the bare substrate is ready for the first "half-cycle" in which the first metal organic reactive precursor is introduced until the surface has become saturated, Figure 1.6(b). The precursor is pulsed into the chamber and given sufficient time for it to react with the surface in a self-limiting manner. This allows for a single monolayer to form at the surface. In Figure 1.6(c) and (d) a carrier gas is used to purge the chamber of any unreacted precursor or by-products of the reaction. The carrier gas is usually either nitrogen, (N_2) or argon, (Ar) but this can depend on the material being deposited. This is followed by the second "half-cycle" in Figure 1.6(e), where the substrate is exposed to the reactive gas or plasma, which in the case of Al_2O_3 growth is water. Following another purge (Figure 1.6(f)) one monolayer of metal oxide material has been successfully deposited (Figure 1.6(g)). This process is repeated until the desired film thickness is attained[20,60,61]. Other factors such as sample temperature and chamber pressure are important during deposition, but these can depend on the nature of the material being deposited.

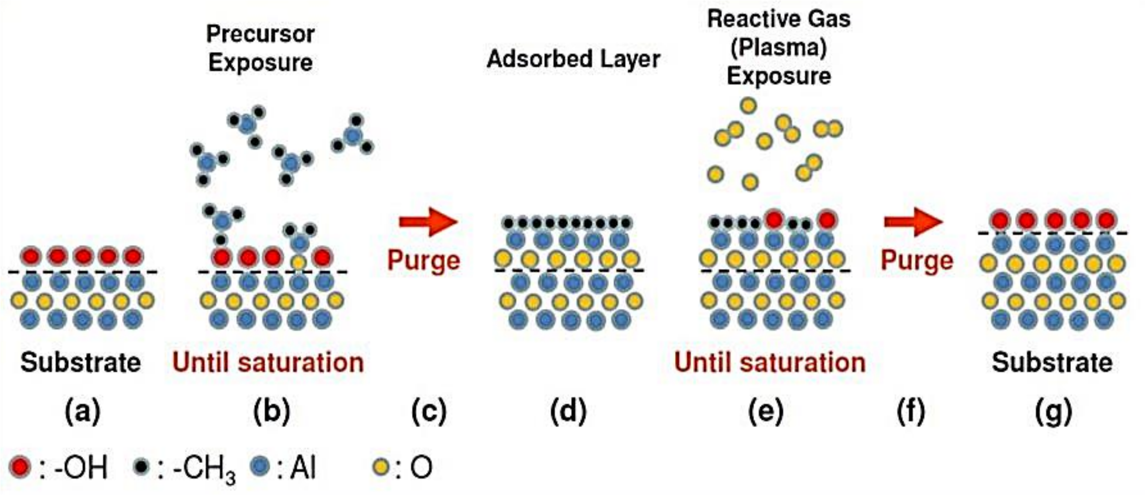

Figure 1.6 Schematic illustrating one full cycle of the ALD process to deposit a thin Al2O3 film[60]

For some materials the thermal energy received from heating the sample during deposition is insufficient to allow the precursors to chemically react. Also, some single-element materials such as metals and semiconductors are not compatible with the normal ALD process. In this case a plasma is employed to promote the desired reactions, this is known as plasma enhanced ALD (PEALD). Plasmas produce a range of species such as highly reactive radicals and ions, which are used to facilitate the chemical reactions that cannot take place with either thermal energy or other gas reactants. It has been reported however, that PEALD has reduced conformality compared to traditional ALD and that the plasma can damage the sample[60,62,63].

ELD is a highly selective and conformal electrochemical deposition technique. It is reported to have first been developed by the Moche Indians of Peru ~100 BC when they electroless deposited gold onto copper masks[64]. Films produced by ELD are very uniform and can be used for depositing in high aspect ratio trenches either for barriers or for filling the copper line[65,66]. In ELD, a metal is deposited by an autocatalytic process where metal ions are reduced by a chemical agent in a solution. ELD is different from electroplating in that it does not require an external current source and so can be used to deposit metals on insulating surfaces as well as conducting ones. However, ELD does require a metal on metal contact so insulating surfaces are activated with a catalyst layer such as palladium (Pd) or Co, then the metal of interest can be deposited. Most common metals for ELD include copper, cobalt, nickel (Ni), gold (Au), silver (Ag) and a range of alloys.

The ELD solution can be quite complex and is generally made up of metal ions, reducing agents and pH buffers. For depositing cobalt, the most common reducing agents are phosphorus or boron-based compounds. These however, can become incorporated into the film. To deposit Co, a Pd catalyst is first deposited from a $PdCl_2$ solution. The Pd forms small nano-islands across the surface with diameters of ~6-10 nm[67]. Once the Pd activated surface is introduced to the ELD Co solution, both metals are reduced which allows nucleation of the cobalt. The cobalt then grows from these nucleation sites to form a mostly metallic thin film[21].

There are some disadvantages to this process which can lead to unsatisfactory results. The solution can age quickly and so should be made just as it is about to be used. The reaction creates by-products which can affect the deposition. The reducing agents can become incorporated into the film. The metal can sometimes fail to nucleate on the surface due to contamination[21]. Although ELD shows great promise for future integration into the fabrication process it is still a novel technique for depositing on such small length scales and requires more investigation.

1.2 Self-Assembled Monolayers (SAMs)

Self-assembled monolayers or SAMs have garnered a lot of attention from many disciplines of the scientific community for almost forty years starting when Sagiv[68] succeeded in preparing silane based monolayers and Nuzzo and Allara[69] succeeded in preparing ordered monolayers of thiols on gold for the first time. During this time, research on SAMs has expanded rapidly with an increasing range of applications for the use of such monolayers. There is particular interest in their use in the area of biosensors[70,71] and of course for use in the microelectronics industry.

SAMs are essentially two-dimensional nanomolecular assemblies which can display large scale ordering via weak van der Waals interactions, when deposited on a surface. The SAM is comprised of three segments: the head group, the hydrocarbon segment and the terminal functional group as displayed in Figure 1.7. The head group is chosen to ensure a strong affinity for the substrate and permits the bonding of the SAM to the surface. It is this segment of the SAM that impacts the surface coverage and thermal stability of the SAM. The hydrocarbon chain impacts on the SAM thickness, packing density and crystallinity. This segment which usually consists of alkyl chains is frequently tilted with respect to the surface and uses lateral interactions to minimise free volume. The terminal function group is the part of the SAM furthest from the surface and this segment impacts on the adhesion between subsequently deposited metal films and the SAM.

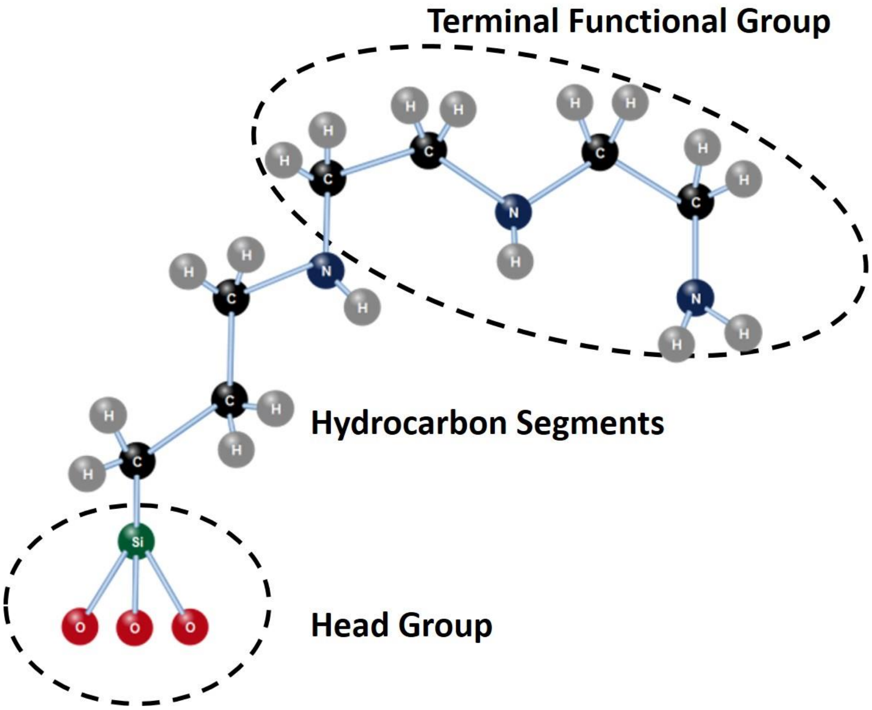

Figure 1.7 Figure of the DETA SAM showing the different segments, the head group, hydrocarbon chain and the terminal functional group.

Thiol SAMs deposited on metals, with gold mainly being the metal of choice, represent the most studied group of SAMs with many reviews and papers detailing their deposition and many functions[72–75]. Thiol SAMs on gold represent a model system which has primarily been studied for several reasons: (i) it is easy to deposit a uniform gold film (ii) gold does not form a stable oxide making it easy to work with in ambient conditions (iii) sulphur has a strong affinity for noble metals especially gold and forms a strong covalent bond and (iv) gold is easily cleaned[76]. There are many different types of SAMs including silane based SAMs and phosphonic acid based SAMs[77,78] which are of interest in the microelectronics industry.

The main SAM employed throughout this study is a silane-based SAM known as (3-trimethoxysilylpropyl) diethylenetriamine or DETA SAM which contains the elements silicon, oxygen, carbon, nitrogen and hydrogen and it is designed to chemically bond to a SiO2 surface. The terminal functional group of the DETA SAM contains nitrogen which is of interest due to its adhesion properties with copper. All of the SAMs utilised in this study were prepared in IMEC in Belgium and subsequently packaged and shipped to DCU for surface modification and characterisation.

1.2.1 Surface Bonding and Deposition of SAMs

SAMs can be deposited several different ways, for example liquid tank phase, vapour phase, spin-on[79,80], micro-contact printing[81] and by supercritical fluids[82]. The two most commonly used methods, liquid tank and vapour phases, will be described here. These two methods are compatible with standard fabrication processes already in use in the semiconductor industry and they show the best coverage. Before deposition however, the surface must be modified to allow the SAMs to create a chemical bond with the surface. The silicon dioxide surface can be pre-treated by a variety of different treatments including plasma activation,[83,84] piranha cleaning,[85,86] or an RCA process[87] prior to SAM deposition. The purpose of these treatments is to make the surface more hydrophilic and to generate OH terminal groups at the surface to facilitate the SAMs adherence to the silicon dioxide surface. The SAM bonds to the hydroxyl terminated surface via a hydrolysis reaction resulting in the elimination of water to form a direct covalent bond between the Si in the SAM head group and the oxygen from the surface terminating group[74,85,88] which is schematically shown in Figure 1.8.

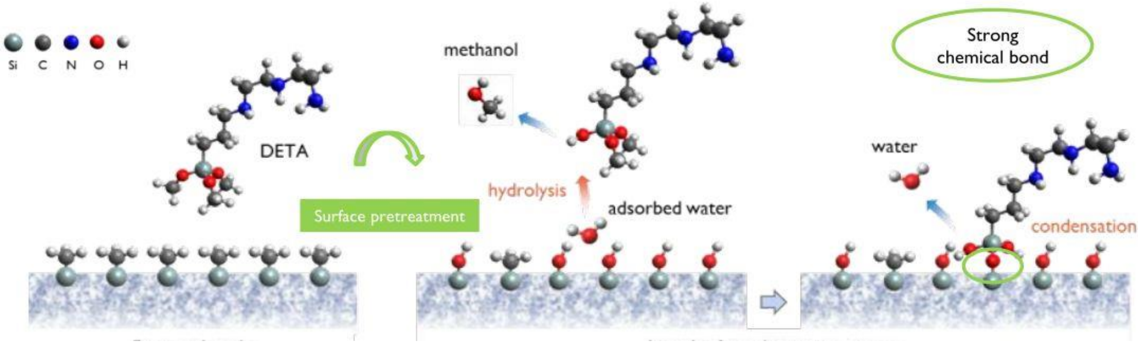

Figure 1.8 ***SAM molecule adhering to the surface.*** *On the left a pristine wafer before treatments and the SAM molecule. The middle diagram shows the change in the surface after the pre-treatments, now the surface has OH terminal groups that will bond to the head group of the SAM with the expulsion of methanol. In the diagram on the right the SAM has now made a strong chemical bond with the surface as water is expelled.*

In a liquid tank deposition, illustrated in Figure 1.9, the OH terminated silicon substrate is immersed in a tank containing a dilute silane solution which contains the SAM precursor molecules dissolved in a solution such as ethanol or carbon tetrachloride[85]. The substrate is left in the solution for several hours maybe up to 24 hours to allow the SAMs to chemisorb to the surface. The longer the deposition the higher the quality of the SAMs film. The substrate is then removed and rinsed multiple times with solvents to remove any unbonded molecules and finally it is dried with N_2. The main disadvantages of this method are the length of time taken to form an ordered monolayer and the large quantities of solvents used[75,85].

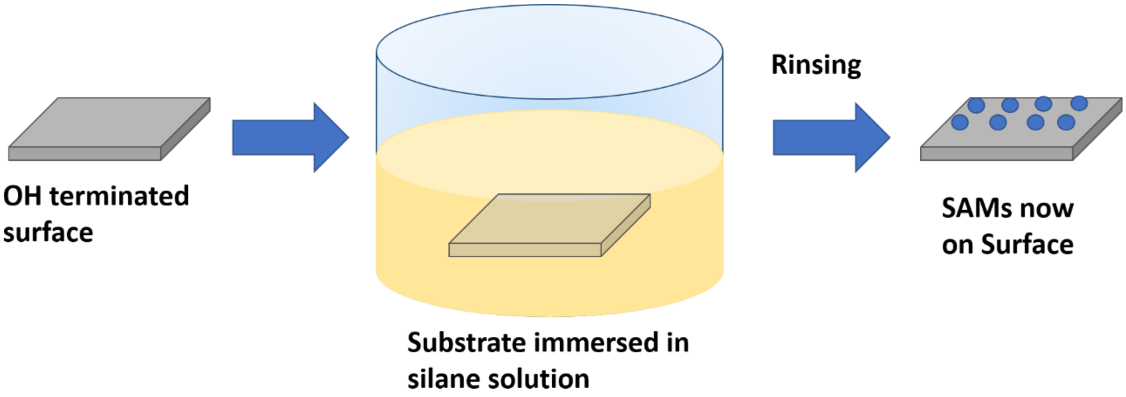

Figure 1.9 Schematic of the liquid tank deposition process.

Vapour phase deposition is usually carried out in a UHV chamber where the silane precursor is heated until it evaporates, shown in Figure 1.10. The vaporised SAM then assembles on the surface. This form of deposition is much quicker than the liquid phase technique and uses much less solvent. It is also advantageous as in-situ pre- and post-analysis can be performed. The main drawback is the density of the SAMs film is said to be lower for this type of deposition[75].

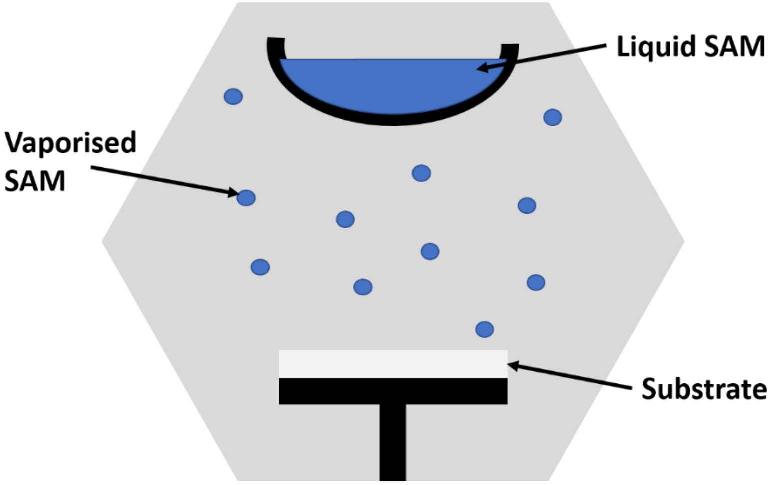

Figure 1.10 Schematic showing the deposition of SAMs via the vapour phase technique.

1.2.2 How can SAMs Benefit the Microelectronics Industry?

Silane based SAMs are of particular interest to the microelectronics industry for a variety of reasons. With a thickness in the nanometre dimensional range, depending on the chain length, there is little overall increase in resistivity owing to the cross-sectional area of the line mainly being occupied by copper. Due to the strong covalent bond formed between the silane head group of the SAM and the silicon substrate they are highly stable against thermal desorption and can create a near perfect monolayer with low defect density. They can form on differently oriented surfaces making conformal deposition effortless. Different patterns of SAMs can be fabricated by various deposition techniques such as micro contact printing[81]. They can be used as a blocker to prevent film growth on a surface. Most importantly they can be used to tailor the interfacial properties of the underlying substrate. This can make a deposited metal film adhere more easily to a SAM terminated SiO_2 surface than to the untreated surface, by altering the chemistry of the terminal functional group[72,74,77].

Technically these attributes can be used for a variety of different applications. SAMs have been proposed as an ideal pore sealant for porous low-*k* dielectric materials as they are of a comparable size to the pores[80,89,90]. It has been suggested that SAMs could even be considered as a barrier layer themselves as they possess many of the barrier layer criteria[91,92].

Area-selective ALD allows the deposition of a material on only certain parts of the underlying sample. It has been proposed that SAMs could be used as a blocker for area-selective ALD. On a patterned surface consisting of alternate lines of copper and SiO_2, a silane-based SAM could be deposited which would preferentially bond to the SiO_2. Subsequently a metal could be deposited by ALD which would adhere to the copper and not the SAM terminated SiO_2. This could also be performed the other way around with the SAM attached to the copper leaving the material to deposit only on the SiO_2[93–95].

Finally, SAMs can help activate the surface for ELD deposition on insulating dielectric materials. Unlike electroplating, ELD can be used to deposit on insulating materials but it needs a catalyst. For ELD Co, palladium acts as a catalyst but first the SAMs are used to trap the palladium.

1.3 Thesis Layout and Organisation

Chapter 2 of this thesis introduces some of the various analysis techniques used in this study. It outlines the principles behind their operation and analysis methods following data collection. The principle technique employed in this work is X-ray photoelectron spectroscopy (XPS) with secondary techniques including hard x-ray photoelectron spectroscopy (HAXPES) and atomic force microscopy (AFM) also explained. The ultra-high vacuum (UHV) XPS system used for experiments is briefly described along with the Diamond Light Source beamline I09 where HAXPES measurements were obtained. The Veeco Dimension AFM is also described.

In Chapter 3 the interaction of a thin manganese film deposited on a DETA SAM is investigated. This chapter can be separated into three sections. The first section deals with the characterisation of the DETA SAM. Its chemical composition along with its stability in UHV is explored. The next section looks at the interaction of the manganese film with the DETA SAM deposited on a native silicon oxide substrate. With the final section detailing the interaction of the manganese with the DETA SAM deposited on a low-*k* spin-on-glass (SOG) substrate.

Chapter 4 presents a comparative study on the effect the chain length and composition of the terminal group has on the nucleation and adhesion of subsequent deposited copper film. Three different SAMs are employed, one with no terminal group and two with amino terminal groups. The two amino-terminated SAMs also have varying chain lengths. XPS, 4-point probe and AFM are used to characterise both thin and thick copper films. A new method for semi-quantitative analysis for tape test measurements is introduced.

Chapter 5 focuses on the effects of in-situ atomic oxygen treatments of SAM terminated dielectric substrates. The atomic oxygen is analogous to O_2 plasma which is frequently used in ALD, where oxygen radicals react with the sample. Two different self-assembled monolayers, the DETA and a long chain carbon SAM, are subjected to small highly controlled exposures of atomic oxygen. The manner in which these SAMs are impacted by this oxygen etch treatment is investigated.

HAXPES investigation of the role of SAMs in cobalt electroless deposition is reported in Chapter 6. This chapter looks at replacing copper interconnects with cobalt via a novel deposition technique which is compatible with standard microprocessor fabrication methods. The chemical composition of the cobalt film and the interactions at the Si-Co interface are investigated.

And finally, Chapter 7 reviews the main findings of this work and suggests some possible future studies that could be explored.

1.4 References

(1) Vyas, A. A.; Zhou, C.; Yang, C. Y. On-Chip Interconnect Conductor Materials for End-of-Roadmap Technology Nodes. *IEEE Trans. Nanotechnol.* **2018**, *17* (c), 1–1.

(2) Moore, G. E. Cramming More Components onto Integrated Circuits. *Electronics* **1965**, *38* (8), 114–117.

(3) Intel. Intel Technology and Manufacturing Day in China Showcases 10 nm Updates, FPGA Progress and Industry's First 64-Layer 3D NAND for Data Center https://newsroom.intel.com/newsroom/wpcontent/uploads/sites/11/2017/09/mark-bohr-on-intels-technology-leadership.pdf (accessed Jan 22, 2018).

(4) Zhao, L. Tech Brief: An Introduction to Interconnects https://blog.lamresearch.com/tech-brief-an-introduction-to-interconnects/.

(5) Auth, C.; Aliyarukunju, A.; Asoro, M.; Bergstrom, D.; Bhagwat, V.; Birdsall, J.; Bisnik, N.; Buehler, M.; Chikarmane, V.; Ding, G.; Fu, Q.; Gomez, H.; Han, W.; Hanken, D.; Haran, M.; Hattendorf, M.; Heussner, R.; Hiramatsu, H.; Ho, B.; Jaloviar, S.; Jin, I.; Joshi, S.; Kirby, S.; Kosaraju, S.; Kothari, H.; Leatherman, G.; Lee, K.; Leib, J.; Madhavan, A.; Marla, K.; Meyer, H.; Mule, T.; Parker, C.; Parthasarathy, S.; Pelto, C.; Pipes, L.; Post, I.; Prince, M.; Rahman, A.; Rajamani, S.; Saha, A.; Santos, J. D.; Sharma, M.; Sharma, V.; Shin, J.; Sinha, P.; Smith, P.; Sprinkle, M.; Amour, A. St.; Staus, C.; Suri, R.; Towner, D.; Tripathi, A.; Tura, A.; Ward, C.; Yeoh, A. A 10nm High Performance and Low-Power CMOS Technology Featuring 3rd Generation FinFET Transistors, Self-Aligned Quad Patterning, Contact over Active Gate and Cobalt Local Interconnects. *2017 IEEE Int. Electron Devices Meet.* **2017**, 29.1.1-29.1.4.

(6) Mont, F. W.; Zhang, X.; Wang, W.; Kelly, J. J.; Standaert, T. E.; Quon, R.;

Todd, E. Cobalt Interconnect on Same Copper Barrier Process Integration at the 7nm Node. In *IITC 2017 - 2017 IEEE International Interconnect Technology Conference*; 2017; pp 7–9.

(7) Willis, B. G.; Lang, D. V. Oxidation Mechanism of Ionic Transport of Copper in SiO_2 Dielectrics. *Thin Solid Films* **2004,** 467, 284-293.

(8) Fisher, I.; Eizenberg, M. Copper Ion Diffusion in Porous and Nonporous SiO_2-Based Dielectrics Using Bias Thermal Stress and Thermal Stress Tests. *Thin Solid Films* **2008,** 516 (12), 4111-4121.

(9) Raghavan, G.; Chiang, C.; Anders, P. B.; Tzeng, S.-M.; Villasol, R.; Bai, G.; Bohr, M.; Fraser, D. B. Diffusion of Copper through Dielectric Films under Bias Temperature Stress. *Thin Solid Films* 1995, 262, 168-176.

(10) Kohn, A.; Lipp, E.; Eizenberg, M.; Shacham-Diamand, Y. Copper-Related Degradation of SiO_2 in Metal-Oxide-Semiconductor Capacitors Subjected to Bias Thermal Stress: Leakage of the Minority Charge Carriers in the Inversion Layer. *Appl. Phys. Lett.* **2004,** 85 (4), 627-629.

(11) Lipp, E.; Kohn, A.; Eizenberg, M. Lifetime-Limited Current in Cu-Gate Metal-Oxide-Semiconductor Capacitors Subjected to Bias Thermal Stress. *J. Appl. Phys.* **2006,** 99 (3), 034504.

(12) Li, B.; Christiansen, C.; Badami, D.; Yang, C. C. Electromigration Challenges for Advanced On-Chip Cu Interconnects. *Microelectron. Reliab.* **2014**, *54* (4), 712–724.

(13) Neishi, K.; Aki, S.; Matsumoto, K.; Sato, H.; Itoh, H.; Hosaka, S.; Koike, J. Formation of a Manganese Oxide Barrier Layer with Thermal Chemical Vapor Deposition for Advanced Large-Scale Integrated Interconnect Structure. *Appl. Phys. Lett.* **2008**, *93* (3), 3–6.

(14) Ablett, J. M.; Woicik, J. C.; Tőkei, Z.; List, S.; Dimasi, E. Phase Identification

of Self-Forming Cu-Mn Based Diffusion Barriers on p-SiOC:H and SiO_2 Dielectrics Using x-Ray Absorption Fine Structure. *Appl. Phys. Lett.* **2009**, *94* (4), 28–31.

(15) Byrne, C.; Brennan, B.; McCoy, A. P.; Bogan, J.; Brady, A.; Hughes, G. In Situ XPS Chemical Analysis of $MnSiO_3$ Copper Diffusion Barrier Layer Formation and Simultaneous Fabrication of Metal Oxide Semiconductor Electrical Test MOS Structures. *ACS Appl. Mater. Interfaces* **2016**, *8* (4), 2470–2477.

(16) Xie, Q.; Qu, X. P.; Tan, J. J.; Jiang, Y. L.; Zhou, M.; Chen, T.; Ru, G. P. Superior Thermal Stability of Ta/TaN Bi-Layer Structure for Copper Metallization. *Appl. Surf. Sci.* **2006**, *253* (3), 1666–1672.

(17) Traving, M.; Zienert, I.; Zschech, E.; Schindler, G.; Steinhögl, W.; Engelhardt, M. Phase Analysis of TaN/Ta Barrier Layers in Sub-Micrometer Trench Structures for Cu Interconnects. *Appl. Surf. Sci.* **2005**, *252* (1), 11–17.

(18) Van Der Veen, M. H.; Vandersmissen, K.; Dictus, D.; Demuynck, S.; Liu, R.; Bin, X.; Nalla, P.; Lesniewska, A.; Hall, L.; Croes, K.; Zhao, L.; Bömmels, J.; Kolics, A.; Tökei, Z. Cobalt Bottom-up Contact and via Prefill Enabling Advanced Logic and DRAM Technologies. In *2015 IEEE International Interconnect Technology Conference and 2015 IEEE Materials for Advanced Metallization Conference, IITC/MAM 2015*; 2015; pp 25–27.

(19) Byrne, C.; Brennan, B.; Lundy, R.; Brady, A.; Hurley, P.; Hughes, G. Physical, Chemical and Electrical Characterisation of the Diffusion of Copper in Silicon Dioxide and Prevention via a CuAl Alloy Barrier Layer System. *Mater. Sci. Semicond. Process.* **2017**, *63* (February), 227–236.

(20) Johnson, R. W.; Hultqvist, A.; F, B. S. A Brief Review of Atomic Layer Deposition: From Fundamentals to Applications. *Mater. Today* **2014**, *17* (5), 236.

(21) Shacham-Diamand, Y.; Osaka, T.; Okinaka, Y.; Sugiyama, A.; Dubin, V. 30

Years of Electroless Plating for Semiconductor and Polymer Micro-Systems. *Microelectron. Eng.* **2015**, *132*, 35–45.

(22) Edelstein, D.; Heidenreich, J.; Goldblatt, R.; Cote, W.; Uzoh, C.; Lustig, N.; Roper, P.; McDevitt, T.; Motsiff, W.; Simon, a.; Dukovic, J.; Wachnik, R.; Rathore, H.; Schulz, R.; Su, L.; Luce, S.; Slattery, J. Full Copper Wiring in a Sub-0.25 Mm CMOS ULSI Technology. *Electron Devices Meet. 1997. IEDM '97. Tech. Dig. Int.* **1997**, *4*, 773–776.

(23) Bohr, M. Interconnect Scaling-the Real Limiter to High Performance ULSI. *Proceesings of the IEEE International Electronic Devices Meeting*. 1995, pp 241–244.

(24) Li, B.; Sullivan, T. D.; Lee, T. C.; Badami, D. Reliability Challenges for Copper Interconnects. *Microelectron. Reliab.* **2004**, *44* (3), 365–380.

(25) Baklanov, M.; Ho, P. S.; Zschech, E. *Advanced Interconnects for ULSI Technology*; Baklanov, M., Ho, P. S., Zschech, E., Eds.; Wiley: West Sussex, 2012, pp 1-19.

(26) Tőkei, Z. End of Cu Roadmap and beyond Cu. In *2016 IEEE International Interconnect Technology Conference / Advanced Metallization Conference (IITC/AMC)*; 2016, 1-58.

(27) Maex, K.; Baklanov, M. R.; Shamiryan, D.; Iacopi, F.; Brongersma, S. H.; Yanovitskaya, Z. S. Low Dielectric Constant Materials for Microelectronics. *J. Appl. Phys.* **2003**, *93* (11), 8793–8841.

(28) Gupta, T. *Copper Interconnect Technology*, 1st ed.; Springer: Watertown, USA, 2009, pp 67-110.

(29) Ho, P. S.; Leu, J.; Lee, W. W. Overview on Low Dielectric Constant Materials for IC Applications. In *Low Dielectric Constant Materials for IC Applications*; Ho, P. S., Leu, J., Lee, W. W., Eds.; Springer: Germany, 2003; pp 1–19.

(30) Volksen, W.; Miller, R.; Dubois, G. Low Dielectric Constant Materials. *Chem. Rev.* **2010**, *110*, 56–110.

(31) Palov, A.; Rakhimova, T. V.; Krishtab, M. B.; Baklanov, M. R. Dependence of Dielectric Constant of SiOCH Low-k Films on Porosity and Pore Size. *J. Vac. Sci. Technol. B, Nanotechnol. Microelectron. Mater. Process. Meas. Phenom.* **2015**, *33* (2), 020603.

(32) El Sabahy, J.; Castellan, G.; Ricoul, F.; Jousseaume, V. Porous SiOCH Thin Films Obtained by Foaming. *J. Phys. Chem. C* **2016**, *120* (17), 9184–9191.

(33) Bogan, J.; Lundy, R.; P. McCoy, A.; O'Connor, R.; Byrne, C.; Walsh, L.; Casey, P.; Hughes, G. In-Situ Surface and Interface Study of Atomic Oxygen Modified Carbon Containing Porous Low-κ Dielectric Films for Barrier Layer Applications. *J. Appl. Phys.* **2016**, *120* (10), 105305.

(34) Michalak, D. J.; Blackwell, J. M.; Torres, J. M.; Sengupta, A.; Kreno, L. E.; Clarke, J. S.; Pantuso, D. Porosity Scaling Strategies for Low-k Films. *J. Mater. Res.* **2015**, *30* (22), 3363–3385.

(35) Vanstreels, K.; Wu, C.; Baklanov, M. R. Mechanical Stability of Porous Low-k Dielectrics. *ECS J. Solid State Sci. Technol.* **2014**, *4* (1), N3058–N3064.

(36) McBrayer, J.; Swanson, R. M.; Sigmon, T. W. Diffusion of Metals in SiO_2. *J. Electrochem. Soc.* **1986**, *133* (6).

(37) Thompson, C. V; Lloyd, J. R. Electromigration and IC Interconnects. *MRS Bull.* **1993**, *18* (12), 19–25.

(38) Hsu, Y. L.; Fang, Y. K.; Chiang, Y. T.; Chen, S. F.; Lin, C. Y.; Chou, T. H.; Chang, S. H. Failure Mechanism of Electromigration in Via Sidewall for Copper Dual Damascene Interconnection. *J. Electrochem. Soc.* **2006**, *153* (8), G782.

(39) Frank L. Wei, Chee Lip Gan, Tam Lyn Tan, Christine S. Hau-Riege, Amit P.

Marathe, Joost J. Vlassak, and C. V. T. Electromigration-Induced Extrusion Failures in Cu/Low-k Interconnects. *J. Appl. Phys.* **2008**, *104, 023529*.

(40) Baumann, J.; Kaufmann, C.; Rennau, M.; Werner, T.; Gessner, T. Investigation of Copper Metallization Induced Failure of Diode Structures with and without a Barrier Layer. *Microelectron. Eng.* **1997**, *33* (1–4), 283–291.

(41) He, M.; Lu, T.-M. *Metal-Dielectric Interfaces in Gigascale Electronics: Thermal and Elcetrical Stability*; Springer: New York USA, 2012, pp 57-89.

(42) Byrne, C.; Brady, A.; Walsh, L.; McCoy, A. P.; Bogan, J.; McGlynn, E.; Rajani, K. V.; Hughes, G. Chemical and Electrical Characterisation of the Segregation of Al from a CuAl Alloy (90%:10% Wt) with Thermal Anneal. *Thin Solid Films* **2016**, *599*, 59–63.

(43) Suwwan De Felipe, T.; Murarka, S. P.; Bedell, S.; Lanford, W. A. Capacitance-Voltage, Current-Voltage, and Thermal Stability of Copper Alloyed with Aluminium or Magnesium. *Thin Solid Films* **1998**, *335* (1–2), 49–53.

(44) Len, V. S. C.; Hurley, R. E.; McCusker, N.; McNeill, D. W.; Armstrong, B. M.; Gamble, H. S. Investigation into the Performance of Diffusion Barrier Materials against Copper Diffusion Using Metal-Oxide-Semiconductor (MOS) Capacitor Structures. *Solid. State. Electron.* **1999,** 43 (6), 1045-1049.

(45) Franz, M.; Ecke, R.; Kaufmann, C.; Kriz, J.; Schulz, S. E. Investigation of Barrier Formation and Stability of Self-Forming Barriers with CuMn, CuTi and CuZr Alloys. *2015 IEEE Int. Interconnect Technol. Conf. 2015 IEEE Mater. Adv. Met. Conf. IITC/MAM 2015* **2015**, *156*, 95–97.

(46) Koike, J.; Wada, M. Self-Forming Diffusion Barrier Layer in Cu-Mn Alloy Metallization. *Appl. Phys. Lett.* **2005**, *87* (4), 1–4.

(47) Lozano, J. G.; Bogan, J.; Casey, P.; McCoy, A. P.; Hughes, G.; Nellist, P. D. Scanning Transmission Electron Microscopy Investigations of Self-Forming

Diffusion Barrier Formation in Cu(Mn) Alloys on SiO_2. *APL Mater.* **2013**, *1* (4).

(48) Nagao, K.; Neaton, J. B.; Ashcroft, N. W. First-Principles Study of Adhesion at Cu/SiO_2 Interfaces. *Phys. Rev. B* **2003**, *68* (7), 125403.

(49) Mittal, K. L. Adhesion Measurement of Thin Films. *Electrocompon. Sci. Technol.* **1976**, *3* (1), 21–42.

(50) Au, Y.; Lin, Y.; Gordon, R. G. Filling Narrow Trenches by Iodine-Catalyzed CVD of Copper and Manganese on Manganese Nitride Barrier/Adhesion Layers. *J. Electrochem. Soc.* **2011**, *158* (5), D248.

(51) Roy, G.; Kim, H.; Au, Y.; Wang, H.; Harish, B.; Liu, Y.; Lee, D. K.; Chemical, Y. L.; Link, C.; Gordon, R. G.; Bhandari, H. B. Chemical Vapor Deposition (CVD) of Manganese Self-Aligned Diffusion Barriers for Cu Interconnections in Microelectronics. In *Advanced Metallization Conference 2008*; San Diego, Califonia, 2008, pp 1-9.

(52) Gandhi, D. D.; Lane, M.; Zhou, Y.; Singh, A. P.; Nayak, S.; Tisch, U.; Eizenberg, M.; Ramanath, G. Annealing-Induced Interfacial Toughening Using a Molecular Nanolayer. *Nature* **2007**, *447* (7142), 299–302.

(53) Kleinbichler, A.; Pfeifenberger, M. J.; Zechner, J.; Moody, N. R.; Bahr, D. F.; Cordill, M. J. New Insights into Nanoindentation-Based Adhesion Testing. *Jom* **2017**, *69* (11), 2237–2245.

(54) Lahmar, A.; Assaf, A.; Durand, M. J.; Jouanneau, S.; Thouand, G.; Garnier, B. Factors Influencing Adhesion of Submicrometer Thin Metal Films: A Critical Review. *Rev. Adhes. Adhes.* **2016**, *4* (1), 47–68.

(55) Kleinbichler, A.; Zechner, J.; Cordill, M. J. Buckle Induced Delamination Techniques to Measure the Adhesion of Metal Dielectric Interfaces. *Microelectron. Eng.* **2017**, *167*, 63–68.

(56) Le Houérou, V.; Gauthier, C.; Schirrer, R. Energy Based Model to Assess

Interfacial Adhesion Using a Scratch Test. *J. Mater. Sci.* **2008**, *43* (17), 5747–5754.

(57) Boddaert, X.; Covarel, G.; Bensaid, B.; Mattei, M.; Benaben, P.; Bois, J. Organic Ultrathin Film Adhesion on Compliant Substrate Using Scratch Test Technique. *Thin Solid Films* **2013**, *528*, 194–198.

(58) Volinsky, A. A.; Moody, N. R.; Gerberich, W. W. Interfacial Toughness Measurements for Thin Films on Substrates. *Acta Mater.* **2002**, *50* (3), 441–466.

(59) Seidel, T. E. Atomic Layer Deposition. In *Handbook of Semiconductor Manufacturing Technology*; Doering, R., Nishi, Y., Eds.; CRC Press: Florida, 2008, pp 14-1 – 14-37.

(60) Oehrlein, G. S.; Metzler, D.; Li, C. Atomic Layer Etching at the Tipping Point: An Overview. *ECS J. Solid State Sci. Technol.* **2015**, *4* (6), N5041–N5053.

(61) George, S. M. Atomic Layer Deposition: An Overview. *Chem. Rev.* **2010**, *110* (1), 111–131.

(62) Profijt, H. B.; Potts, S. E.; van de Sanden, M. C. M.; Kessels, W. M. M. Plasma-Assisted Atomic Layer Deposition: Basics, Opportunities, and Challenges. *J. Vac. Sci. Technol. A Vacuum, Surfaces, Film.* **2011**, *29* (5), 050801.

(63) Kim, H.; Oh, I. Review of Plasma-Enhanced Atomic Layer Deposition : Technical Enabler of Nanoscale Device Fabrication Review of Plasma-Enhanced Atomic Layer Deposition: Technical Enabler of Nanoscale Device Fabrication. *Jpn. J. Appl. Phys.* **2014**, *53*, 03DA01 1-7.

(64) Greene, J. E. Tracing the 5000-Year Recorded History of Inorganic Thin Films from ~3000 BC to the Early 1900s AD. *Appl. Phys. Rev.* **2014**, *1* (4), 041302.

(65) Chen, S. Te; Liu, Y. Y.; Chen, G. S. Ultrathin Cobalt-Alloyed Barrier Layers for Copper Metallization by a New Seeding and Electroless-Deposition Process.

Appl. Surf. Sci. **2015**, *354*, 144–147.

(66) Yang, Z.; Li, N.; Wang, X.; Wang, Z.; Wang, Z. Bottom-Up Filling in Electroless Plating with an Addition of PEG–PPG Triblock Copolymers. *Electrochem. Solid-State Lett.* **2010**, *13* (7), D47.

(67) Kind, H.; Bittner, A. M.; Cavalleri, O.; Kern, K.; Greber, T. Electroless Deposition of Metal Nanoislands on Aminothiolate-Functionalized Au(111) Electrodes. *J. Phys. Chem. B* **1998**, *102* (39), 7582–7589.

(68) Sagiv, J. Organized Monolayers by Adsorption. 1. Formation and Structure of Oleophobic Mixed Monolayers on Solid Surfaces. *J. Am. Chem. Soc.* **1980**, *102* (1), 92–98.

(69) Nuzzo, R. G.; Allara, D. L. Adsorption of Bifunctional Organic Disulfides on Gold Surfaces. *J. Am. Chem. Soc.* **1983**, *105* (13), 4481–4483.

(70) Chaki, N. K.; Vijayamohanan, K. Self-Assembled Monolayers as a Tunable Platform for Biosensor Applications. *Biosens. Bioelectron.* **2002**, *17* (1–2), 1–12.

(71) Emmenegger, C. R.; Brynda, E.; Riedel, T.; Sedlakova, Z.; Houska, M.; Alles, A.B. Interaction of Blood Plasma with Antifouling Surfaces. *Langmuir* **2009**, *25* (11), 6328–6333.

(72) Love, J. C.; Estroff, L. A.; Kriebel, J. K.; Nuzzo, R. G.; Whitesides, G. M. *Self-Assembled Monolayers of Thiolates on Metals as a Form of Nanotechnology*; 2005; Vol. 105.

(73) Ulman, A. Formation and Structure of Self-Assembled Monolayers. *Chem. Rev.* **1996**, *96* (4), 1533–1554.

(74) Schreiber, F. Structure and Growth of Self-Assembling Monolayers. *Prog. Surf. Sci.* **2000**, *65* (5–8), 151–256.

(75) Kind, M.; Wöll, C. Organic Surfaces Exposed by Self-Assembled Organothiol Monolayers: Preparation, Characterization, and Application. *Prog. Surf. Sci.*

2009, *84* (7–8), 230–278.

(76) Pradeep, T. *Nano: The Essentials. Understanding Nanoscience and Nanotechnology*; The McGraw-Hill Companies Inc.: United States of America, 2008, pp 128-155.

(77) Herzer, N.; Hoeppener, S.; Schubert, U. S. Fabrication of Patterned Silane Based Self-Assembled Monolayers by Photolithography and Surface Reactions on Silicon-Oxide Substrates. *Chem. Commun. (Camb).* **2010**, *46* (31), 5634–5652.

(78) Khassanov, A.; Steinrück, H. G.; Schmaltz, T.; Magerl, A.; Halik, M. Structural Investigations of Self-Assembled Monolayers for Organic Electronics: Results from X-Ray Reflectivity. *Acc. Chem. Res.* **2015**, *48* (7), 1901–1908.

(79) Ito, Y.; Virkar, A. a; Mannsfeld, S.; Oh, J. H.; Toney, M. Crystalline Ultra Smooth Self-Assembled Monolayers of Alkylsilanes for Organic Field-Effect Transistors_SI. *J. Am. Chem. Soc.* **2009**, *131* (13), 1–5.

(80) Sun, Y.; Negreira, A. R.; Meersschaut, J.; Hoflijk, I.; Vaesen, I.; Conard, T.; Struyf, H.; Tokei, Z.; Boemmels, J.; Moinpour, M.; De Feyter, S.; Armini, S. Optimization and Upscaling of Spin Coating with Organosilane Monolayers for Low-*k* Pore Sealing. *Microelectron. Eng.* **2017**, *167*, 32–36.

(81) Wilbur, J. L.; Kumar, A.; Biebuyck, H. a; Kim, E.; Whitesides, G. M. Microcontact Printing of Self-Assembled Monolayers: Applications in Microfabrication. *Nanotechnology* **1999**, *7* (4), 452–457.

(82) Zemanian, T. S.; Fryxell, G. E.; Liu, J.; Mattigod, S.; Franz, J. A.; Nie, Z. Deposition of Self-Assembled Monolayers in Mesoporous Silica from Supercritical Fluids. *Langmuir* **2001**, *17* (26), 8172–8177.

(83) Kaya, S.; Rajan, P.; Dasari, H.; Ingram, D. C.; Jadwisienczak, W.; Rahman, F. A Systematic Study of Plasma Activation of Silicon Surfaces for Self

Assembly. *ACS Appl. Mater. Interfaces* **2015**, *7* (45), 25024–25031.

(84) Sun, Y.; Krishtab, M.; Mankelevich, Y.; Zhang, L.; De Feyter, S.; Baklanov, M.; Armini, S. Surface-Confined Activation of Ultra Low-k Dielectrics in CO_2 Plasma. *Appl. Phys. Lett.* **2016**, *108* (26), 1–5.

(85) Lessel, M.; Bäumchen, O.; Klos, M.; Hähl, H.; Fetzer, R.; Paulus, M.; Seemann, R.; Jacobs, K. Self-Assembled Silane Monolayers: An Efficient Step-by-Step Recipe for High-Quality, Low Energy Surfaces. *Surf. Interface Anal.* **2015**, *47* (5), 557–564.

(86) Armini, S.; Loyo Prado, J.; Krishtab, M.; Conard, T.; Meersschaut, J.; Le, Q. T.; Verdonck, P.; Baklanov, M. R. Study of Wet Surface Activation Routes to Enable the Deposition of Monomolecular Organic Thin Films on *k* 2.0 Porous Dielectrics. *ECS J. Solid State Sci. Technol.* **2014**, *3* (1), N3106–N3111.

(87) Aswal, D. K.; Lenfant, S.; Guerin, D.; Yakhmi, J. V.; Vuillaume, D. Self Assembled Monolayers on Silicon for Molecular Electronics. *Anal. Chim. Acta* **2006**, *568* (1–2), 84–108.

(88) Ulman, A. *An Introduction to Ultrathin Orgaic Films From Langmuir-Blodgett Films to Self-Assembly*; Academic Press, Inc.: San Diego, Califonia, 1991, pp 237-304.

(89) Brady-Boyd, A.; O'Connor, R.; Armini, S.; Selvaraju, V.; Hughes, G.; Bogan, J. On the Use of (3-Trimethoxysilylpropyl) Diethylenetriamine Self-Assembled Monolayers as Seed Layers for the Growth of Mn Based Copper Diffusion Barrier Layers. *Appl. Surf. Sci.* **2018**, *427*, 260–266.

(90) Sun, Y.; Levrau, E.; Zhang, L.; Geypen, J.; Meersschaut, J.; Franquet, A.; Le, Q. T.; De Marneffe, J. F.; Bender, H.; Struyf, H.; Detavernier, C.; Baklanov, M.; De Feyter, S.; Armini, S. Stuffing-Enabled Surface Confinement of Silanes Used as Sealing Agents on CF_4 plasma-Exposed 2.0 p-OSG Films. *Microelectron. Eng.* **2015**, *137* (1), 70–74.

(91) Naik, T. R.; Singh, V.; Ravikanth, M.; Rao, V. R. A Vapor Phase Self-Assembly of Porphyrin Monolayer as a Copper Diffusion Barrier for Back-End-of-Line CMOS Technologies. *IEEE Trans. Electron Devices* **2016**, *63* (5), 2009–2015.

(92) Sharma, S.; Kumar, M.; Rani, S.; Kumar, D. Deposition and Characterization of 3-Aminopropyltrimethoxysilane Monolayer Diffusion Barrier for Copper Metallization. *Metall. Mater. Trans. B* **2014**, *46* (2), 928–932.

(93) Hashemi, F. S. M.; Bent, S. F. Sequential Regeneration of Self-Assembled Monolayers for Highly Selective Atomic Layer Deposition. *Adv. Mater. Interfaces* **2016**, *3* (21).

(94) Minaye Hashemi, F. S.; Birchansky, B. R.; Bent, S. F. Selective Deposition of Dielectrics: Limits and Advantages of Alkanethiol Blocking Agents on Metal-Dielectric Patterns. *ACS Appl. Mater. Interfaces* **2016**, *8* (48), 33264–33272.

(95) Fang, M.; Ho, J. C. Area-Selective Atomic Layer Deposition: Conformal Coating, Subnanometer Thickness Control, and Smart Positioning. *ACS Nano* **2015**, *9* (9), 8651–8654.

Chapter 2

2 Principals of Experimental Theory & Techniques

The principal technique employed throughout this work to investigate and characterise the SAMs and thin metal films is X-ray photoelectron spectroscopy (XPS). The secondary techniques include hard X-ray photoelectron spectroscopy (HAXPES) and atomic force microscopy (AFM). In this chapter, the theory of these techniques and the practical use of the experimental systems will be discussed.

2.1 X-Ray Photoelectron Spectroscopy

X-ray photoelectron spectroscopy (XPS), also known as ESCA (Electron Spectroscopy for Chemical Analysis) is a very powerful surface analysis tool which can give a wealth of information about the electronic structure, the elemental composition and the chemical state of the first 5 – 10 nm of a solid material[1]. The development and use of XPS as a surface analysis technique was pioneered by Kai Siegbahn and his group through the 1950's and 1960's. In XPS, the surface of a solid in vacuum, is illuminated with energetic photons from the X-ray range of the electromagnetic spectrum. Due to the photoelectric effect electrons are photoemitted from the surface of the material. The emitted electrons are evaluated according to their kinetic energy and a spectrum is created as a plot of the number of detected electrons per energy interval versus their kinetic energy. XPS is sensitive to all elements apart from H and He, which are the only elements not to be observed. The other elements all have their own distinct photoelectron spectrum[2,3].

2.1.1 Basic Principals

Figure 2.1 schematically shows the basic set-up for a conventional XPS system. The main components are the X-ray source, the grounded sample, the electron collection lens, the electron energy analyser, the detection system and the computer system which displays the acquired spectra.

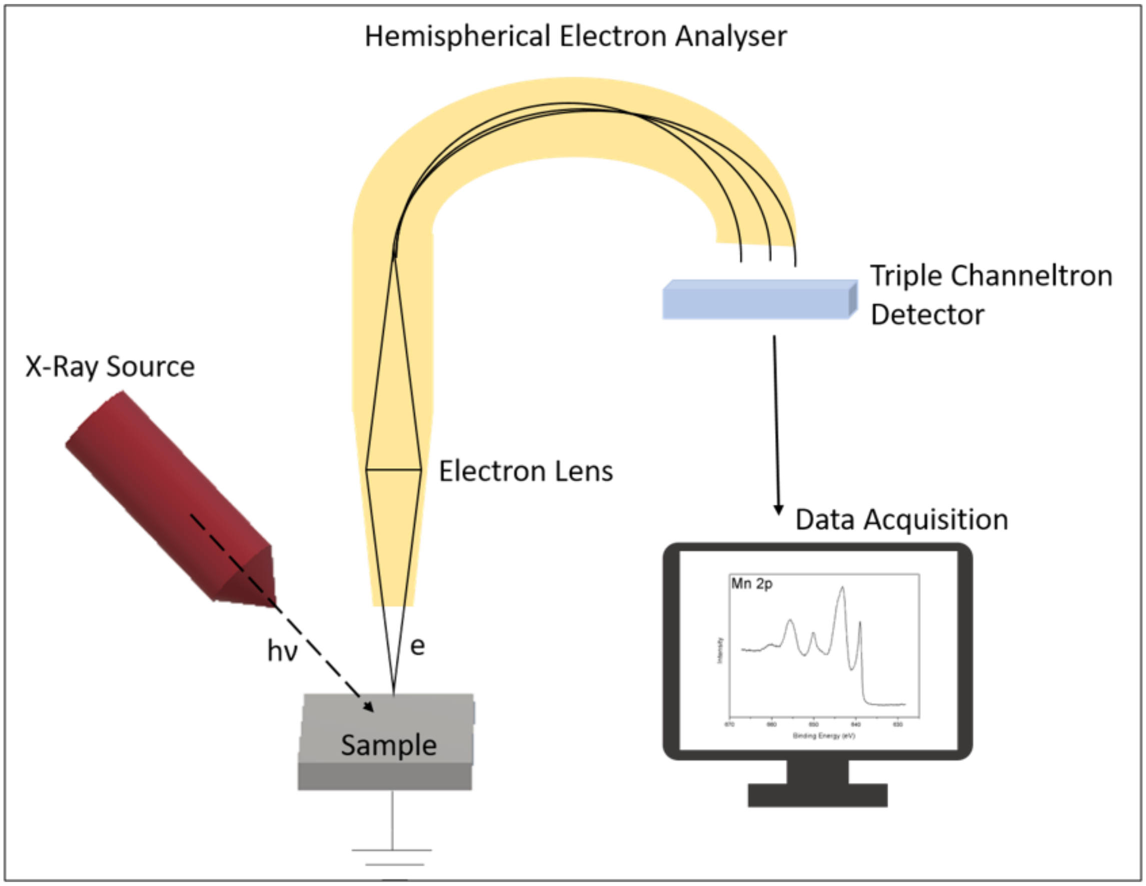

Figure 2.1 A schematic showing the experimental set-up for a conventional XPS system.

The sample of interest is loaded into the ultra-high vacuum (UHV) chamber and is then irradiated with X-rays. These X-rays are generated by a twin anode X-ray source which allows the user to select one of two different excitation energies. The anode is water-cooled and consists of a copper target with two distinct sides, one of which is coated with a thin film of aluminium (Al) and the other a thin film of magnesium (Mg). Electrons from a hot tungsten filament are accelerated using a high voltage, ranging from 10 – 15 kV, towards the water-cooled anode. X-ray energies of either 1253.6 eV with a line width of 0.7 eV for Mg Kα or 1486.6 eV with a line width of 0.85 eV for Al Kα are emitted as the electrons bombard the anode. The anode must be water-cooled as the high electron flux can generate high levels of heat which could potentially evaporate the Al or Mg coatings on the anode. The twin anode configuration is used in situations where a photoemission peak overlaps with an Auger peak. By switching anodes, the binding energy position of the Auger peak will change allowing for access to the photoemission peak of interest.

To fully appreciate XPS as a technique, an understanding of how photons and electrons interact is vital. When photons bombard a surface and interact with the atoms several different events may occur: (i) the photon may not interact with the atom, (ii) Compton scattering may occur where some energy is lost when the photon is scattered by an orbital electron and (iii) the photoelectron effect may occur where there is total transfer of the photon energy to the orbital electron which may result in the electron being ejected from the atom[4]. XPS is based on the principle of the photoelectron effect and obeys Einstein's equation;

$$E_B = hv - E_{kin} \tag{2.1}$$

where E_B is the binding energy of the electron in the atom with respect to the Fermi level, E_{kin} is the kinetic energy of the emitted photoelectron, h is Planck's constant and v is the frequency and the product hv is the energy of the incident x-ray photons. Since the X-ray energy is known, the binding energy can be found by measuring the kinetic energy of the emitted photoelectrons. Elemental composition of any sample can be determined as each element has a discrete binding energy associated with every energy level. These values can be measured against known values, so the correct element can be identified. However, any photon interacting with an electron in a material must be capable of transferring enough energy so that the electron can liberate itself from the surface of the material. Equation 2.1 now becomes:

$$E_B = hv - E_{kin} - \Phi_s \tag{2.2}$$

where Φ_s is the sample material's work function and is defined as the energy difference between the vacuum level and the Fermi level ($E_{vac} - E_F$). This is shown in Figure 2.2 which displays an energy level diagram for the photoemission process inside an XPS system, where a conducting sample and the spectrometer are in electrical contact. It can clearly be seen that the sum of the electron's initial binding energy measured up to the Fermi level (E_B^F), and its kinetic energy after being emitted (E_{kin}^1), does not equal the photon energy of the incident x-rays.

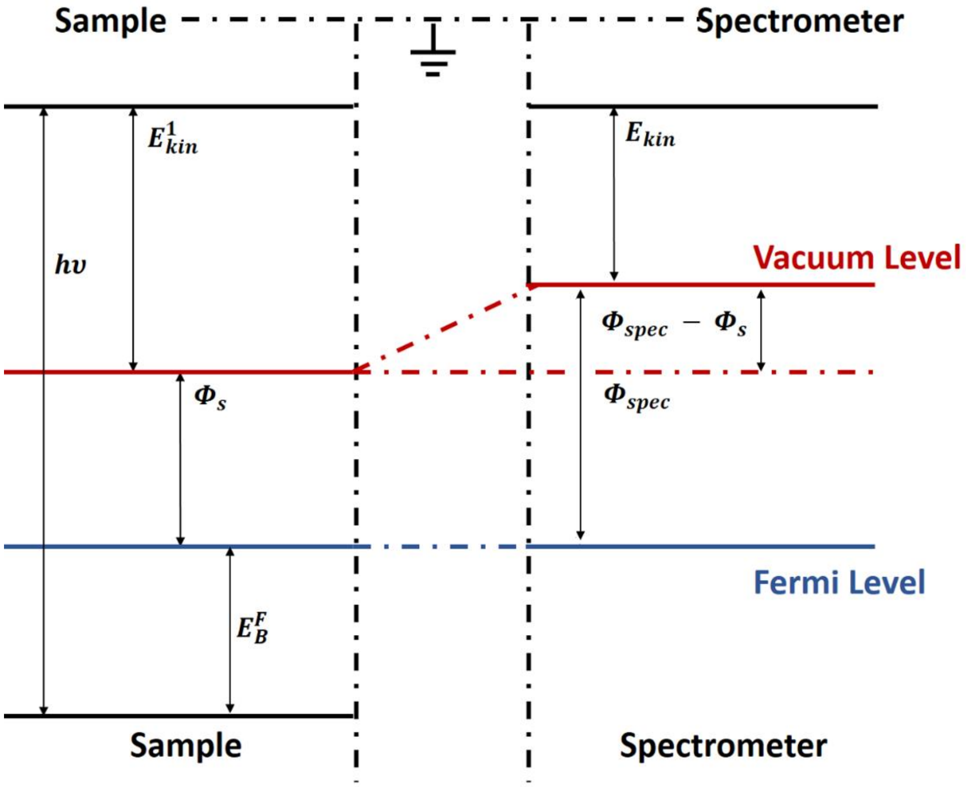

Figure 2.2 Schematic of the energy level for the binding energy measurements where the sample and spectrometer are in electrical contact.

Once the sample and the spectrometer are both grounded, the Fermi level of the sample is equal to the Fermi level of the spectrometer[5]. As the photoelectron passes from the sample surface into the spectrometer it will feel a potential equal to the difference between the spectrometer (Φ_{spec}) and the sample material work functions (Φ_s). Hence, the measured kinetic energy can be defined as

$$E_{kin} = E^1_{kin} + \left(\Phi_s - \Phi_{spec}\right) \tag{2.3}$$

Substituting this into equation 2.2 yields the following expression

$$E_B = h\upsilon - E_{kin} - \Phi_{spec} \tag{2.4}$$

Equation 2.4 shows that once the X-ray photon energy ($h\upsilon$), the measured kinetic energy (E_{kin}) and the spectrometer work function (Φ_{spec}) are known the binding energy of the electron can be obtained. The binding energy is shown to be independent of the sample work function (Φ_s) but dependent on the spectrometer work function (Φ_{spec}). The spectrometer work function is usually determined using a reference sample of known binding energy like gold or copper by setting the energy scale to zero at the Fermi edge of the reference sample.

For insulating materials, the electrical conductivity of the material is lower than the emitted current of photoelectrons, due to the loss of electrons the charge on the surface can change. A net positive charge can then reduce the kinetic energy of the emitted photoelectrons. This can have the effect of shifting the binding energy in the photoemission spectra. To remedy this a flood gun can be used to supply a low energy flux of electrons to the surface. Alternatively, all the photoemission peaks can be charge referenced to a peak with a well-known binding energy position. The C 1s peak is generally chosen as almost every sample will have adventitious carbon present from atmospheric contamination. This peak has a binding energy of 284.8 eV. The difference between the measured carbon spectra and this reference value is then applied to all other peaks to shift them to their correct binding energy value.

2.1.2 Inelastic Mean Free Path and Sampling Depth

Incident X-ray photons of 1keV can typically penetrate up to ~1µm into the solid material, while the escape depth of the electrons however, is significantly smaller <10nm. The excited electrons travelling from deeper in the material have a much higher probability of interacting with other atoms and electrons through inelastic collisions and scattering events. Furthermore, through these inelastic collisions the electrons lose their kinetic energy on their journey to the surface. These electrons might have just enough kinetic energy to escape the surface but will not produce any peaks in a spectrum, instead they will add to the background. Electrons which are situated closer to the surface have a much higher probability of escaping without experiencing any collisions or scattering events. These electrons produce very narrow intense peaks at specific binding energies which can be related to the elements present at the surface. These electron emission processes are schematically shown in Figure 2.3.

The probability of these interactions occurring can be statistically predicted based on the inelastic mean free path (IMFP) of a given material. The IMFP is defined as the mean distance an electron with a given energy will travel in a material before engaging in a collision in which it loses energy. It is the main material parameter that is used to describe inelastic scattering of electrons in XPS. Seah and Dench compiled the first universal mean free path curve in 1979[6], illustrated in Figure 2.4.

By compiling data from a large number of researchers they developed an expression in which the inelastic mean free path λ_{IMFP}, in nm, is a function of the electron energy:

$$\lambda_{IMFP} = \frac{538}{E^2} + 0.41a^{3/2}E^{1/2} \tag{2.5}$$

where a is the mean atomic distance and E is the kinetic energy.

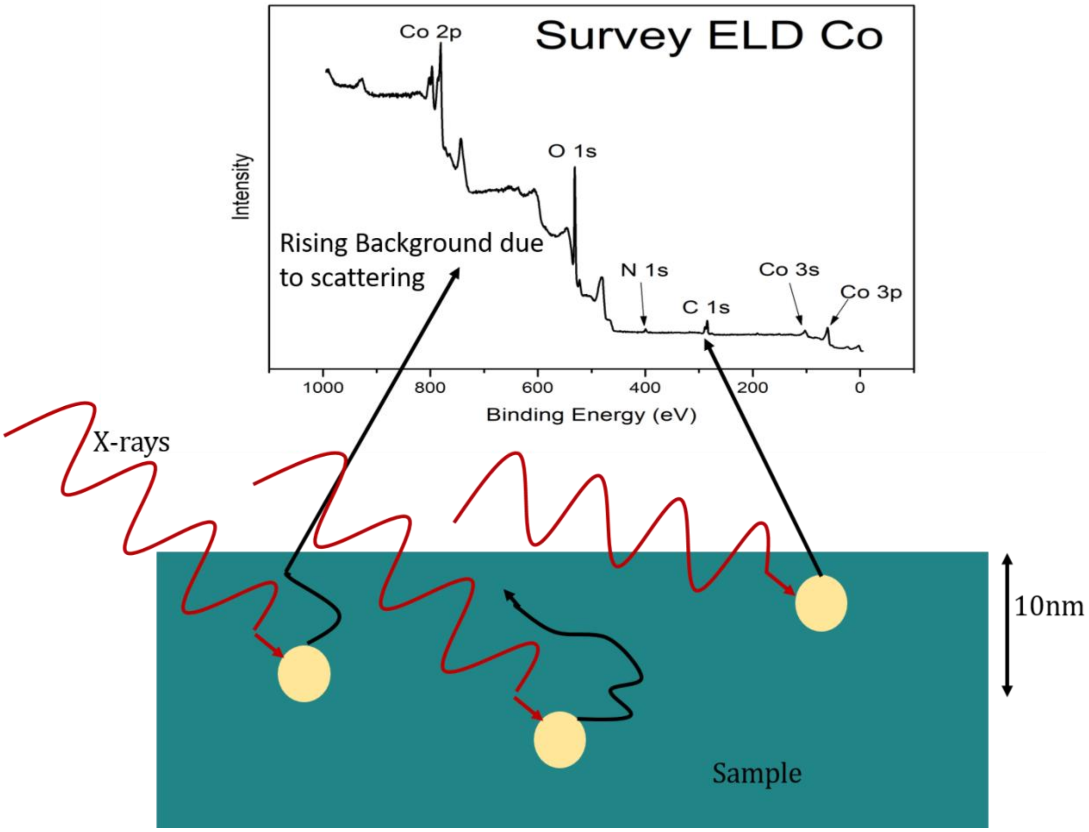

Figure 2.3 XPS survey scan of a 20nm ELD cobalt film with all the main core level peaks labelled. The diagram underneath shows the various electron emission processess that give either the core level peaks or add to the rising secondary electron background.

For energies greater than 100 eV the first term can be neglected, giving rise to a proportionality between the inelastic mean free path and $E^{1/2}$. To calculate a

$$a = \left(\frac{M}{\rho N_{Av}}\right)^{1/3} \tag{2.6}$$

where M is the atomic mass, ρ is the density and N_{Av} is Avogadro's number[7]. From the universal curve it can be seen that photoelectrons with a low kinetic energy are primarily emitted from the near surface region.

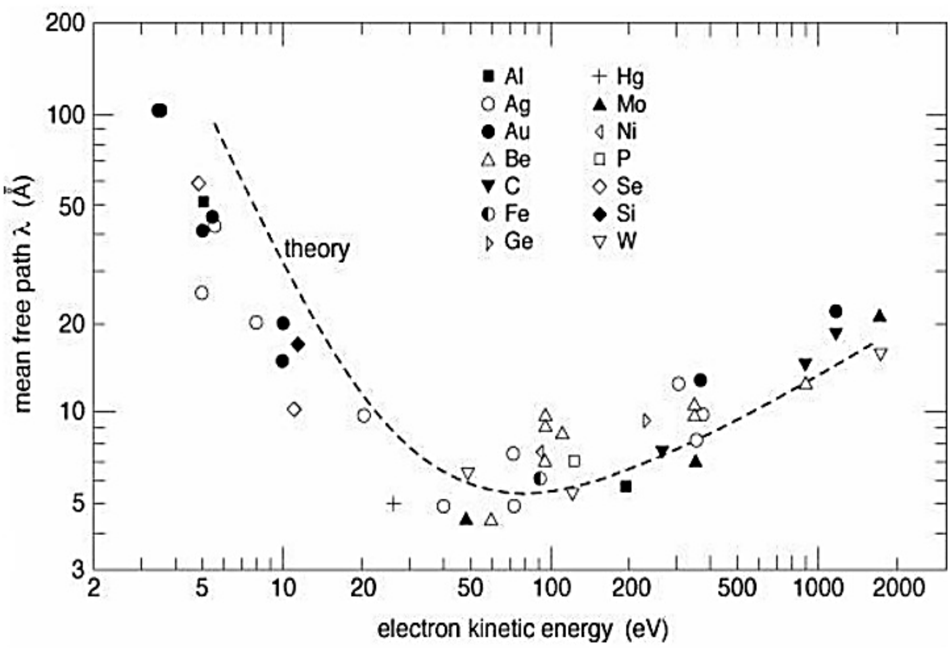

Figure 2.4 The universal mean free path (MFP) created by Seah and Dench [6].

Below ~50eV the curve is seen to increase, this is due to a change in the scattering process in this energy range. Although this curve is a good fit for most materials, there can be large deviations. To more accurately predict the IMFP of different elements Tanuma et al.[8] formulated the so-called TPP-2M equation (2.7), graphically represented in Figure 2.5. This equation is used to precisely fit and model the IMFP of a particular element from energies of 10eV right up to 30keV [9].

$$\lambda_{in} = \frac{E}{E_p^2\left\{\beta ln(\gamma E) - \left({}^{C}\!/_{E}\right) + \left({}^{D}\!/_{E^2}\right)\right\}} \tag{2.7}$$

where E is the electron energy, E_p is the free electron plasmon energy.

The parameters β, γ, C, D and U are defined as:

$$\beta = -0.10 + \frac{0.994}{\left(E_p^2 + E_g^2\right)^{1/2}} + 0.069\rho^{0.1}, \tag{2.8a}$$

$$\gamma = {}^{0.191}\!\Big/_{\sqrt{\rho}}\ , \tag{2.8b}$$

$$C = 1.97 - 0.91U, \qquad (2.8c)$$

$$D = 53.4 - 20.8U, \qquad (2.8d)$$

and finally,

$$U = {}^{N_v\rho}\!/_{M} = {}^{E_p^2}\!/_{829.4} \qquad (2.8e)$$

such that E_g is the band gap energy, ρ is the density of the material, N_v is the number of valence electrons per atom or molecule and M is the atomic mass. By using these four material parameters Tanuma et al are able to determine the IMFP for a given element thereby removing the need for a universal curve.

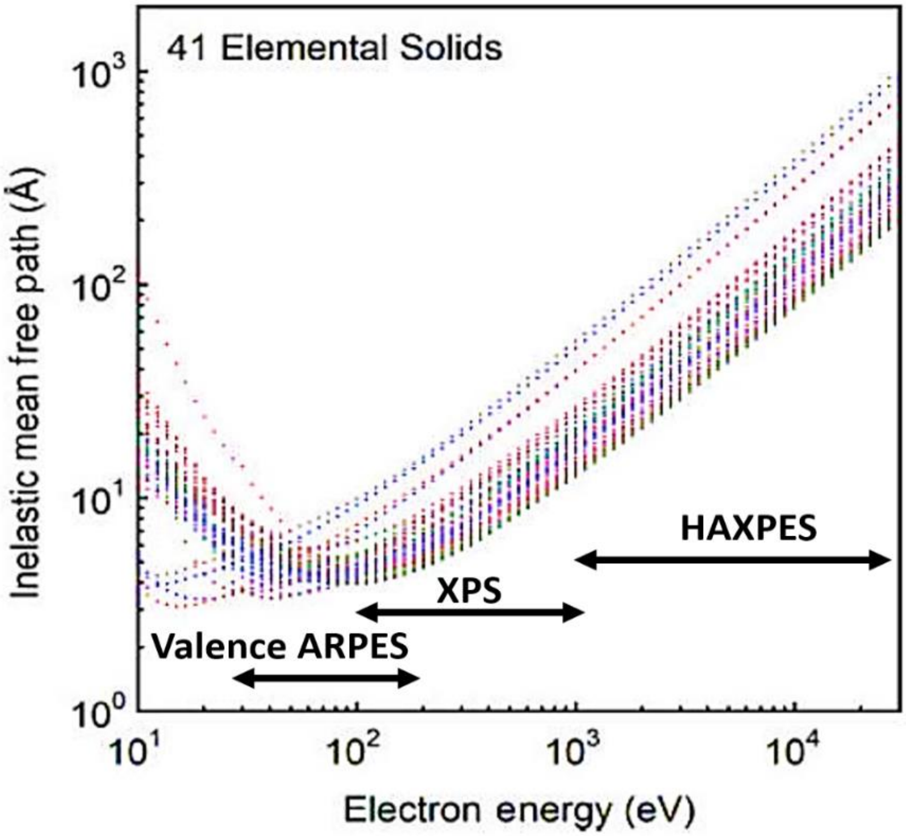

Figure 2.5 Graphical representation of the TPP-2M equation for the IMFP. The graph also illustrates what techniques are employed for different energy ranges[10].

This is important as it is the IMFP that determines the effective sampling depth of the material. In XPS approximately 95% of the signal comes from a depth of $d = 3\lambda$, with d defined as the sampling depth. Depending on the material of interest the sampling depth can range from 5-8nm.

2.1.3 Elemental Identification & Spectral Features

The most common first step when carrying out XPS analysis of a sample is to record a wide energy scan that ranges from 0 eV – 1000eV in binding energy. This is called a survey scan and is very important in determining the elemental composition of the sample. XPS spectra are usually displayed as a plot of intensity as a function of binding energy, with the intensity taken as the number of electron counts per second. From equation 2.4, the kinetic and binding energies have different signs, so the spectra are plotted with increasing binding energy from right to left. In other words, a low binding energy represents a high kinetic energy and a high binding energy represents a low kinetic energy. When the photoemission process occurs, the electrons are emitted at discrete energies which produce intense peaks in the spectra as shown in Figure 2.6 for a survey scan of the DETA SAM deposited on a native SiO_2 substrate. The binding energy at which these peaks are positioned allows the user to identify the elements present at the surface region as each element has a unique set of core level binding energies. As discussed previously, any scattered electrons that lose energy are emitted with a random energy and add to the rising background of the spectrum.

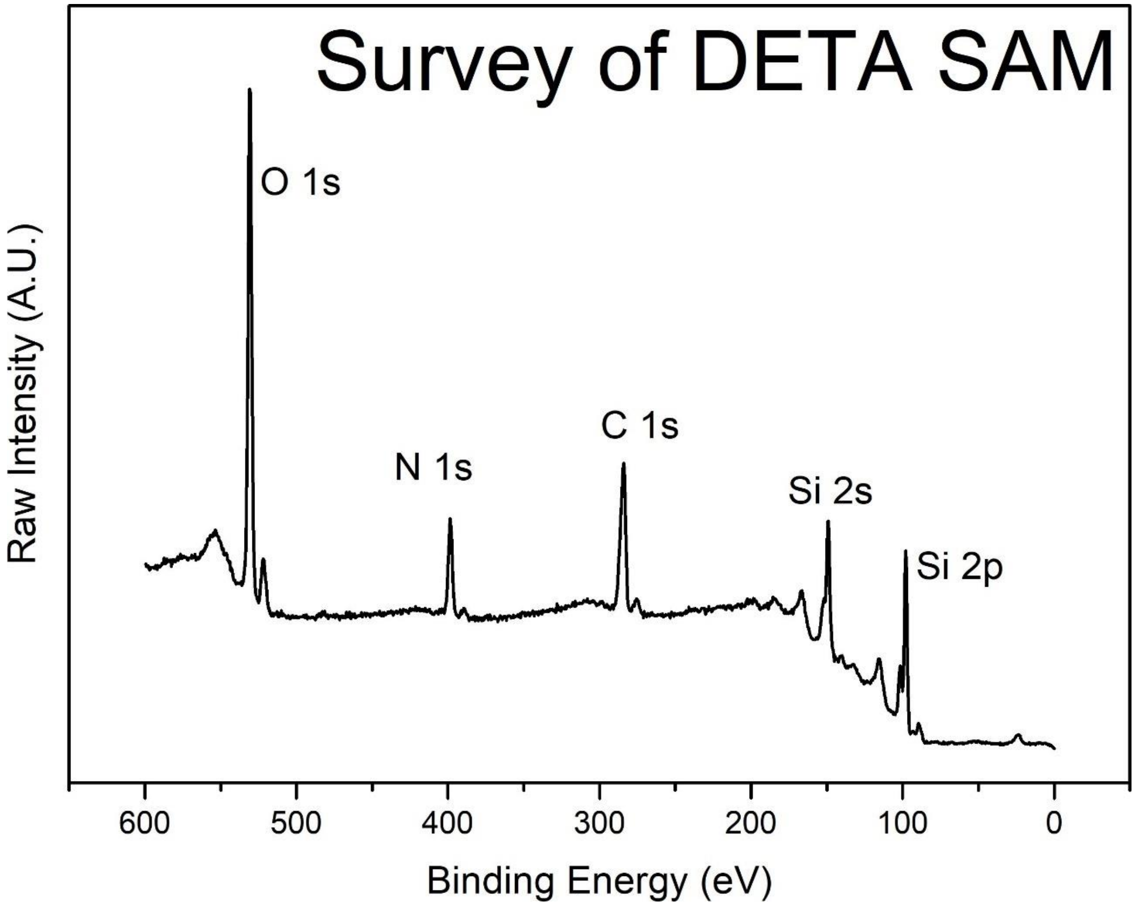

Figure 2.6 Survey scan of DETA SAM deposited on SiO_2 substrate with the principal core levels labelled.

Also, commonly observed in survey spectra are X-ray induced Auger lines. Auger electron emission features arise when a core level electron transitions to a deeper empty energy level. The electron can then transfer energy to another electron in that energy level providing it with enough kinetic energy to be emitted from the surface. In this process the energy of the emitted electron is dependent only on the energy separation between the core levels. One can easily distinguish Auger lines from photoemission lines by changing the energy of the X-ray source. The Auger lines will always appear at the same energy position irrespective of the incident photon energy, while the photoemission peak will be shifted by the difference in photon energy between the Mg and Al anodes. Tables of measured and calculated binding energies exist for almost all elements. There are many books and websites available to aid in the identification process such as the NIST online database[3,11].

Once all elements have been identified from the survey scan, high resolution narrow energy scans are typically performed on the principle peaks seen in the survey scan for each element present. A standard non-monochromated XPS can be used to identify the presence of elements which are at atomic concentration levels greater than ~ 0.1 % - 1 %. Elements are generally identified by the presence of their most intense spectral feature, for example in the case of copper one would generally examine the Cu 2p peak. Although each element has its own unique set of core level binding energies, other elements may overlap with these positions. The Si 2p and the Co 3s peaks have binding energy positions of 99.8 eV and 101 eV respectively; as the two peaks are so close together it is not possible to resolve them. In this case, other core level peaks would be examined such as the Si 2s and the Co 2p.

Several different spectral features can also be present in the recorded spectra. These features can give more information on the sample including chemical states. Spectral features can arise for a variety of different reasons including instrumental, X-ray electron interactions and electron-electron interactions. When using a non-monochromated X-ray source, a satellite peak accompanies the main photoemission peak. These satellite peaks are caused by low intensity X-rays from $K\alpha_{3,4}$ emission and is common from both anodes. The peaks created by these X-rays are generally less than 10% of the main peak intensity and are shifted to between 8.4 – 10.1 eV lower binding energy from the main peak for the Mg anode and 9.8 – 11.8 eV lower binding energy from the main peak for the Al anode[3]. To remove these satellite peaks an X-ray monochromator must be used.

Quite often plasmon loss peaks are observed at higher binding energies from the main peak and are specific to clean metal or highly doped semiconductor surfaces. Plasmon loss peaks are caused by discrete energy loss due to collective oscillations of conduction electrons. Any photoemitted electron passing through these oscillations will experience an energy loss characteristic of the mode of oscillation of the conduction electrons. Typically, these peaks are seen at a binding energy ~10 eV greater than the main peak, with higher harmonics of the oscillations occurring at regular intervals above the bulk loss feature.

Shake up structures occur when photoelectrons lose energy through the promotion of valence electrons. An outgoing photoelectron can interact with a valence electron and "shake it up" to a higher energy level. The kinetic energy of the emitted photoelectron is then reduced resulting in a peak at a higher binding energy than the main peak. A very strong shake up peak is observed for CuO where energy loss is tied to a specific transition in the atom[12]. Figure 2.7 shows a Cu 2p spectrum for a CuO sample.

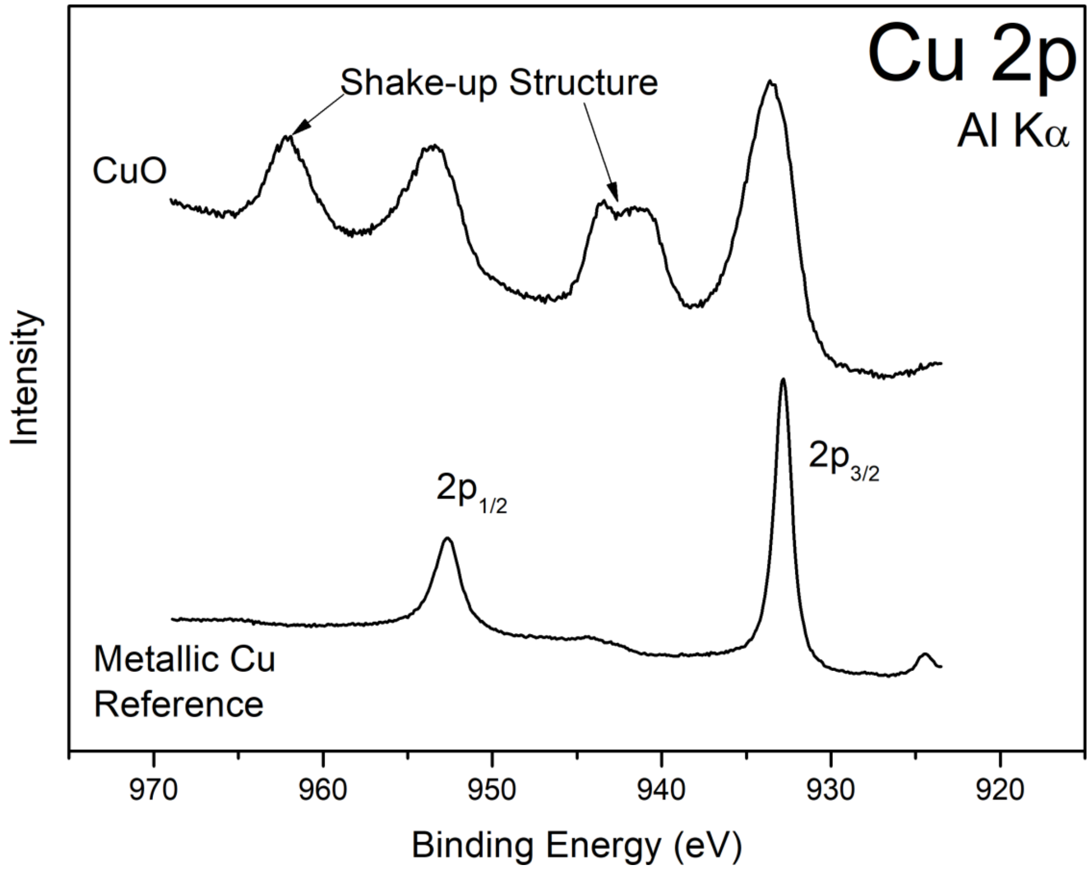

Figure 2.7 Difference between metallic Cu and CuO. The shakeup features of CuO are clearly visible.

The shape of these shake up peaks allows for the distinction between different oxides species, as Cu_2O does not possess these features and shake up peaks for $Cu(OH)_2$ have a different shape.

2.1.4 Chemical Shifts

One of the most invaluable pieces of information that XPS analysis can provide is the ability to distinguish between different chemical states of the same element. If there is a significant change in the bonding state of an atom there will be observable changes in the spectrum, such as a shift in binding energy. A change in the chemical bonding causes what is called a chemical shift, for instance when oxygen bonds to a metal, the metal peak shifts to a higher binding energy. This process can be explained by considering the silicon / silicon dioxide peaks within the Si 2p spectrum in Figure 2.8. In this figure a thin 5.4 nm SiO_2 layer has been thermally grown on a Si substrate. The photoemitted electrons from the Si substrate emerge at a binding energy ~99.3 eV. At this point the Si atoms are covalently bonded to each other and the valence electrons are shared equally among the Si atoms in the bulk. The SiO_2 appears at a binding energy of 103.8 eV, approximately a 4.5 eV higher binding energy position than the bulk signal. The bonding of O atoms (which have considerably greater electronegativity than Si) to Si atoms, results in the majority of the negative charge residing around the O atom creating a slight positive charge on the Si atom. This slight positive charge on the Si atom has the effect of decreasing the kinetic energy of the emitted electrons and thus the SiO_2 peak is positioned at a higher binding energy. In practice, the electronegativity values of the elements present in a sample and hence, the chemical shifts can be used to identify chemical state of the element. Figure 2.9 schematically shows the effect of electronegativity on the chemical bonding environment for this thin SiO_2 film on silicon.

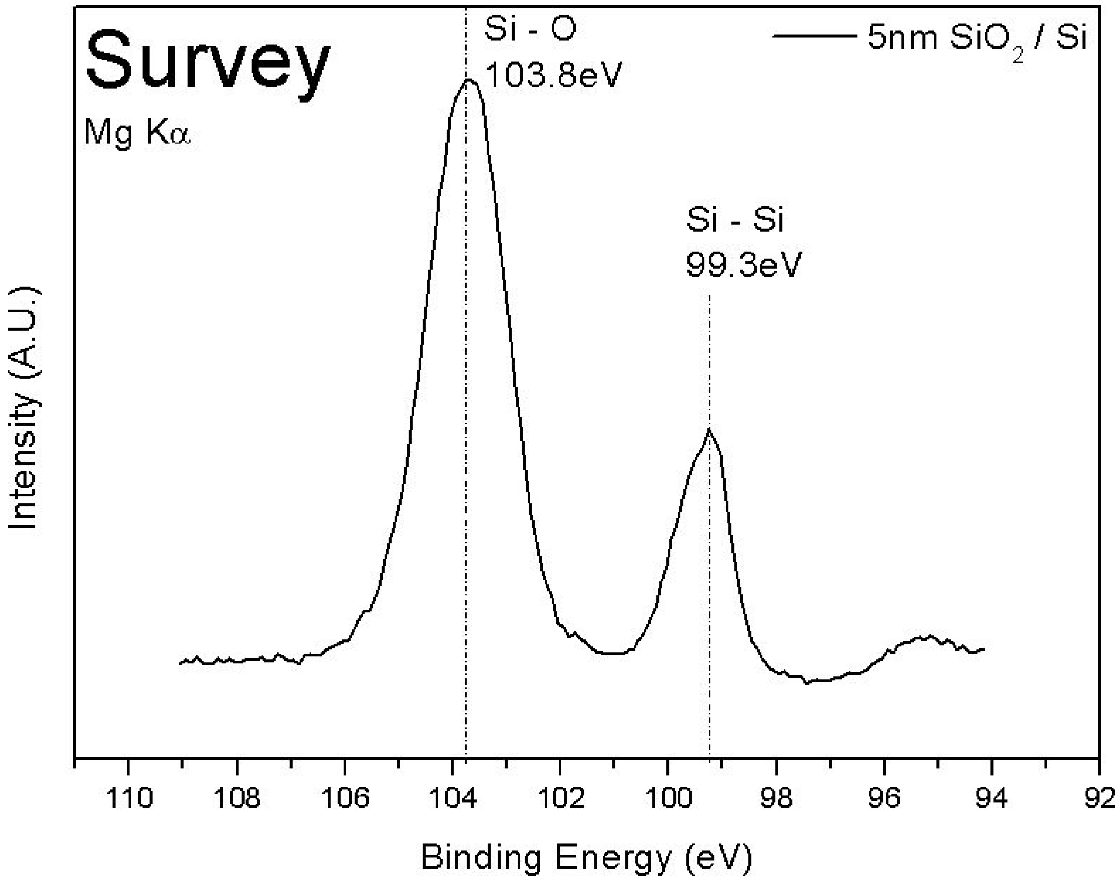

Figure 2.8 Si 2p spectrum showing the chemical shift of 4.5eV between the Si component peak and the SiO_2 component peak.

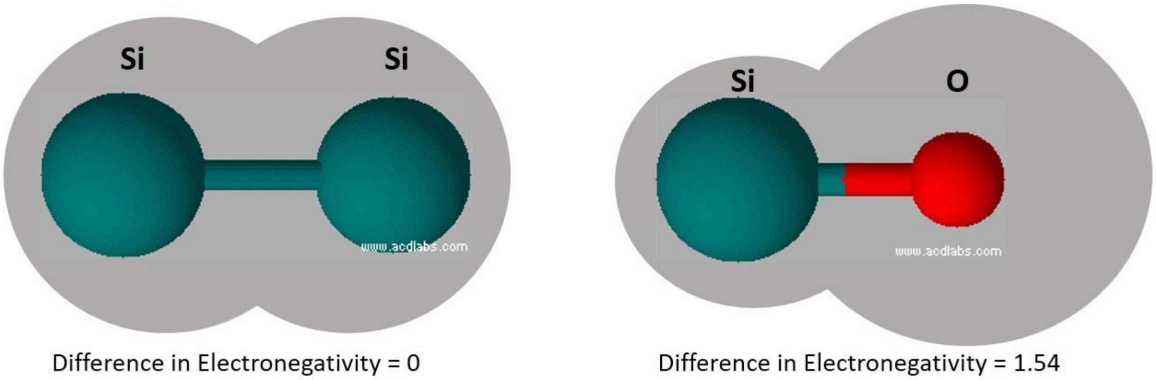

Figure 2.9 Schematic diagram showing the influence the electronegativity can have on the electron cloud densities in the different bonding environments of Si – Si and Si - O.

2.1.5 Quantification

A semi-quantitative analysis of the chemical composition can be very useful to obtain a general overview of any changes in surface chemistry over the course of an experiment. To find the relative concentration of different elements in the sample one can compare the signal intensities of the relevant core level peaks from a survey scan with the aim of converting peak intensities to atomic concentrations. There are however, several factors that must be taken into account in order to perform this type of analysis. Firstly, it is assumed that the film is chemically homogenous within the sampling depth of the XPS measurement. If the film is of non-uniform composition perpendicular to the surface, conclusive elemental ratios cannot be extracted. Secondly, the kinetic energy of the peak must be taken into account as electrons emerging from the surface with a higher kinetic energy are in fact emerging from a greater depth than electrons with a lower kinetic energy. Thirdly, the photo-ionisation cross section of the specific core level which is the probability that an electron from that core level will be excited[13] is elemental specific. Finally, a spectrometer related factor must be included, which is the transmission function of the analyser. This parameter determines the sensitivity of the analyser to the electrons as a function of kinetic energy.

This type of analysis can be carried out with the use of elemental relative sensitivity factors (RSF). Each core level in an element has its own RSF value based on the factors above. By using these RSF values a chemical composition of the surface can be acquired. There are many published tables of elemental RSF values available from XPS reference websites and manuals [14,15] and these allow a semi-quantitative analysis of chemical composition of the surface to be achieved. As already stated this analysis is only semi-quantitative and the use of standard reference samples is common for more accurate studies.

The atomic percentage of all the elements present can be found by using the following equation:

$$\text{atomic \%} = \left\{ \frac{\left({}^{I_A}/_{F_A} \right)}{\sum_i \left({}^{I}/_{F_i} \right)} \right\} \text{ x } 100\% \, , \tag{2.9}$$

where I_A is the intensity of a particular element, F_A is the relative sensitivity factor for that element and the parameter ${}^{I}/_{F_i}$ is the summation of all the adjusted intensities[12]. The percentages found by this method are not absolute. However, this approach can be very helpful with comparative studies of elemental composition before and after treatment and have been mostly used for this purpose throughout this study.

2.1.6 Depth Profiling using ARXPS

Angular resolved XPS (ARXPS) is a non-destructive technique that allows for depth profiling analysis of the chemical composition within the sampling depth of the sample. For normal emission, the photoelectrons are emitted perpendicular to the surface. In this case the analyser is positioned directly above the sample giving the maximum sampling depth of ~8nm as shown in Figure 2.10 (a). If the sample is rotated with respect to the analyser, the photoelectrons emerge from an increasing surface localised area, Figure 2.10 (b) and (c). The electrons still emerge perpendicular to the surface and the sampling depth has not changed from that of normal emission. The only difference is at these glancing angles of detection the effective sampling depth is reduced. Therefore, spectra taken at glancing angles of emission are more surface sensitive and are particularly useful for characterising thin film over layers.

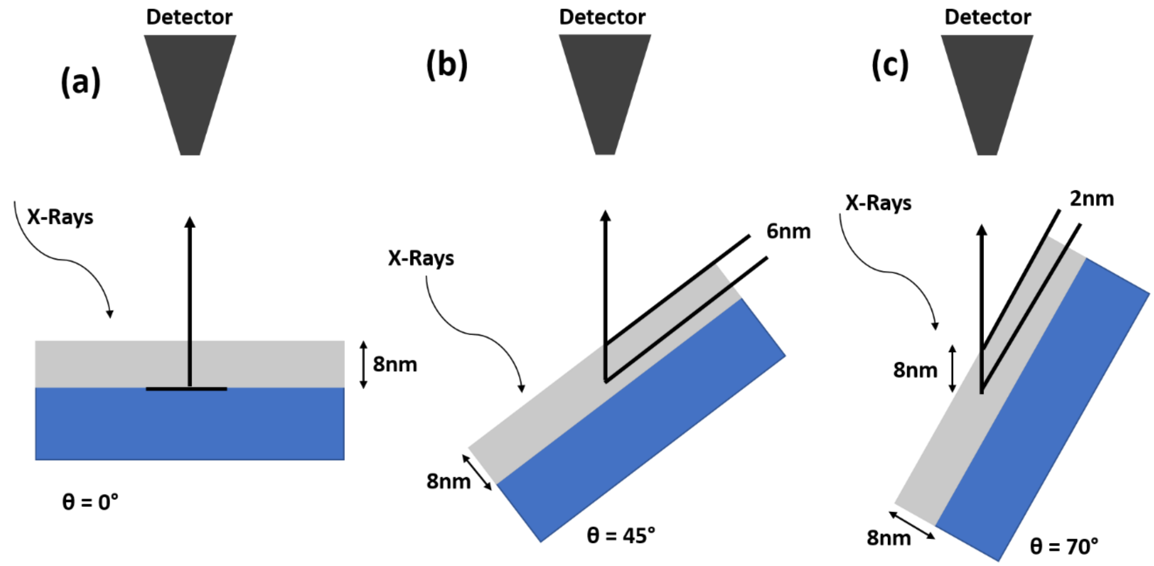

Figure 2.10 Schematic showing the effective sampling depth in ARXPS.

2.1.7 Peak width and Peak Fitting

The spectral shape of a photoemission peak can be curve fitted with a combination of Lorentzian and Gaussian line shape component peaks, otherwise known as a Voigt function. The peak width can be determined by two main features; the core-hole lifetime and the instrumental resolution. The inherent line shape of the photoemission process is given by the Lorentzian function and is related to the core-hole lifetime. The core-hole lifetime reduces with atomic number and with proximity to the nucleus of the orbital shell due to the increased number of electrons available to fill the vacated core level. The natural line width due to the core-hole lifetime, ΔE_L in eV, can be estimated by the Heisenberg uncertainty principle:

$$\Delta E_L = \frac{h}{\tau} \tag{2.10}$$

where h is Planck's constant and τ is the core-hole lifetime in seconds which shows that the line width is inversely proportional to the lifetime. This implies that for elements with a higher atomic number and for higher binding energy core levels, the Lorentzian peak width will be broader. The Gaussian component of the peak is determined by the linewidth of the incident x-rays and the resolution of the electron energy analyser.

Peak fitting is carried out on recorded spectra to evaluate the different bonds and chemical states present at the surface. A photoemission peak can comprise of several different component peaks, which may not be resolvable due to the resolution of the measurement. Each component peak represents a different chemical state and will have its own associated binding energy. Through peak fitting, the spectrum can be deconvoluted into its separate components. In this study Aanalyzer software was used for peak fitting[16]. Background subtraction by a Shirley-Sherwood line shape was employed.

2.1.8 Systems Used

The XPS system used for this study is shown in Figure 2.11. This system is a fully dedicated surface science UHV chamber with a base pressure ~8×10^{-10} mbar. The system has been designed for in-situ thin film depositions, high temperature annealing in vacuum and exposures to different gases. Modified sample stubs have been created so two samples can be loaded into the system at the same time. This allows for simultaneous identical anneals, metal deposition and any other surface treatments all within UHV conditions and without a break in vacuum. This allows for the direct comparison between samples, normally a control sample and the sample of interest. The samples are mounted via a metal bar to hold them in place and can be seen in Figure 2.12. This means no adhesive is used and this limits any contamination of the sample.

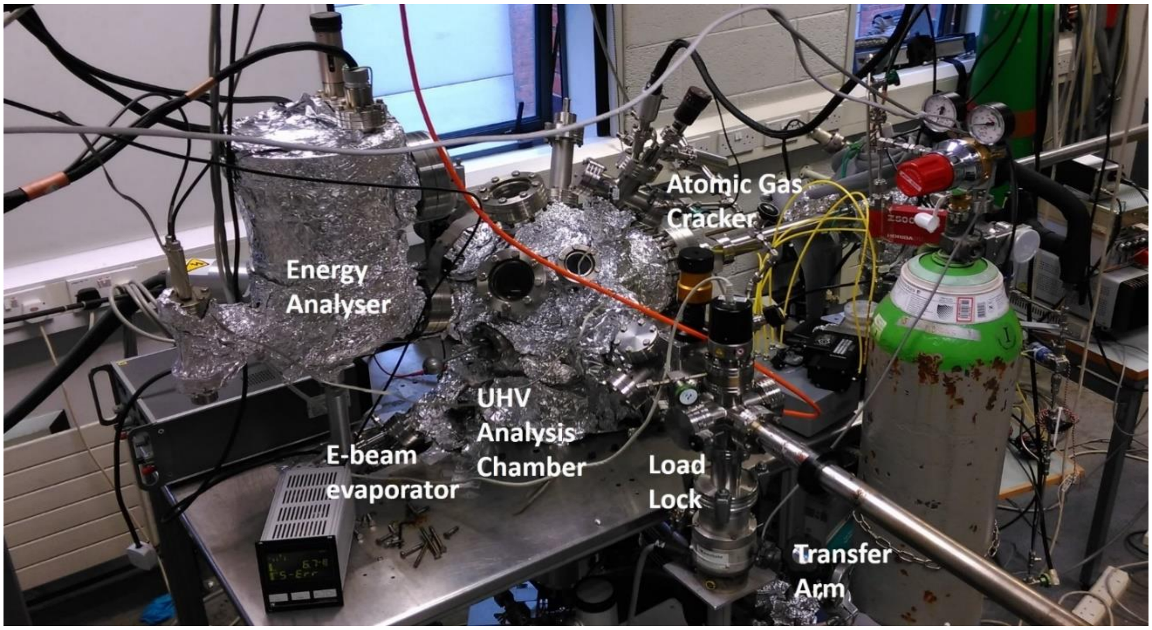

Figure 2.11 Dedicated UHV surface science chamber equipped with XPS, e-beam and atomic gas cracker.

Figure 2.12 Sample stub with bar, showing how two samples can be characterised at the same time.

The system contains a dual anode X-ray source and a VG CLAM electron energy analyser. Thin film deposition is performed by a four-pocket mini e-beam evaporator. During deposition the system pressure does not go above 5×10^{-8} mbar ensuring a clean metallic film deposition. A range of metals can be deposited including Mn, Cu, Ru, Ti, Mo and Co. Normally, one metal is deposited at a time to investigate the substrate metal interactions or to investigate a bimetallic stack. Metal alloys can also be deposited but it can be difficult to predict the exact composition of the alloy. Annealing temperatures of ~550°C can be achieved in the system. Molecular gases can be cracked using a thermal gas cracker. In this process atomic species are created by passing the molecular gas through a high temperature capillary which dissociates the molecule. As well as the e-beam and gas cracker the system is also equipped with a mass spectrometer.

2.2 Hard X-Ray Photoelectron Spectroscopy

Due to its surface sensitivity of ~5-7 nm, XPS is not ideal for probing the chemical composition deeper into the material to analyse a buried interface or multi-layered structures. This is where hard X-ray photoelectron spectroscopy or HAXPES becomes a valuable technique. HAXPES is a high energy variant of XPS and uses hard x-rays (energy >2 keV) while XPS uses soft x-rays (energy < 1.5 keV), as seen in Figure 2.5. HAXPES measurements are generally performed at synchrotrons that can produce high energy radiation in the form of hard X-rays (energy up to ~ 10 keV), which can increase surface sensitivity to ~30 nm. This allows for the study of buried interfaces, multi-layered structures and can also provide information on the bulk chemical composition of the material.

2.2.1 History of HAXPES

The discovery of synchrotron radiation in 1947 at the General Electric Research Laboratory in Schenectady, New York was fortuitous. Scientists performing experiments on the particle collider noticed a bright light as the electrons were accelerated around a bending magnet. This bright light corresponds to the loss of energy by the electrons and was seen as an undesirable consequence of the particle collider design. It was several years before the potential of this type of synchrotron radiation was discovered.

Following this discovery, some experimental end stations were constructed on some accelerators and were referred to as "parasitic" as they were only secondary to the high energy or nuclear physics research and experiments being performed. These parasitic end stations are known as the first generation of synchrotron radiation sources. The second generation of synchrotron sources were fully dedicated light sources with larger numbers of beamlines and end stations like SRS in Daresbury, England and NSLS in Brookhaven, New York. Such facilities first came into operation in the late 1970's and early 1980's. These second generation facilities now employed storage rings and bending magnets to harness the synchrotron radiation[17–19].

During the 1990's the third generation of synchrotrons were introduced. The third generation are characterised by the inclusion of wigglers and undulators or insertion devices as they are collectively called. These insertion devices give the synchrotron the capacity to produce extremely narrow beams of high intensity X-rays. In other words, they are designed for optimum brilliance.

Properties of synchrotron radiation include[17,18,20]:

- High brightness, which is orders of magnitude greater than conventional XPS;
- High brilliance, which at the Diamond Synchrotron in the UK for example is 10^{20} photons/s/mm^2/mrad^2/0.1 %BW;
- The radiation is highly polarised. This can be linear or elliptical depending on the magnetic field of the insertion device;
- The beam is highly collimated, i.e., small angular divergence of the beam;

- Low emittance, i.e., the product of the source cross section and solid angle of emission is small. SPRING-8 in Tokyo, Japan has an emittance of 2.4 nm.rad;
- The light is pulsed with a pulse duration of ~ 1 nanosecond;
- Using a monochromator, the desired photon energy can be selected from the broad spectral range of emitted radiation for particular applications.

The ability to tune the photon energy allows the user to vary the sampling depth into the material. A higher photon energy allows for an increase in sampling depth.

2.2.2 Sampling Depth in HAXPES

The main advantage of HAXPES over conventional XPS is the increase in sampling depth. With the high energy X-rays employed in HAXPES (<10 keV) the sampling depth can be increased up to 20 – 30 nm depending on the material of interest. The soft X-rays utilised in XPS fail to provide valuable information on a layered stack or any information on interactions taking place at buried interfaces deeper into the material than ~7-9 nm.

Figure 2.13 displays two survey scans of a ~20 nm thick Co film on a native oxide silicon surface acquired simultaneously at the Diamond Light Source, one with hard X-rays at a photon energy of 5.9 keV and the other with soft X-rays at a photon energy of 1.2 keV, with insets of the Co 2p also taken at these energies. The hard x-ray scan shows a very intense and mostly metallic Co signal, as seen in the Co 2p inset. On the other hand, in the soft x-ray scans a very prominent O 1s peak is present. The Co 2p does not appear to be metallic in nature but oxidised.

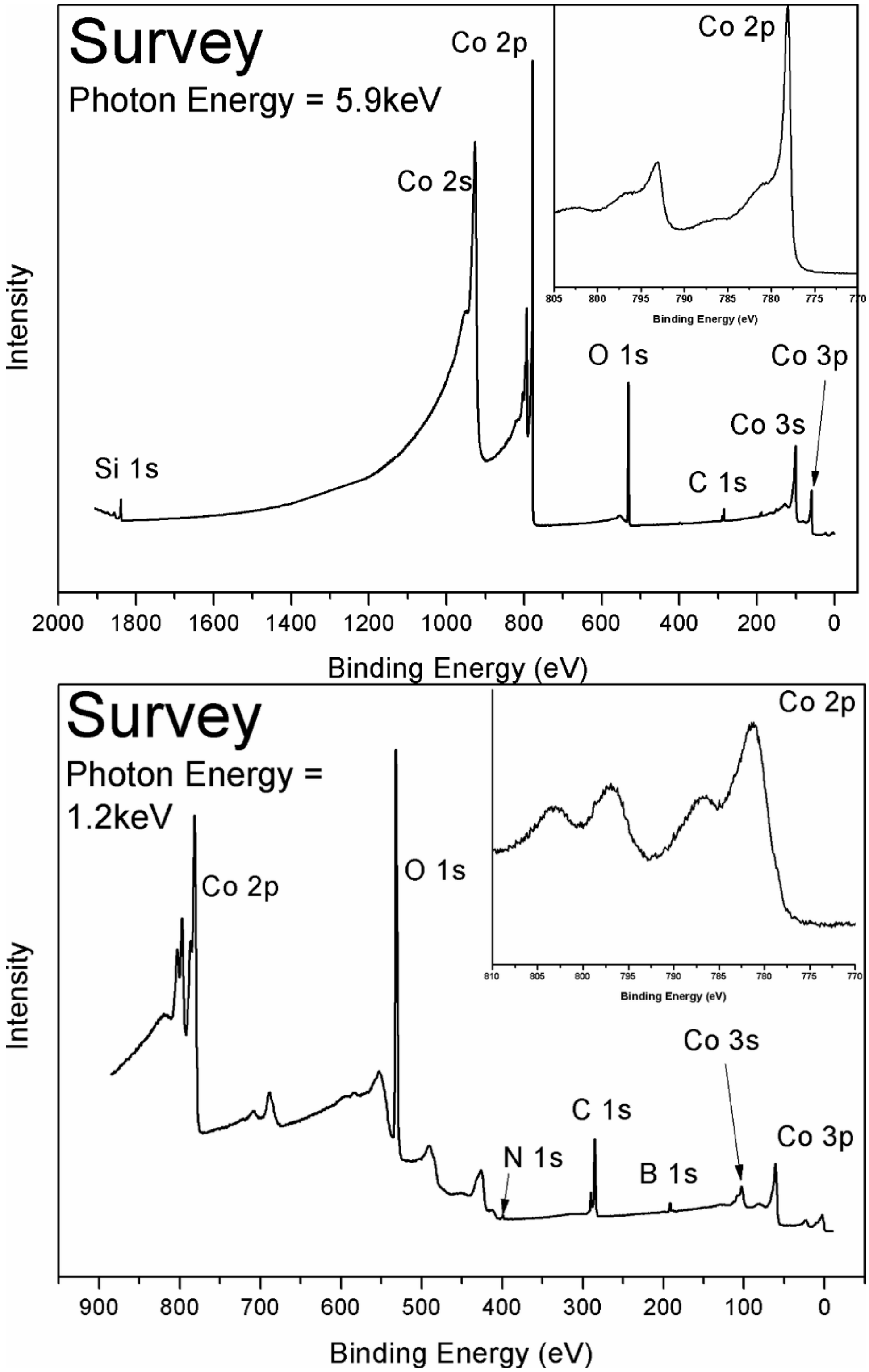

Figure 2.13 (a) Hard X-ray scan and (b) soft X-ray scan taken of a 20nm thick Co sample at the Diamond Light Source. Insets show the Co 2p in detail highlighting both the bulk and surface properties.

Within the sampling depth of the soft x-rays the Co film appears to be oxidised but from the hard x-ray scans one can see that the film is predominantly metallic. This exhibits the surface sensitive characteristics of the soft X-ray spectrum as the cobalt oxide is surface localised. In contrast, the hard X-ray spectrum exhibits the increased sampling depth by the presence of a Si 1s peak. Furthermore, this Si signal can only originate from the underlying substrate, which implies that with the hard X-rays the whole 20 nm Co film is observed.

2.2.3 Synchrotron Sources

Figure 2.14 shows an example of a third-generation synchrotron facility. The electrons are generated by an electron gun, most commonly through thermionic emission from a hot filament. The electrons are then accelerated in a linear accelerator or linac, which is a straight section. The electrons then enter the booster ring where they are accelerated to relativistic velocities. Once the electron current in the storage ring drops by a certain amount, more electrons are injected from the booster ring into the larger storage ring. This helps maintain an almost constant energy in the storage ring so that there is little variation over the course of an experiment. This is known as the “constant top up mode” and alleviates any discrepancy that could have previously occurred in the acquired data from a reducing photon flux intensity.

Once the electrons are in the storage ring they are held on a closed loop by the magnet lattice or bending magnets. The bending magnets are very strong, and they force the electrons to bend to the arc of the storage ring. In Diamond Light Source for example the bending magnets have a maximum operating gradient of 15 T/m [21]. The number of bending magnets can be increased or decreased to suit the storage ring facility. As the electrons travel around the storage ring, energy is lost due to the emission of synchrotron radiation from the deflection of the bending magnets.

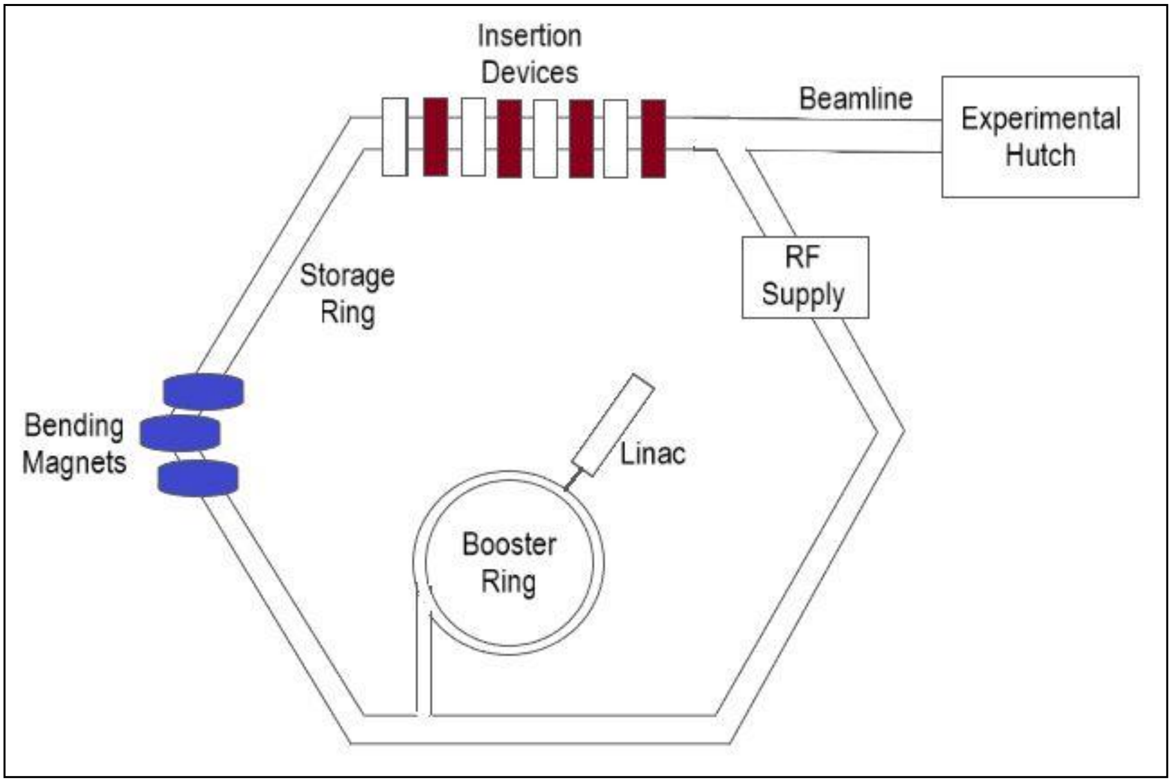

Figure 2.14 A schematic of a third-generation synchrotron. The storage ring is not a true ring but has more of a polygon shape.

Wigglers and undulators are used to produce very high brilliance and are positioned in the straight sections of the storage ring between the bending magnets. The electrons are deflected between alternating magnetic fields and when they change their direction radiation is released. The magnetic field from the insertion devices creates a Lorentz force on the electrons which is perpendicular to both their direction of motion and to the magnetic field. This Lorentz force causes the electrons to oscillate or "wiggle" giving off the radiation. The Lorentz force does not do any work; therefore, the electrons leave the magnet with no net deflection or displacement[20,22]. This is the basic operation of insertion devices shown in Figure 2.15.

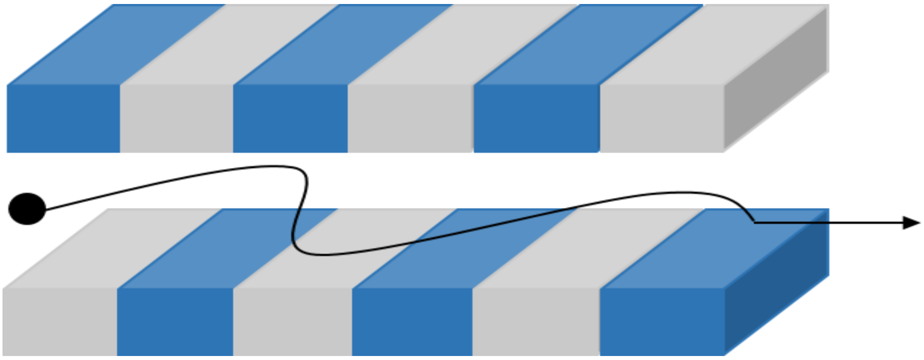

Figure 2.15 Schematic of how an electron moves due to an insertion device.

Wigglers are similar to bending magnets in that they release a broad spectrum of radiation. When an electron enters the wiggler magnet, it essentially "wiggles" causing deflections which release radiation. The emitted radiation from each deflection is in the form of short pulses. These pulses add together to increase the intensity of the emitted radiation. This gives the emitted radiation a broad spectral range. Wigglers emit intense radiation over a wide spectral range, however for a lot of experiments it is more beneficial to have a narrow range of wavelengths and thus a narrow band of radiation.

Undulators release radiation that is highly collimated with a narrow band of radiation. Undulators produce smaller deflections than wigglers. In this case the emitted radiation pulse can constructively interfere with successive emitted pulses which create a narrow beam[17,18,20,22]. The emitted radiation has a higher intensity than bending magnets or wigglers. The difference between undulators and wigglers is shown in Figure 2.16(a) and (b).

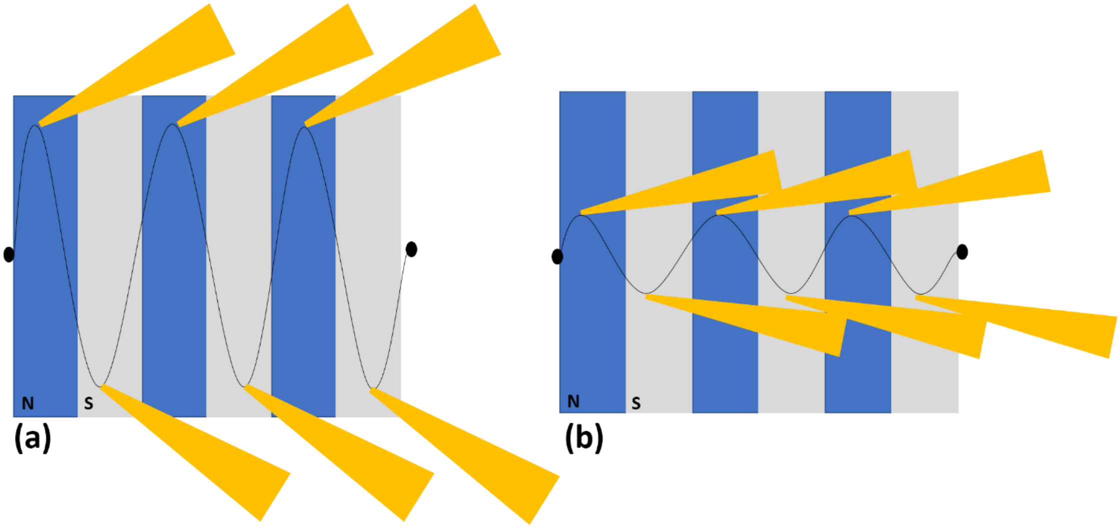

Figure 2.16 In (a) the radiation emitted from a wiggler is quite broad whereas in (b) the radiation from an undulator is narrow.

As shown in Figure 2.14 the beamlines run in a straight section from the insertion devices. In the first section of the beamline or "front end" several important tasks are performed. Firstly, the ring vacuum and beamline vacuum are separated by a series of valves. This is to ensure that the UHV conditions are kept in the storage ring at all times so that the electron's circulation is not interrupted. Secondly, it blocks Bremsstrahlung radiation and filters out unwanted low energy radiation which can interfere with the optics of the beamline. Thirdly, the photon beam position can be observed at different positions along the beamline by beam position monitors. This is for alignment purposes as the sample chamber can be a long distance from the storage ring. Finally, the front end is responsible for defining the angular acceptance of the beam which can be done by the use of apertures.

The optical setup consists of focusing mirrors and lenses that use reflection, refraction and diffraction to direct the X-rays towards the sample chamber. Due to the fact that X-rays are not reflected at incident angles above a few milliradians, the beam optics are designed such that all the incident radiation hits the focusing mirrors at glancing incidence. The Kirkpatrick-Baez is a popular mirror configuration that uses two cylindrical mirrors to achieve both horizontal and vertical focusing.

Although the radiation from the insertion devices is from a narrow band it is not monochromatic and cannot be used for photoemission experiments where precise determination of the photon energy is required. Grating monochromators and crystal monochromators are used to select the photon energy. The grating monochromators work like reflection gratings for visible light. Crystal monochromators use Bragg diffraction to accurately select a certain photon energy. Si is predominantly used as the crystal of choice with two preferred configurations, a double crystal monochromator and a channel cut monochromator. These monochromators are actively cooled using liquid nitrogen or water, as any increase in the thermal energy due to the incidence of high flux radiation, could change the lattice spacing of the crystal which alters the photon energy of the emerging X-rays.

The signal intensity from a buried interface can be severely attenuated and the photoionization cross section decreases with increasing photon energy. Therefore, high flux photon beams are used in HAXPES measurements and frequently the acceptance angle of the detector is increased to improve signal detection.

2.2.4 Systems Used

HAXPES measurements were acquired from three different facilities across Europe, i.e., Diamond Light Source just outside Oxford, PETRA III DESY in Hamburg and SOLEIL synchrotron outside Paris. The data presented in Chapter 6 was taken from Diamond Light Source.

Beamline I09 at Diamond is specially designed for high resolution studies of surfaces and interfaces, Figure 2.17 shows the beamline layout which is especially beneficial to this work as one can employ both soft and hard X-rays at the same time and to the exact same spot on the sample. This gives the unique advantage of simultaneously recording surface and bulk properties at each and every experimental step.

The soft x-ray incident energy was 1.2 keV, while the hard x-ray incident energy was 5.9 keV. A VG Scienta EW4000 HAXPES energy analyser was used to record the spectra. Figures 2.18 and 2.19 show the inside of the experimental hutch with views of the analyser, manipulator arm and the analysis chamber.

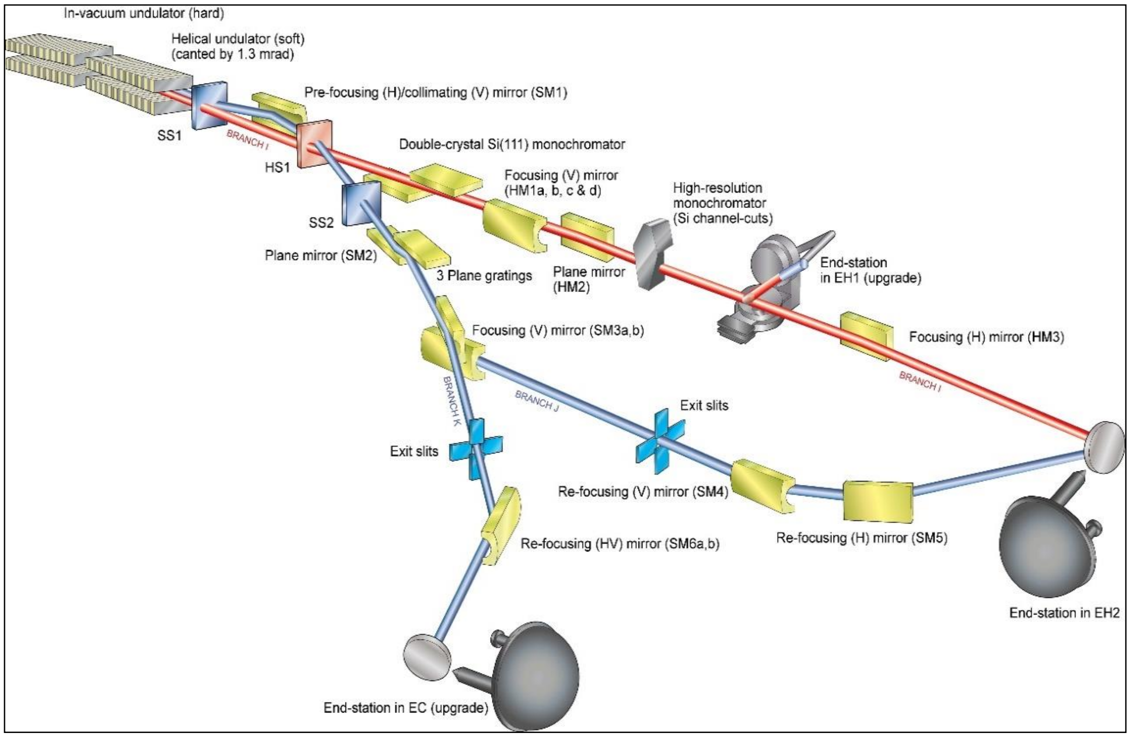

Figure 2.17 Full beamline layout for I09 in Diamond Light Source [23].

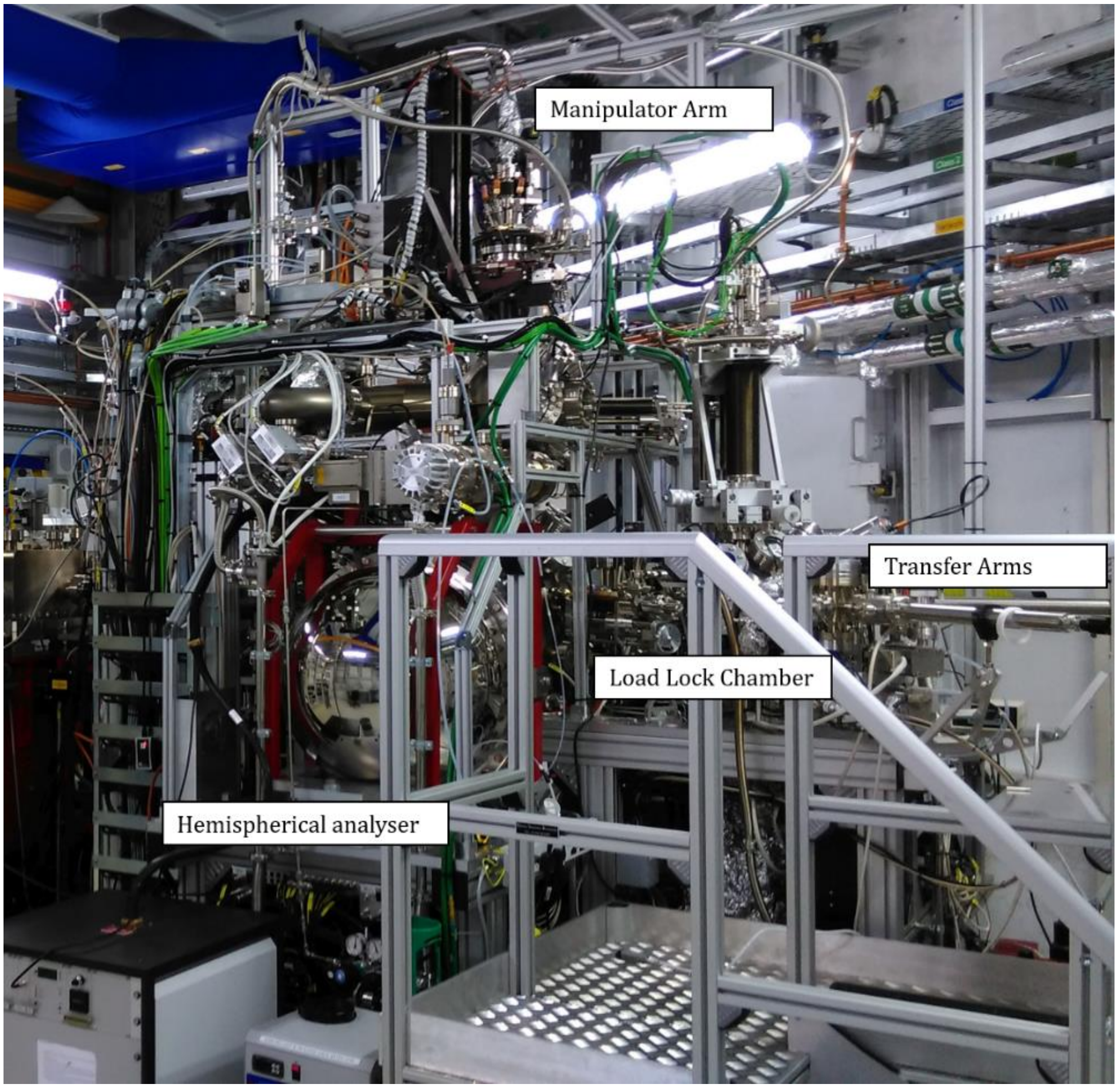

Figure 2.18 Inside experimental hutch i09 at Diamond.

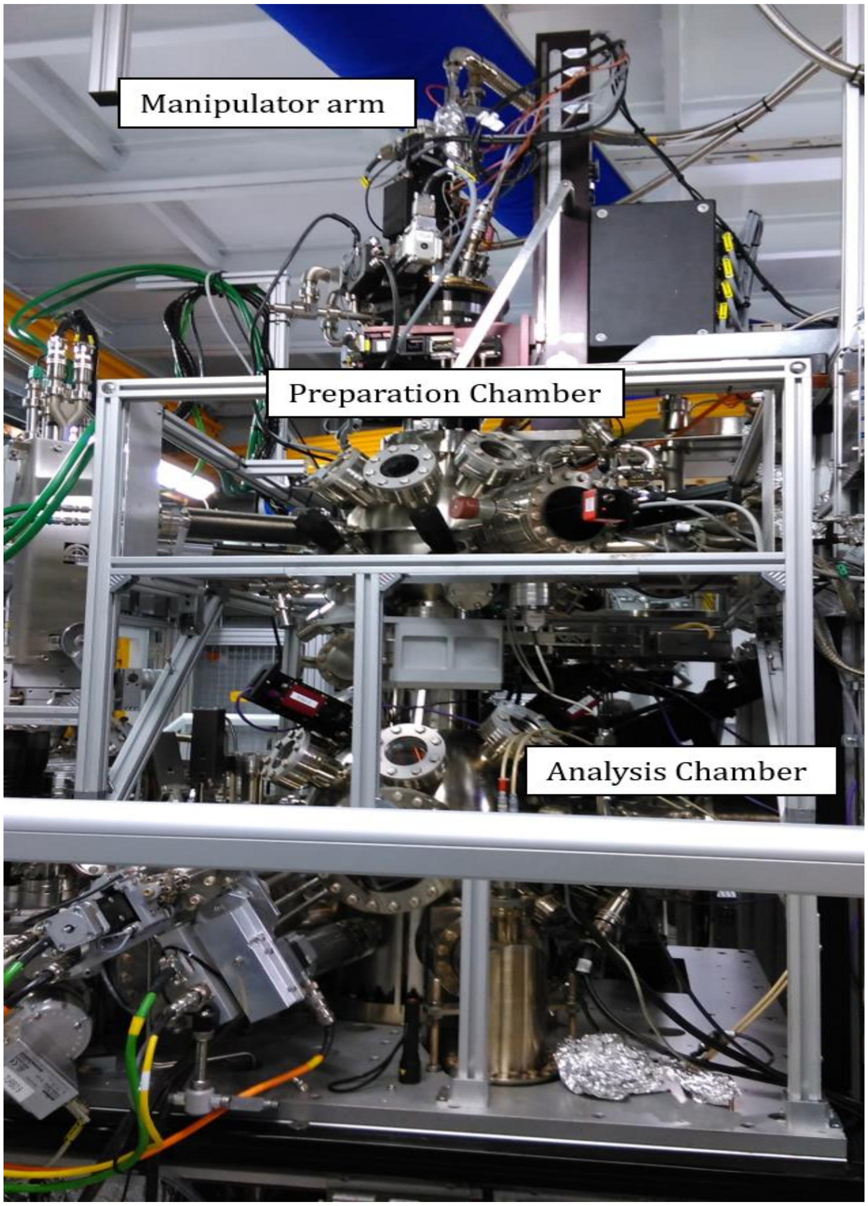

Figure 2.19 Shown is the analysis chamber, sample preparation chamber and the manipulator arm.

2.3 Atomic Force Microscopy

Atomic force microscopy (AFM) is a very powerful surface imaging technique, particularly beneficial for imaging the surface topography of non-conductive and insulating samples. AFM has exceptionally high resolution and can achieve atomic lattice resolution with the state of the art equipment. It can be performed under vacuum, at low temperatures, in a liquid environment or in atmospheric conditions. Almost all types of samples can be imaged from very hard surfaces like metal films[24], uneven surfaces like nanostructures[25,26] and soft samples like cells[27,28]. Variations of the technique can also be used to probe other properties of a sample, such as conductivity, surface energy, surface potential and adhesion to name a few[29]. These characteristics make AFM an invaluable technique in many disciplines of science.

2.3.1 Basic Principals

The atomic force microscope, invented by Binnig, Quate and Gerber in 1986 is based on the idea of using inter-atomic forces as a short-range probe of surface topography[30]. This makes the AFM very unique from other techniques as it does not form an image by using light (traditional optical microscopy) or electrons (SEM and Transmission Electron Microscope (TEM)). Their initial idea was to use a modified Scanning Tunnelling Microscope (STM) to measure small deflections in a cantilever arm that was raster scanned across a surface, however this technique is no longer used as it has been shown to be unreliable [31].

The basic principle of the AFM is to scan the surface with a cantilever arm that has a sharp tip attached. By using Hooke's Law the deflection of the cantilever due to inter-atomic forces between the tip and sample such as Van der Waals, electrostatic and magnetostatic forces can be investigated. At different heights above the surface the tip is subject to different repulsive and attractive forces as seen in Figure 2.20 [30].

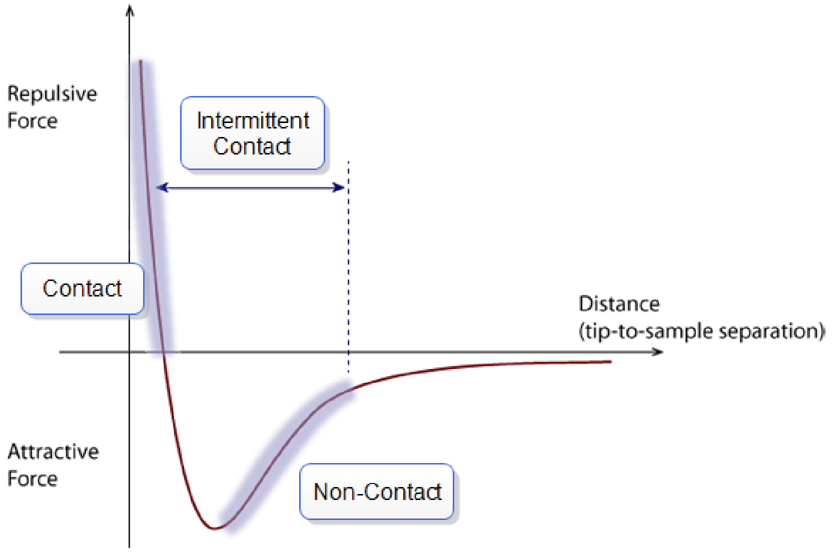

Figure 2.20 The diagram shows the effect of tip to sample distance and how the distance sets the acquisition mode[32].

In their initial set up Binnig et al, were able to show two very important points that underpin modern AFMs. The first point was that a high resonant frequency, f_0, could be achieved with a small spring constant, k, as long as the mass m_0, was also small [30]. This is shown by:

$$f_0 = \frac{1}{2\pi}\sqrt{\frac{k}{m_0}} \tag{2.11}$$

A high resonant frequency gives the AFM a remarkably vibrational stability that is needed to isolate the system from external vibrations reducing them to subatomic amplitudes. The system can be viewed as a damped harmonic oscillator [31]. The second point was that a small deflection of the cantilever arm was related to the detection of a very small force. Binnig's group reported that the force for an ionic bond is approximately 10^{-7} N and for van der Waals bond is approximately 10^{-11} N. Both forces were easily detectable with their system [30].

In modern AFM systems, an optical detection system is used to measure any changes in the cantilever arm deflection. In order to be highly reflective, the back of the cantilever is usually coated in gold or aluminium. A laser is incident on the back of the cantilever and is reflected to a split photodiode. As the cantilever deflects, it causes a change in the position of the signal on the photodiode. The motion of the cantilever is measured by monitoring this signal change. A two quadrant or four quadrant photodiode can be used. The cantilever is used as a spring balance to measure the interaction force[31]. To keep the cantilever at a fixed force a feedback circuit is used. As the cantilever is raster scanned across the surface it will experience different forces at different regions reflecting topographic changes in the surface profile. The feedback circuit is used to maintain a constant force as an image is created from the deflection signal on the photodiode detector. The basic mode of operation of AFM is shown in Figure 2.21.

2.3.2 AFM Modes

Many different AFM scanning modes exist including contact modes, non-contact modes, multipass techniques and intermittent contact modes. In contact mode the tip is in contact with the surface and measures a repulsive force. This repulsion has the effect of deflecting the cantilever arm rather than bringing the tip in closer to the surface. The main drawback of this mode is that the probe tip can damage or even alter the surface during the scanning process. The advantages of this mode are that the scan rate is fast, and it is good for rough samples. In non-contact mode the tip is held at a distance above the surface so that it no longer feels a repulsive force but an attractive force. The main disadvantage of this mode is that it needs to be performed in vacuum to prevent water contamination on the surface impacting on the measurement [5,33].

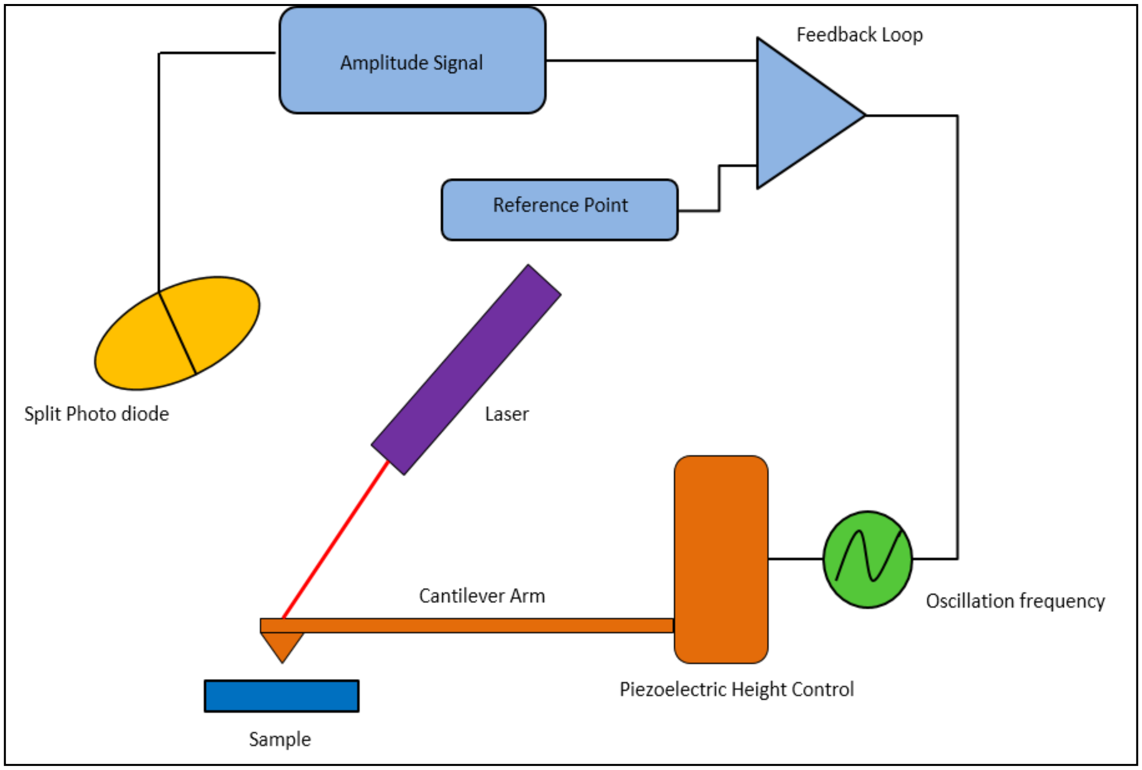

Figure 2.21 Schematic of an AFM.

The imaging mode employed in this work is tapping mode which is also known as intermittent contact mode. In tapping mode, a certain oscillation frequency, close to the resonant frequency of the probe is applied to the AFM tip. The probe taps the surface repeatedly as it scans. This removes some of the lateral forces on the probe tip. The feedback loop adjusts the height of the tip, so it remains at a constant amplitude of oscillation [31].

2.3.3 Image Artefacts

As with all microscopy, AFM is susceptible to image artefacts. Image artefacts can arise from several different sources including the tip, the scanner and the way the image is processed. The shape of the tip is very important as it is this profile that limits the resolution that can be achieved. AFM tips are usually made by a microfabrication process that includes several steps such as photolithography, thin film deposition and etching steps, where typically a Si wafer is etched to have a cantilever shape and then a tip is grown on the Si[31]. The tips usually have a radius of <10nm. An image can take on features at its edges that reflect the radius of curvature of the tip, known as tip broadening shown in Figure 2.22. If the shape of the tip is known, then any features related to the tip profile can be removed from the image. As the shape of the tip is so critical for a good image, its preparation and manufacture have to be of the highest quality. If the tip becomes contaminated with material from the surface or gets damaged from scanning the surface, the resulting image can include a repeating pattern or shape. It is not possible to remove these artefacts and so the image must be taken again.

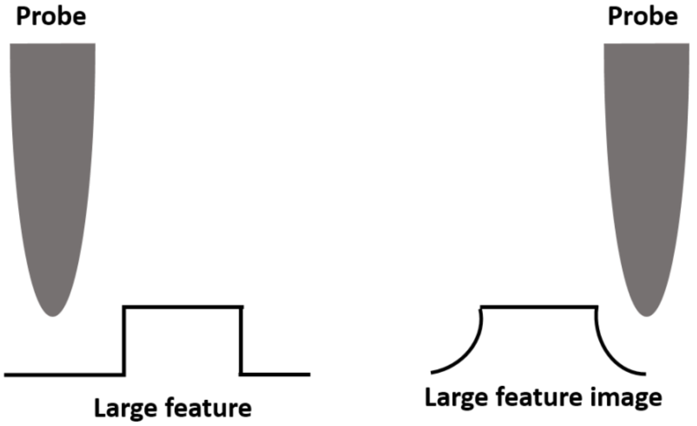

Figure 2.22 Example of tip broadening.

The piezoelectric tube scanners are very popular AFM scanners, but they can also introduce some image artefacts. Calibration of the x, y and z axes is extremely important as this is where problems can arise. If the x and y axes are not correctly calibrated the measured distances can be incorrect which can cause features in an image to appear smaller on one side of the image to the other. Likewise, if the z scanner does not behave linearly and is not calibrated correctly, inaccurate height information can be collected. Another scanner related artefact is scanner bow. This occurs when one end of the tube scanner is fixed, and the other end is free to move which can cause the probe to follow a curved motion. The final image will then appear to be curved or bowed. This problem can be corrected by some image processing.

2.3.4 Image Processing & Analysis

AFM can provide some very valuable information that cannot be found using other microscopy techniques. The AFM data is already calibrated, unlike SEM and TEM images where scale bars are needed. The data is intrinsically 3D and so it is easy to switch between 2D and 3D modes. Several different modes of information can be collected at the same time on the same position. AFM can build a topographical image of the surface, which can be displayed as a false colour map with each colour representing a different height. An amplitude image can also be created which represents how the tip was deflected as it maps out the surface topography. In essence, it represents the error in the deflection of the cantilever arm as it raster scans the surface. A phase image can also be created which reflects the tip response to variations in adhesion and elasticity on the surface. As the cantilever arm moves in and out of contact with the surface there can be changes in the oscillation of the cantilever or in other words a slight phase shift can be introduced. This phase shift is essentially a measure of how the energy dissipates between the tip and the sample. Phase imaging is very useful as it can readily show up features that might not be so clear in a topographic image[33,34].

Gwyddion was the principle software used for processing and analysing the AFM images acquired in this thesis[35]. Over processing of images can lead to loss of image information so it is of the upmost importance to perform as few processing steps as possible to retain the integrity of the data. The most important first step is to level the data, this gets rid of any scanner bow or tilt in the image. This can be done several ways for example, by fitting a polynomial equation to the image or by three-point fitting which selects three points in the image and defines a plane through these points. Once the image is levelled it is best not to perform any more processing unless certain information is required. The use of low-pass filters, Fourier transforms, or Hough transforms allow for specific information to be obtained.

In this work all images were levelled. Due to electronic feedback in the z scanner some frequency noise was introduced to some of the images. This presented as horizontal lines in the images which were removed by applying a Fourier transform. Great care was taken to exclude the correct frequency, so the image would be clarified but not altered.

From Gwyddion, information like the root mean square roughness of the sample, grain size and distances between features can all be determined. The root mean square roughness represents the standard deviation of the surface heights of each point on the image. Grain size and feature distance can be acquired from line profiles extracted from the image.

2.4 References

(1) Chusuei, C. C. .; Goodman D Wayne. “X-Ray Photoelectron Spectroscopy.” *Encycl. Phys. Sci. Technol.* **2002**, *921* (938).

(2) Vickerman, J. *Surface Analysis - The Principal Techniques*, 2nd ed.; John Wiley & Sons: Chichester, UK, 2009, pp 47-113.

(3) Moulder, J. *Handbook of X Ray Photoelectron Spectroscopy: A Reference Book of Standard Spectra for Identification and Interpretation of XPS Data*, 2nd ed.; Chastin, J., Ed.; Perkin-Elmer Corporation: USA, 1992, pp 9-29.

(4) Woodruff, D. P.; Delchar, T. A. *Modern Techniques of Surface Science*, 1st ed.; Cambridge University Press: Cambridge UK, 1988, pp 96-126.

(5) Alford, T.; Feldman, L.; Mayer, J. *Fundamentals of Nanoscale Film Analysis*; Springer: New York USA, 2007.

(6) Seah, M. P.; Dench, W. A. Quantitative Electron Spectroscopy of Surfaces: A Standard Data Base for Electron Inelastic Mean Free Paths in Solids. *Surf. Interface Anal.* **1979**, *1* (1), 2–11.

(7) Hofmann, S. *Auger- and X-Ray Photoelectron Spectroscopy in Materials Science*, 1st ed.; Springer Series in Surface Sciences; Springer Berlin Heidelberg: Berlin, Heidelberg, 2013; Vol. 49, pp 1-204.

(8) Tanuma, S.; Powell, C. J.; Penn, D. R. Calculations of Electron Inelastic Mean Free Paths. V. Data for 14 Organic Compounds over the 50-2000 eV Range. *Surf. Interface Anal.* **1994**, *21* (3), 165–176.

(9) Tanuma, S.; Powell, C. J.; Penn, D. R. Calculations of Electron Inelastic Mean Free Paths. IX. Data for 41 Elemental Solids over the 50 eV to 30 keV Range. *Surf. Interface Anal.* **2011**, *43* (3), 689–713.

(10) Fadley, C. S.; Nemšák, S. Some Future Perspectives in Soft- and Hard- X-Ray Photoemission. *J. Electron Spectros. Relat. Phenomena* **2014**, *195*, 409–422.

(11) National Institute of Standards and Technology. NIST Database https://srdata.nist.gov/xps/main_search_menu.aspx.

(12) Watts, J.; Wolstenholme, J. *An Introduction to Surface Analysis by XPS and AES*, 1st ed.; John Wiley & Sons, Ltd: West Sussex, England, 2003, pp 1-89.

(13) Alvarez, G.; Silverstone, H. J. Photoionization Cross Section: Exact Expansion over Resonances and Natural Line Shape. *Phys. Rev. A* **1989**, *40* (7), 3690–3697.

(14) Biesinger, M. C. X-ray Photoelectron Spectroscopy (XPS) Reference Pages http://www.xpsfitting.com/2009/04/relative-sensitivity-factors-rsf.html (accessed Mar 13, 2018).

(15) Wagner, C. D.; Davis, L. E.; Zeller, M. V.; Taylor, J. A.; Raymond, R. H.; Gale, L. H. Empirical Atomic Sensitivity Factors for Quantitative Analysis by Electron Spectroscopy for Chemical Analysis. *Surf. Interface Anal.* **1981**, *3* (5), 211–225.

(16) Orozco, P. AAnalyzer http://rdataa.com/aanalyzer/aanaHome.htm.

(17) Winick, H. *Synchrotron Radiation Sources - A Primer*; World Scientific Publishing Co Pte Ltd: Singapore, 1994, pp 1-85.

(18) *Hard X-Ray Photoelectron Spectroscopy (HAXPES)*, 1st ed.; Woicik, J., Ed.; Springer Series in Surface Sciences; Springer International Publishing: Cham, 2016; Vol. 59, pp 1-110.

(19) Willmott, P. *An Introduction to Synchrotron Radiation: Techniques and Applications*, 1st ed.; John Wiley & Sons, Ltd: West Sussex, 2011, pp 39-133.

(20) *X-Ray Absorption and X-Ray Emission Spectroscopy*; Van Bokhoven, J. A., Lamberti, C., Eds.; John Wiley & Sons, Ltd: Chichester, UK, 2016, pp 23-50.

(21) Mhaskar, S.; Bailey, C. P.; Duller, G. M. A.; Kempson, V. C.; Marks, N.; Source, D. L.; Hauge, N.; Bodker, F.; Helmersen, L.; Danfysik, A. S. Magnets for the 3

Gev Booster Synchrotron for the Diamond Light Source. In *EPAC 2006*; 2006; pp 2535–2537.

(22) Winick, H.; Brown, G.; Halbach, K.; Harris, J. Wiggler and Undulator Magnets. *Phys. Today* **1981**, *34* (5), 50–63.

(23) Diamond Light Source Ltd. Diamond Light Source http://www.diamond.ac.uk/Beamlines/Surfaces-and-Interfaces/I09/Beamline-layout.html (accessed Jan 6, 2018).

(24) Salem, M.; Massoudi, I.; Akir, S.; Litaiem, Y.; Gaidi, M.; Khirouni, K. Photoelectrochemical and Opto-Electronic Properties Tuning of ZnO Films: Effect of Cu Doping Content. *J. Alloys Compd.* **2017**, *722*, 313–320.

(25) Martín, J.; Muñoz, M.; Encinar, M.; Calleja, M.; Martín-González, M. Fabrication and Mechanical Characterization of Semi-Free-Standing (Conjugated) Polymer Thin Films. *Langmuir* **2014**, *30* (18), 5217–5223.

(26) Becker, C. R.; Strawhecker, K. E.; McAllister, Q. P.; Lundgren, C. A. In Situ Atomic Force Microscopy of Lithiation and Delithiation of Silicon Nanostructures for Lithium Ion Batteries. *ACS Nano* **2013**, *7* (10), 9173–9182.

(27) Li, M.; Dang, D.; Liu, L.; Xi, N.; Wang, Y. Atomic Force Microscopy in Characterizing Cell Mechanics for Biomedical Applications: A Review. *IEEE Trans. Nanobioscience* **2017**, *16* (6), 523–540.

(28) Barnes, W. J. P.; Baum, M.; Peisker, H.; Gorb, S. N. Comparative Cryo-SEM and AFM Studies of Hylid and Rhacophorid Tree Frog Toe Pads. *J. Morphol.* **2013**, *274* (12), 1384–1396.

(29) Bruker. AFM Modes and Techniques https://www.bruker.com/products/surface-and-dimensional-analysis/atomic-force-microscopes/modes/modes.html (accessed Jan 25, 2018).

(30) Binnig, G.; Quate, C. F. Atomic Force Microscope. *Phys. Rev. Lett.* **1986**, *56* (9), 930–933.

(31) Lindsay, S. M. *Introduction to Nanoscience*, 1st ed.; Oxford University Press: New York USA, 2010, pp 144-158.

(32) Corporation, B. Nanostructure Physics, KTH Royal Institute of Technology http://www.nanophys.kth.se/nanophys/facilities/nfl/afm/icon/bruker-help/Content/SPM Training Guide/Atomic Force Microscopy (AFM)/Atomic Force Microscopy (AFM).htm (accessed Feb 2, 2018).

(33) Oliveira, R. R. L. De; Albuquerque, D. a. C.; Cruz, T. G. S.; Leite, F. M. Y. and F. L. Measurement of the Nanoscale Roughness by Atomic Force Microscopy: Basic Principles and Applications. *At. Force Microsc. - Imaging, Meas. Manip. Surfaces At. Scale* **2012**, 256.

(34) Eaton, P.; West, P. *Atomic Force Microscopy*; Oxford University Press: New York USA, 2010.

(35) Nečas, D.; Klapetek, P. Gwyddion: An Open-Source Software for SPM Data Analysis. *Cent. Eur. J. Phys.* **2012**, *10* (1), 181–188.

Chapter 3

3 Use of Self-Assembled Monolayers as Seed Layers for the Growth of Mn Copper Diffusion Barrier Layers

This chapter describes an XPS study of the interaction of (3-trimethoxysilylpropyl) diethylenetriamine self-assembled monolayers or DETA SAM with a native Si oxide substrate and a carbon containing low-*k* spin-on-glass (SOG) substrate. The stability of the DETA SAM in UHV is investigated along with its thermal stability. Finally, the interaction of an in-situ deposited thin film manganese metal with the DETA SAM, deposited on both a native silicon wafer and on a low-k dielectric, is investigated by XPS.

3.1 Introduction

With copper's propensity to diffuse into the silicon dioxide interlayer dielectric (ILD), diffusion barrier layers are required to maintain the integrity of the interconnect, as discussed in Chapter 1. As a result of the continuation of backend scaling, the traditional Ta/TaN barrier layer can no longer function as an effective barrier without increasing line resistance which would lead to a loss in performance. A number of different copper alloys have attracted interest as potential new barriers through self-forming barrier mechanisms including Cu:Al, Cu:Ti and Cu:Zr[1–3]. However, manganese based barrier layers appear to be one of the main contenders to replace Ta/TaN barriers, with manganese silicate ($MnSiO_3$)[4–6] and manganese nitride (MnN)[7] both receiving a lot of attention from researchers. These materials have good thermal stability, good adhesion to Cu, Si and to low-*k* dielectric materials. They have also been shown to be effective at inhibiting Cu diffusion [6,8–12].

Any new potential barrier material must also be compatible with low-*k* ILD's. Low dielectric constant materials have been studied extensively for the purpose of replacing silicon dioxide as the interlayer dielectric material of choice for future technology nodes. There are two ways of reducing the dielectric constant (i) by introducing carbon into the oxide and (ii) by adding pores as described in Chapter 1 [13–15]. It has been shown that the dielectric constant of these materials is dependent on the pore size so by altering the pore diameter, the dielectric constant can be modified[15,16]. In a porous low-k dielectric, all of the pores must be physically connected, in order to aid expulsion of the porogen in the film during the burning out process, as shown in Figure 3.1. As a result of this structure, both the copper and barrier layer material can readily diffuse into the dielectric[17] unless preventative measures are taken. These difficulties have hindered the integration of porous dielectric materials into the back end of line (BEOL) interconnect fabrication processes. The integration of these materials therefore necessitates the development of a pore stuffing or pore sealant treatment prior to diffusion barrier layer formation.

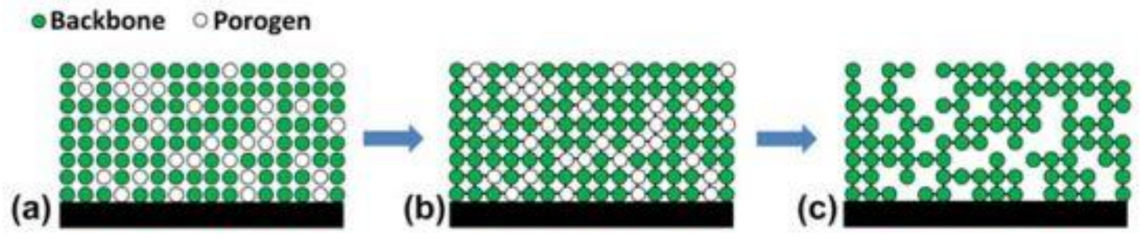

Figure 3.1 Schematic showing the formation of a porous dielectric, (a) the porogen (usually CPO or BMO) is deposited with the low-k precursor, (b) the low-k precursor then crosslinks into a solid layer formed via covalent bonds and finally (c) the porogen is then "burned out" by thermal annealing leaving a porous dielectric [15].

The many advantages of SAMs discussed in Chapter 1 make them a potential candidate for sealing porous low-k dielectric materials to stop Cu diffusion. The silane head group of the DETA molecule promotes adhesion of the SAM to the SiO_2 surface while the amino terminal functional group promotes adhesion of the subsequently deposited metals to the SAM. For the DETA SAM to adhere to the surface, the substrate must first receive a pre-treatment that will generate -OH groups and make the surface more hydrophilic. For an SiO_2 surface a UV ozone treatment is sufficient to activate the surface in preparation for SAM deposition[18]. Low-*k* dielectrics however, require a treatment which will activate the surface, but which will not appreciably affect the bulk properties of the film, especially porous films. Sun *et al.*[19] investigated several different plasmas as a way to modify the low-*k* film surface. It was found that a CO_2 plasma was successful in activating the surface by removing CH_3 groups, without causing damage to the bulk of the low-*k* film. Sun *et al.* then deposited a SAM film on the modified low-*k* showing that the CO_2 plasma also produced hydroxyl groups to allow the SAM to adhere to the surface[19]. The DETA's small size will not significantly increase the cross-sectional area in the interconnect trench, keeping the resistance to a minimum. If the pore size is comparable to the size of the SAM, it should be able to create a bridge across the pore effectively sealing it. However, if the pore diameter is greater than the size of the SAM, then there is a chance of diffusion.

Uedono *et al.*[20] have used positron annihilation spectroscopy to investigate several pore sealing techniques. Their studies suggest that samples whose pores have been sealed by SAMs demonstrate no metal diffusion into the substrate. Armini *et al.*[21] and Sun *et al.*[22] have investigated the effect that different plasma treatments can have on pore sizes and on the sealing of ultra-low-*k* materials. They have found that aggressive plasma treatments can penetrate into the pore and by doing so, allow the SAM to adhere to the pore walls. This has the undesirable effect of increasing the dielectric constant. By using a less aggressive plasma treatment only the pore opening would be modified, which permits the SAMs to only adhere to the pore neck and not infiltrate into the pore. In this case, they have shown that the SAM can essentially seal the pore at its opening by blocking any subsequent deposited metal from infiltrating the pores. This is shown in Figure 3.2.

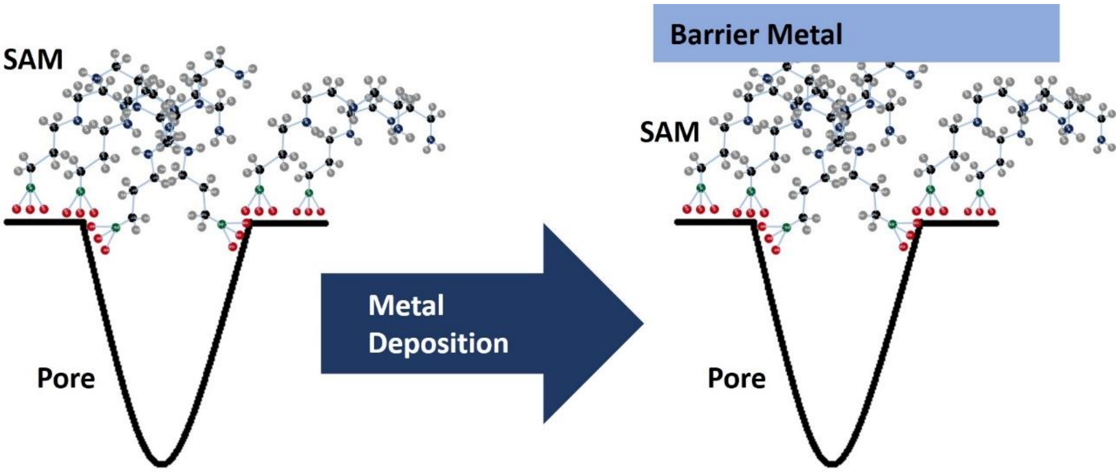

Figure 3.2 The mechanism by which a SAM can act as a pore sealant by blocking the metal barrier at the top of the pore.

The aim of this study is to examine how Mn metal interacts with the DETA SAM which has been deposited on two different substrates, SiO_2 and high carbon content spin-on-glass (SOG). The interaction of the Mn with the DETA SAM will be investigated after metal deposition and with several post metallisation anneals with particular emphasis on the terminal and head groups. An interaction with the head group of the SAM would indicate the diffusion of the Mn through the DETA layer. The stability of the DETA in UHV conditions are investigated along with the thermal stability.

3.2 Experimental Details

The DETA SAM was deposited by IMEC in Belgium and then sent to DCU for analysis. The DETA SAM was deposited via vapour phase deposition on a native silicon dioxide layer on a Si (100) substrate. Initially the oxide substrates were cleaned by 15-min exposure to UV-ozone treatment in a Jelight UVO Cleaner. This treatment was performed to make the surface more hydrophilic and to generate the hydroxyl groups. SAM films were then deposited using 100 μL of a silane precursor at a temperature of 140°C for 1 h with a chamber pressure of ≈10 mbar. Low-*k* SOG films were deposited from a sol based organosilica precursor featuring both terminal and linking carbon groups, and polyethylene oxide containing non-ionic surfactant. The sol was spin-coated on top of 300 mm Si wafers with native oxide. The films were subjected to a 2-min soft bake at 150°C and then hard-baked for 2 hours at 400°C in an N_2 atmosphere. The SOG received CO_2 plasma treatment prior to SAM deposition which was undertaken in a commercial Capacitive-Coupled Reactive Ion Etching (CCP-RIE) chamber with a dual-frequency source (13.6 MHz and 40 MHz) coupled to the bottom electrode. The plasma was ignited and maintained for a duration of 3 s at a chamber pressure of ≈130 mbar by applying 100 W from high-frequency source (40 MHz)[19]. This plasma treatment was used to generate surface -OH groups on the SOG substrates, to aid the adhesion of the DETA SAM. The substrates required different treatments due to the SOG having a much higher carbon content than the Si substrates.

For a full and complete surface chemical analysis, both the reference substrate and SAM coated substrate were mounted on a single sample holder for subsequent loading into the XPS system. This allowed for simultaneous identical anneals, manganese deposition, and surface treatments all within the UHV XPS system. This experimental approach provides a direct comparison between the reference sample and the sample of interest, in this case the SAM coated sample. The samples were introduced into the UHV chamber (base pressure 1×10^{-9} mbar) and did not receive an initial anneal to remove adventitious carbon, so as to maintain the integrity of the received SAM[23]. Mn chips (~99.9 % purity) etched in hydrochloric acid (HCl) were used to deposit metallic manganese via an Oxford Applied Research EGC04 mini electron beam evaporator. The chamber pressure during Mn deposition was 1×10^{-8} mbar. Following Mn deposition, the samples received two thermal anneals, at 200°C and 400°C, at a base pressure of 1×10^{-9} mbar.

XPS analysis was carried out using a VG Microtech electron spectrometer at a base pressure of 1×10^{-9} mbar. The photoelectrons were excited with a conventional Mg Kα (hν = 1253.6 eV) X-ray source and an electron energy analyser operating at 20 eV pass energy, yielding an overall resolution of 1.2 eV. All XPS curve fitting analysis presented in this study was performed using AAnalyzer curve fitting software program version 1.20[24]. Si 2p spectra were fitted with Voigt doublet profiles composed of Gaussian and Lorentzian line shapes. O 1s, C 1s and N 1s spectra were fitted with single Voigt profiles. The metallic components of the Mn 2p spectra were fitted with double Lorentzian asymmetric profiles, while the oxidised components were fitted with Voigt profiles. All peak fitting parameters are listed in Table 3.1. The parameters used in the fitting were the same for both substrates with the exception of the CH component peak in the C 1s spectra which had a Gaussian of 1.95 eV for the SiO_2 substrate but 2.27 eV for the SOG. This is attributed to the fact that the SOG substrate itself contains carbon.

Table 3.1 Peak fitting parameters for all component peaks.

Peak Fitting Parameters					
Si 2p	**Gaussian (eV)**	**Lorentzian (eV)**	**O 1s**	**Gaussian (eV)**	**Lorentzian (eV)**
Bulk	0.6	0.39	**SiO_2**	1.4 -1.5	0.55
SiO_2	1.2	0.39	**MnO**	0.9	0.55
$MnSiO_3$	1.3	0.39	**$MnSiO_3$**	1.5	0.55
C 1s			**N 1s**		
CH (SiO_2)	1.95	0.3	**C-N**	1.5	0.5
CH (SOG)	2.27	0.3	**NH_2**	1.5	0.5
CH_3	2.6	0.3	**Nitride**	1.5	0.5
Carbide	1	0.3			

3.3 Results and Discussion

3.3.1 Chemical Characterisation and Stability of DETA SAM deposited on SiO_2

The survey spectrum of the bare SiO_2 substrate displayed in Figure 3.3 (normalised to the Si 2p substrate component at 98.9 eV) shows the core level peaks associated with the silicon and the oxygen, and a carbon contamination peak at 284.9 eV binding energy. The peaks are normalised to the Si bulk peak as the majority of the XPS signal comes from the underlying substrate. Hence, this peak is not expected to change over the course of the experiment and as such is an internal binding energy reference. Also displayed in the figure is the SAM terminated SiO_2 surface showing the presence of nitrogen (399.1 eV) and fluorine and carbon, in addition to oxygen (532.1 eV) and silicon. Given the relatively small carbon contamination signal observed in the SiO_2 control sample, it is reasonable to assume that almost all of the carbon signal can be attributed to the SAM film. As the DETA does not contain any fluorine, it is thought to have been introduced during the SAM deposition process from contamination that was present in the deposition chamber.

Chemical composition calculations based on these survey spectra have been deduced by applying relative sensitivity factors and calculating integrated peak areas. These are shown in pie chart form inset in Figure 3.3. The percentages are an average measured over four samples, and the range of compositions measured for each element is presented in Table 3.2. All four samples were taken from different positions across the same wafer. This approach is taken to verify that the DETA SAM is uniformly deposited across the wafer.

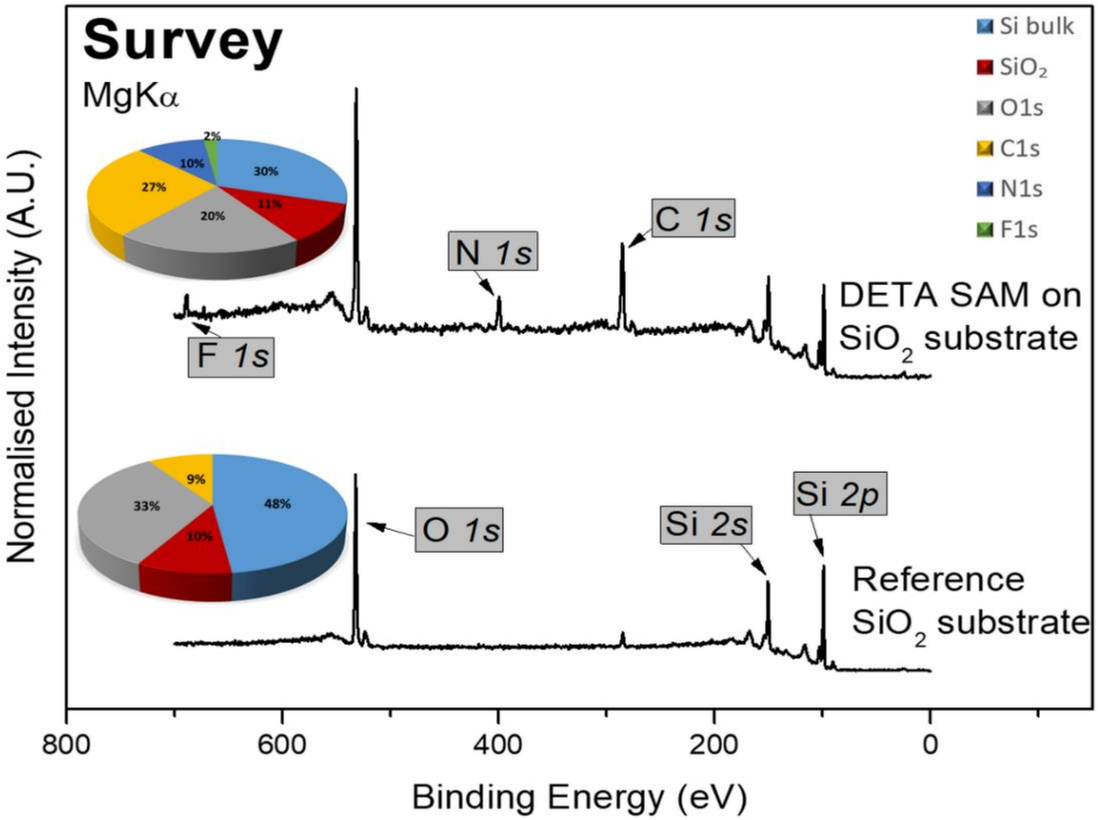

Figure 3.3 The survey scans for the reference substrate and the SAM on SiO2 as loaded with the chemical composition inset.

Table 3.2 Chemical compositions of reference SiO_2 substrate and DETA SAM on SiO_2 as loaded from four samples.

Substrate	**Chemical Compositions**					
	Si Bulk	**SiO_2**	**Oxygen**	**Carbon**	**Nitrogen**	**Fluorine**
Reference SiO_2 Substrate	47 - 49%	8 - 12%	31 - 35%	4 - 14%	-	-
DETA SAM on SiO_2 Substrate	28 - 32%	10 - 12%	19 - 21%	27 - 28%	9 - 11%	2 - 3%

In the reference SiO_2 substrate, the Si bulk signal at ~48 % is attributed to the underlying substrate. In an ideal sample, the elemental ratio between the O 1s (which would come entirely from the SiO_2) and the SiO_2 component of the Si 2p peak should have a 2:1 ratio. In the pie chart the ratio is ~3:1 which is attributed to residual surface contamination from atmospheric exposure, where carbon and oxygen species can adsorb onto the surface. This is also the origin of the surface carbon signal observed on this surface.

After SAM deposition a similar analysis applies and we see a C:N ratio of ~7:3, which agrees well with the actual chemical composition and C:N ratio of the DETA SAM molecule as seen in Chapter 1 Figure 1.7. Survey spectra recorded at an emission angle of 60° is displayed in Figure 3.4 along with the normal emission survey, which show increased N 1s and C 1s signals with respect to the Si and O signals, confirming that the SAM is surface localised. Inset is the chemical composition for the 60° emission angle survey which also reflects this increase in both the C and N 1s signals. Again, both spectra are normalised to the Si 2p.

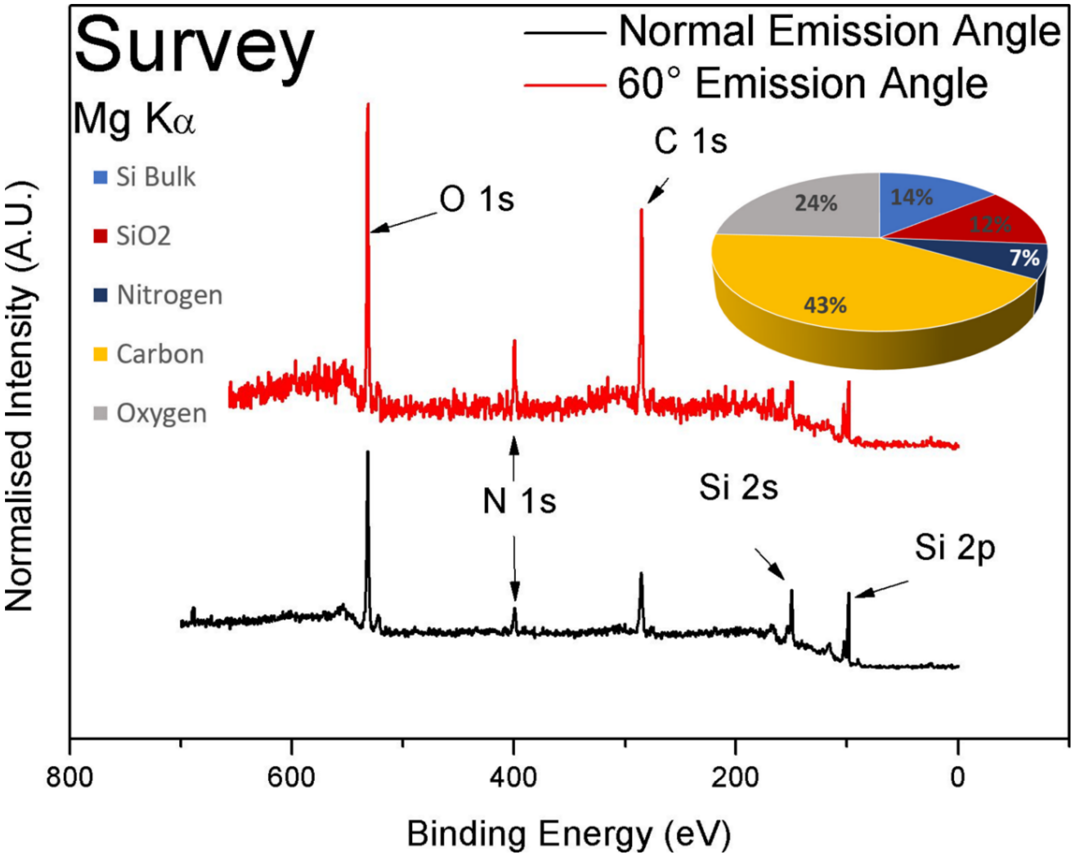

Figure 3.4 Survey spectra of the DETA on SiO_2 taken at both normal emission and at a 60° emission angle showing that the carbon and nitrogen are surface localised.

As discussed in chapter 1, the DETA SAM bonds to the underlying substrate via its own Si atom which should increase the thickness of the SiO_2 component peak. Over layer thickness calculations were performed on the reference SiO_2 sample, a UV-ozone treated sample and the DETA SAM covered sample. These calculations use the ratio of Si bulk to Si oxide signals to estimate the thickness t, of the SiO_2 layer from the equation[25]:

$$t_{ox} = 3.206 \ln\left(\frac{\text{SiO}_2 \text{ intensity area}}{\text{Si intensity area } (0.85)} + 1\right), \tag{3.1}$$

The pre-factor value of 3.206 was experimentally determined for our own XPS system using reference samples of know thicknesses. Figure 3.5 shows that the control sample has an oxide thickness of 0.68 nm. The UV ozone treatment sees an increase in the thickness of the SiO_2 over layer to 0.84 nm. While the DETA SAM appears to have an even thicker SiO_2, with an estimated thickness of 1.1 nm. It is observed that the difference in thickness between the steps is equal to the bond length of Si-O which ranges between 0.155 nm and 0.165 nm[26]. The UV ozone treatment grows an additional monolayer of SiO_2 on the surface and similarly the deposition of the DETA also adds a monolayer to the surface. The additional intensity following SAM deposition is attributed to the SiO_2 based head group in the DETA molecule. This effectively means that the DETA SAM has bonded to the SiO_2 substrate, adding an additional layer of SiO_2. The UV ozone treatment along with the addition of the DETA SAM has increased the thickness of the SiO_2 layer.

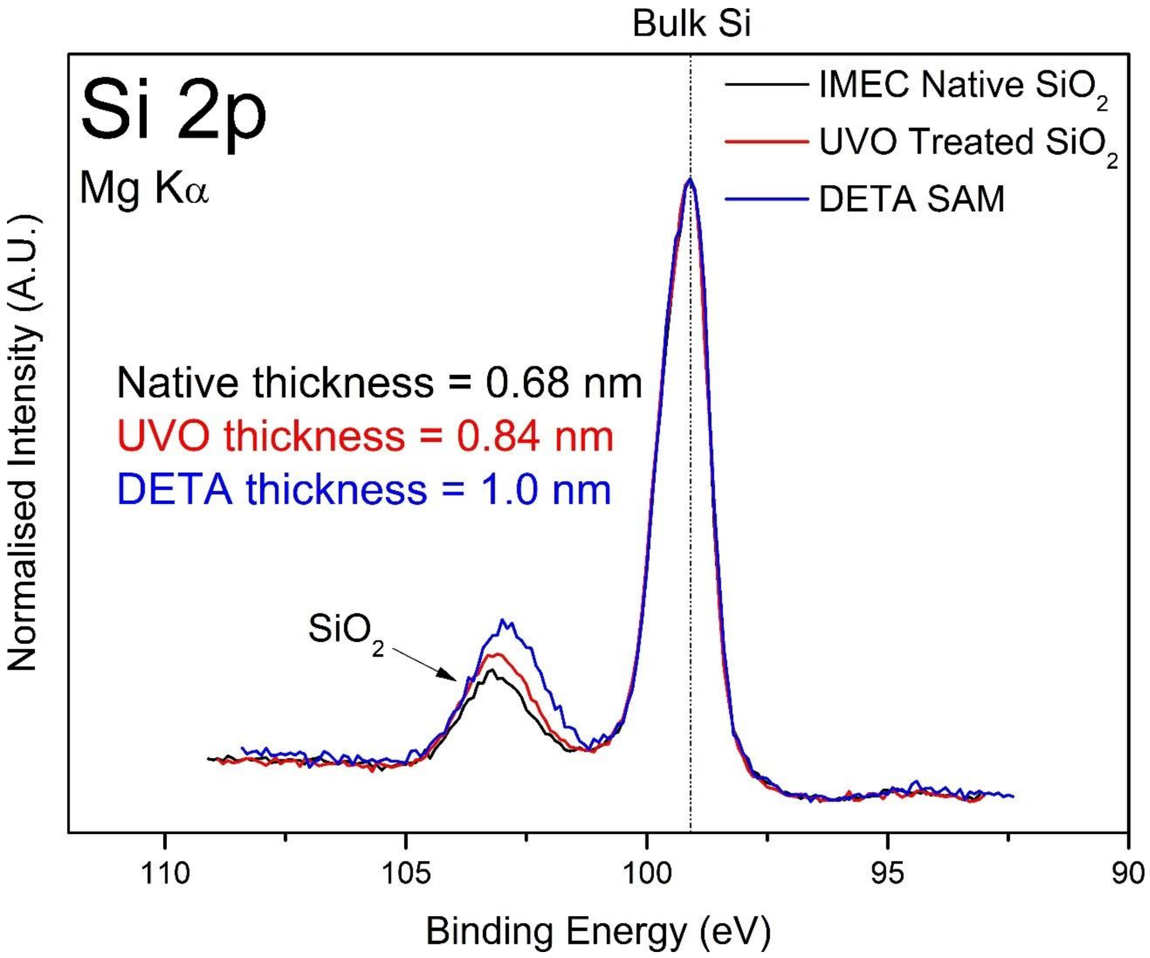

Figure 3.5 The change in SiO2 thickness is seen between each experimental step.

The stability of the SAM film in UHV was established by rescanning the sample after two days in vacuum to reveal no change in the chemical composition, shown in Figure 3.6. Traces of fluorine contamination from the SAM deposition process were observed on the SAM-on-SiO_2 sample representing an elemental composition of ~2 % upon loading. The fluorine signal was reduced to <1 % after two days in vacuum and was below the detection limits of XPS after Mn deposition.

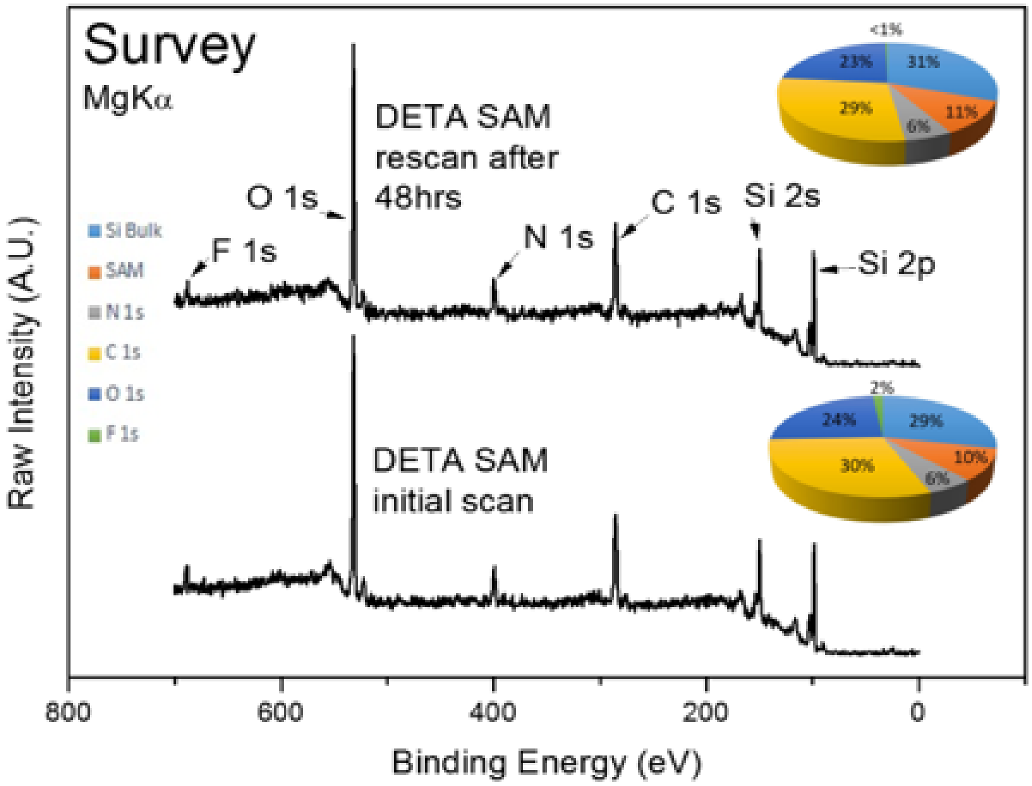

Figure 3.6 Stability of the DETA SAM in UHV after 48 hours.

3.3.2 Interaction of DETA SAM deposited on SiO_2 with ultrathin deposited Mn layer

Following analysis of the starting substrates and the establishment of the DETA SAM's stability in UHV, a Mn deposition was carried out simultaneously on both the control SiO_2 and the SAM-on-SiO_2 samples. Attenuation of both component peaks in the Si 2p spectra, from the underlying substrates was to approximately 70 % of its original intensity. This gave an estimated thickness of ~0.5 nm for the deposited Mn films[27], as seen in Figure 3.7. This thickness was estimated using the NIST Electron Effective-Attenuation-Length or EAL Database, software version 1 [27]. Values for the electron EAL in solid elements are provided by the programme. First the user selects several initial settings such as what elements are being used (in this case Si and Mn), the electron energy and an estimated thickness range for the deposited film. The programme then generates a table of values for the over layer thickness in the selected range. Each value for the over layer thickness has a corresponding value for the percentage attenuation of the substrate. Hence, in this case a 70 % attenuation of the Si 2p corresponded to a thickness of 0.5 nm. The equal thickness of the Mn in both cases suggests similar adhesion to both substrates, and no evidence that the Mn diffuses readily through the SAM upon deposition.

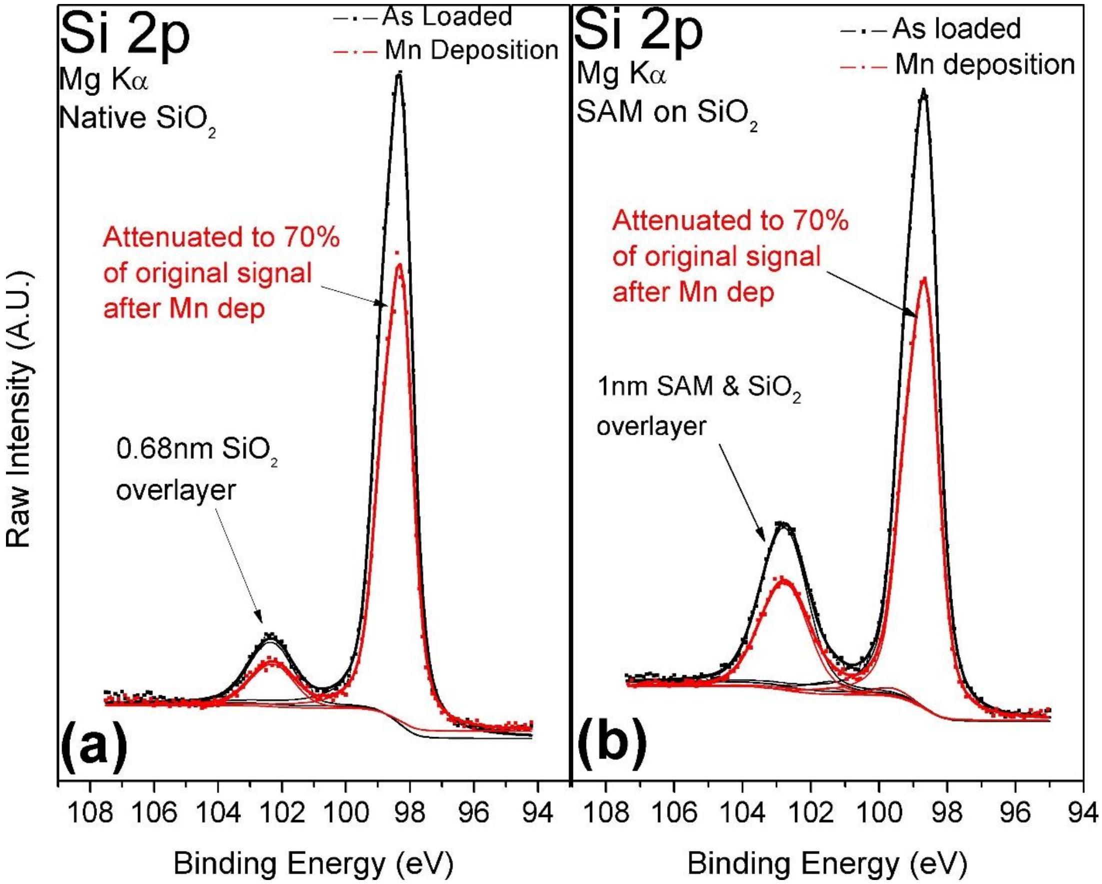

Figure 3.7 Si 2p of (a) the reference native oxide and (b) the DETA on SiO_2. The thicker SiO_2 peak is clearly visible along with the attenuation following Mn deposition.

The O 1s and Si 2p spectra for the reference native oxide sample following Mn deposition and thermal anneals at 200°C and 400°C is presented in Figure 3.8. Mn silicate ($MnSiO_3$) is seen to form in both the O 1s and the Si 2p upon deposition of the Mn. In the O 1s the growth of the $MnSiO_3$ peak is seen at a binding energy of

530.2 eV [28]. Another peak emerges at a binding energy of 528.8 eV which is attributed to Mn oxide (MnO)[29]. The appearance of an oxidised manganese species after a thin 'metallic' manganese deposition, even at UHV pressures, is routinely observed due to traces of residual oxygen in the vacuum system, and the facile nature of Mn oxidation. In the Si 2p the $MnSiO_3$ peak is observed at a binding energy of 101.4 eV [30].

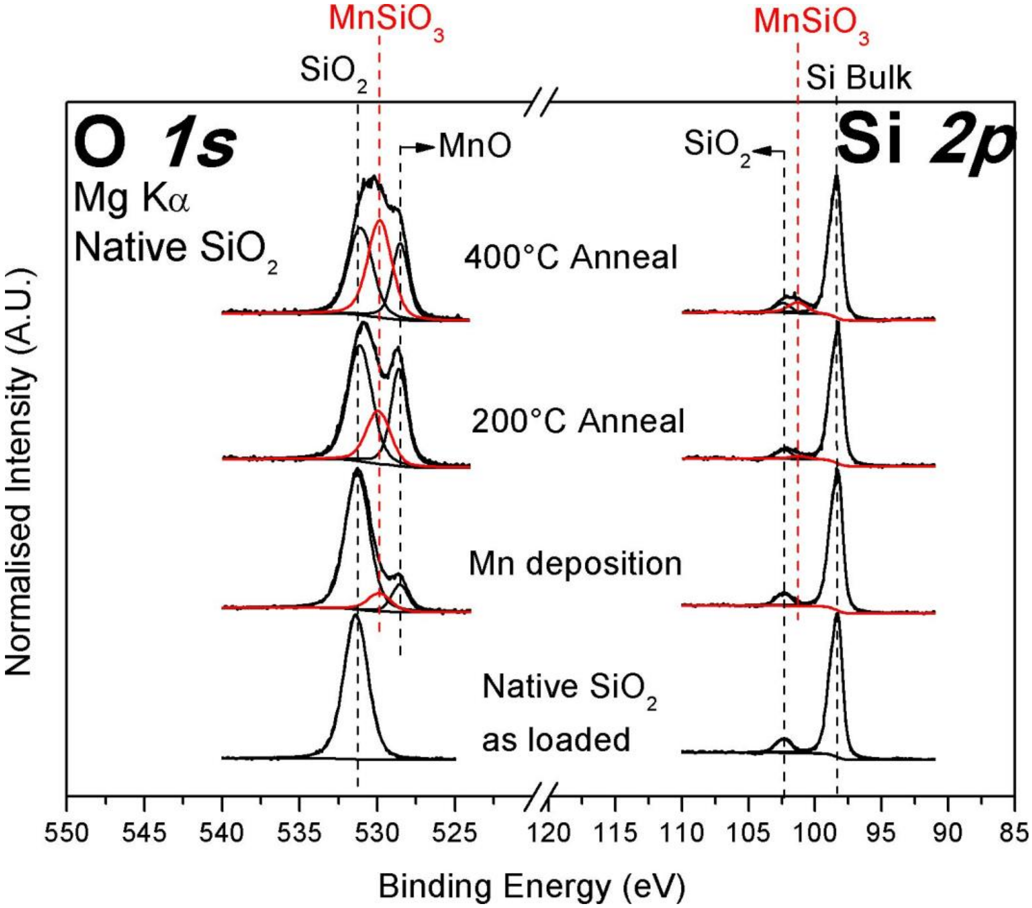

Figure 3.8 O 1s and Si 2p core level spectra for the reference SiO_2 substrate for each experimental step. Following the Mn deposition there is the growth of a silicate peak which grows with thermal anneal.

Following the 200°C anneal there is a significant growth in the MnO component peak in the O 1s suggesting that the Mn is reacting with residual oxygen in the XPS chamber. Also, seen is a significant increase in the Mn silicate component peak in both the spectra. The growth of these peaks suggest that the Mn metal is converting to Mn-oxide and Mn-silicate. The 400°C anneal grows the Mn-silicate peak further still, with the Mn 2p (Figure 3.9) confirming that the Mn metal has fully converted.

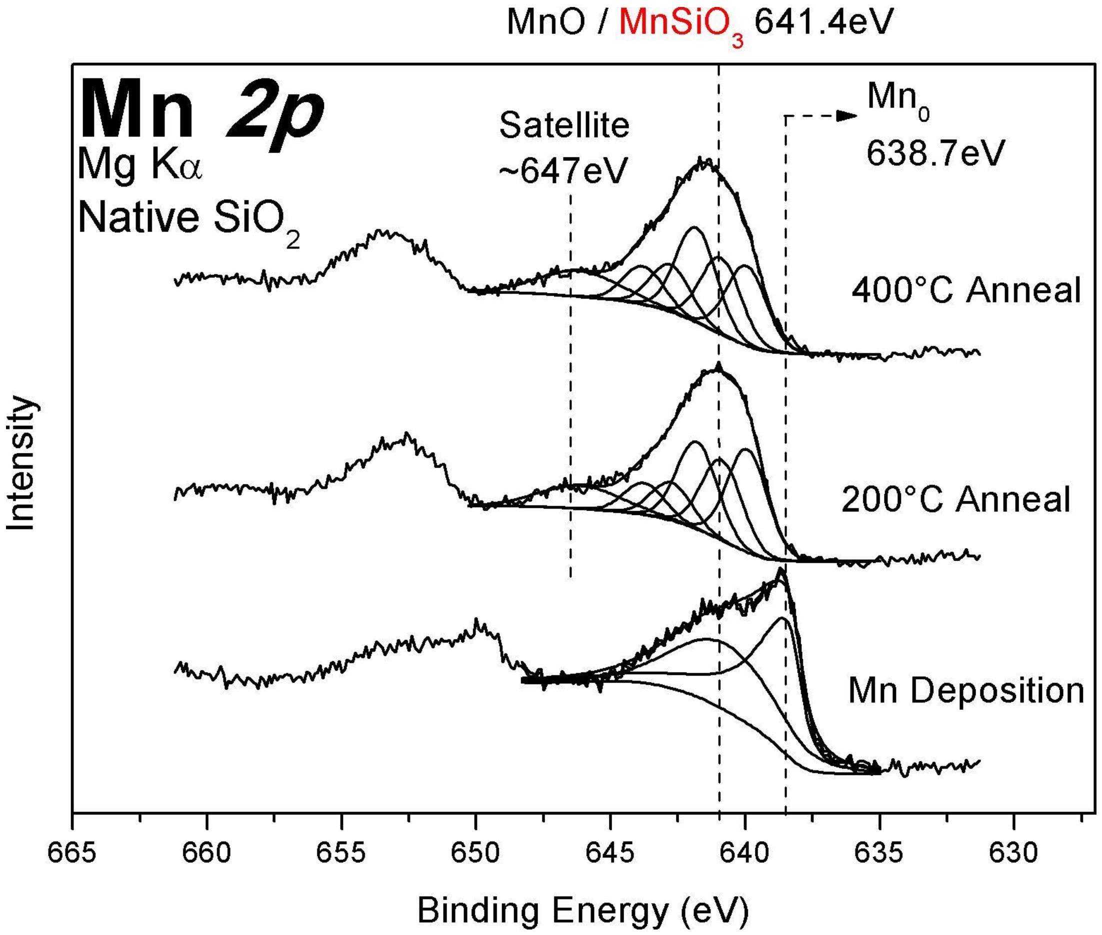

Figure 3.9 Mn 2p for the reference SiO₂ sample showing a mostly metallic deposition. Following thermal annealing the Mn is fully converted to MnO and MnSiO₃.

Following the Mn deposition on the reference SiO_2 sample, a mostly metallic profile is observed in the Mn 2p at a binding energy of 638.7 eV, as shown in Figure 3.9. There is some oxide present in a +2-oxidation state which is indicative of $MnO/MnSiO_3$ formation. This correlates to the $MnSiO_3$ peak observed upon deposition in the O 1s spectra. Following thermal annealing it appears as though all of the Mn has been fully converted to MnO and $MnSiO_3$. This is evidence of the Mn metal reacting with the residual oxygen in the chamber.

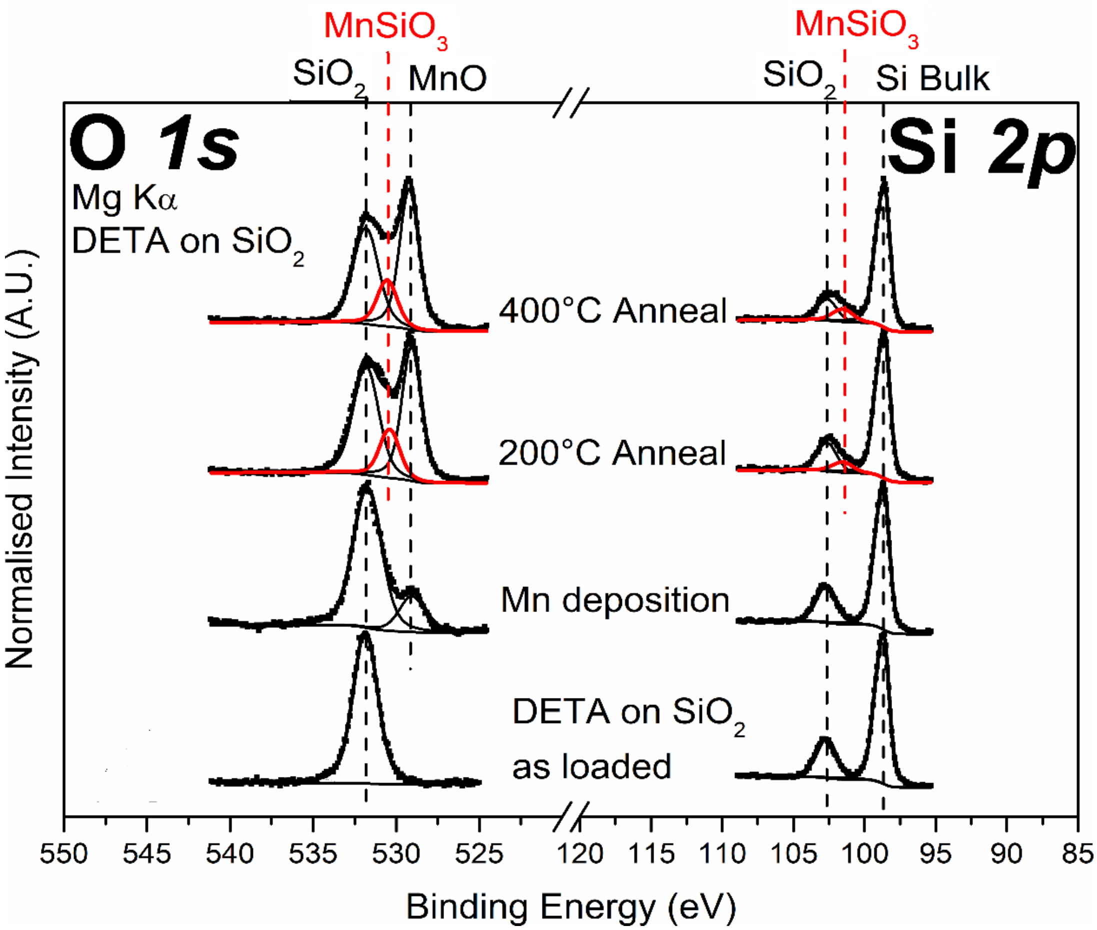

Figure 3.10 O 1s and Si 2p core level spectra for the DETA on SiO_2 for each experimental step. After Mn deposition and the first anneal the growth of a silicate peak is evident.

Upon deposition of the Mn on the SAM on SiO_2 sample, the O 1s spectrum in Figure 3.10 shows the growth of a peak at 529 eV which is attributed to Mn oxide. After a 200°C thermal anneal the Mn-oxide component increases significantly which would suggest a further reaction with residual oxygen but there is also the emergence of the $MnSiO_3$ peak in both the O 1s and in the Si 2p. The silicate peak corresponds to the binding energy positions observed in the reference sample and is separated from the SiO_2 related component peak in the O 1s by 1.3 eV and the Si

2p by 1.1 eV. These peak positions are consistent with the formation of $MnSiO_3$, in agreement with previous studies[31,30]. These $MnSiO_3$ related peaks remain relatively constant in intensity with a further anneal up to 400°C. This reflects the self-limiting nature of the reaction which is due to the small amount of deposited Mn which has been able to interact with the Si interface. The emergence of the peaks related to $MnSiO_3$ formation suggests that the Mn diffuses through the SAM and interacts with the underlying SiO_2 to form Mn-silicate.

The profile of the Mn 2p peak for the DETA on SiO_2, displayed in Figure 3.11 reveals a predominantly metallic profile upon Mn deposition, with the metal component at 638.7 eV [32]. The initial peak fit contains components related to the Mn +2 and +3-oxidation states, indicating traces of mixed phase manganese oxide after the deposition[33]. This is different to the reference sample where there only appears to be evidence of MnO and silicate formation upon deposition. It is thought that this is due to the scanning order following Mn deposition. After the Mn deposition, the DETA sample was scanned before the reference sample and it would appear that the reference sample has oxidised more during this time. Following the 200°C anneal, the Mn 2p profile shows complete conversion of the metallic Mn signal to the +2-oxidation state, indicative of $MnO/MnSiO_3$ formation. The satellite feature observed at a binding energy of 647 eV is consistent with the +2 oxidation state in agreement with previous studies[34]. The lack of any significant change in the Mn 2p peak profile for the SAM on SiO_2 following the 400°C anneal, is consistent with the observation of thermal stability of the O1s and Si 2p peaks in Figure 3.10.

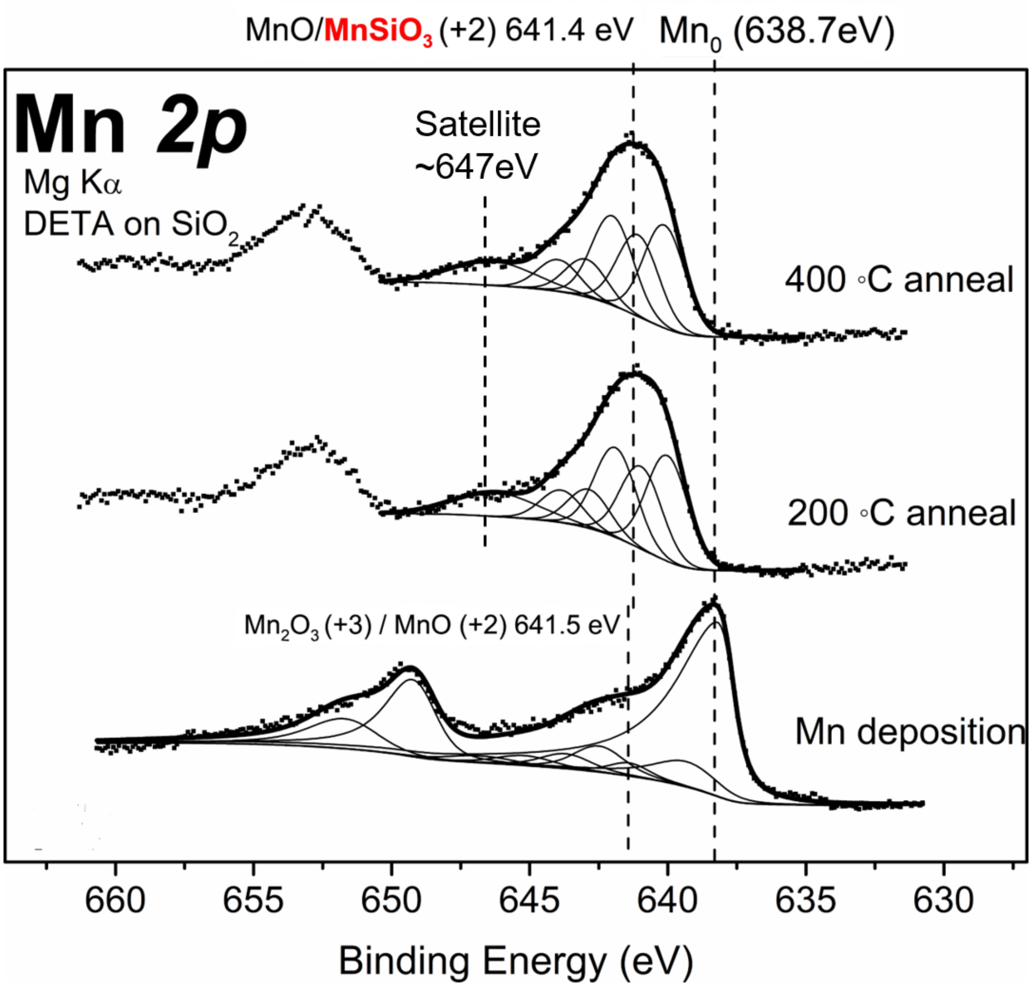

Figure 3.11 Mn 2p spectrum displays a metallic profile upon deposition and the growth of Mn-silicate and conversion of metal to oxide following anneal.

In the C 1s spectrum presented in Figure 3.12(a) two component peaks are attributed to C-C and C-H bonds at 284.9 eV BE and a C-N bonds at 286.8 eV[35] BE. Upon Mn deposition there is the appearance of a peak attributable to Mn-carbide on the lower binding energy side of the main peak at 282 eV. This is similar to the interaction which has been previously observed following the deposition of Mn on a carbon containing low-*k* substrate[31,36]. After the 200° C anneal the Mn carbide peak is no longer observed, as Mn-carbide is unstable at elevated temperatures in the presence of oxygen[35]. The residual oxygen present in the chamber is enough to decompose this carbide. Upon further, higher temperature annealing the peak profile remains largely unchanged other than a slight reduction in intensity indicative of desorption or thermal decomposition of the SAM molecular layer.

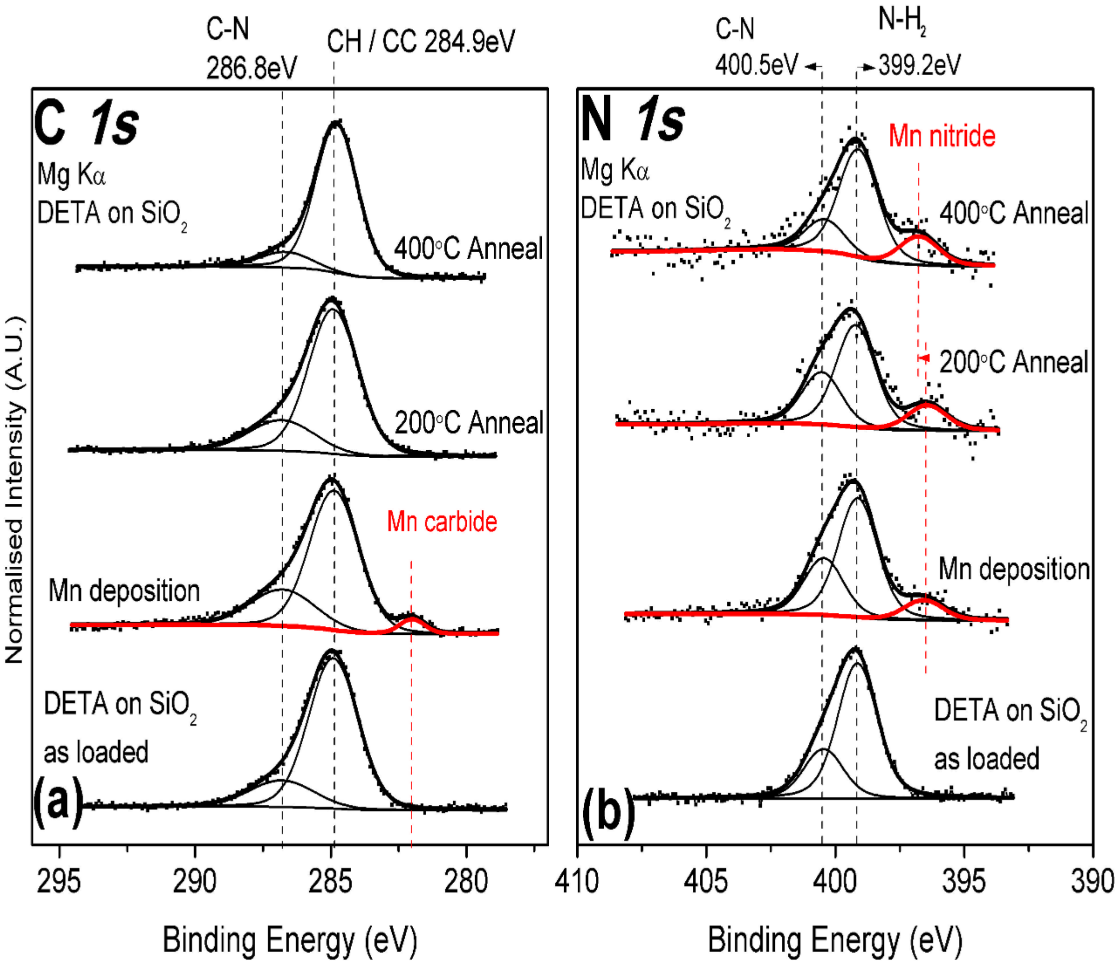

Figure 3.12 (a) C 1s spectrum shows the formation of Mn-carbide upon Mn deposition and its subsequent decomposition following thermal annealing. (b) N 1s spectrum showing the formation of Mn-nitride upon Mn deposition and its stability even after high temperature annealing.

Curve fitting analysis for the N 1s spectrum of the as-deposited SAM-on SiO_2 sample, displayed in Figure 3.12(b), shows two component peaks which are attributed to NH_2 bonds at a binding energy at 399.2 eV and C-N bonds at a binding energy of 400.5 eV[37,38]. Following Mn deposition, there is the emergence of a weak spectral feature on the lower binding energy side at 396.5 eV. This additional peak is in the correct binding energy position for a metal nitride[39] (in this case Mn-nitride[40]) indicating a bonding interaction between the deposited Mn and the N terminal group of the SAM. These component peaks remain largely unchanged through the annealing cycles except for a reduction in the signal-to-noise ratio, possibly reflecting a partial desorption or decomposition of the SAM.

In summary, the interaction of the Mn with the SAM suggests three distinct chemical interactions: (i) $MnSiO_3$ near the bottom interface; (ii) Mn-carbide throughout the SAM's hydrocarbon chain; and (iii) Mn-nitride bonding interaction with the terminal group of the SAM. In the context of integration, this arrangement could be beneficial in that $MnSiO_3$ has been shown to be an effective barrier layer, while MnN has been shown to promote adhesion of copper to the low-k material[7]. The remaining Mn on the surface forms MnO.

3.3.3 Interaction of DETA SAM on Spin-on-glass with ultrathin deposited Mn layer.

The same experimental procedure was followed for a control SOG substrate, and a SAM-on-SOG prior to manganese deposition. The analysis of the SOG sample is complicated by (i) the fact that the substrate contains carbon, making analysis of the C 1s peak more difficult and (ii) the fact that the film thickness is larger than the XPS sampling depth (there is no silicon bulk signal detected) which can be used for binding energy referencing and over layer thickness calculations. Figure 3.13 shows the C 1s and Si 2p spectra for the reference SOG and the SAM on SOG. The component peaks from the SOG and from the SAM are indistinguishable from each other. However, in the Si 2p a small silicon peak at a binding energy of 99.3 eV is present in the as-received spectrum which is tentatively attributable to some residual free silicon due to the incomplete bonding of the silane-based head group of the SAM to the carbon containing SOG surface. This is further supported by the lack of such a feature in the bare SOG spectrum shown in Figure 3.13 indicating that it is related to the deposition of the SAM.

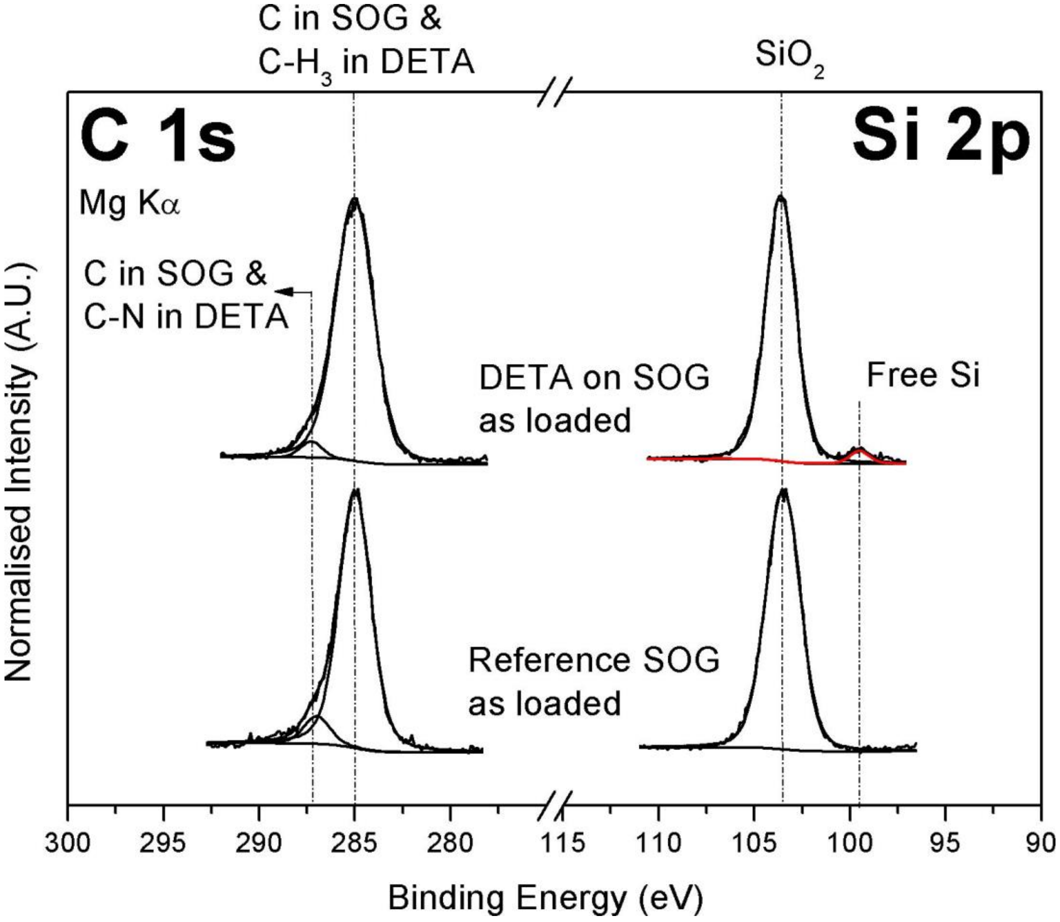

Figure 3.13 (a) C indistinguishable (b) Free Si only present in the SAM on SOG.

The reference SOG and SAM-on-SOG samples were loaded on the same sample holder and received simultaneous Mn deposition and thermal anneals, again up to a temperature of 400°C. Using the attenuation of the low-k substrate peak in the Si 2p spectrum indicates a Mn thickness of ~1.3 nm. Figure 3.14 shows the changes in the peak fitted profiles of the O 1s and Si 2p spectra following Mn deposition and anneal of the SOG reference substrate. Unlike the SiO_2 samples, there is no Si substrate signal visible owing to the fact that the thickness of the spin-on-glass film is greater than the sampling depth of XPS. Unlike the reference SiO_2 sample there is no evidence of silicate formation upon Mn deposition but the growth of MnO at a binding energy of ~529 eV is observed.

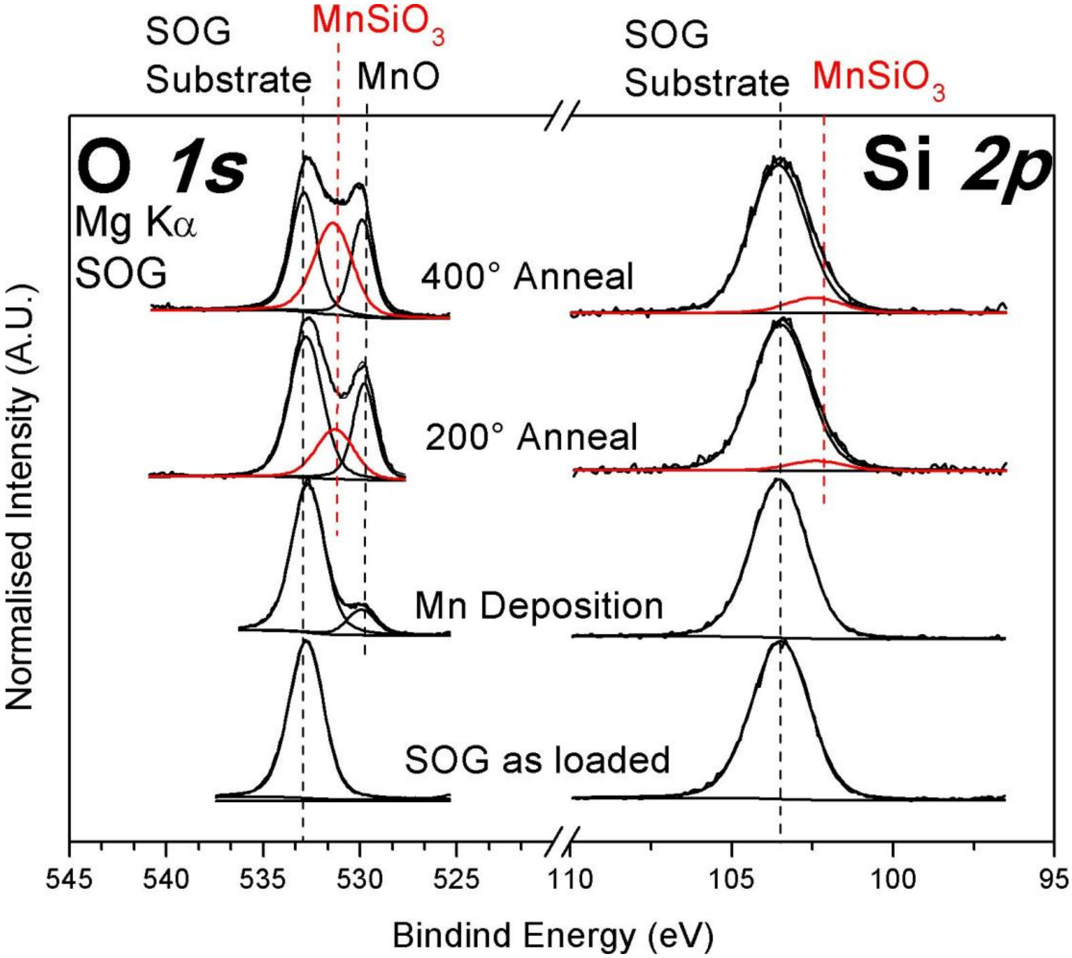

Figure 3.14 O 1s and Si 2p for the reference SOG substrate.

Thermal annealing is required to drive silicate formation and following the 200°C anneal a silicate peak is seen in the O 1s at ~531 eV BE and in the Si 2p at 102.5 eV BE. The MnO is also seen to increase in intensity following anneal. The oxide and silicate are seen to grow with the higher temperature annealing.

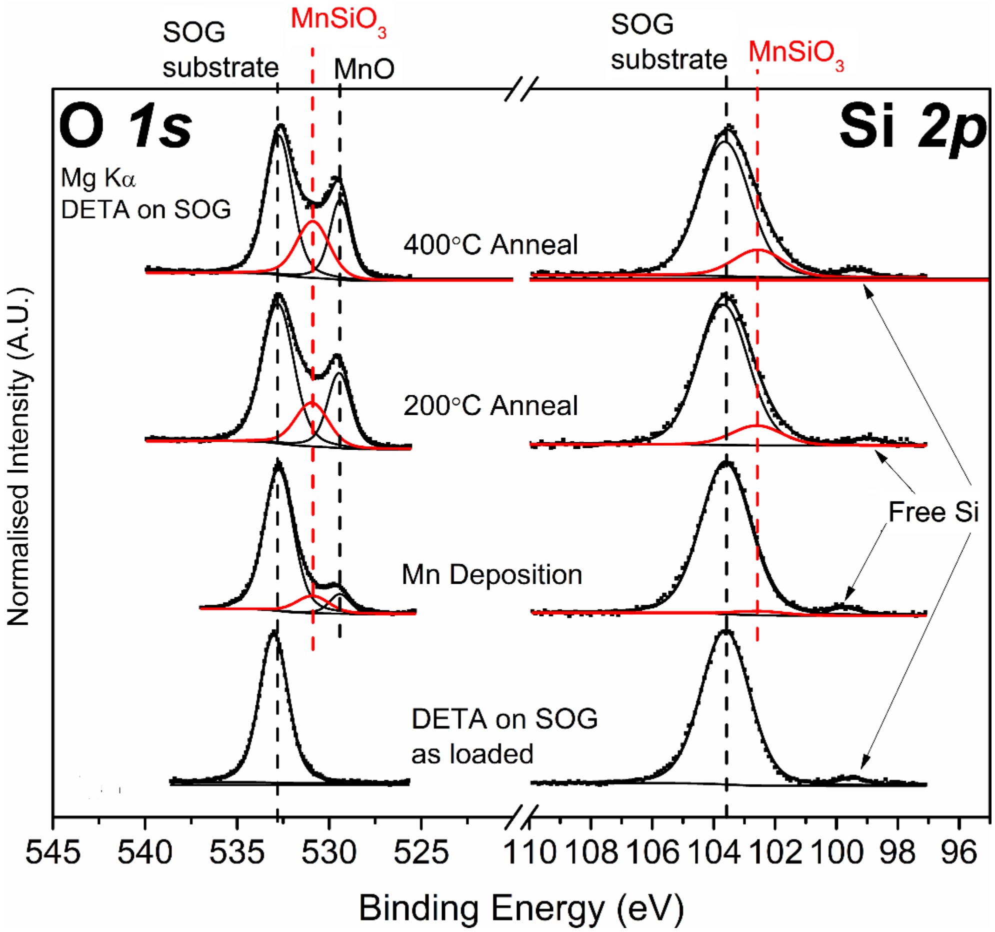

Figure 3.15 O 1s and Si 2p spectra for the DETA-on-SOG showing Mn-silicate formation upon Mn deposition.

Figure 3.15 displays the deconvoluted O 1s and Si 2p spectra for the DETA SAM on SOG. Similar to the DETA SAM on SiO_2, upon Mn deposition the O 1s core level spectrum shows the presence of a peak at ~529 eV BE which is attributed to manganese oxide. Unlike the previous sample, the DETA SAM on spin-on-glass also displays the growth of a small amount Mn-silicate in both the O 1s (~531 eV) and the Si 2p (~102.5 eV) upon Mn deposition.

Evidently, the deposited Mn does not require heating above room temperature to chemically interact with the DETA SAM on this low-k substrate. As stated previously the presence of free silicon can be attributed to dangling silicon bonds within the head group of the DETA SAM which have not bonded to the SOG substrate. It is suggested that this can be understood in the context of the SOG substrate containing a high percentage of carbon. Therefore, it does not have a complete SiO_2 structure to facilitate the co-ordinated bonding of the DETA SAM, even after CO_2 plasma pre-treatment.

In the O 1s core level spectra shown in the same figure, the Mn-oxide component grows significantly with a 200°C anneal and increases further still with anneal up to 400°C. The Mn-silicate component peaks also show an increase in intensity in the O 1s and the Si 2p spectra with the initial 200°C anneal and up to the 400°C anneal. As with the DETA SAM on SiO_2 the Mn can diffuse through the SAM and form Mn-silicate. The profile of the Mn 2p, shown in Figure 3.16, displays a mostly metallic Mn profile upon Mn deposition which, after the 200°C anneal is almost completely converted into a mixed phase, +2 oxidation state of MnO and $MnSiO_3$. However, there is still a small metal shoulder visible on the lower binding energy side of the peak. This could be due to the fact that the Mn film is slightly thicker on this sample than the previous SAM on SiO_2 sample. It appears that the dangling silicon bonds at the SAM-SOG interface drive the formation of Mn-silicate at room temperature. This can be seen from Figure 3.14 where there is no silicate formation upon Mn deposition. However, it is unclear as to whether the oxygen for the reaction comes from the UHV chamber or the SAM/spin-on-glass interface.

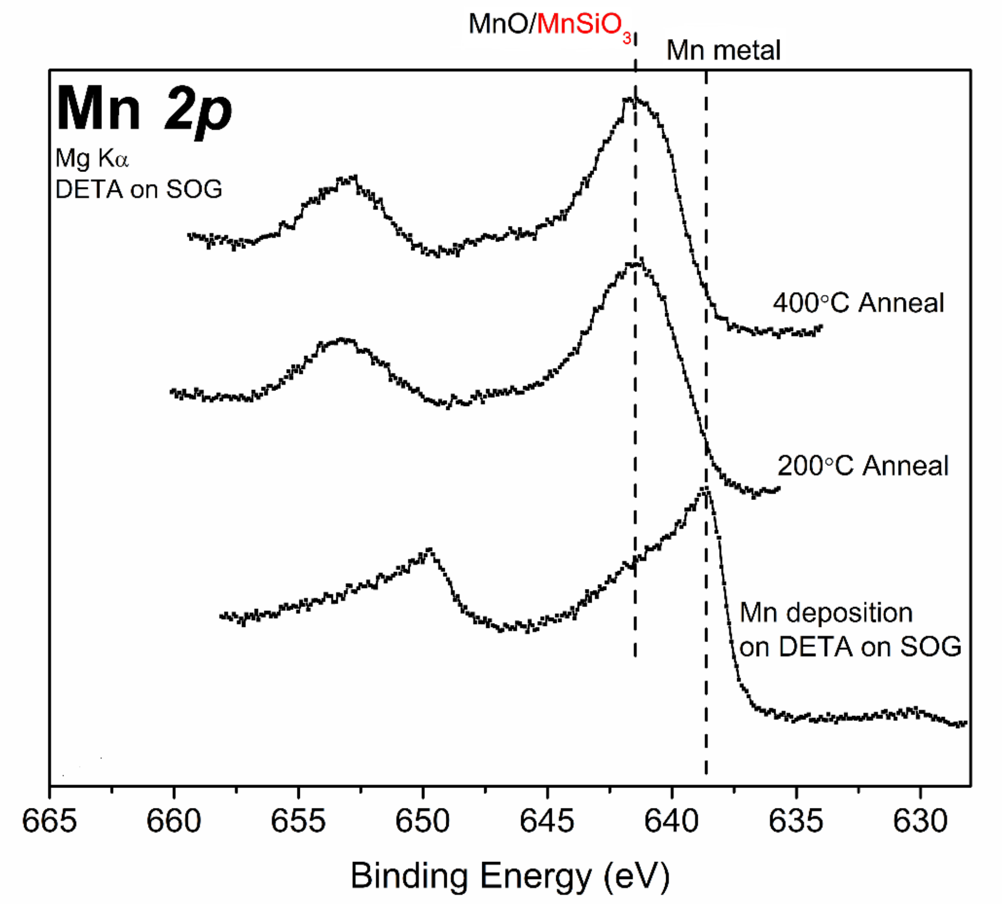

Figure 3.16 Mn 2p spectrum for the SAM on SOG showing an almost metallic deposition and then conversion to a mixed phase oxide and silicate.

The curve fitted C 1s spectra are presented in Figure 3.17(a). The peak profile before manganese deposition is very similar to that for the SAM on SiO_2 shown in Figure 3.12(a). This is firstly due to the fact that both samples are dominated by the signal from the over layer (SAM) which is the same in both cases. Secondly, the carbon-containing SOG used in this work has, as part of its structure, carbon-carbon and carbon-oxygen bonds which have binding energies of 284.5 eV and 287 eV, respectively[30]. These binding energies are the same as those for the carbon species in the SAM and as such are indistinguishable by XPS. This reasoning was confirmed by scanning a bare SOG substrate which confirmed the above-mentioned binding energies shown in Figure 3.13(a).

As was the case with the SiO_2 substrate, on Mn deposition the interaction between the Mn and the carbon-based chain of the DETA SAM is observed via the formation of Mn-carbide at a binding energy of 282 eV. On the SOG substrate the Mn-carbide is present on deposition, before any thermal annealing takes place just like with the SAM on SiO_2. Furthermore, on the SOG substrate it takes a higher temperature thermal anneal to decompose the carbide and it is only fully removed after the 400°C thermal anneal. The presence of Mn-carbide on deposition is commonly observed when Mn is deposited on carbon containing low-k substrates[35]. The other peak components remain essentially unaffected after annealing other than a slight decrease in intensity which, similar to the SAM on SiO_2, is indicative of partial desorption or thermal decomposition of the SAM molecular layer.

The curve fitted N 1s spectra are presented in Figure 3.17(b). The as-loaded SAM on spin-on-glass shows the same NH_2 and the C-N component peaks as was the case for the DETA SAM deposited on SiO_2 and again Mn-nitride is evident following Mn deposition at a binding energy of 396.5 eV. Corresponding to the SiO_2 substrate, the presence of this component peak is indicative of an interaction taking place between the DETA SAM terminal group and the subsequent deposited Mn. The signal-to-noise ratio of the N 1s peak profile decreases, which like the previous sample, is indicative of partial desorption or thermal decomposition of the SAM molecules.

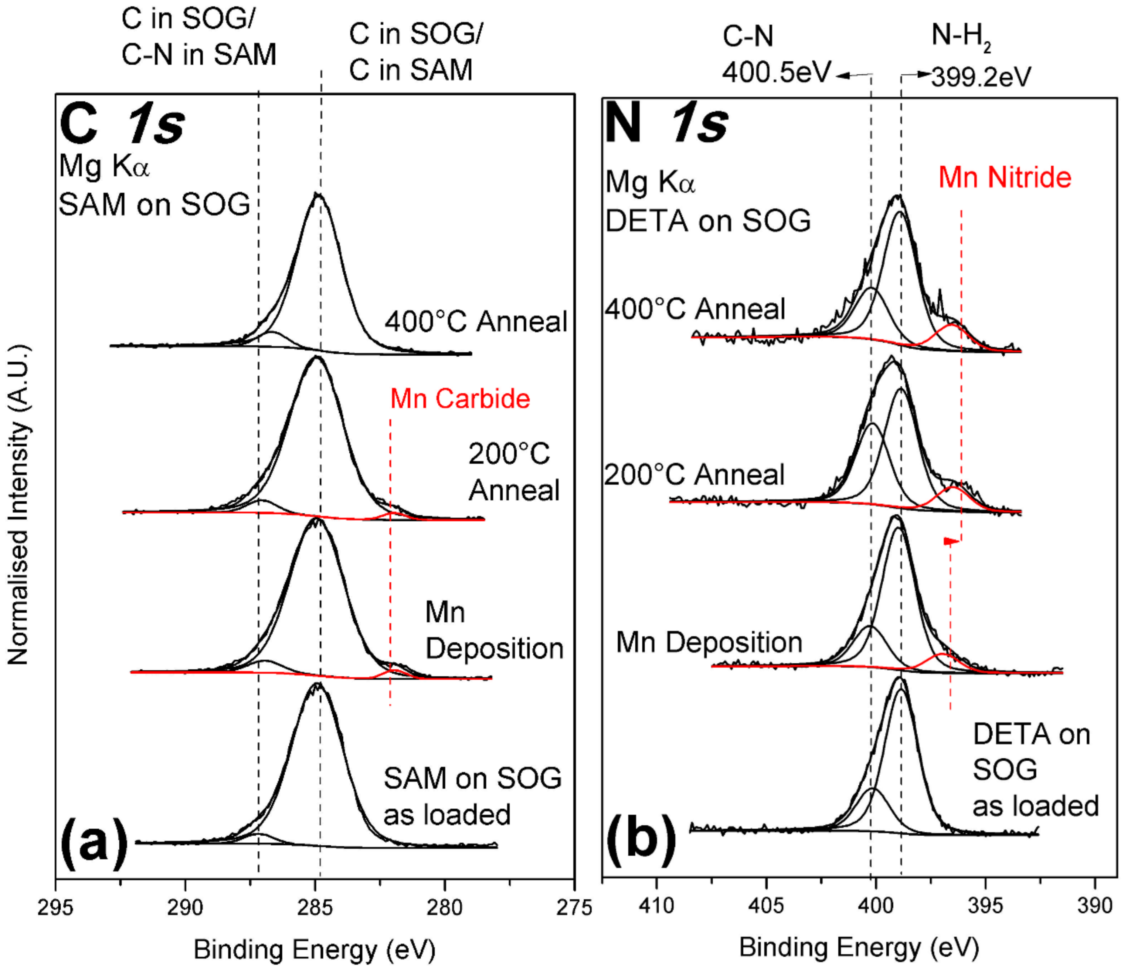

Figure 3.17(a) Curve fitted C 1s spectrum showing Mn-carbide upon Mn deposition and its decomposition upon 400◦C anneal. (b) Curve fitted N 1s spectrum showing the formation of Mn-nitride upon Mn deposition.

3.4 Chapter Conclusion

To summarise, the interaction of metallic manganese with (3-trimethoxysilylpropyl) diethylenetriamine self-assembled monolayers on both SiO_2 and spin-on-glass substrates has been investigated. It has been shown that Mn metal interacts with the carbon and nitrogen in the DETA SAM by forming Mn-carbide and Mn-nitride respectively. The Mn-carbide is converted to Mn-oxide upon thermal anneal reflecting the instability of these bonds in the presence of oxygen. Furthermore, the Mn is also seen to diffuse through the SAM to form Mn-silicate at the SAM/substrate interface.

On the SiO_2 substrate, this process occurs after thermal annealing. However, on the low-k SOG substrate, diffusion of the Mn through the SAM takes place upon deposition, at room temperature. Residual oxygen in the UHV system, along with the thermal annealing, facilitates and drives the formation and growth of Mn-silicate at the SAM/dielectric interface on both substrates.

These chemical interactions are beneficial in that $MnSiO_3$ has been shown to be an effective copper diffusion barrier layer, and MnN which is present at the SAM functional group has been shown to promote adhesion of metals to the ILD. The results of these studies warrant further investigation into the effectiveness of this approach to barrier layer formation on low-k dielectric materials and in particular how subsequently deposited metal layers interact and adhere to this proposed barrier layer.

3.5 References

(1) Byrne, C.; Brady, A.; Walsh, L.; McCoy, A. P.; Bogan, J.; McGlynn, E.; Rajani, K. V.; Hughes, G. Chemical and Electrical Characterisation of the Segregation of Al from a CuAl Alloy (90%:10% Wt) with Thermal Anneal. *Thin Solid Films* **2016**, *599*, 59–63.

(2) Byrne, C.; Brennan, B.; Lundy, R.; Brady, A.; Hurley, P.; Hughes, G. Physical, Chemical and Electrical Characterisation of the Diffusion of Copper in Silicon Dioxide and Prevention via a CuAl Alloy Barrier Layer System. *Mater. Sci. Semicond. Process.* **2017**, *63* (February), 227–236.

(3) Franz, M.; Ecke, R.; Kaufmann, C.; Kriz, J.; Schulz, S. E. Investigation of Barrier Formation and Stability of Self-Forming Barriers with CuMn, CuTi and CuZr Alloys. *2015 IEEE Int. Interconnect Technol. Conf. 2015 IEEE Mater. Adv. Met. Conf. IITC/MAM 2015* **2015**, *156*, 95–97.

(4) Ablett, J. M.; Wilson, C. J.; Phuong, N. M.; Koike, J.; Tokei, Z.; Sterbinsky, G. E.; Woicik, J. C. Characterization of Chemically Vapor Deposited Manganese Barrier Layers Using X-Ray Absorption Fine Structure. *Jpn. J. Appl. Phys.* **2012**, *51* (5 PART 2), 05EB01.

(5) McCoy, A. P.; Bogan, J.; Walsh, L.; Byrne, C.; O'Connor, R.; Woicik, J. C.; Hughes, G. The Impact of Porosity on the Formation of Manganese Based Copper Diffusion Barrier Layers on Low- κ Dielectric Materials. *J. Phys. D. Appl. Phys.* **2015**, *48* (32), 325102.

(6) Nguyen, M. P.; Sutou, Y.; Koike, J. Diffusion Barrier Property of $MnSi_xO_y$ Layer Formed by Chemical Vapor Deposition for Cu Advanced Interconnect Application. *Thin Solid Films* **2015**, *580*, 56–60.

(7) Au, Y.; Lin, Y.; Gordon, R. G. Filling Narrow Trenches by Iodine-Catalyzed CVD of Copper and Manganese on Manganese Nitride Barrier/Adhesion Layers. *J. Electrochem. Soc.* **2011**, *158* (5), D248.

(8) Casey, P.; Bogan, J.; Lozano, J. G.; Nellist, P. D.; Hughes, G. Chemical and Structural Investigation of the Role of Both Mn and Mn Oxide in the Formation of Manganese Silicate Barrier Layers on SiO2. *J. Appl. Phys.* **2011**, *110* (5), 154507.

(9) Byrne, C.; Brennan, B.; McCoy, A. P.; Bogan, J.; Brady, A.; Hughes, G. In Situ XPS Chemical Analysis of $MnSiO_3$ Copper Diffusion Barrier Layer Formation and Simultaneous Fabrication of Metal Oxide Semiconductor Electrical Test MOS Structures. *ACS Appl. Mater. Interfaces* **2016**, *8* (4), 2470–2477.

(10) Ablett, J. M.; Woicik, J. C.; Tökei, Z.; List, S.; Dimasi, E. Phase Identification of Self-Forming Cu-Mn Based Diffusion Barriers on p-SiOC:H and SiO_2 Dielectrics Using x-Ray Absorption Fine Structure. *Appl. Phys. Lett.* **2009**, *94* (4), 28–31.

(11) Koike, J.; Wada, M. Self-Forming Diffusion Barrier Layer in Cu-Mn Alloy Metallization. *Appl. Phys. Lett.* **2005**, *87* (4), 1–4.

(12) Zhang, X.; Chae, M.; Zhao, L. Hybrid Manganese and Manganese Nitride Barriers for Back-End-of-Line Metallization and Methods for Fabricating the Same. Patent Number: 20150108647, 2015.

(13) Maex, K.; Baklanov, M. R.; Shamiryan, D.; Iacopi, F.; Brongersma, S. H.; Yanovitskaya, Z. S. Low Dielectric Constant Materials for Microelectronics. *J. Appl. Phys.* **2003**, *93* (11), 8793–8841.

(14) Volksen, W.; Miller, R.; Dubois, G. Low Dielectric Constant Materials. *Chem. Rev.* **2010**, *110*, 56–110.

(15) Michalak, D. J.; Blackwell, J. M.; Torres, J. M.; Sengupta, A.; Kreno, L. E.; Clarke, J. S.; Pantuso, D. Porosity Scaling Strategies for Low-k Films. *J. Mater. Res.* **2015**, *30* (22), 3363–3385.

(16) Palov, A.; Rakhimova, T. V.; Krishtab, M. B.; Baklanov, M. R. Dependence of

Dielectric Constant of SiOCH Low-k Films on Porosity and Pore Size. *J. Vac. Sci. Technol. B, Nanotechnol. Microelectron. Mater. Process. Meas. Phenom.* **2015**, *33* (2), 020603.

(17) Bogan, J.; Lundy, R.; P. McCoy, A.; O'Connor, R.; Byrne, C.; Walsh, L.; Casey, P.; Hughes, G. In-Situ Surface and Interface Study of Atomic Oxygen Modified Carbon Containing Porous Low-κ Dielectric Films for Barrier Layer Applications. *J. Appl. Phys.* **2016**, *120* (10), 105305.

(18) Guo, L.; Zaera, F. Spatial Resolution in Thin Film Deposition on Silicon Surfaces by Combining Silylation and UV/Ozonolysis. *Nanotechnology* **2014**, *25* (50), 504006.

(19) Sun, Y.; Krishtab, M.; Mankelevich, Y.; Zhang, L.; De Feyter, S.; Baklanov, M.; Armini, S. Surface-Confined Activation of Ultra Low-k Dielectrics in CO_2 Plasma. *Appl. Phys. Lett.* **2016**, *108* (26), 1–5.

(20) Uedono, A.; Armini, S.; Zhang, Y.; Kakizaki, T.; Krause-Rehberg, R.; Anwand, W.; Wagner, A. Surface Sealing Using Self-Assembled Monolayers and Its Effect on Metal Diffusion in Porous Low-k Dielectrics Studied Using Monoenergetic Positron Beams. *Appl. Surf. Sci.* **2016**, *368*, 272–276.

(21) Armini, S.; Prado, J. L.; Swerts, J.; Sun, Y.; Krishtab, M.; Meersschaut, J.; Blauw, M.; Baklanov, M.; Verdonck, P. Pore Sealing of Porous Ultralow-k Dielectrics by Self-Assembled Monolayers Combined with Atomic Layer Deposition. *ECS Solid State Lett.* **2012**, *1* (2), P42–P44.

(22) Sun, Y.; Krishtab, M.; Struyf, H.; Verdonck, P.; De Feyter, S.; Baklanov, M. R.; Armini, S. Impact of Plasma Pretreatment and Pore Size on the Sealing of Ultra-Low-k Dielectrics by Self-Assembled Monolayers. *Langmuir* **2014**, *30* (13), 3832–3844.

(23) Caro, A. M.; Armini, S.; Richard, O.; Maes, G.; Borghs, G.; Whelan, C. M.; Travaly, Y. Bottom-Up Engineering of Subnanometer Copper Diffusion

Barriers Using NH2-Derived Self-Assembled Monolayers. *Adv. Funct. Mater.* **2010**, *20* (7), 1125–1131.

(24) Orozco, P. AAnalyzer http://rdataa.com/aanalyzer/aanaHome.htm.

(25) Cole, D. A.; Shallenberger, J. R.; Novak, S. W.; Moore, R. L.; Edgell, M. J.; Smith, S. P.; Hitzman, C. J.; Kirchhoff, J. F.; Principe, E.; Nieveen, W.; Huang, F. K.; Biswas, S.; Bleiler, R. J.; Jones, K. SiO_2 Thickness Determination by X-Ray Photoelectron Spectroscopy, Auger Electron Spectroscopy, Secondary Ion Mass Spectrometry, Rutherford Backscattering, Transmission Electron Microscopy, and Ellipsometry. *J. Vac. Sci. Technol.* **2000**, *18* (1), 440.

(26) Baur, W. H. Silicon-Oxygen Bond Lengths, Bridging Angles Si-O-Si and Synthetic Low Tridymite. *Acta Cryst* **1977**, *33*, 2615–2619.

(27) Powell, C.; Jablonski, A. NIST Estimated Attenuation Length (EAL) Database. Version 1. Warsaw 2001.

(28) Qin, X.; Sun, H.; Zaera, F. Thermal Chemistry of $Mn_2(CO)_{10}$ during Deposition of Thin Manganese Films on Silicon Oxide and on Copper Surfaces. *J. Vac. Sci. Technol. A Vacuum, Surfaces, Film.* **2012**, *30* (1), 01A112.

(29) Oku, M.; Hirokawa, K.; Ikeda, S. X-Ray Photoelectron Spectroscopy of Manganese-Oxygen Systems. *J. Electron Spectros. Relat. Phenomena* **1975**, *7* (5), 465–473.

(30) Sun, H.; Qin, X.; Zaera, F. Chemical Nature of the Thin Films That Form on SiO_2/Si(100) Surfaces upon Manganese Deposition. *J. Phys. Chem. Lett.* **2011**, *2* (20), 2525–2530.

(31) Casey, P.; Bogan, J.; Hughes, G. Photoemission Study of Carbon Depletion from Ultralow-Carbon Doped Oxide Surfaces during the Growth of Mn Silicate Barrier Layers. *J. Appl. Phys.* **2011**, *110* (12), 124512.

(32) Biesinger, M. C.; Payne, B. P.; Grosvenor, A. P.; Lau, L. W. M.; Gerson, A. R.;

Smart, R. S. C. Resolving Surface Chemical States in XPS Analysis of First Row Transition Metals, Oxides and Hydroxides: Cr, Mn, Fe, Co and Ni. *Appl. Surf. Sci.* **2011**, *257* (7), 2717–2730.

(33) Biesinger, M. C.; Lau, L. W. M.; Gerson, A. R.; Smart, R. S. C. Resolving Surface Chemical States in XPS Analysis of First Row Transition Metals, Oxides and Hydroxides: Sc, Ti, V, Cu and Zn. *Appl. Surf. Sci.* **2010**, *257* (3), 887–898.

(34) Bogan, J.; McCoy, A. P.; O'Connor, R.; Casey, P.; Byrne, C.; Hughes, G. Photoemission Study of the Identification of Mn Silicate Barrier Formation on Carbon Containing Low-k Dielectrics. *Microelectron. Eng.* **2014**, *130*, 46–51.

(35) National Institute of Standards and Technology Gaithersburg. NIST X-ray Photoelectron Spectroscopy Database, Version 4.1 http://srdata.nist.gov/xps/.

(36) Bogan, J.; Casey, P.; McCoy, A.; Hughes, G. Photoemission Study of the Growth of Mn Silicate Barrier Layers on Ultra Low-k Carbon Doped Oxide Surfaces. *2012 IEEE Int. Interconnect Technol. Conf. IITC 2012* **2012**, 12–13.

(37) De Bonis, A.; Galasso, A.; Santagata, A.; Teghil, R. Ultrashort Pulsed Laser Ablation of Magnesium Diboride: Plasma Characterization and Thin Films Deposition. *J. Nanomater.* **2015**, *2015* (April 2016), 596328.

(38) Scardamaglia, M.; Susi, T.; Struzzi, C.; Snyders, R.; Di Santo, G.; Petaccia, L.; Bittencourt, C. Spectroscopic Observation of Oxygen Dissociation on Nitrogen-Doped Graphene. *Sci. Rep.* **2017**, *7* (1), 1–11.

(39) Bertóti, I. Characterization of Nitride Coatings by XPS. *Surf. Coatings Technol.* **2002**, *151–152*, 194–203.

(40) Miura, A.; Takei, T.; Kumada, N. Low-Temperature Nitridation of Manganese and Iron Oxides Using NaNH2 Molten Salt. *Inorg. Chem.* **2013**, *52* (20), 11787–11791.

Chapter 4

4 Nucleation and Adhesion of Ultra-Thin Copper Films on Self-Assembled Monolayers

This chapter describes the nucleation, growth and adhesion of thin Cu films deposited on three distinct self-assembled monolayers in ultra-high vacuum. A range of SAMs are considered such as amino terminated, carbon terminated and both long and short chain arrangements. XPS is used to characterise the interaction of ultra-thin Cu films deposited in-vacuo on the different SAM layers. Adhesion tests were performed on thick patterned Cu films deposited on the same SAM layers and the results were correlated with the interface chemistry studies derived from the XPS analysis.

4.1 Introduction

The experimental findings in Chapter 3 highlight the potential of using SAM terminating layers in conjunction with ultra-thin Mn films as a pore sealant and barrier formation layer for low-*k* dielectrics. A further potential benefit of using self-assembled monolayers is their potential to improve the adhesion of Cu to the underlying interlayer dielectric (ILD). As discussed in Chapter 1, one of the main problems facing the microelectronics industry is the adhesion of copper to the interlayer dielectric. While the conventionally used Ta/TaN barriers display good copper adhesion properties[1], the increasing difficulty of scaling the thickness of this barrier layer material system means that alternative material solutions for future technology nodes are needed[2–4]. Previously in the DCU surface science research group Byrne *et al.*[5] performed tape tests to show the superior adhesion properties of Cu deposited on a $MnSiO_3$ barrier on SiO_2 compared to Cu on SiO_2. Koike *et al.*[6] performed tape tests on a CuMn alloy deposited on SiO_2, showing improved adhesion after annealing. Recently, Hosseini *et al.*[7] have performed tape tests of $CoTi_x$ barriers on SiO_2 to investigate its adhesion to the dielectric. Although these tape tests only provide a qualitative analysis, they all demonstrate improved adhesion to the underlying SiO_2 following the insertion of a diffusion barrier layer.

Several papers have suggested that self-assembled monolayers could indeed replace metal barrier layers as they themselves meet the criteria for barrier layers described in Chapter 1. Ramanath *et al.*[8] showed that a thiol terminated SAM had the ability to improve adhesion of thick copper layers to the underlying SiO_2. This is not surprising as thiol SAMs are known to chemically bond with a Cu surface. They also carried out bias thermal stress (BTS) tests which exhibited the ability of the SAMs to delay copper diffusion across the SiO_2 interface. Mikami *et al.*[9] studied a long chain phosphorus terminated SAM and its ability to halt copper diffusion. In this study they electrically probed MOS (metal-oxide-semiconductors) capacitors of layered stacks with and without the SAM. Analysis of the leakage current following BTS show an estimated lifetime of ~10 years which is comparable to the conventional Ta/TaN barrier. A number of studies have looked at the efficacy of using amino terminated SAMs as a copper diffusion barrier layer on silicon oxide-based dielectrics. These studies have used electrical characterisation[10,11] on MOS capacitor structures, such as I-V (current - voltage) and C-V (capacitance – voltage), to evaluate the SAMs and even simulations have been used[12]. Caro *et al.*[13] demonstrated improved adhesion of Cu to the underlying SiO_2 substrate, by insertion of a short chain amino-terminated SAM. Four-point bending tests showed that following a thermal anneal, the interfacial roughness, which is a measure of the fracture energy, increased and was comparable to the traditional Ta/TaN barrier. TEM (transmission electron microscopy) and EELS (electron energy loss spectrometry) analysis verifies that there is no copper diffusion into the silicon layer.

This chapter presents an investigation into nucleation and adhesion properties of copper on several different self-assembled monolayers. Amino-terminated SAMs are investigated as nitrogen is known as an adhesion promoter for copper as it is already used in barrier applications. The effect of the SAM hydrocarbon chain length upon the deposited copper film is studied. The influence of the amino-terminal group compared to a hydrocarbon terminated chain is also examined. The results of these studies are presented in two sections. The first section presents an XPS characterisation of ultra-thin copper films deposited in-situ on three different self-assembled monolayers and compared to a reference SiO_2 surface. The second section presents results associated with the characterisation of thicker Cu films deposited on the same SAMs using adhesion testing, AFM surface roughness measurements and copper film resistivity measurements.

4.2 Experimental Details

4.2.1 Substrate Details

The three SAMs used in this study were derived from trimethoxy(propyl)silane (PTMS), (3-Aminopropyl)-trimethoxy-silane (APTMS), and (3-trimethoxysilylpropyl)-diethylenetriamine (DETA) and are schematically shown in Figure 4.1. The three organic films were deposited by research colleagues in the IMEC laboratory from the vapor phase during one-hour exposure at 140°C at a base pressure of 20 mbar on native silicon dioxide (SiO_2) on Si (100) substrates. The oxide substrates were cleaned prior to SAM deposition by 15-minute exposure to UV-ozone treatment in a Jelight UVO Cleaner. The molecular length of the SAMs were 0.4 nm for PTMS, 0.5 nm for APTMS and 1.1 nm for DETA.

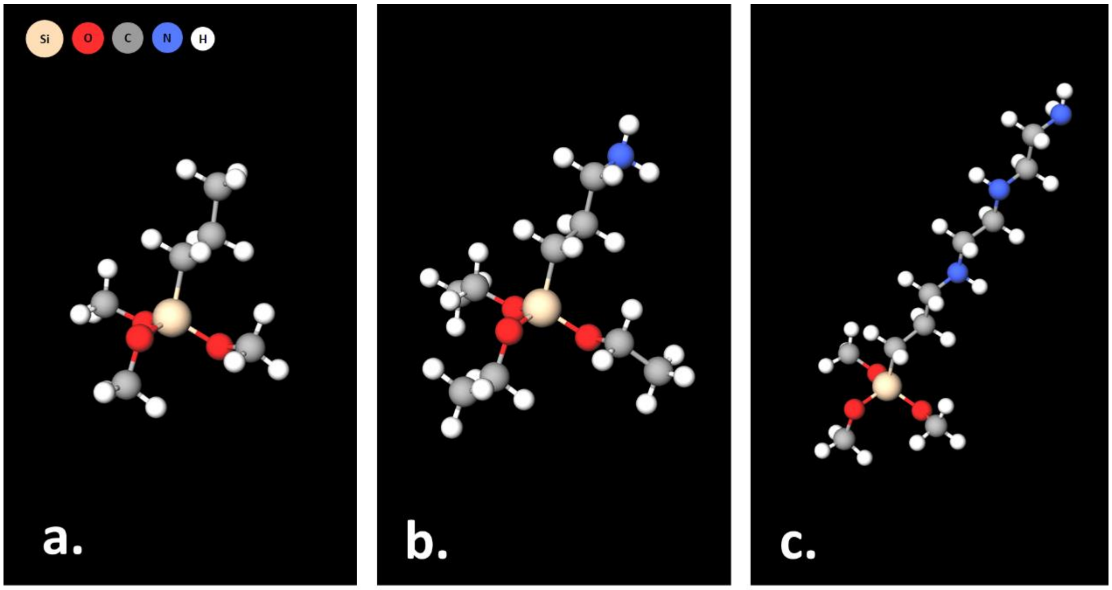

Figure 4.1 Schematic diagram of (a) (3-Propyl) trimethoxy-silane (PTMS) (b) (3-Aminopropyl) trimethoxy-silane (APTMS) and (c) (3-trimethoxysilylpropyl) diethylenetriamine (DETA) self-assembled monolayers.

Four sample sets were fabricated for investigation by different techniques. Each set consisted of a UV-ozone cleaned SiO_2 reference sample, a PTMS sample, an APTMS sample and a DETA sample. An ultra-thin Cu film (thickness ~0.5 nm) was deposited for investigation by XPS. Two sample sets of thick (~ 60 nm) patterned Cu structures were fabricated by employing a shadow mask for adhesion testing, with one set receiving a 400°C thermal vacuum anneal. The final set received a thick blanket copper deposition with a thickness of ~100 nm. This set was for AFM imaging and 4-point probe, sheet resistance measurements. Figure 4.2 summarises the different sample sets and details the deposition method used along with the characterisation technique used for each set.

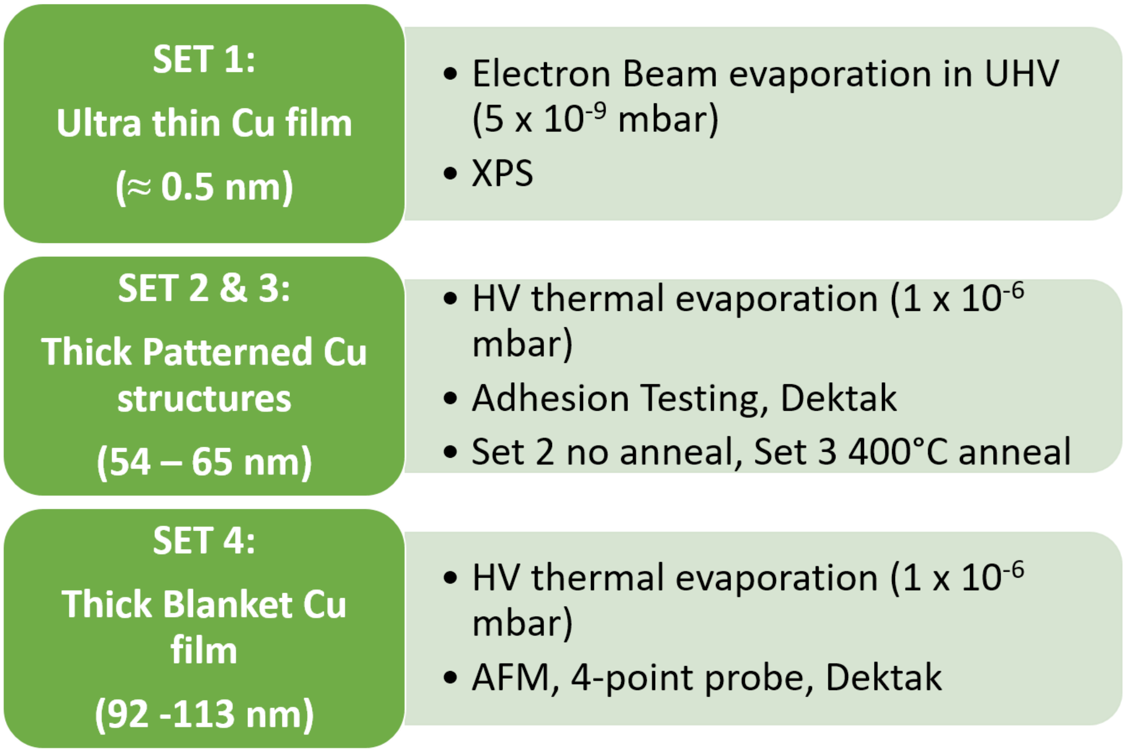

SET 1: **Ultra thin Cu film** **(≈ 0.5 nm)**	• Electron Beam evaporation in UHV (5×10^{-9} mbar) • XPS
SET 2 & 3: **Thick Patterned Cu structures** **(54 – 65 nm)**	• HV thermal evaporation (1×10^{-6} mbar) • Adhesion Testing, Dektak • Set 2 no anneal, Set 3 400°C anneal
SET 4: **Thick Blanket Cu film** **(92 -113 nm)**	• HV thermal evaporation (1×10^{-6} mbar) • AFM, 4-point probe, Dektak

Figure 4.2 Summary of the sample sets fabricated during the study outlining both the deposition and characterisation techniques which were used.

4.2.2 Photoemission Surface Characterisation

When considering the UV-ozone cleaned SiO_2 substrate and the three SAM films, two samples were mounted on a single sample holder. This allowed for simultaneous metal depositions and identical thermal anneals, all within the ultra-high-vacuum (UHV) system and without a break in vacuum. This setup allowed for direct comparison between the SiO_2 control surface and the surfaces with SAMs present. Samples were not degassed prior to measurement following insertion into the UHV chamber of base pressure 1×10^{-9} mbar so as to preserve the integrity of the as-deposited SAM[13]. Thermal annealing at 400 °C was carried out in UHV at a pressure of 1×10^{-9} mbar, with samples maintained at the target temperature for 60 minutes.

Copper chips (~99.9 % purity) were used as a source material for the room temperature deposition of Cu thin films via an Oxford Applied Research EGC04 mini electron-beam evaporator, at a deposition pressure of 5×10^{-9} mbar. XPS analysis is as described in Chapter 3. It should be noted that the use of a non-monochromatic Mg Kα source results in the presence of minor X-ray satellites in all measured photoemission spectra. These features are included in appropriate peak-fitted spectra in order to obtain an accurate fit for the Si 2p/Cu 3p. They are also included in the complete analysis of the Cu 2p spectra where the presence of the satellite features obscures the weak features indicative of Cu_2O at a binding energy of 943 eV. The Si 2p spectra were fitted with Voigt doublet profiles composed of Gaussian and Lorentzian line shapes with a doublet separation 0.6 eV, a peak area ratio of 0.5 and a Lorentzian value of 0.39 eV. The O 1s, C 1s and N 1s spectra were fitted with Voigt profiles with Lorentzian values of 0.55 eV, 0.3 eV and 0.5 eV respectively. Cu 2p and 3p spectra were fitted with double Lorentzian profiles with an asymmetry value of 0.9 eV[14]. Cu 3p spectra were fitted with a doublet separation 2.0 eV and a peak area ratio of 0.5. Shirley-Sherwood type background was used for all core level spectra. Peak fitting parameters are summarised in Table 4.1.

Table 4.1 Peak fitting parameters for all samples are given in the table.

UV-ozone Reference Peak Fitting Parameters					
Si 2p	**Gaussian (eV)**	**Lorentzian (eV)**	**Cu 3p**	**Gaussian (eV)**	**Lorentzian (eV)**
Si Bulk	0.6	0.39	**Cu Metal**	2.4	0.39
SiO_2	1.2	0.39	**Cu(I) Oxide**	2	0.39
O 1s			**C 1s**		
SiO_2	1.45	0.55	**C-C / C-H**	1.5	0.5
			C-O	1.5	0.5
Cu 2p					

Cu metal/ Cu(I) oxide	0.77	0.87			
PTMS Peak Fitting Parameters					
Si 2p	**Gaussian (eV)**	**Lorentzian (eV)**	**Cu 3p**	**Gaussian (eV)**	**Lorentzian (eV)**
Si Bulk	0.6	0.39	**Cu Metal**	2.5	0.39
SiO_2	1.4	0.39			
O 1s			**C 1s**		
SiO_2	1.4	0.55	**C-C / C-H**	1.8	0.3
Cu oxide	1	0.55	**C-O**	2	0.3
Cu 2p					
Cu metal/ Cu(I) oxide	1	0.87			
APTMS Peak Fitting Parameters					
Si 2p	**Gaussian (eV)**	**Lorentzian (eV)**	**Cu 3p**	**Gaussian (eV)**	**Lorentzian (eV)**
Si Bulk	0.6	0.39	**Cu Metal**	2.5	0.39
SiO_2	1.5	0.39			
O 1s			**C 1s**		
SiO_2	1.3	0.55	**C-C / C-H**	1.8	0.3
Cu oxide	1	0.55	**C-O**	2	0.3
C-O	1	0.55	**C-O-N**	2	0.3
Cu 2p			**N 1s**		
Cu metal/ Cu(I) oxide	1	0.87	**NH**	2	0.5
			C-O-N	1.6	0.5
DETA Peak Fitting Parameters					
Si 2p	**Gaussian (eV)**	**Lorentzian (eV)**	**Cu 3p**	**Gaussian (eV)**	**Lorentzian (eV)**
Si Bulk	0.6	0.39	**Cu Metal**	2.3	0.39
SiO_2	1.3	0.39	**Cu(I) oxide**	2	0.39

O 1s			**C 1s**		
SiO_2	1.3	0.55	**C-C / C-H**	2.1	0.3
Cu oxide	1.3	0.55	**C-O**	2	0.3
C-O	1	0.55			
Cu 2p			**N 1s**		
Cu metal/ Cu(I) oxide	0.76	0.87	**NH**	2	0.5

4.2.3 Adhesion Testing, AFM and 4-point probe measurements

Thicker Cu films were deposited for the purpose of adhesion testing, AFM and 4-point probe measurements. Cu (99.99 % purity) was thermally evaporated simultaneously onto both the control SiO_2 and SAM covered SiO_2 substrates from a tungsten filament in a Leybold Univex high vacuum evaporator system with a typical base pressure of 2 x 10^{-6} mbar. Cu blanket layers were deposited for AFM and 4-point probe thin film resistivity measurements. For adhesion tests, Cu was evaporated through a shadow mask to create the patterned structures as shown in Figure 4.3. The shadow masks, which were fabricated in the Tyndall National Institute, are made from a single crystal Si wafer that has been laser cut to produce three square areas of dimensions 1 x 1 mm, 750 x 750 µm and 500 x 500 µm, and three circles with diameters of dimensions 1 mm, 750 µm and 500 µm. The three different SAMs and a native oxide control sample were placed upon a removable anneal stage with a shadow mask in place and then loaded into the chamber. One set of samples was then annealed to 400°C in-situ following Cu deposition. The thickness of the Cu films was established by performing step height measurements from both the circles and squares with a Bruker Dektak XT stylus profilometer. The average height was calculated from at least 10 measurements which were taken from different structures across the sample. Some variation in thickness is observed from sample to sample, even though the sample sets were fabricated simultaneously.

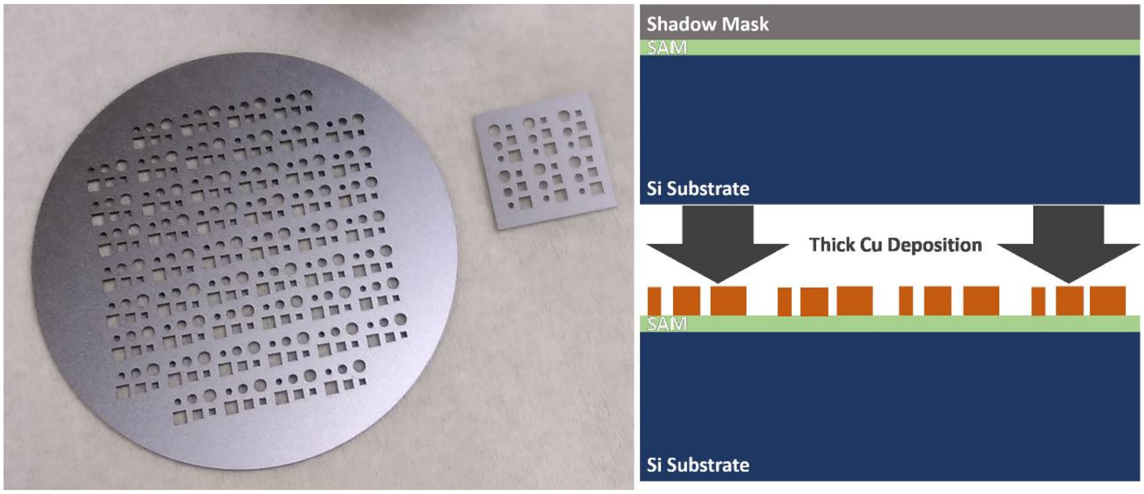

Figure 4.3 Different size shadow masks are shown on the left. On the right is a schematic of a thick Cu deposition through the shadow mask.

Microscope images and image analysis were carried out on a Keyence VHX 2000E 3D Digital Microscope. The microscope images of the pattern structures were recorded at 50x magnification. Using the microscope software, a threshold/mask was applied to the image. The applied threshold had the ability to distinguish colours, so the Cu patterns were easily differentiated from the underlying substrate. Once the Cu areas had been extracted the software was able to provide a percentage of the surface which was covered in Cu. This was undertaken on three to four areas across the surface so up to eighty structures could be analysed on one sample alone, producing reliable and repeatable statistics for each sample. A strip of tape was then placed over the sample, pressed down and pulled off. The same area was then viewed again, and the analysis process repeated to see if there was any difference in the metal covered area before and after the tape test.

AFM images were acquired by a Veeco Dimension 3100, using tapping mode. The AFM silicon cantilever probes with an Al reflective coating, were supplied by Budget Sensors with dimensions of: L x W x T = 125 x 30 x 4 μm^3, resonant frequency = 300 kHz, force constant = 40 N/m, tip radius of <10nm. Images were obtained from several different areas across the sample and were then examined to ensure uniformity of the copper film across the sample. Uniformity was established by comparing the root mean square roughness (R_{rms}) and the grain size over a single sample, and across the different samples in the set. All AFM images were processed and analysed using Gwyddion software version 2.39 [15]. Four-point probe sheet resistance measurements were performed on the blanket layers by a Jandel RM3-AR. Several measurements were taken at different points on the sample and averaged to find the sheet resistance and also the resistivity of the film.

4.3 Results and Discussion

4.3.1 X-Ray Photoelectron Spectroscopy

Four samples were considered in this work. Firstly, a UV ozone treated native SiO_2 layer which was chosen as a control sample as it was the starting substrate prior to self-assembled monolayer deposition for the remaining samples. Three self-assembled monolayers were considered in order to analyse the effect of amino-based terminal functional groups and chain length on the surface chemistry, nucleation, and adhesion of subsequently deposited copper. PTMS is employed as a reference self-assembled monolayer with short hydrocarbon chain and no functional end group. APTMS is identical in structure to PTMS with the addition of an NH_2 terminal functional group. Finally, the DETA SAM has the same functional group as APTMS but a longer hydro-carbon with two additional NH_2 moieties in the chain. Figure 4.4 shows the overall chemical compositions derived from the XPS measurements of the first sample set which contained all four substrates as received, following a concurrent in-situ ~0.5 nm copper deposition on all substrates, and following a 400°C vacuum anneal with all steps performed without breaking vacuum. In the case of the chemical composition of the SiO_2 reference substrate, a concentration of ~61 % silicon, ~31 % oxygen and 8 % carbon were recorded. A relatively small amount of carbon contamination was detected and is consistent with air exposed films which were not degassed in vacuum prior to measurement. Upon copper deposition, just ~3 % of the XPS signal comes from the copper indicating quite a thin over layer. Following a 400°C anneal, all of the copper is desorbed from this reference surface.

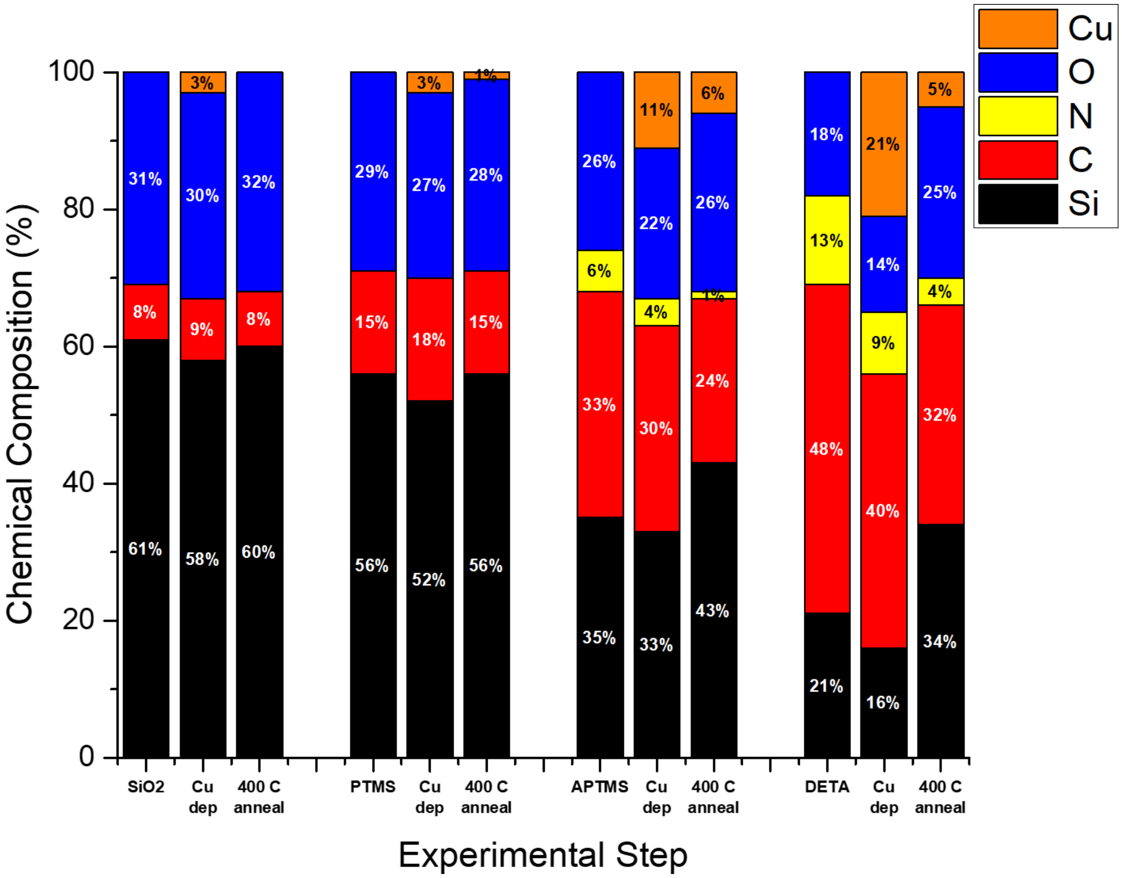

Figure 4.4 Chemical compositions of all samples, across all experimental steps showing the deposition and subsequent desorption of copper following a 400°C anneal.

In the case of the three SAMs considered, the PTMS has the lowest recorded concentration of carbon, despite nominally having the same hydrocarbon structure as the APTMS. This may indicate that the deposited PTMS film is of lower density than the APTMS film resulting in a lower overall coverage. The DETA SAM has the highest carbon signal reflecting the additional carbon atoms present in the longer chain. A nitrogen signal is detected in both the APTMS and DETA SAMs, with a higher signal observed in the DETA which is in keeping with the molecular structure.

Upon copper deposition, the PTMS covered SiO_2 substrate displays a copper signal of ~3 %, similar to that seen for SiO_2 indicating little difference in the adhesion between the two surfaces. APTMS showed ~11 % of the signal emanating from copper following deposition with ~21 % on the DETA indicating that the amino groups contribute significantly to the nucleation of copper on the surface and is consistent with a copper-amine complex formation. Following thermal anneal however, similar amounts of copper remain on both the APTMS and the DETA samples indicating that although the DETA SAM promotes nucleation, the APTMS appears to be as beneficial for thermal stability / adhesion of the copper film.

X-ray photoelectron spectroscopy spectra for a wide kinetic energy window that encompasses both the Cu 3p and Si 2p regions are shown for all samples in Figure 4.5. This enables monitoring of the behaviour of the intensity of both the copper and underlying SiO_2 photoemission signals during deposition and anneal with reference to the Si 2p substrate component peak which remains unchanged. In all cases, the data is normalized to the silicon substrate peak at 99.1 eV BE as no chemical interactions occur within the bulk silicon making it an ideal reference peak.

The silicon 2p peak shows an SiO_2 component in all four samples at 103.2 eV binding energy, in addition to the silicon bulk signal at 99.1 eV binding energy. The SiO_2 component is smallest on the native silicon dioxide reference sample reflecting that the thickness of this oxide layer is approximately 0.4 nm. As previously explained, each SAM bonds to the substrate via a silane-based head-group. All three SAMs have the same head group and when it bonds to the substrate, it adds an additional monolayer of SiO_2 to the surface which is observed in the peak at 103.2 eV binding energy. This is confirmed for all SAMs in Figures 4.5(b), (c) and (d). However, the intensity

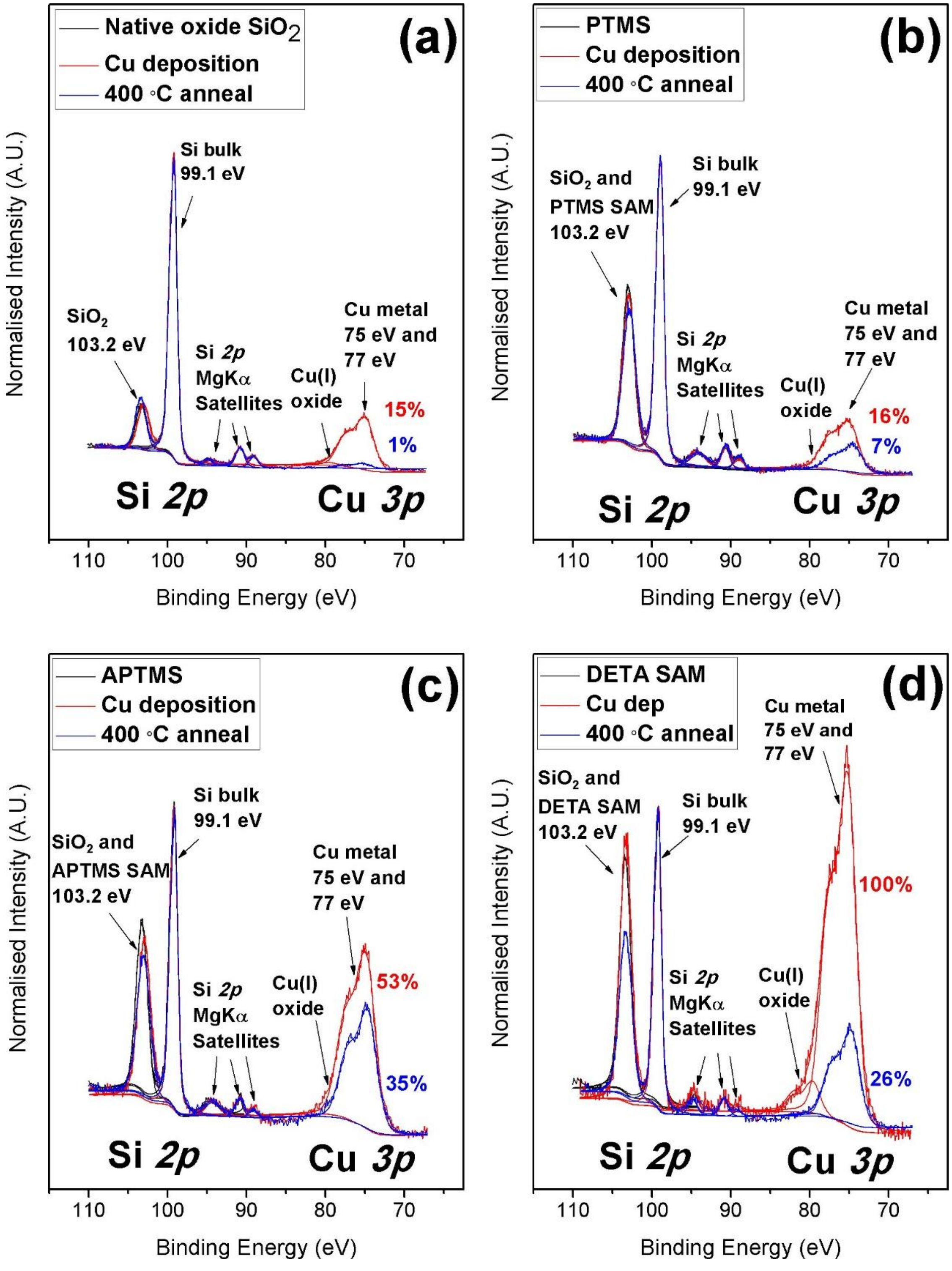

Figure 4.5 Si 2p and Cu 3p spectra for all samples and all experimental steps. DETA shows the best nucleation of copper, but the adhesion following anneal is poor in comparison with APTMS.

of the SiO_2 peak in each case is significantly higher than would be expected for the addition of a single monolayer. The DETA SAM shows the largest SiO_2 peak before annealing, however, following a 400°C anneal the SiO_2 signal from all three SAMs are at approximately the same height with respect to the Si substrate peak. A possible explanation for the initially larger SiO_2 component peak observed on the DETA SAM would be the presence of a multi-layer structure where additional SAMs are not covalently bonded to the substrate but lying atop the initial SAM layer[16,17]. These unbonded molecules are subsequently desorbed upon anneal. This effect is observed for all three SAMs but is most pronounced for the DETA SAM.

The Cu 3p region of the spectra details the role of the SAMs in the nucleation and thermal stability of copper, as discussed above in reference to Figure 4.5. Following identical Cu deposition on all substrates, a primarily metallic copper 3p signal is observed as evidenced by the peak profile which shows components at 75 eV and 77 eV binding energy corresponding to the Cu $3p_{1/2}$ and $3p_{3/2}$ components respectively. Note that there is evidence of trace amounts of oxidised Cu(I) in all samples, identified by the small component peak present at approximately 79 eV. The substrate which is covered with the DETA SAM shows the largest Cu 3p signal (labelled 100 % in the figure) which is taken as the benchmark for comparing the Cu 3p peak intensity on the other substrates and the post-anneal behaviour. This is followed by the APTMS (~53 % of DETA Cu signal), PTMS (~16 % of DETA Cu signal), and SiO_2 (~15 % of DETA Cu signal).

Following the 400°C anneal, the copper signal intensity on the DETA SAM covered substrate is reduced to ~26 % of the original signal. This suggests that despite excellent nucleation, the DETA SAM behaves poorly when it comes to the thermal stability of the deposited copper. The APTMS with its shorter hydrocarbon chain retains considerably more of the initially deposited copper, which corresponds to ~35 % of the initial DETA reference signal. As such, the APTMS is left with more copper following anneal than the DETA.

In the case of the PTMS with no functional group, it retains 44 % of the small amount of copper that was initially deposited on the surface. There is almost complete desorption of the deposited copper from the reference SiO_2 surface (which was only 15 % of that which was measured for the DETA SAM) upon anneal.

It is evident then, that the presence of the amino-functional group significantly improves both nucleation and thermal stability of deposited copper. However, there is a significant difference between the substrate covered with the DETA SAM and that covered with APTMS, which differs in hydrocarbon chain length and nitrogen content. One possible reason why the DETA SAM would afford better nucleation upon deposition, is the increased length of the molecule and the higher concentration of nitrogen over APTMS. The relatively weak Van der Waals bonds which drive the self-assembly of the SAMs could potentially allow for the infiltration of copper atoms between the SAM molecules [18]. However, referring back to the SiO_2 component of the Si 2p spectra, the reduction in signal for the DETA SAM following anneal has been attributed to the desorption of SAM molecules which were not covalently bonded to the surface. It is possible that these molecules afford additional sites for copper atoms to bond upon deposition. Following annealing, as well as losing the unbonded SAMs to desorption, the copper which was bound to these SAM molecules is also desorbed.

It appears as though there is little interaction between the copper and the silicon in the SAM/substrate as the copper is primarily metallic in peak profile. Although there appears to be slight shifts in the peak profile in each case at 103.1 eV, this is due to charging effects upon deposition of the copper, and not representative of a chemical interaction[19]. Insulating materials like SiO_2, are electrostatically charged during the photoemission process which causes a decrease in the kinetic energy of the emitted photoelectrons. The resulting photoemission peak is then observed to be at a higher binding energy. Deposition of a thin metal film can then provide sufficient energy to emitted electrons to shift the peak to lower binding energy.

When spectra are normalised to this peak component (not shown), the peak profiles are identical.

In order to understand the interface chemistry of the SAMs following copper deposition and further investigate any potential interaction between the deposited copper and the SAMs following thermal anneal, the N 1s and C 1s spectra were studied in detail. Figure 4.6 shows the data for all four samples. All figures show the raw intensity which offers a direct comparison between the intensities of the carbon and nitrogen signals across the four samples. There is no nitrogen present in the native oxide or PTMS samples as expected. Furthermore, the DETA has a larger nitrogen signal than the APTMS owing to the presence of more amino groups along the chain of the DETA SAM. The nitrogen in the DETA appears to be in a single chemical state at 399.1 eV binding energy, consistent with the molecular structure. Although nitrogen is also bonded to hydrogen, XPS is not sensitive to hydrogen and peak profiles are not significantly altered by the presence of hydrogen.

In the APTMS there is an additional nitrogen peak at 400.3 eV binding energy which, due to electronegativity considerations can be attributed to the incorporation of oxygen in the nitrogen environment[20].

Upon copper deposition, this peak at 400.3 eV binding energy disappears indicating that the oxygen is weakly bonded to the functional group. The main peak at 399.1 eV BE is suppressed in intensity upon copper deposition as expected. The suppression in the case of the DETA is slightly more pronounced, and is further evidence of better nucleation on this SAM. No additional peak components are observed (aside from the presence of the Cu LMM auger) indicating no obvious chemical interaction between the nitrogen and copper.

Following thermal anneal, the nitrogen signal is significantly reduced in both the DETA and APTMS. However, in this case the reduction is attributed to the partial decomposition of the SAMs resulting in the desorption of the nitrogen (and copper as previously discussed). This effect is more pronounced in the APTMS where only 17 % of the nitrogen remains, compared with 31 % for the DETA. The loss of nitrogen is in contrast to what happens to copper following the anneal, where the DETA retains 26 % of the deposited copper while the APTMS retains 66 %. Normalized N 1s spectra (not shown) for both SAMs and experimental steps show identical FWHM values again indicating no chemical interaction between copper and nitrogen at any stage in the experiment, even following the partial decomposition of the SAMs.

The C 1s spectra which are also shown in Figure 4.6 provide further information about the behaviour and structure of the SAMs during the experiment. The native oxide control sample shows a small peak attributed to adventitious carbon at 284.8 eV[21] binding energy with a shoulder at 286 eV[21] binding energy which is representative of C-O bonds[22].

The chemical compositions of PTMS and APTMS molecules have identical carbon concentrations and this should be reflected in the intensity of the C 1s spectra. However, the PTMS shows significantly less carbon, indicating that the surface coverage could be less than for the APTMS film.

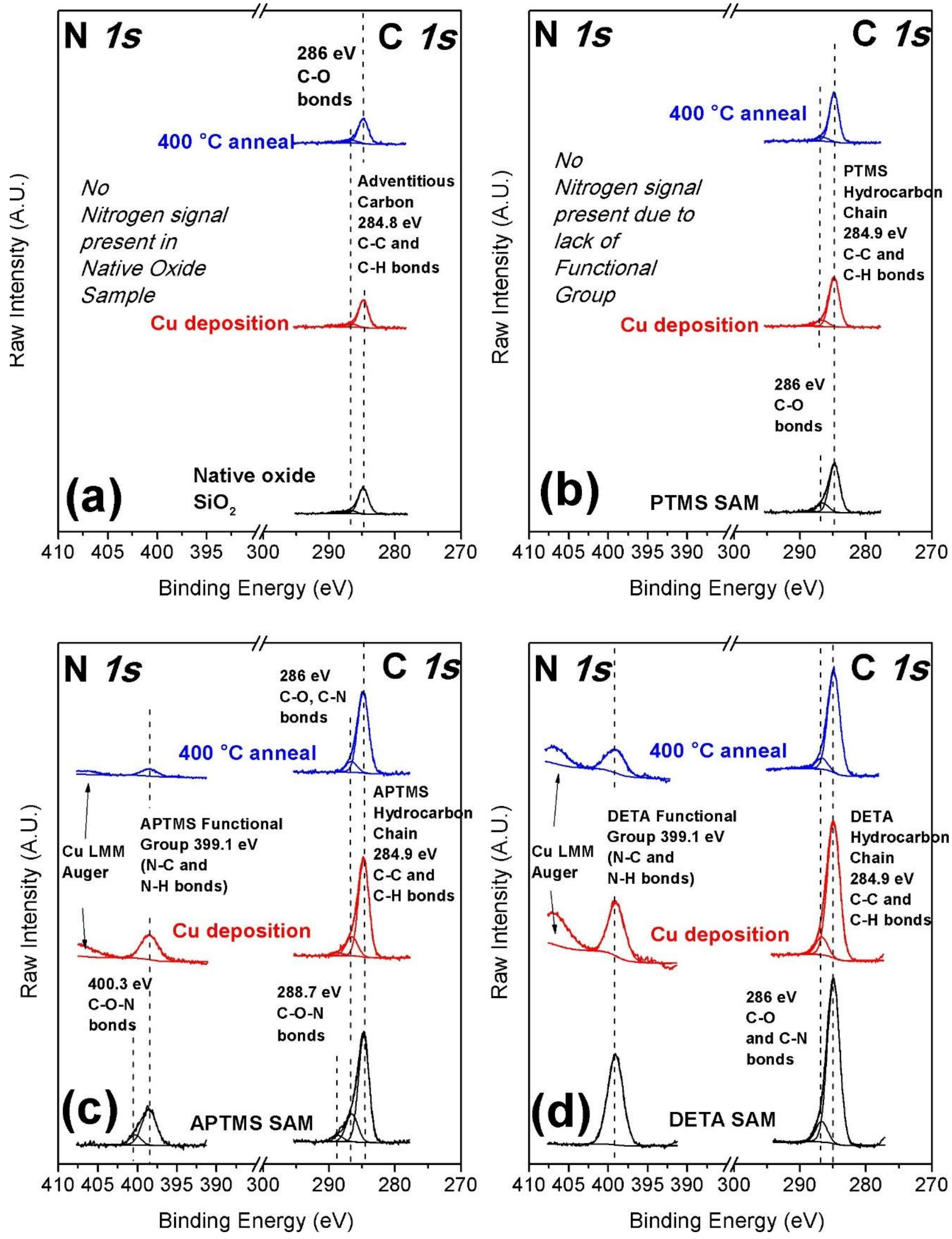

Figure 4.6 N 1s and C 1s spectra for all samples. The data shows that the deposited copper has little chemical interaction with the SAMs.

C-H bonds are reported as having the same binding energy as C-C bonds and are observed at 284.9 eV binding energy[21,22]. As the DETA has a longer hydrocarbon chain and there is earlier evidence of extra molecules resting on the surface, it shows a larger C 1s peak than the APTMS at 284.9 eV binding energy. In both cases, there is an additional peak at 286 eV which is attributed to either C-O or C-N which are unresolvable due to the similarity in electronegativity of nitrogen and oxygen[10]. Furthermore, APTMS shows a very small peak at 288.7 eV binding energy which is due to carbon in a higher oxidation state and is also seen in the N 1s spectrum as mentioned above. One possible source of this oxygen in an ideal environment is from unreacted methyl groups within the silane-based head group used to bond the SAM to the silicon surface. Another possible source is contamination from the deposition chamber or the vacuum system.

As was observed in the N 1s spectra, the simultaneous deposition of copper on all SAMs (and SiO_2) results in the attenuation of the C 1s signal. The attenuation is more pronounced in the DETA and APTMS covered substrates due to the improved nucleation. In the case of APTMS, the C-O-N component is no longer visible after copper deposition as previously discussed in reference to the N 1s spectrum. Following anneal, there is a further reduction in the C 1s peak in all cases, but the reduction is less marked than was the case in the N 1s, indicating that the hydrocarbon-based chain is less affected by the anneal than the nitrogen containing functional group. Normalised C 1s spectra (not shown) display similar peak profiles and peak positions across all samples following deposition and anneal, again showing no evidence of the copper and the SAMs chemically interacting.

Normalised Cu 2p and O 1s spectra are shown in Figure 4.7 which were acquired in order to further understand the chemical bonding environment of the deposited copper. In all cases, the Cu 2p peak profile is consistent with that expected for a metallic film[23]. Oxidation states of copper above the +1 display peak profiles significantly different to the metallic profile due to the emergence of shake-up features[24,25]. As such, CuO and Cu_2O are unlikely to be present in these samples. The +1 oxidation state has a Cu 2p peak profile that is very similar to metallic copper with the primary difference being a small feature at 947 eV [26]. However, this feature coincides with the presence of an Mg Kα satellite at the same binding energy and so confirmation of the +1-oxidation state proves difficult from analysis of the Cu 2p spectrum. In all cases there is no change in the chemical state of the copper following thermal anneal, however the loss of copper is evident from the decreased signal-to-noise ratio.

In the O 1s spectra, the primary source of oxygen is from the underlying SiO_2 as seen at a binding energy of 532.9 eV[27]. In the nitrogen containing SAMs there is evidence of C-O bonds at 531.8 eV binding energy. Upon copper deposition, this peak becomes unresolvable due to the emergence of a peak at 531.6 eV binding energy attributed to Cu-O bonds, as metal oxides appear at lower binding energy than C-O bonds[28]. Note that this peak is quite small, indicating that the copper is indeed primarily metallic with slight amounts of what is most likely to be Cu_2O. Following anneal, the copper-oxide signal disappears, probably by dissociation and the overall copper signal is significantly attenuated by desorption.

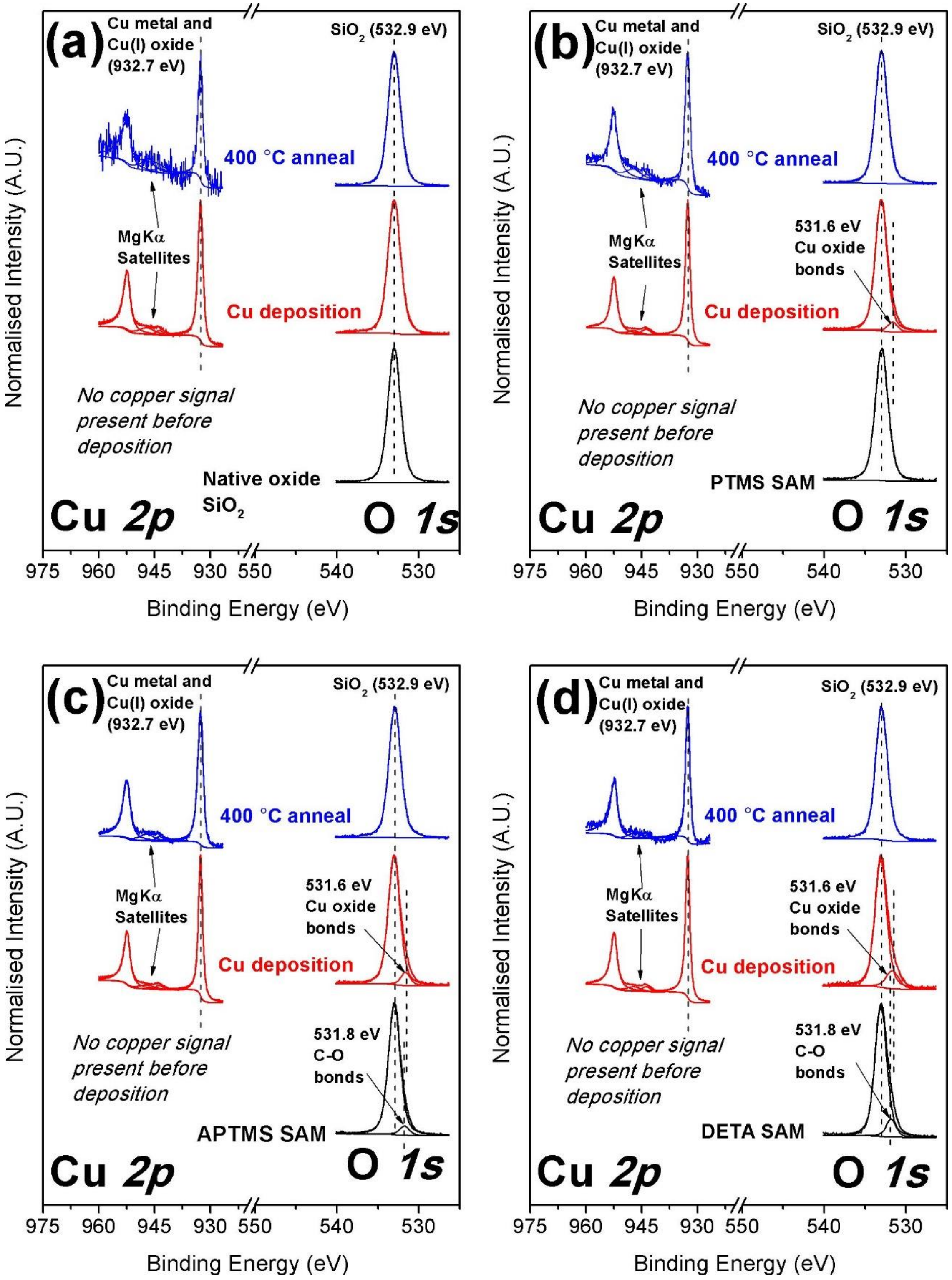

Figure 4.7 Cu 2p and O 1s spectra for all samples. The data shows that the deposited copper is primarily metallic in nature and that the majority of oxygen within all samples is attributed to the underlying SiO2 substrate.

4.3.2 Adhesion Testing, AFM and Resistivity Measurements

In order to investigate whether the differences observed in terms of the thermal stability of the ultra-thin copper films on the different SAMs contribute to improved adhesion for thicker films on the same surfaces, a detailed quantitative study of adhesion was carried out. Copper was deposited through a silicon shadow mask onto each of the substrates considered in this work in the form of both circles and squares of varying size as shown in Figure 4.3. Profilometry was conducted to establish the thickness of the adhesion test structures and the blanket copper films for four-point probe and AFM measurements. The blanket copper films used for 4-point probe measurements were fabricated thicker as the resistivity of the copper increases as the film thickness decreases [29,30]. In thin copper films, changes in resistivity can be attributed to several different events like scattering at grain boundaries, defects in the film and surface roughness to name a few. To counteract these affects thicker films were deposited.

Figure 4.8 displays the thickness, of the three thick deposited copper sample sets. Dektak profilometry measurements show thickness variation within each sample set which reinforce the XPS observations of the ultrathin films. For all sample sets, the amino terminated SAMs have consistently thicker films than the PTMS and the reference SiO_2 sample.

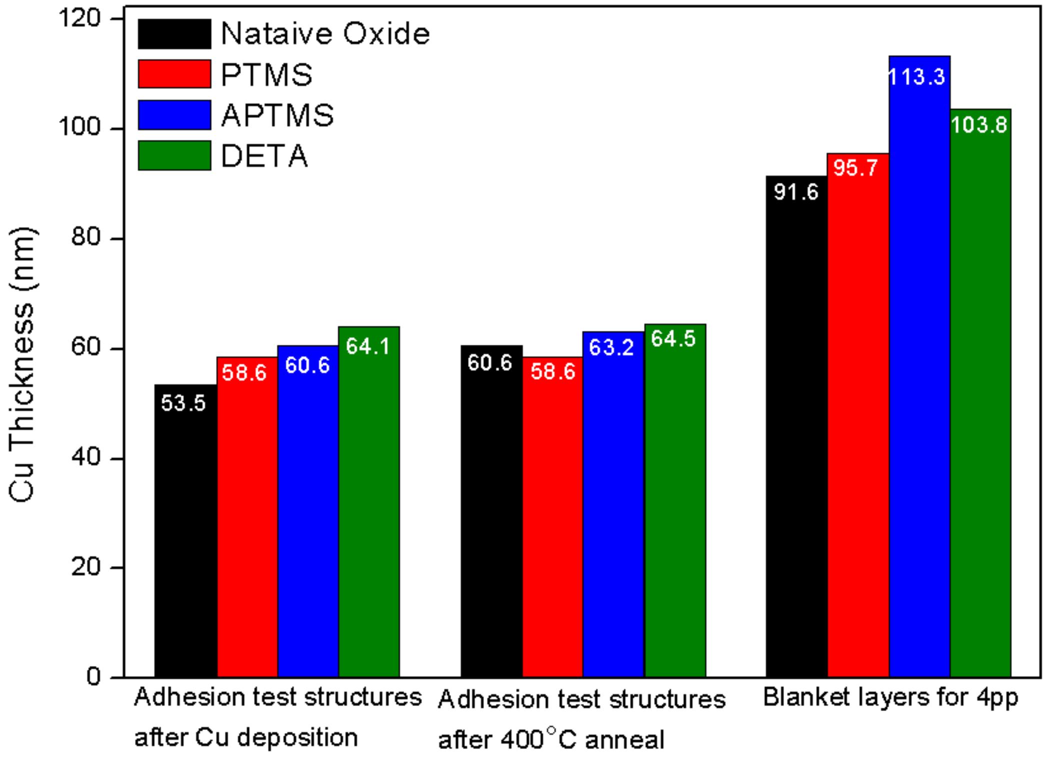

Figure 4.8 Thickness of deposited Cu films on the different sample sets as determined by Dektak measurements.

The strength of adhesion as determined by conventional tape test measurements was quantified by using image analysis to set a threshold on the microscope images. The threshold was used to distinguish between the copper areas and the substrate. Then a percentage of copper coverage was found both before and after the tape test. Figure 4.9 shows the microscope images (left of each panel) and the false colour threshold images (right of each panel) before (a-d) and after (e-h) tape testing for each substrate following a thick copper deposition. In each case, four areas of the wafer were sampled in order to achieve an accurate measurement for the adhesion, independent of local effects. Only one area is shown in Figure 4.8 as an indication of the test structures and performance.

Panel (a) and (e) show that the native oxide retains ~81 % of the deposited copper following the tape test, which is slightly better than PTMS (panels (b) and (f)) which performed the worst, retaining just ~72 % of the deposited copper. This shows that the absence of an amino terminal group negatively impacts adhesion, which correlates with the XPS discussed earlier. In the APTMS and DETA samples where the amino functional group was present, effectively 100 % of the copper is retained in both cases. The percentage area of copper coverage is presented in Table 4.2.

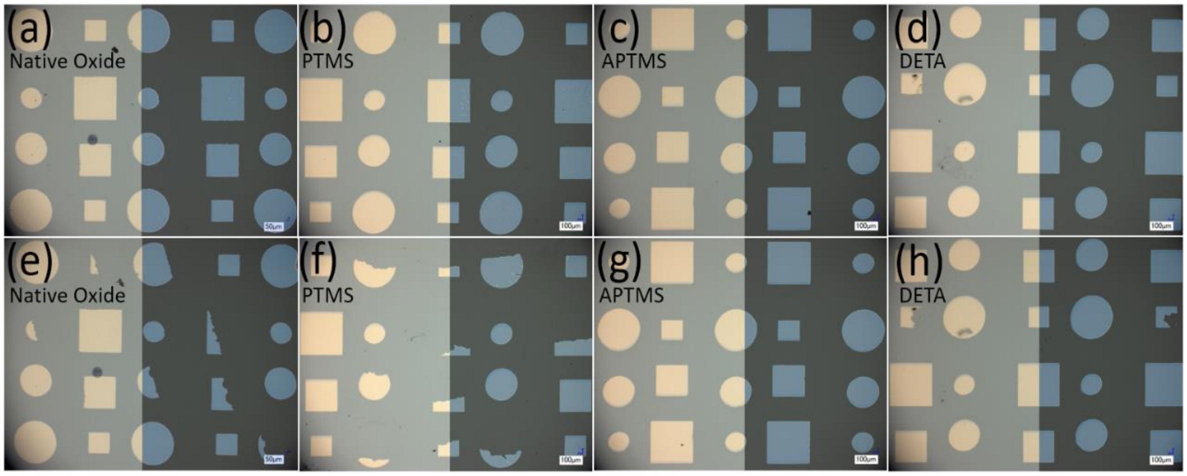

Figure 4.9 Microscope images (left of each panel) and the false colour threshold images (right of each panel) before (a-d) and after (e-h) tape testing for each substrate for the as deposited Cu. Improved Cu adhesion seen in both samples with amino SAM present.

Table 4.2 Percentage of area covered obtained from microscopy analysis for as deposited films

	Native Oxide		**PTMS SAM**		**APTMS SAM**		**DETA SAM**	
	Before Test %	After Test %	Before Test %	After Test %	Before Test %	After Test %	Before Test %	After Test %
Copper Coverage	28.9	23.4	27.9	20.1	27.3	27.3	27.2	27.1
Remaining Copper	80.9		71.9		100		99.7	

A similar test was performed on a second sample set which was annealed in-situ at 400°C for one hour prior to tape testing, to simulate post metallisation processing, this is illustrated in Figure 4.10. The same trend was observed with APTMS retaining 99.9 % and DETA retaining 99.5 %. The PTMS performs the worst overall retaining only ~82 % of the copper, although this is an increase from the as-deposited films. A marked improvement is observed for the native oxide sample where, ~97 % of the Cu film is retained. This could indicate that the copper has diffused into the SiO_2 which is common even at modest temperatures[31,32]. Similarly, to the as-deposited films the DETA and the ATPMS performed the best with both SAMs effectively retaining 100 % of the copper film. The photoemission studies on the ultrathin copper films showed improved nucleation and adhesion for the DETA and the ATPMS SAMs and this improvement is also apparent in the adhesion tape tests for thicker films both as-deposited and following anneal.

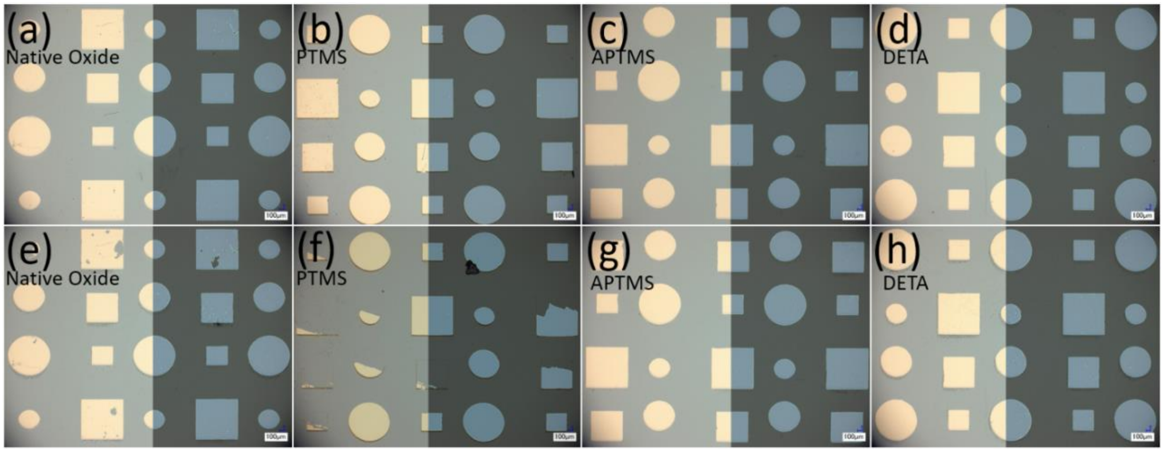

Figure 4.10 Microscope images (left of each panel) and the false colour threshold images (right of each panel) before (a-d) and after (e-h) tape testing for each substrate after a 400°C Anneal.

Table 4.3 Percentage of area covered obtained from microscopy analysis after 400°C anneal

	Native Oxide		**PTMS SAM**		**APTMS SAM**		**DETA SAM**	
	Before Test %	After Test %	Before Test %	After Test %	Before Test %	After Test %	Before Test %	After Test %
Copper Coverage	28.1	27.3	26.0	21.5	26.9	26.9	28.6	28.5
Remaining Copper	97.4		82.7		99.9		99.5	

AFM measurements were performed on all substrates following thick Cu deposition. From Figure 4.11, it can be seen that all samples appear very similar in their surface topography. The root mean square roughness (R_{rms}) and grain size are all comparable with a slight variation from sample to sample. Upon deposition, the Cu forms a granular morphology with grains of approximately 35 – 41 nm in size showing that the Cu was deposited very uniformly across all samples.

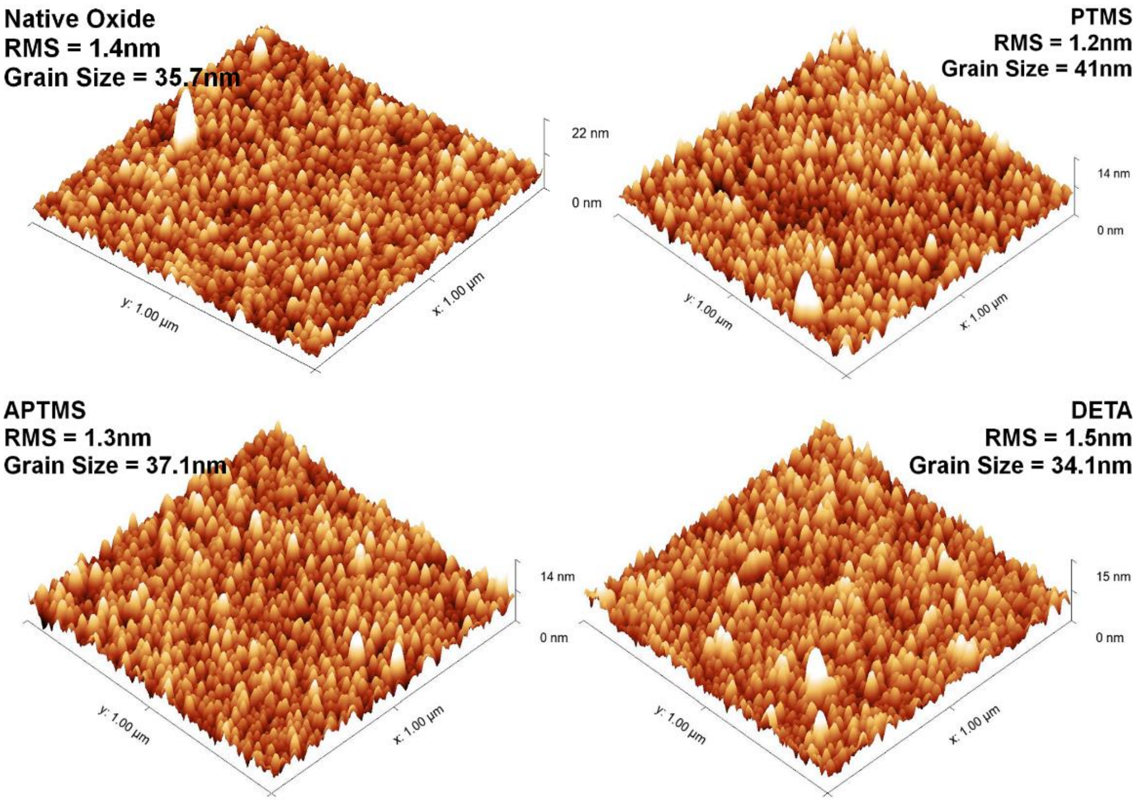

Figure 4.11 3D AFM images following Cu deposition, showing a uniform deposition across all samples. Scan size 1µm x 1µm.

Following a 400°C post metallisation vacuum anneal, a large change in the topography can be seen in all samples. The small distinguished grains appear to agglomerate to form larger connected regions of copper, typical for an annealed film, displayed in Figure 4.12 [33]. The APTMS and DETA display a similar morphology with the copper appearing to form a more homogenous film on these SAMs. There is only a small increase in the surface roughness with the R_{rms} of APTMS ~2nm and the DETA ~ 2.3 nm. However, the native oxide and the PTMS show more deviation from a homogenous film.

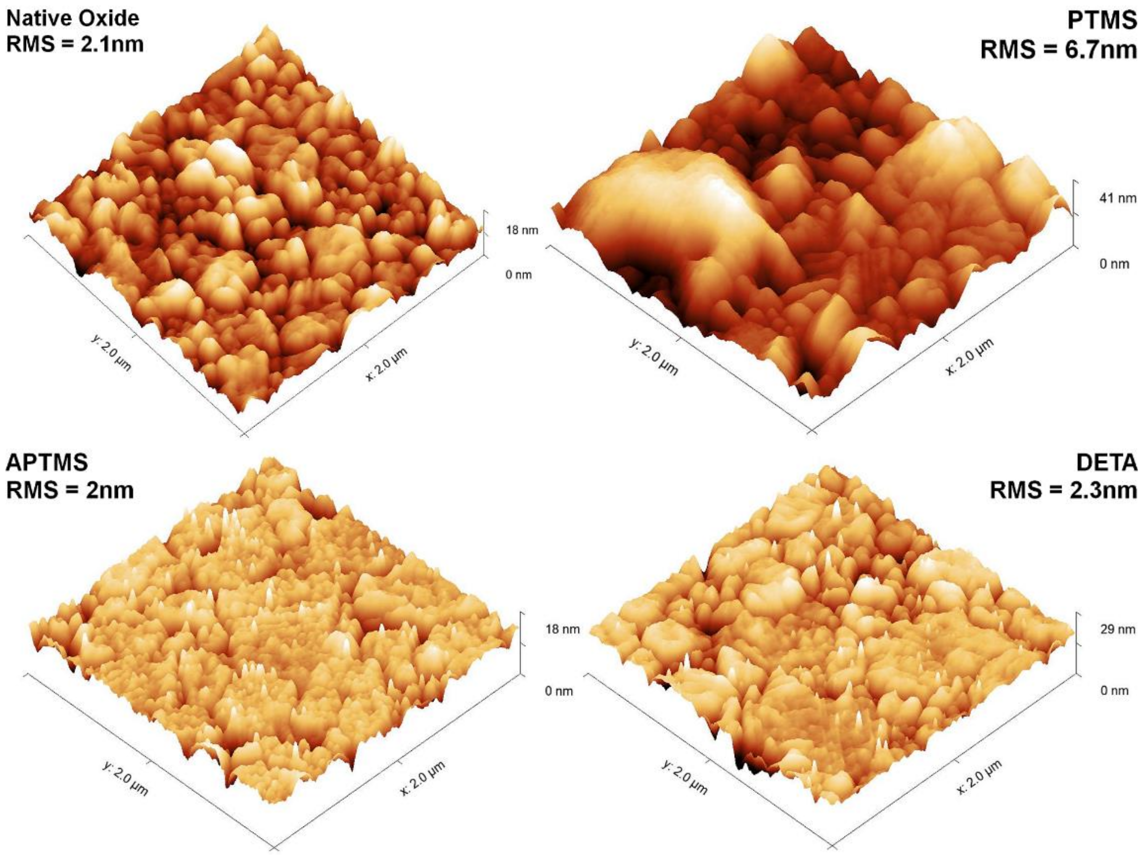

Figure 4.12 3D AFM images showing the change in morphology following a 400°C post metallization vacuum anneal. Scan size 2µm x 2µm.

Figure 4.13 displays 4-point probe measurements following a thick blanket copper deposition and these films measured again following a 400°C anneal. The data was calculated from the average of five measurements taken on different areas of the sample to ensure consistency. Initial results after copper deposition show that all samples have very similar sheet resistance and resistivity values. The annealed samples all demonstrate a decrease in resistivity values as they approach the reported value of 1.68 x 10^{-8} Ωm. These values are summarised in Table 4.4 below. These results would suggest that the presence of the self-assembled monolayer has little to no impact on the measured resistivity of the copper film.

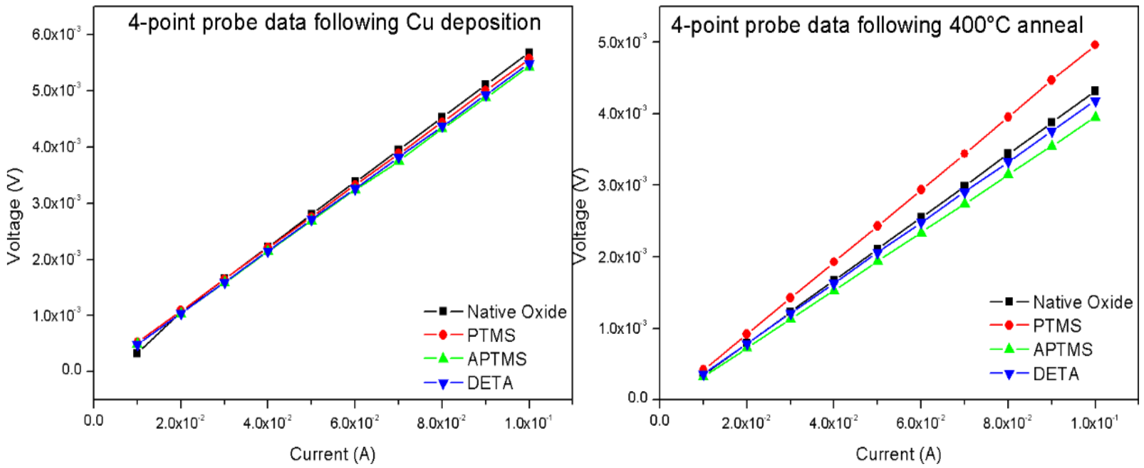

Figure 4.13 4-point probe measurements for the as-deposited and 400C anneal samples.

Table 4.4 Sheet resistance and resistivity values for all samples before and after annealing.

Cu Deposition	**Sheet Resistance (Ω /sq)**	**Resistivity (Ωm)**	**400°C Anneal**	**Sheet Resistance (Ω /sq)**	**Resistivity (Ωm)**
Ref. SiO_2	0.24	2.23 x 10^{-8}	**Ref. SiO_2**	0.19	1.72 x 10^{-8}
PTMS	0.25	2.38 x 10^{-8}	**PTMS**	0.22	2.08 x 10^{-8}
APTMS	0.24	2.73 x 10^{-8}	**APTMS**	0.17	1.95 x 10^{-8}
DETA	0.24	2.52 x 10^{-8}	**DETA**	0.19	1.91 x 10^{-8}

4.4 Chapter Conclusion

In summary, the x-ray photoelectron spectroscopy studies have shown that amino-terminated self-assembled monolayers offer significant benefits in terms of both nucleation and adhesion over both SiO_2 and non-amine terminated SAMs. In ultra-thin films the DETA SAM shows the best nucleation performance for metallic copper, however upon anneal the APTMS retains more of the deposited copper and the overall effect is that both DETA and APTMS show similar amounts of copper following the deposition and anneal cycle. Tape testing performed with thicker films showed almost identical performance for both the DETA and APTMS SAMs, again significantly better than for native SiO_2 and PTMS. AFM measurements demonstrate that all samples are essentially indistinguishable in the as-deposited state. However, upon annealing the surface morphology can be seen to change especially for the PTMS in which the R_{rms} increases to 6.7 nm. This demonstrates a correlation between the thermal stability of the Cu films on the differently terminated surfaces and the tape test results. Finally, 4-point probe measurements show that the presence of the SAM has no negative effect on the resistivity values for the copper films.

These results all indicate that SAMs containing an amino terminal group show several advantages over non amino-terminated SAMs and SiO_2. Furthermore, it appears that although the extended hydrocarbon chain in the DETA SAM displays excellent nucleation, it does not help with the retention of the copper film. APTMS with its shorter hydrocarbon chain however, retains equal quantities of the copper film. Both amino terminated SAMs in terms of nucleation and adhesion of Cu appear to be effective candidates as seed layers for copper based BEOL applications. If scaling does continue, APTMS would be the superior choice for smaller dimensional technology nodes, as its shorter chain length would occupy less of the cross-sectional area of the interconnect, thereby keeping line resistance to a minimum.

4.5 References

(1) Lane, M.; Dauskardt, R. Adhesion and Reliability of Copper Interconnects with Ta and Ta Barrier Layers. *J. Mater. Res.* **2000**, *15* (1), 203–211.

(2) Liao, Z.; Gall, M.; Yeap, K. B.; Sander, C.; Mühle, U.; Gluch, J.; Standke, Y.; Aubel, O.; Vogel, N.; Hauschildt, M.; Beyer, A.; Engelmann, H. J.; Zschech, E. In-Situ Study of the TDDB-Induced Damage Mechanism in Cu/Ultra-Low-k Interconnect Structures. *Microelectron. Eng.* **2015**, *137* (1), 47–53.

(3) Xie, Q.; Qu, X. P.; Tan, J. J.; Jiang, Y. L.; Zhou, M.; Chen, T.; Ru, G. P. Superior Thermal Stability of Ta/TaN Bi-Layer Structure for Copper Metallization. *Appl. Surf. Sci.* **2006**, *253* (3), 1666–1672.

(4) Traving, M.; Zienert, I.; Zschech, E.; Schindler, G.; Steinhögl, W.; Engelhardt, M. Phase Analysis of TaN/Ta Barrier Layers in Sub-Micrometer Trench Structures for Cu Interconnects. *Appl. Surf. Sci.* **2005**, *252* (1), 11–17.

(5) Byrne, C.; Brennan, B.; McCoy, A. P.; Bogan, J.; Brady, A.; Hughes, G. In Situ XPS Chemical Analysis of $MnSiO_3$ Copper Diffusion Barrier Layer Formation and Simultaneous Fabrication of Metal Oxide Semiconductor Electrical Test MOS Structures. *ACS Appl. Mater. Interfaces* **2016**, *8* (4), 2470–2477.

(6) Koike, J.; Wada, M. Self-Forming Diffusion Barrier Layer in Cu-Mn Alloy Metallization. *Appl. Phys. Lett.* **2005**, *87* (4), 1–4.

(7) Hosseini, M.; Ando, D.; Sutou, Y.; Koike, J. Co and $CoTi_x$ for Contact Plug and Barrier Layer in Integrated Circuits. *Microelectron. Eng.* **2018**, *189*, 78–84.

(8) Ramanath, G.; Cui, G.; Ganesan, P. G.; Guo, X.; Ellis, A. V.; Stukowski, M.; Vijayamohanan, K.; Doppelt, P.; Lane, M. Self-Assembled Subnanolayers as Interfacial Adhesion Enhancers and Diffusion Barriers for Integrated Circuits. *Appl. Phys. Lett.* **2003**, *83* (2), 383–385.

(9) Mikami, N.; Hata, N.; Kikkawa, T.; Machida, H. Robust Self-Assembled

Monolayer as Diffusion Barrier for Copper Metallization. *Appl. Phys. Lett.* **2003**, *83* (25), 5181–5183.

(10) Ganesan, P. G.; Singh, A. P.; Ramanath, G. Diffusion Barrier Properties of Carboxyl- and Amine-Terminated Molecular Nanolayers. *Appl. Phys. Lett.* **2004**, *85* (4), 579–581.

(11) Sharma, S.; Kumar, M.; Rani, S.; Kumar, D. Deposition and Characterization of 3-Aminopropyltrimethoxysilane Monolayer Diffusion Barrier for Copper Metallization. *Metall. Mater. Trans. B* **2014**, *46* (2), 928–932.

(12) Kong, Z.; Wang, Q.; Chen, E.; Wu, T. Study on Preparation Method for Short-Chain Alkylsiloxane Self-Assembled Monolayers and the Diffusion Behavior of Copper on Silica Surfaces. *Appl. Surf. Sci.* **2013**, *279*, 171–179.

(13) Caro, A. M.; Armini, S.; Richard, O.; Maes, G.; Borghs, G.; Whelan, C. M.; Travaly, Y. Bottom-Up Engineering of Subnanometer Copper Diffusion Barriers Using NH_2-Derived Self-Assembled Monolayers. *Adv. Funct. Mater.* **2010**, *20* (7), 1125–1131.

(14) Herrera-Gomez, A. *A Double Lorentzian Shape for Asymmetric Photoelectron Peaks*; 2011.

(15) Nečas, D.; Klapetek, P. Gwyddion: An Open-Source Software for SPM Data Analysis. *Cent. Eur. J. Phys.* **2012**, *10* (1), 181–188.

(16) Hamoudi, H.; Guo, Z.; Prato, M.; Dablemont, C.; Zheng, W. Q.; Bourguignon, B.; Canepa, M.; Esaulov, V. A. On the Self Assembly of Short Chain Alkanedithiols. *Phys. Chem. Chem. Phys.* **2008**, *10* (45), 6836.

(17) Hamoudi, H.; Prato, M.; Dablemont, C.; Cavalleri, O.; Canepa, M.; Esaulov, V. A. Self-Assembly of 1,4-Benzenedimethanethiol Self-Assembled Monolayers on Gold. *Langmuir* **2010**, *26* (10), 7242–7247.

(18) Takenaga, M.; Jo, S.; Graupe, M.; Lee, T. R. Effective van Der Waals Surface

Energy of Self-Assembled Monolayer Films Having Systematically Varying Degrees of Molecular Fluorination. *J. Colloid Interface Sci.* **2008**, *320* (1), 264–267.

(19) Pertsin, A. J.; Pashunin, Y. M. Differential Charging in XPS Studies of Polymer/Metal Interfaces. *Appl. Surf. Sci.* **1990**, *44* (3), 171–178.

(20) Turner, N. H. Surface Analysis: X-Ray Photoelectron Spectroscopy and Auger Electron Spectroscopy. *Anal. Chem.* **1994**, *66* (12), 163–185.

(21) Miller, D. J.; Biesinger, M. C.; McIntyre, N. S. Interactions of CO_2 and CO at Fractional Atmosphere Pressures with Iron and Iron Oxide Surfaces: One Possible Mechanism for Surface Contamination? *Surf. Interface Anal.* **2002**, *33* (4), 299–305.

(22) Beamson, G.; Briggs, D. *High Resolution XPS of Organic Polymers: The Scienta ESCA300 Database*; Wiley: New York, 1992.

(23) Casey, P.; Bogan, J.; Mccoy, A.; Lozano, J. G.; Nellist, P. D.; Hughes, G. Chemical and Structural Investigations of the Interactions of Cu with $MnSiO_3$ Diffusion Barrier Layers. *J. Appl. Phys.* **2012**, *112*.

(24) Lee, S. Y.; Mettlach, N.; Nguyen, N.; Sun, Y. M.; White, J. M. Copper Oxide Reduction through Vacuum Annealing. *Appl. Surf. Sci.* **2003**, *206* (1–4), 102–109.

(25) Lozano, J. G.; Bogan, J.; Casey, P.; McCoy, A. P.; Hughes, G.; Nellist, P. D. Scanning Transmission Electron Microscopy Investigations of Self-Forming Diffusion Barrier Formation in Cu(Mn) Alloys on SiO2. *APL Mater.* **2013**, *1* (4).

(26) Poulston, S.; Parlett, P. M.; Stone, P.; Bowker, M. Surface Oxidation and Reduction of CuO and Cu_2O Studied Using XPS and XAES. *Surf. Interface Anal.* **1996**, *24* (12), 811–820.

(27) Paparazzo, E. XPS and AUGER Spectroscopy Studies on Mixtures of the Oxides SiO_2, Al_2O_3 , Fe_2O_3, and Cr_2O_3. *J. Electron Spectros. Relat. Phenomena* **1987**, *43* (2), 97–112.

(28) Dupin, J.-C.; Gonbeau, D.; Vinatier, P.; Levasseur, A. Systematic XPS Studies of Metal Oxides, Hydroxides and Peroxides. *Phys. Chem. Chem. Phys.* **2000**, *2* (6), 1319–1324.

(29) Mallikarjunan, A.; Sharma, S.; Murarka, S. P. Resistivity of Copper Films at Thicknesses Near the Mean Free Path of Electrons in Copper. *Electrochem. Solid-State Lett.* **2000**, *3* (9), 437–438.

(30) Liu, H. D.; Zhao, Y. P.; Ramanath, G.; Murarka, S. P.; Wang, G. C. Thickness Dependent Electrical Resistivity of Ultrathin (<40 Nm) Cu Films. *Thin Solid Films* **2001**, *384* (1), 151–156.

(31) Raghavan, G.; Chiang, C.; Anders, P. B.; Tzeng, S.-M.; Villasol, R.; Bai, G.; Bohr, M.; Fraser, D. B. Diffusion of Copper through Dielectric Films under Bias Temperature Stress. *Thin Solid Films*. 1995, 262*,* 168-176.

(32) McBrayer, J.; Swanson, R. M.; Sigmon, T. W. Diffusion of Metals in SiO_2. *J. Electrochem. Soc.* **1986**, *133* (6).

(33) Figueiredo, V.; Elangovan, E.; Gonçalves, G.; Barquinha, P.; Pereira, L.; Franco, N.; Alves, E.; Martins, R.; Fortunato, E. Effect of Post-Annealing on the Properties of Copper Oxide Thin Films Obtained from the Oxidation of Evaporated Metallic Copper. *Appl. Surf. Sci.* **2008**, *254* (13), 3949–3954.

Chapter 5

5 Atomic Oxygen treatments of DETA and OTMS SAMs

The following chapter describes the behaviour of a DETA SAM deposited on SiO_2, when exposed *in-situ* to an atomic oxygen rich environment in an ultra-high vacuum system. The decay of the DETA SAM signal when exposed to both short (100 L) and long (1000 L) Langmuir exposures is systematically monitored. One Langmuir is defined as an exposure to a gas at a pressure of 1×10^{-6} Torr for 1 second. An octadecyltrimethoxysilane (OTMS) SAM with a long hydrocarbon chain, consisting of 18 C atoms is also investigated with medium 500 L exposures.

5.1 Introduction

ALD has greatly enhanced the ability to deposit very uniform and conformal thin films on high aspect ratio structures allowing for the continued down-scaling of feature sizes in microelectronic devices. As described in Chapter 1, ALD is compatible with the semiconductor device fabrication processes and has many other advantages that make it an attractive deposition method. One main drawback for ALD is the fact that it deposits on all surfaces when sometimes patterning of the surface is required. Area selective ALD (AS-ALD) is proposed as a method for preferentially depositing one material on a specific area on the surface while the remainder is left uncoated by the material. Essentially, what AS-ALD gives is spatial control over a deposited thin film[1].

One approach being adopted to achieve area selective ALD is through the use of SAMs in which microscale and nanoscale patterns can be achieved[2–4]. The adaptability of the SAMs chemistry make them a prime candidate for selectively adhering to particular sections of the surface allowing them to block any subsequently deposited material. Herregods *et al*. describe a bottom-up manufacturing process for electronic devices in the BEOL which consists of using SAMs to passivate the surface and consequently block film growth by ALD[5]. Devices consist of alternating patterns of metal and dielectric material and sometimes it is desired to deposit only on one of the materials. In this instance, a thiol SAM can be deposited on the metal surface and by choosing an appropriate terminal functional group it will block the subsequent deposited material from bonding to the surface. In this way the material is only deposited on the dielectric and not the metal[6–8]. Using a silane based SAM the material will only deposit on the metal and not the dielectric. The SAM is then removed by etching[9,10] or electrochemically by applying a potential bias[11]. The area selective process is displayed in Figure 5.1.

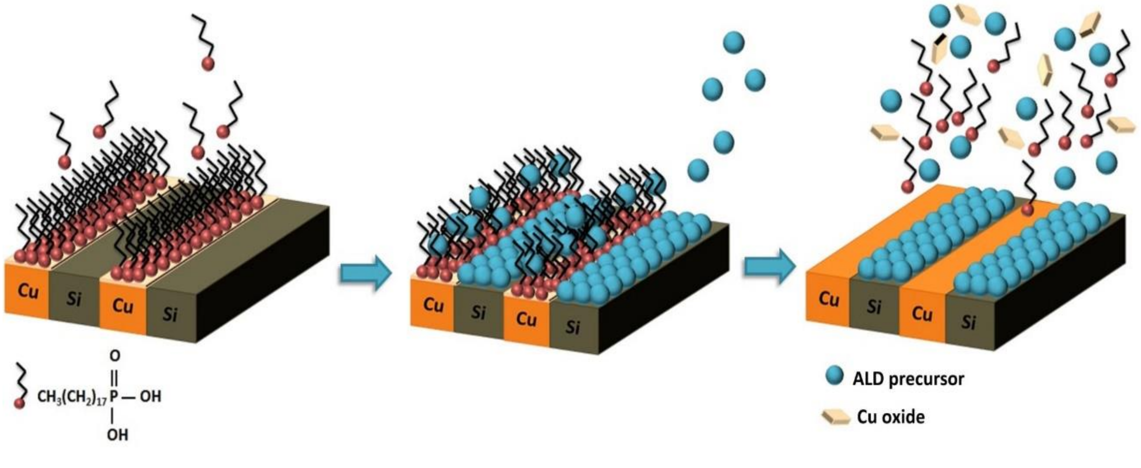

Figure 5.1 Schematic showing the area selective ALD process using a SAM as a blocker. A SAM is first deposited and adheres only to the Cu surface. A material is deposited via ALD and adheres to the uncovered Si. The SAM layer blocks the material adhering to the Cu. The sample is then etched to remove the SAM layer but leaving the deposited material on the Si[12].

This method can also be used for depositing on 3D nanostructures. Chopra *et al.* have shown how AS-ALD can differ on planar surfaces and non-planar surfaces. They were able to selectively block TiN deposition on hafnium dioxide (HfO_2) on the planar surfaces but grow TiN films on the nanolines and nanopillars where the SAM film had difficulty creating a uniform layer[13]. Dong *et al.* have also demonstrated their AS-ALD technique for successfully coating the vertical surfaces of nanopillars with zinc oxide (ZnO)[14].

During ALD of a metal oxide, the second half cycle usually consists of using water or a plasma to purge the first cycle precursor and initiate the oxidation reaction on the deposited metal on the surface. Although the use of plasma allows for a greater range of materials to be deposited, at lower temperatures the films are not as conformal or uniform and they are known to cause damage to the underlying layers[15–17]. Lee *et al.* have shown how the choice of plasma during AS-ALD can degrade a SAM film up to the point where no selective deposition is observed. By changing their gaseous plasma from an NH_3 to a H_2 they could deposit thin cobalt films up to 1000 cycles[18]. O_2 plasma is frequently used as the reactant plasma for the growth of a range of materials including, Al_2O_3, HfO_2, SiO_2, Pt, Ru, TiO_2 and ZnO to name a few[15,17,19] and more recently, molecular oxygen has been utilised for metal oxide depositon[20]. However, O_2 plasmas have been shown to cause degradation of low-*k* dielectric films due to ions and oxygen radicals causing damage to the dielectric [21]. This greatly affects the device performance and circuit reliability. With regards to SAMs, George *et al.* have shown how an O_2 plasma can be used to etch an OTMS SAM and remove it completely from the surface. In their study the SAM, which was deposited on a gold covered Si substrate, was covered in parts by a poly(dimethylsiloxane) or PDMS stamp. Subsequently, an O_2 plasma was used to etch the SAM from regions that were not covered by the PDMS stamp, creating a pattern. SEM and AFM performed after the electrodeposition of ZnO, Ni and Ag onto the patterned samples, found that these materials were only deposited on the underlying gold, while the SAM effectively blocked the deposition of these materials[22].

Atomic oxygen has been used as an ion-free alternative to O_2 plasma as it has the capacity to be less aggressive because it is a low-energy treatment that is also electrically neutral. Chaudhari *et al.* have assessed the role atomic oxygen plays in O_2 plasma induced damage of ultralow-*k* dielectrics[23]. Bogan *et al.* have used atomic oxygen as a less aggressive replacement for plasma treatment to modify dense low-*k* dielectric surfaces[24]. Dai *et al.* using self-assembled monolayers as a substitute for wool fibres, investigated the impact of atomic oxygen and O_2 plasma on an alkylthiolate SAM. They found that the plasma treatment had a more significant effect and etched the SAM more rapidly[25]. Atomic oxygen treatment of different materials is also a very important technique for exploring the performance of polymer coatings used for spacecraft, particularly those in a Low Earth Orbit (LEO). Spacecrafts residing in a LEO are exposed to extreme atmospheric conditions with ~ 80 % of the atmosphere consisting of atomic oxygen as well as being exposed to UV radiation and ionising radiation[26–28]. An atomic oxygen process has even been used to enhance smoke damaged paintings[29].

The study presented in this chapter looks, for the first time, at the impact on an amino-terminated SAM of controlled atomic oxygen exposures. This atomic oxygen treatment essentially mimics the oxidation pulse performed during the ALD cycle. Hence it is important to understand the impact these oxidation pulses can have on the SAMs integrity. The stepwise treatment of the DETA SAM is highly controlled using successive 100 Langmuir (L) exposures and examined using XPS measurements. The impact of these small atomic oxygen exposures is compared with much larger 1000 L exposures, and the changes induced on the DETA SAM terminated SiO_2 substrate is examined. The same process is followed for the carbon-terminated OTMS, although longer 500 L exposures are used. The etch rate of each SAM is studied.

5.2 Experimental methods

The DETA SAM was deposited by IMEC as described in Chapter 3 section 3.2. The second SAM employed in this study was the OTMS SAM. The OTMS SAM requires a different precursor but the methodology of the deposition process is the same.

The SAM was loaded into an ultra-high-vacuum XPS system for *in-situ* atomic oxygen treatment and analysis. The base pressure of the XPS system was typically ~1 x 10^{-9} mbar. Samples were not degassed prior to atomic oxygen exposures, so as not to degrade the SAM film. Atomic oxygen exposures were performed at room temperature using an Oxford Applied Research TC50 thermal gas cracker operating at 60W which was positioned in the line of sight of the sample at a distance of approximately 6cm. Atomic oxygen is generated by passing molecular oxygen through a heated capillary of the gas cracker where it thermally dissociates into atomic oxygen. Molecular oxygen was leaked into the UHV chamber via a needle valve up to partial pressures of ~2 x 10^{-6} mbar. When the cracker was switched on, the partial pressure of O_2 in the vacuum chamber (monitored by a Dycor LC-100 mass spectrometer) is seen to decrease. This decrease is a measure of the efficiency of the cracker at generating atomic oxygen in the system. Using this approach, the exact time for 100 L was calculated for each exposure and any small changes in pressure were accounted for. The atomic oxygen exposures were cumulative with XPS spectra acquired after each exposure. One sample of the DETA SAM received twenty-four successive 100 L exposures followed by three 1000 L exposures and one final 2000 L exposure. A second sample received two successive 1000 L exposures and one 2000 L exposure. The OTMS SAM received nine successive 500 L atomic oxygen exposures, with XPS performed after each exposure.

The XPS analysis was carried out using the same procedures as in the previous chapters. All peaks were equivalently shifted on the binding energy axis such that the C 1s signal was at a binding energy of 284.8 eV. All curve fitting analysis presented in this study was performed using AAnalyzer curve fitting software just as with the previous chapters. All spectral peaks were fitted with a Voigt profile which combines both Gaussian and Lorentzian line shapes, and a Shirley-Sherwood type background was used for all core level spectra. The Si 2p spectra is fitted with a Voigt doublet while the O 1s, N 1s and C 1s were fitted with a single Voigt peak. The Gaussian element of all component peaks for a particular peak envelope remained constant throughout. Full peak fitting parameters are given in Table 5.1. The Gaussian values for the DETA SAM appear to be larger than in the previous DETA samples used in Chapter 3 and Chapter 4, especially for the C 1s.

Table 5.1 Peak fitting parameters for the Si 2p, C 1s, O 1s and N 1s.

Peak Fitting Parameters for DETA SAM					
Si 2p	**Gaussian (eV)**	**Lorentzian (eV)**	**C 1s**	**Gaussian (eV)**	**Lorentzian (eV)**
Si bulk	0.6	0.39	**C-H**	2.1	0.3
SiO_2	1.2	0.39	**C-O/ C-N**	2	0.3
			C-O-N	1.7	0.3
			O-C=O	2	0.3
O 1s			**N 1s**		
SiO_2	1.5	0.55	**NH_3**	2.1	0.5
O-C / O-N	0.7	0.55	**C-O-N**	1.3	0.5

Peak Fitting Parameters for OTMS SAM					
Si 2p	**Gaussian (eV)**	**Lorentzian (eV)**	**C 1s**	**Gaussian (eV)**	**Lorentzian (eV)**
Si bulk	0.6	0.39	**C-H**	1.2	0.3
SiO_2	1.2	0.39	**C-O**	1.6	0.3
			C=O	1.5	0.3
O 1s					
SiO_2	1.5	0.55			
C-O	0.7	0.55			

5.3 Results & Discussions

5.3.1 Etching of the DETA SAM due to Atomic Oxygen Exposure

Figure 5.2 displays the overall chemical composition for selected steps throughout the experiment. It can be seen that as the carbon and nitrogen signals decrease the silicon and oxygen signals increase. This is interpreted as evidence of the removal of the SAM which exposes more of the SiO2 substrate surface and in turn increases its signal. After the twenty-fourth exposure the carbon and nitrogen signals are just above half of their original intensity. The larger exposures at the end decrease the intensity of these peaks more rapidly. The SAM is never fully removed from the surface even though cumulatively the samples have been exposed to 7400 L of atomic oxygen. In the corresponding survey scans in Figure 5.3 these trends are seen.

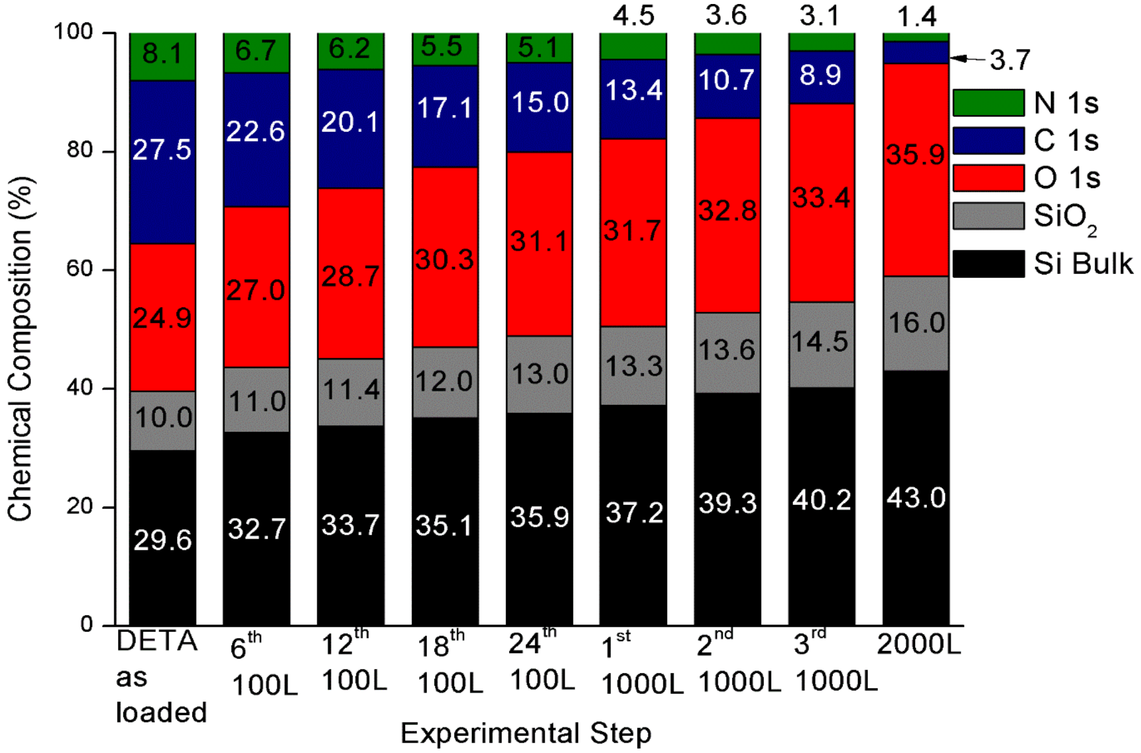

Figure 5.2 Overall chemical composition from selected atomic oxygen experimental steps. The carbon and nitrogen signals sequentially decrease with each successive exposure.

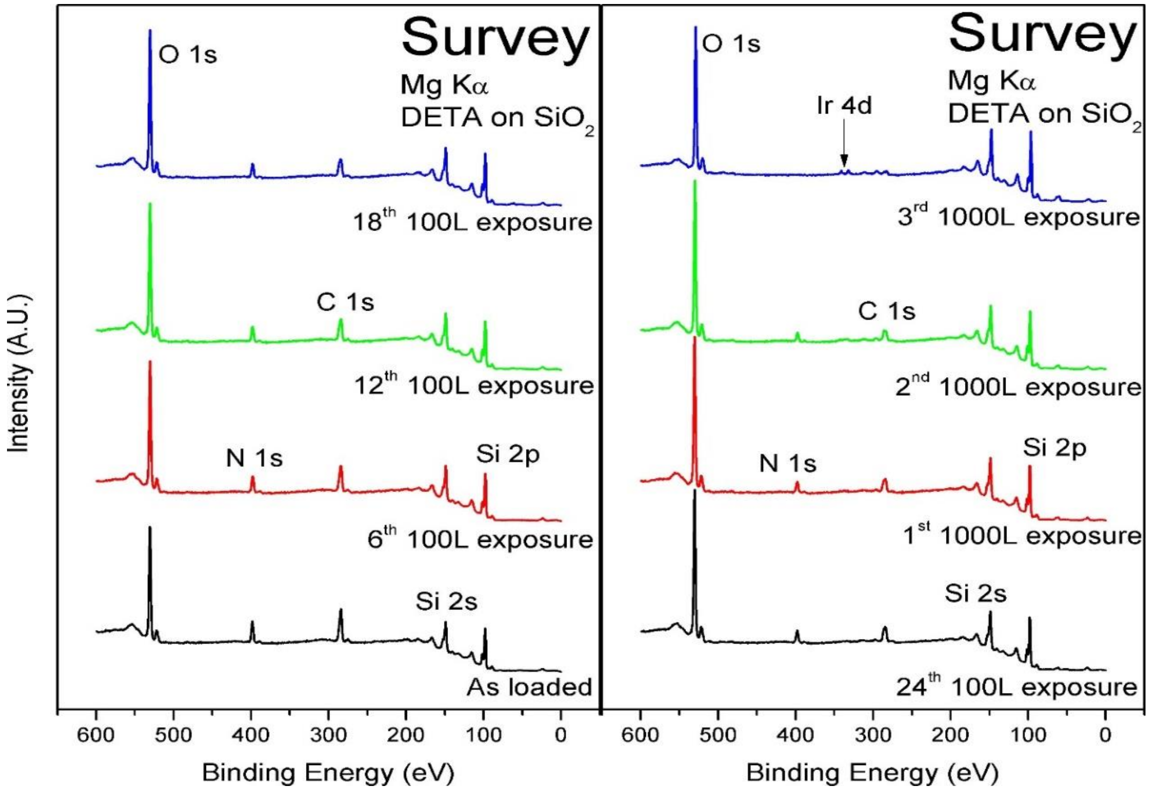

Figure 5.3 Survey spectra for selected experimental steps. With each exposure the C 1s and N 1s decrease in intensity.

It is worth noting that some iridium (Ir) from the capillary filament in the cracker is deposited on the surface during the exposures. XPS is very sensitive to Ir and chemical calculations show that the Ir 4d (~297 eV) represents < 1 % of the total surface. Therefore, it has not been included in the overall chemical composition.

In order to understand the changes induced in the SAM following the atomic oxygen exposures, the C 1s and N 1s core level spectra were studied in detail. Figure 5.4 displays the peak fitted C 1s spectra from unnormalised data. Prior to atomic oxygen exposure, the primary component peak is the C-C / C-H peak at 284.8 eV[30–32]. The C-H bonds from the DETA and the C-C bonds from adventitious carbon are indistinguishable in XPS.

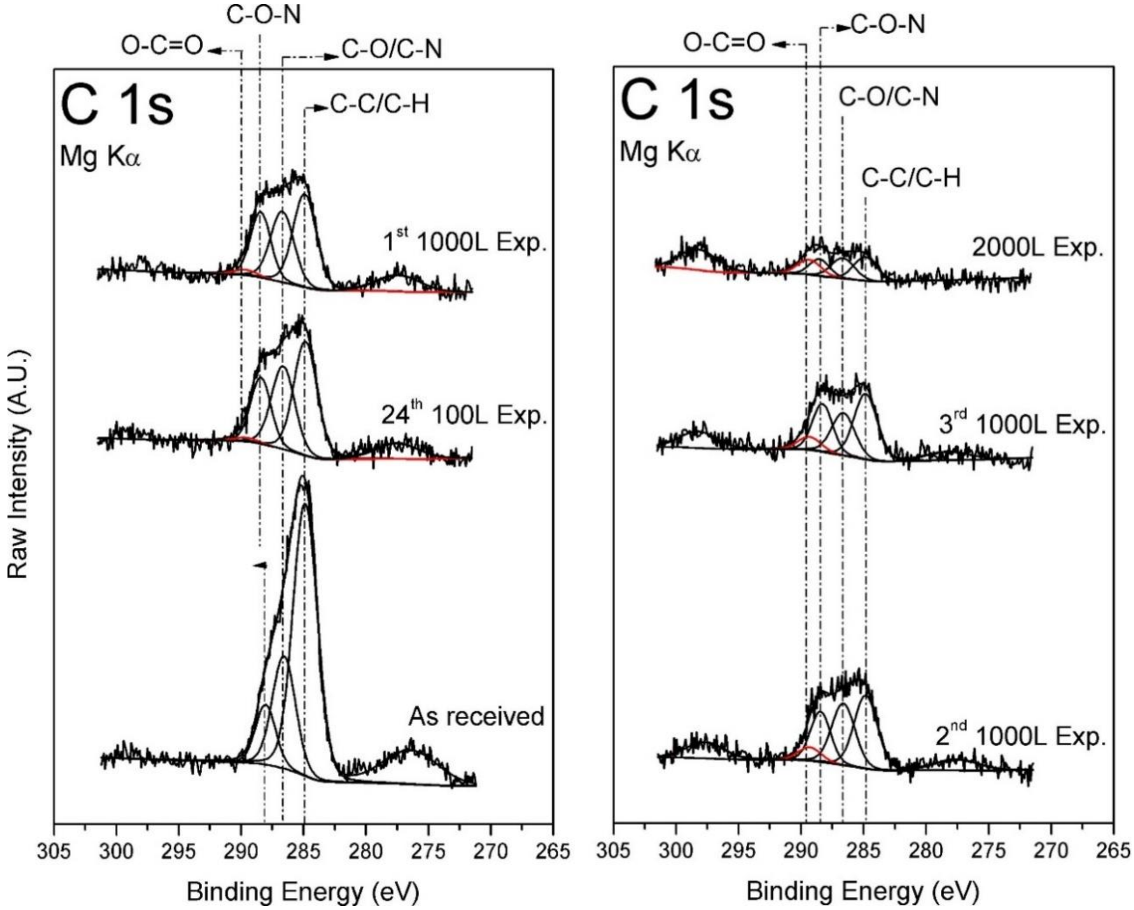

Figure 5.4 C 1s spectra showing the overall decrease in component peaks except for the O-C=O peak which grows with higher exposure to atomic oxygen.

The next peak at 286.6 eV is attributed to C-O / C-N bonds[33,34]. Due to the similar electronegativity values of oxygen and nitrogen it is very difficult to resolve the two different binding environments hence, they cannot be definitively distinguished. The C-O bonds are also indicative of adventitious carbon due to atmosphere exposure. While the C-N bonds are due to bonding in the DETA SAM. The third component peak visible in the spectrum at ~ 288.1 eV which shifts to 288.4 eV after the small exposures, has been ascribed to C-O-N bonds[33,35]. It appears that some oxygen has become incorporated into the DETA SAM and has bonded to the nitrogen and carbon in the terminal group. Following the twenty-fourth 100 L exposure the overall C 1s intensity is almost half of its original value. However, the growth of an additional peak at ~289.5 eV is observed and is indicative of O-C=O bonds[33,36]. This peak confirms that some oxygen is being incorporated into the DETA film. The next larger 1000 L exposure sees a decrease in all peaks except for the O-C=O component peak. This trend is seen for the subsequent exposures although, the growth of the O-C=O peak is very small. The final 2000 L exposure almost completely removes the SAM related signal from the surface.

The decrease in intensity of the C-C/C-H component peak, the increase in intensity of the C-O/C-N, C-N-O peaks and growth of the O-C=O peak indicates that two processes are occurring. Oxygen is being incorporated into the DETA SAM film which results in SAM decomposition and ultimately the removal of the SAM from the surface.

The deconvoluted N 1s spectra are shown in Figure 5.5. The initial N 1s contains two component peaks that have been attributed to N-H bonds at 399.3 eV [37] and a small component peak at 400.5 eV consistent with C-O-N bonds [35]. Again, these C-O-N are due to oxygen bonding to the DETA terminal group. Similar, to the C 1s after the twenty-fourth 100 L exposure, there is a large decrease in the overall intensity of the N 1s leaving it at just above half of its original intensity. With the larger subsequent exposures, the overall intensity decreases. However, the C-O-N peak appears not to decrease at the same rate compared to the N-H peak.

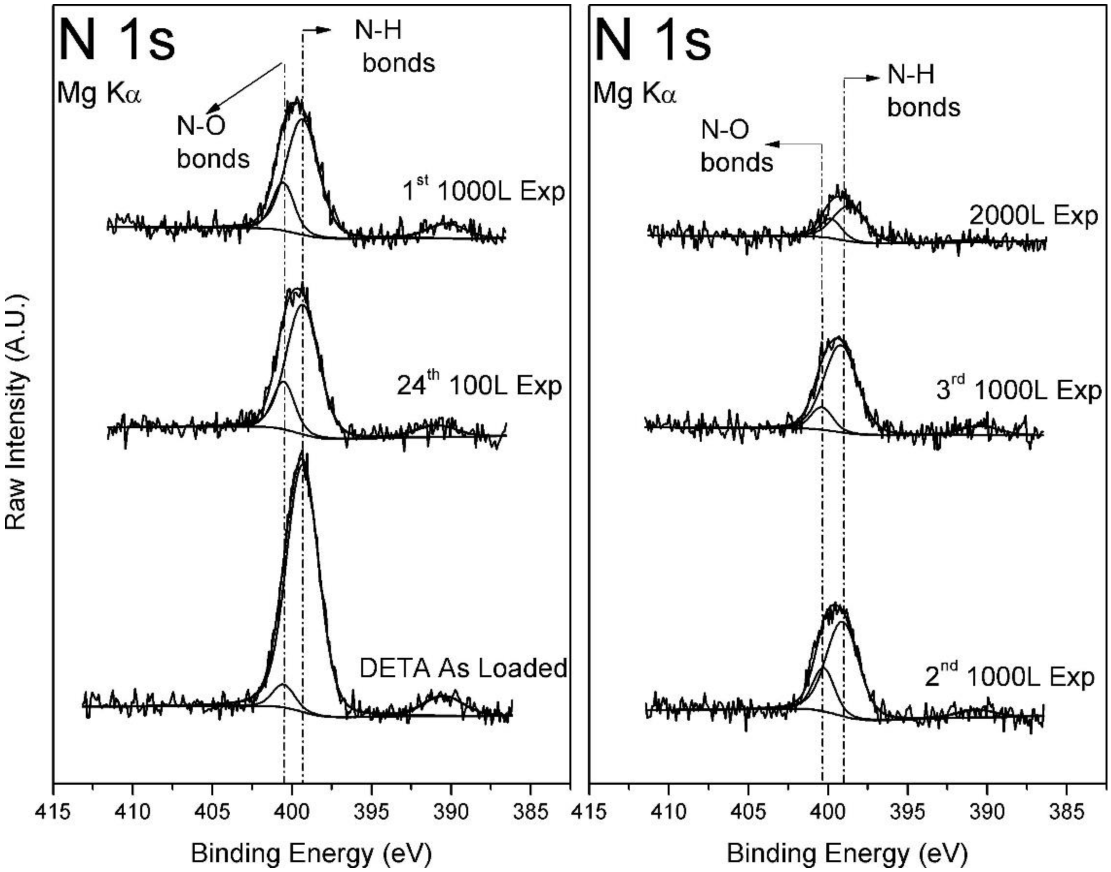

Figure 5.5 Peak fitted N 1s spectra for selected experimental steps. With each exposure the N 1s intensity decreases.

The loss of peak intensity for both the C 1s and N 1s alludes to two possible mechanisms for etching the DETA SAM. The atomic oxygen can be desorbing small moieties at a time or the intact DETA chains are being desorbed[38]. The carbon-nitrogen ratio plotted in Figure 5.6 as a function of oxygen treatments shows a small preferential removal of carbon over nitrogen. However, the overall reduction in intensity for the C and N 1s signals as a function of treatment shown in Figure 5.7 points to an etching process where the full chain is removed from the surface.

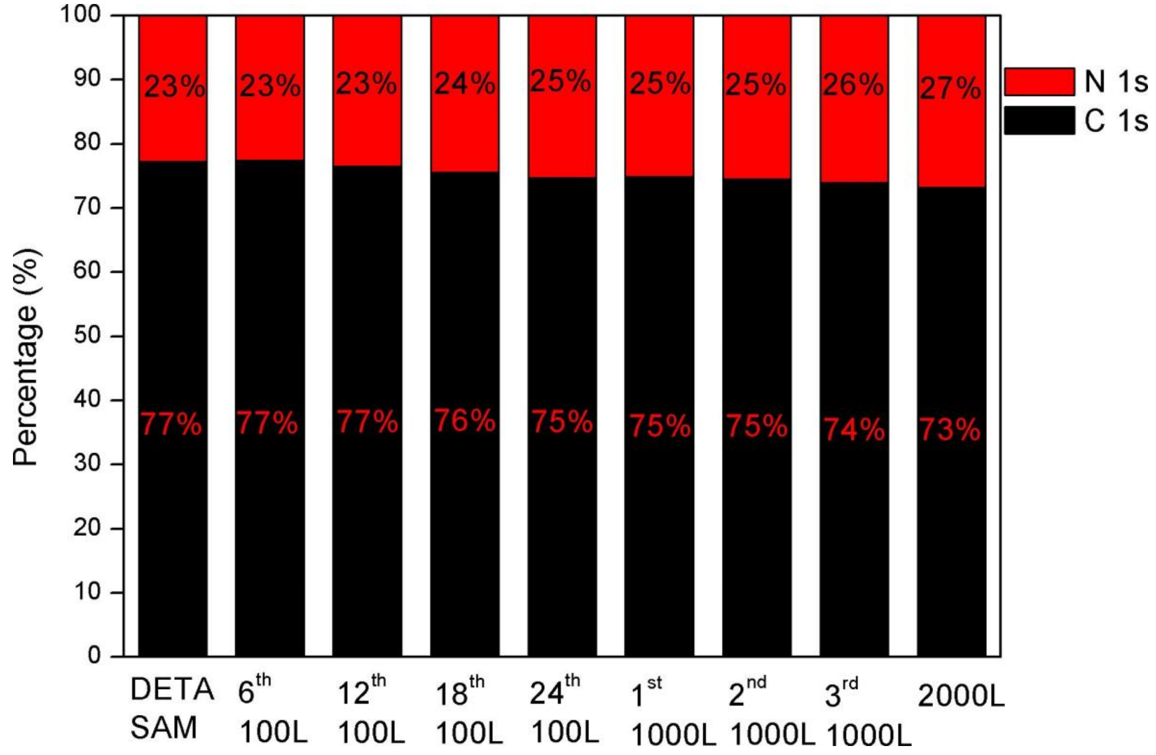

Figure 5.6 The carbon nitrogen ratio displays a slight preference for the removal of C over N.

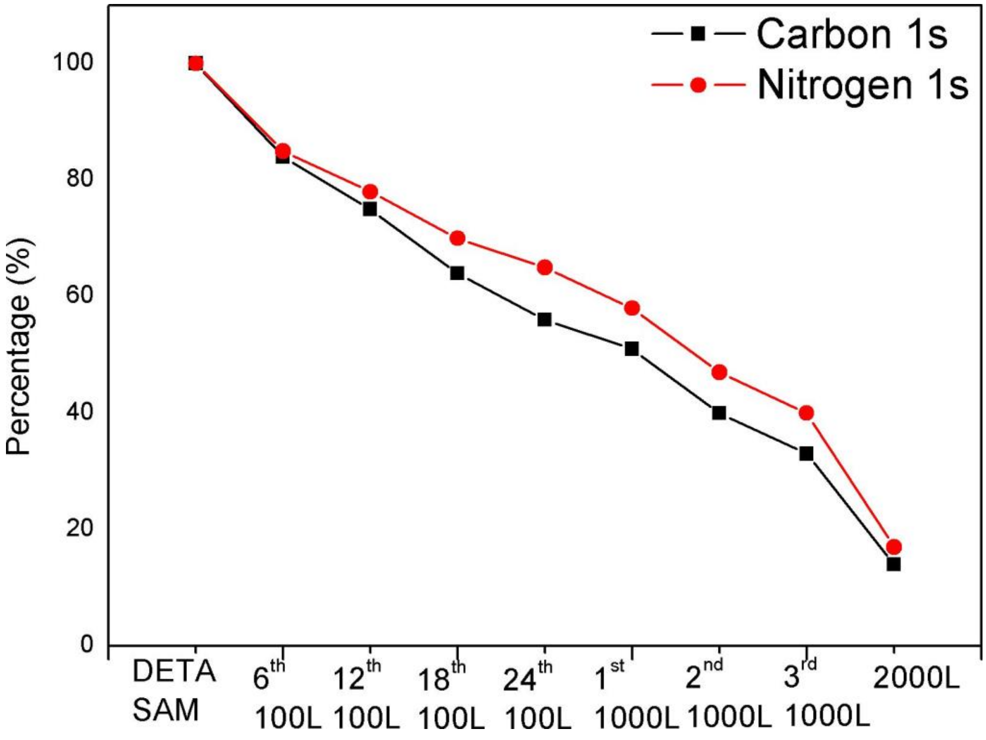

Figure 5.7 The C 1s and N 1s plotted as a function of atomic oxygen treatment showing the magnitude of the total reduction in these signals with atomic oxygen exposures.

The O 1s and the Si 2p of the DETA SAM, illustrated in Figure 5.8(a) and (b) respectively, display very little change over the course of the experiment. Two component peaks are visible in the O 1s which are associated with SiO_2 at 532 eV and C-O at 530.3 eV[39]. The intensity of the SiO_2 component peak is much larger than the C-O peak making it difficult to observe changes in the carbon-oxygen bonding environment. There is a slight increase in the C-O peak with each exposure. A small change in the Si 2p can be associated with the formation of sub-oxides after exposure. Thickness calculations on the SiO_2 peak reveal that there is no change in the thickness of the SiO_2 after any of the exposures. This signifies that the head group of the DETA is unaffected by the atomic oxygen, whereas the rest of the SAM is progressively removed.

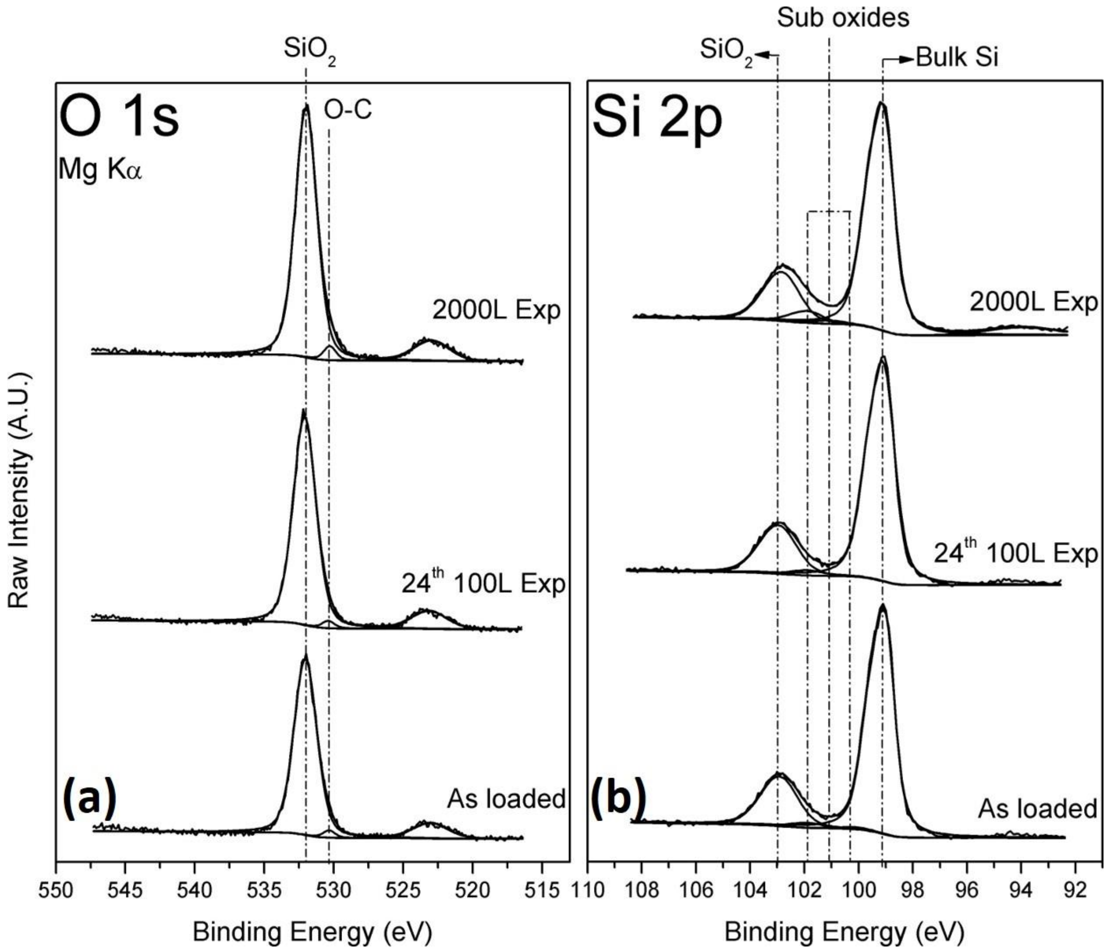

Figure 5.8 O 1s (a) and Si 2p (b) spectra show little to no change over the course of the study.

Another DETA sample was investigated with large 1000 L exposures. This sample received exposures of 1000 L until the DETA SAM was almost completely removed.

5.3.2 Etching of the OTMS SAM due to Atomic Oxygen Exposure

OTMS is a long chain SAM, with 18 carbon atoms in the hydrocarbon chain shown in Figure 5.9. It is approximately 2.3 nm in length which makes it just over twice as long as the DETA SAM. The OTMS also has no terminal functional group. It contains just the silane head group and the hydrocarbon chain.

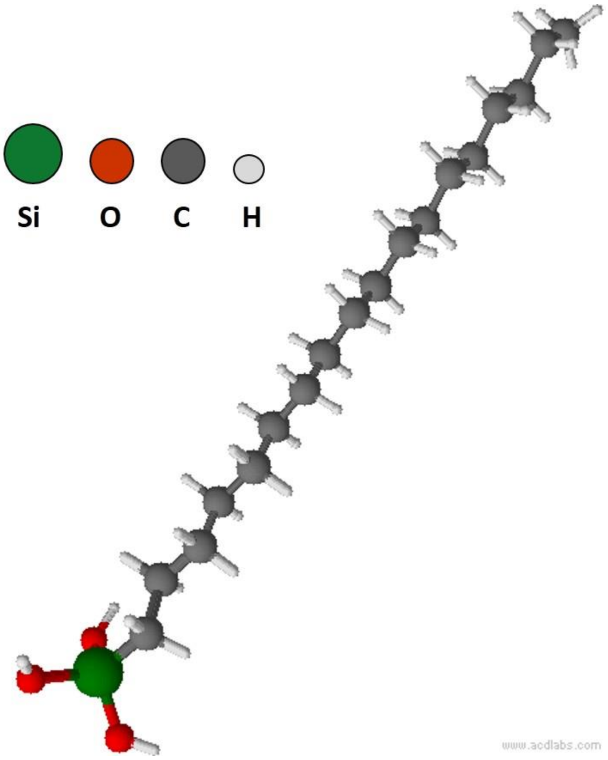

Figure 5.9 Schematic of OTMS SAM.

During this study the OTMS received nine 500 L in situ atomic oxygen exposures. It was presumed that due to the chain length that the smaller 100 L exposures would take a considerable amount of time to etch the SAM. On the other hand, the

1000 L exposures were considered too large to observe the stepwise etching of the SAM like with the DETA. It was decided that 500 L atomic oxygen exposures would be appropriate to investigate the etching process.

Figure 5.10 displays the chemical composition for the OTMS throughout the course of the study. A steady decrease of the C 1s is observed with each atomic oxygen exposure.

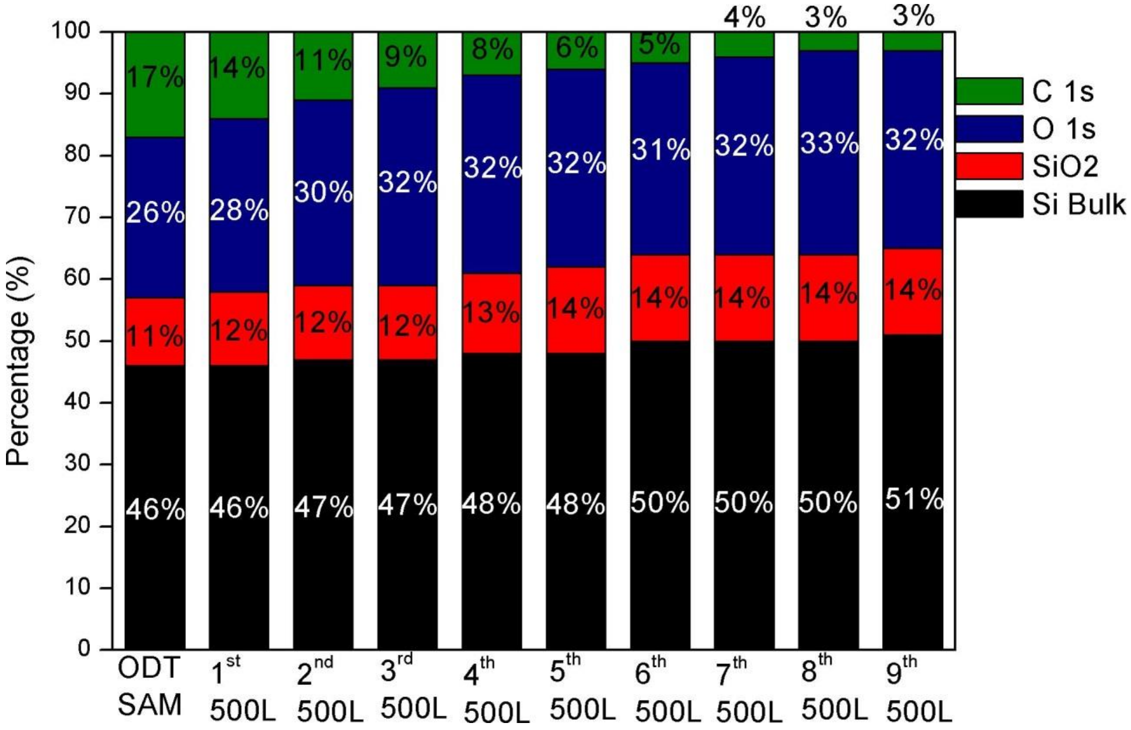

Figure 5.10 Chemical composition of the OTMS SAM.

This corresponds to the removal of the OTMS SAM from the surface. As the C 1s signal intensity decreases the O 1s and Si 2p signals increase. Just as with the DETA SAM, as the OTMS is etched from the surface, more of the underlying substrate is uncovered and this in turn increases the intensity of the Si and O signals. In selected survey spectra shown in Figure 5.11 the significant reduction in the C 1s signal with the atomic oxygen exposures can be clearly observed.

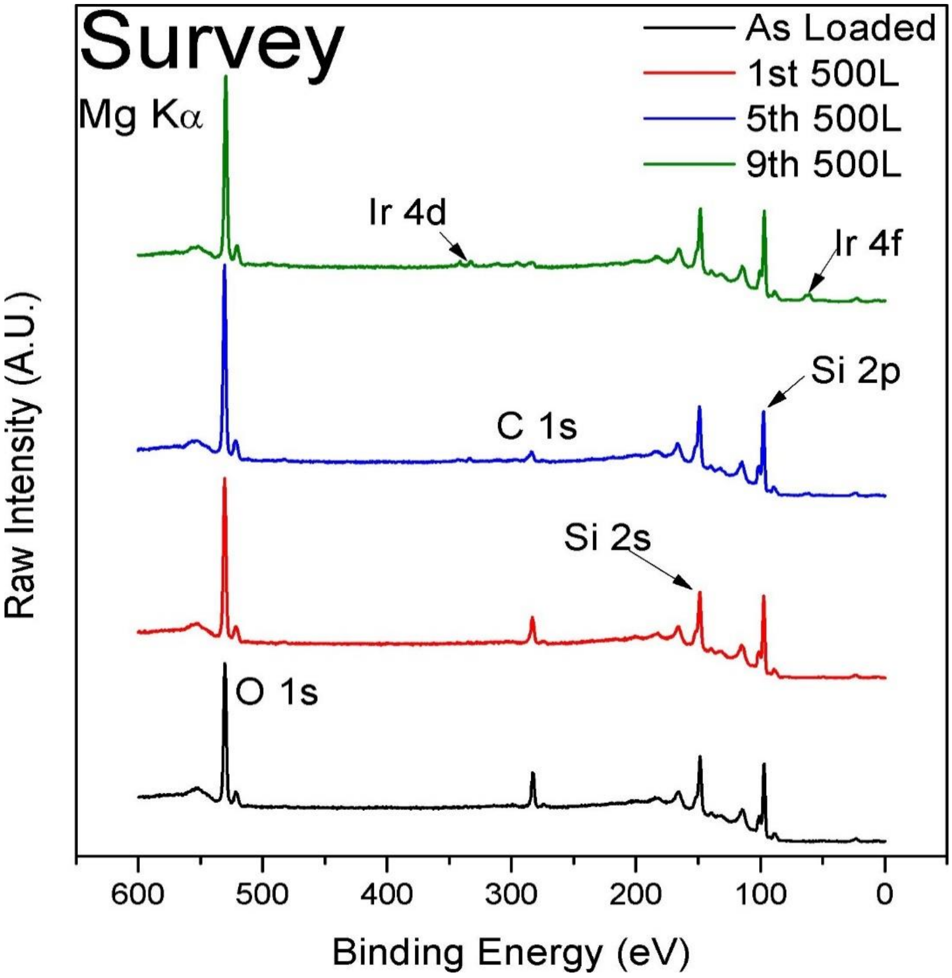

Figure 5.11 Selected survey spectra showing the decrease of the C1s signal intensity with increasing atomic oxygen exposure.

Similar to the DETA sample, the emergence of iridium 4f and 4d peaks is observed in the later exposures. This is again due to the filament in the cracker depositing on the surface during the exposures. Chemical calculations show that the Ir 4d (~297 eV) represents < 1 % of the total surface. Therefore, it has not been included in the overall chemical composition.

The O 1s spectra in Figure 5.12(a) are dominated by the SiO_2 component peak at a binding energy of 532.2 eV. On the lower binding energy side at 530.5 eV, is the presence of a small C-O peak, which is also observed in the C 1s spectra [39]. There is little change in these two peaks over the course of the experiment. The SiO_2 component signal intensity does increase slightly due to the removal of the SAM.

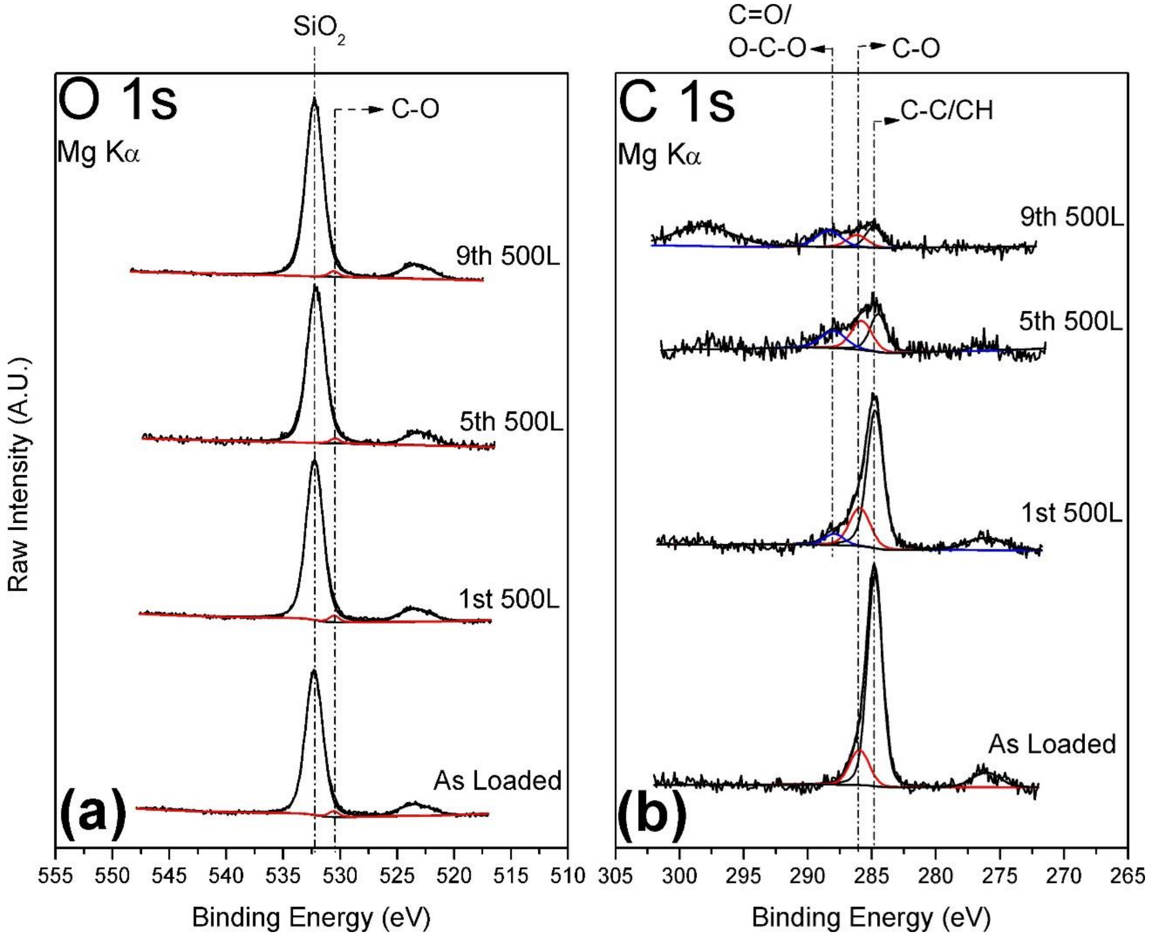

Figure 5.12 The O 1s (a) shows little change due to atomic oxygen exposure while the C 1s (b) shows a dramatic decrease in intensity along with the incorporation of oxygen into the SAM layer.

The C 1s spectrum shown in Figure 5.12(b), displays a peak profile in the as loaded spectrum which can be curve fitted using two component peaks. The main component peak is the C-C/C-H peak at a binding energy of 284.8 eV. On the higher binding energy side is the presence of a C-O peak at 286.1 eV [36]. Following the first 500 L atomic oxygen exposure the emergence of an additional peak on the higher binding energy side is observed at 288.1 eV. This peak is indicative of C=O or O-C-O bonds beginning to form which reveals that the oxygen is being incorporated into the film. A decrease in the intensity of the main component peak is also observed. With the subsequent atomic oxygen exposures, the C-C / C-H peak decreases even more and by the fifth 500 L exposure its intensity has been diminished to less than half of its original size. The C-O peak has not changed considerably while the C=O / O-C-O peak has increased slightly. By the final 500 L exposure the carbon has almost been fully removed by the atomic oxygen.

The Si 2p (not shown) shows no observable change during the course of the experiment. SiO_2 thickness calculations show no change in thickness of the SiO_2 due to atomic oxygen exposure signifying that the Si-O head group remains unaffected.

5.3.3 Decay Rate of the DETA and the OTMS SAMs

To examine the rate at which the DETA was etched from the surface due to the atomic oxygen, the intensities of the C 1s and N 1s after each exposure were plotted. Both the small (100 L) and large (1000 L) exposures are plotted to reveal essentially linear rates of etching for both the C 1s and N 1s, as seen in Figure 5.13 (a) and (b), respectively. It would not be unreasonable to expect that the as-received DETA would have some DETA molecules present which are not chemically bonded on the surface. These unreacted molecules should be easily desorbed, and this is reflected in the significant decrease in the both the C 1s and N 1s intensities from the as-received to the first atomic oxygen exposure. Since the larger exposures were performed after the short exposures these groups have already desorbed due to atmospheric exposure. Hence, the initial intensity for the larger exposures are less than for the short 100 L exposures. From these graphs it is clear that the etch rate is determined by the sum total of the atomic oxygen exposures, as ten individual 100 L exposures produces the same results as a single 1000 L exposure. Interpolation of the data shows the linear relationship remains.

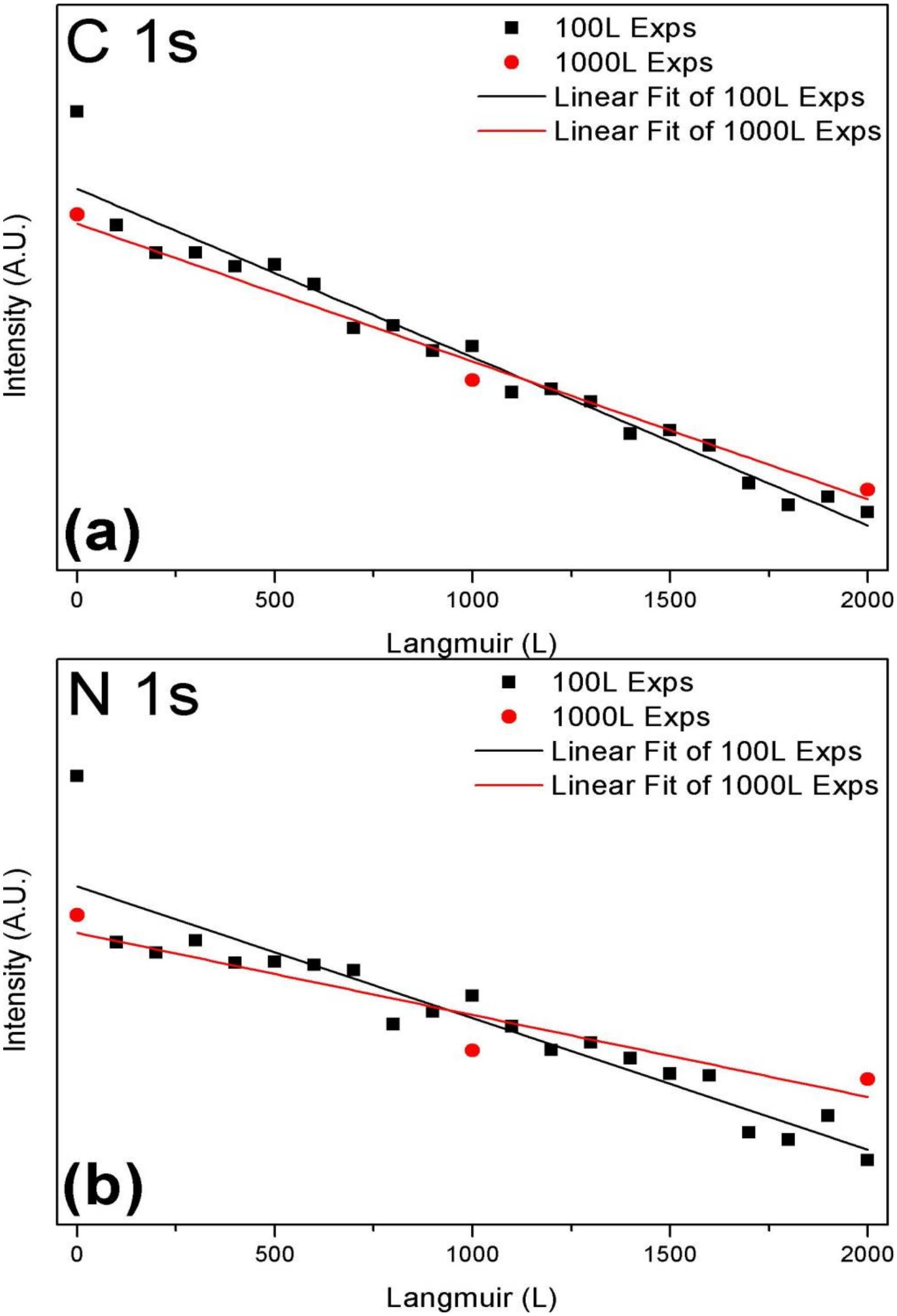

Figure 5.13 Etching of the DETA SAM (a) shows the decrease in intensity of the C 1s and (b) displays the decrease in intensity of the N 1s. Both graphs show a linear decay of the DETA SAM.

The decrease in intensity of the C 1s signal for the OTMS SAM is shown in Figure 5.14 and is fitted with an exponential function. This is in contrast to the DETA which shows a linear trend.

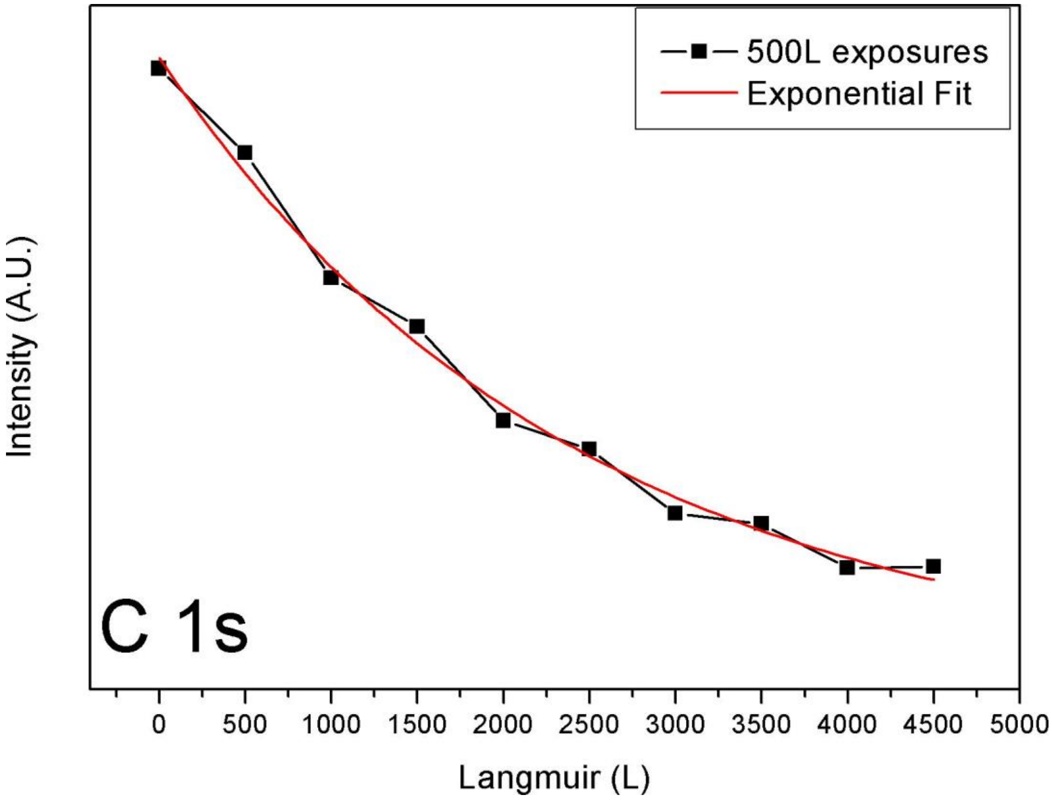

Figure 5.14 Graph showing exponential decay of the OTMS SAM.

Torres *et al.* using a gas cracker, investigated the interaction between a C_{16} SAM deposited on gold with atomic oxygen[36]. They suggested that there were three stages in the etching of the SAM. In the first stage (0 – 60 mins.) the oxygen atoms attached themselves to the hydrocarbon chain. In stage two (60 – 360 mins.) the etching of the SAMs is initiated with the removal of small moieties from the hydrocarbon chain. Essentially, there is a balance between oxidising the SAM and etching the SAM. The final stage (> 360 mins.) sees a change in how the SAM is removed. In this stage the oxygen is able to permeate to the gold interface and can oxidise the surface as well as etching the remaining SAM. Their study showed that the etching starts off linear but changes to a more exponential rate the more the

SAM becomes oxidised. This three-stage process is not observed here for either the DETA or OTMS SAM. The exposures used in our study are much smaller and show greater control over the removal of the SAM.

Gorham *et al.* used atomic hydrogen to investigate the etching of thiol SAMs of various chain lengths (C_9, C_{12}, C_{16} and C_{18}) deposited on gold[43]. They found that shorter chains are desorbed rapidly from the surface in both small segments and full chains. The longer chains however, resist the atomic hydrogen permeating to the gold surface and so are removed in smaller moieties. Their study shows that a C_{18} SAM does follow an exponential etch rate.

It is thought that the terminal group in the DETA SAM gives some protection to oxidation of the hydrocarbon chain, since the terminal group contains nitrogen which the OTMS SAM does not have. Hence it is harder for the atomic oxygen to permeate the DETA layer. The oxygen must look for defects in the film to breach, so it can start the etching process. Once the oxygen can reach the SiO_2 interface it can then remove the hydrocarbon chain and terminal group of the DETA in one step. The OTMS on the other hand, cannot stop the atomic oxygen penetrating the SAM layer as it does not have a terminal group to provide this protection. This leaves the oxygen free to diffuse between the SAM molecules, bond to the hydrocarbon chain and remove smaller moieties by oxidation. This leads to a much quicker initial etching of the film as seen by the exponential dependence. From the chemical composition of the DETA SAM in Figure 5.2 it can be seen that following 4400 L of atomic oxygen, that ~ 10.7 % of the surface signal is from the carbon. However, as seen in Figure 5.10 following 4500 L of atomic oxygen only ~3 % of the surface signal of the OTMS is from the presence of carbon. Even though the OTMS chain length is longer than the DETA, this offers little extra protection against etching. It appears as if the terminal group offers more protection to resist etching than a longer hydrocarbon chain.

5.4 Conclusions

Overall, due to excellent control of atomic oxygen exposures the stepwise modification of a SAM is observed. Upon loading, the photoemission spectra of both the DETA and OTMS SAMs, are essentially as expected, given their chemical composition. In the DETA SAM there is evidence of C-O/C-N and C-O-N bonds in the photoemission spectra of as-received sample which has been attributed to atmospheric exposure. As part of the etching process for the DETA, the atomic oxygen appears to strip the terminal groups and hydrocarbon chain from the SiO_2 while the head group remains unaffected. The integrity of the DETA remains intact as seen by the constant carbon nitrogen ratio. The DETA SAM is observed to be etched from the surface in a linear manner which is independent of the exposure size. In the OTMS SAM the emergence of C=O / O-C-O bonds in the C 1s suggest that the atomic oxygen is incorporating itself into the hydrocarbon chain before desorbing small segments of the chain. Upon loading there is evidence of existing C-O bonds in both the C 1s and the O 1s spectra. These treatments of both the DETA and the OTMS terminated SiO2 substrates result in no observable change in the Si 2p spectra. This implies that the head group remains unaffected by the atomic oxygen treatments. The decay of the OTMS SAM appears to be exponential in nature, which appears to be as a result of the longer chain length. It appears that the terminal group in the DETA, halts fast diffusion of oxygen into the monolayer. This stops oxygen bonding to the SAM chain which in turn slows down the removal of the SAM from the surface. The long chain of the OTMS appears to offer less protection to etching of the SAM layer. The oxygen can readily diffuse into the SAM and bond to the hydrocarbon chain, removing small moieties even after the first exposure. This could be very useful when deciding on what SAM to use for AS-ALD.

5.5 References

(1) Fang, M.; Ho, J. C. Area-Selective Atomic Layer Deposition: Conformal Coating, Subnanometer Thickness Control, and Smart Positioning. *ACS Nano* **2015**, *9* (9), 8651–8654.

(2) Jiang, X.; Bent, S. F. Area-Selective ALD with Soft Lithographic Methods: Using Self-Assembled Monolayers to Direct Film Deposition. *J. Phys. Chem. C* **2009**, *113* (41), 17613–17625.

(3) Färm, E.; Kemell, M.; Ritala, M.; Leskelä, M. Self-Assembled Octadecyltrimethoxysilane Monolayers Enabling Selective-Area Atomic Layer Deposition of Iridium. *Chem. Vap. Depos.* **2006**, *12* (7), 415–417.

(4) Avila, J. R.; Demarco, E. J.; Emery, J. D.; Farha, O. K.; Pellin, M. J.; Hupp, J. T.; Martinson, A. B. F. Real-Time Observation of Atomic Layer Deposition Inhibition: Metal Oxide Growth on Self-Assembled Alkanethiols. *ACS Appl. Mater. Interfaces* **2014**, *6* (15), 11891–11898.

(5) Herregods, S.; Chan, B. T.; Hetel, I. N.; Armini, S.; View, L.; View, N.; Chan, B. T. Vapour Phase Self-Assembled Monolayers for ALD Blocking on 300 Mm Wafer Scale. In *Euro CVD-21 - Baltic ALD-15*; Linkoping, Sweden, 2017; pp 2–4.

(6) Minaye Hashemi, F. S.; Birchansky, B. R.; Bent, S. F. Selective Deposition of Dielectrics: Limits and Advantages of Alkanethiol Blocking Agents on Metal-Dielectric Patterns. *ACS Appl. Mater. Interfaces* **2016**, *8* (48), 33264–33272.

(7) Hashemi, F. S. M.; Prasittichai, C.; Bent, S. F. A New Resist for Area Selective Atomic and Molecular Layer Deposition on Metal–Dielectric Patterns. *J. Phys. Chem. C* **2014**, *118* (20), 10957–10962.

(8) Hashemi, F. S. M.; Bent, S. F. Sequential Regeneration of Self-Assembled Monolayers for Highly Selective Atomic Layer Deposition. *Adv. Mater.*

Interfaces **2016**, *3* (21).

(9) Dae, J. K.; Pitchimani, R.; Snow, D. E.; Hope-Weeks, L. J. A Simple Method for the Removal of Thiols on Gold Surfaces Using an NH_4OH-H_2O_2-H_2O Solution. *Scanning* **2008**, *30* (2), 118–122.

(10) Lee, W.; Chao, C.; Jiang, X.; Hwang, J.; Bengt, S. F.; Prinz, F. B. Oxidative Removal of Self-Assembled Monolayers for Selective Atomic Layer Deposition. *ECS Trans.* **2008**, *16* (4), 173–179.

(11) Prasittichai, C.; Pickrahn, K. L.; Minaye Hashemi, F. S.; Bergsman, D. S.; Bent, S. F. Improving Area-Selective Molecular Layer Deposition by Selective SAM Removal. *ACS Appl. Mater. Interfaces* **2014**, *6* (20), 17831–17836.

(12) Atomic Layer Deposition https://bentgroup.stanford.edu/research_ALD/ (accessed May 14, 2018).

(13) Chopra, S. N.; Zhang, Z.; Kaihlanen, C.; Ekerdt, J. G. Selective Growth of Titanium Nitride on HfO_2 across Nanolines and Nanopillars. *Chem. Mater.* **2016**, *28* (14), 4928–4934.

(14) Dong, W.; Zhang, K.; Zhang, Y.; Wei, T.; Sun, Y.; Chen, X.; Dai, N. Application of Three-Dimensionally Area-Selective Atomic Layer Deposition for Selectively Coating the Vertical Surfaces of Standing Nanopillars. *Sci. Rep.* **2014**, *4* (step 3), 3–6.

(15) Kim, H.; Oh, I. Review of Plasma-Enhanced Atomic Layer Deposition : Technical Enabler of Nanoscale Device Fabrication Review of Plasma-Enhanced Atomic Layer Deposition : Technical Enabler of Nanoscale Device Fabrication. *Jpn. J. Appl. Phys.* **2014**, *53*, 03DA01 1-7.

(16) Oehrlein, G. S.; Metzler, D.; Li, C. Atomic Layer Etching at the Tipping Point: An Overview. *ECS J. Solid State Sci. Technol.* **2015**, *4* (6), N5041–N5053.

(17) Profijt, H. B.; Potts, S. E.; van de Sanden, M. C. M.; Kessels, W. M. M. Plasma-

Assisted Atomic Layer Deposition: Basics, Opportunities, and Challenges. *J. Vac. Sci. Technol. A Vacuum, Surfaces, Film.* **2011**, *29* (5), 050801.

(18) Lee, H.-B.-R.; Kim, H. Area Selective Atomic Layer Deposition of Cobalt Thin Films. *ECS Trans.* **2008**, *16* (4), 219–225.

(19) Mackus, A. J. M.; Bol, A. A.; Kessels, W. M. M. The Use of Atomic Layer Deposition in Advanced Nanopatterning. *Nanoscale* **2014**, *6* (19), 10941–10960.

(20) Singh, J. A.; Thissen, N. F. W.; Kim, W.-H.; Johnson, H.; Kessels, W. M. M. .; Bol, A. A.; Bent, S. F.; Mackus, A. J. M. Area-Selective Atomic Layer Deposition of Metal Oxides on Noble Metals through Catalytic Oxygen Activation. *Chem. Mater.* **2018**, *30* (3), 663–670.

(21) Cheng, Y.-L.; Lin, B.-H.; Huang, S.-W. Effect of O_2 Plasma Treatment on Physical, Electrical, and Reliability Characteristics of Low Dielectric Constant Materials. *Thin Solid Films* **2014**, *572* (6), 44–50.

(22) George, A.; Maijenburg, A. W.; Maas, M. G.; Blank, D. H. A.; Ten Elshof, J. E. Patterning Functional Materials Using Channel Diffused Plasma-Etched Self-Assembled Monolayer Templates. *Langmuir* **2011**, *27* (19), 12235–12242.

(23) Chaudhari, M.; Du, J.; Behera, S.; Manandhar, S.; Gaddam, S.; Kelber, J. Fundamental Mechanisms of Oxygen Plasma-Induced Damage of Ultralow-k Organosilicate Materials: The Role of Thermal Atomic Oxygen. *J. Appl. Phys.* **2009**, *94* (20), 204102.

(24) Bogan, J.; Lundy, R.; P. McCoy, A.; O'Connor, R.; Byrne, C.; Walsh, L.; Casey, P.; Hughes, G. In-Situ Surface and Interface Study of Atomic Oxygen Modified Carbon Containing Porous Low-κ Dielectric Films for Barrier Layer Applications. *J. Appl. Phys.* **2016**, *120* (10), 105305.

(25) Dai, X. J.; Elms, F. M.; George, G. A. Mechanism for the Plasma Oxidation of

Wool Fiber Surfaces from XPS Studies of Self-Assembled Monolayers. *J. Appl. Polym. Sci.* **2001**, *80* (9), 1461–1469.

(26) Liu, K.; Mu, H.; Shu, M.; Li, Z.; Gao, Y. Improved Adhesion between SnO_2/SiO_2 coating and Polyimide Film and Its Applications to Atomic Oxygen Protection. *Colloids Surfaces A Physicochem. Eng. Asp.* **2017**, *529* (March), 356–362.

(27) Li, X.; Al-Ostaz, A.; Jaradat, M.; Rahmani, F.; Nouranian, S.; Rushing, G.; Manasrah, A.; Alkhateb, H.; Finckenor, M.; Lichtenhan, J. Substantially Enhanced Durability of Polyhedral Oligomeric Silsequioxane-Polyimide Nanocomposites against Atomic Oxygen Erosion. *Eur. Polym. J.* **2017**, *92* (December 2016), 233–249.

(28) Hooshangi, Z.; Hossein Feghhi, S. A.; Saeedzadeh, R. The Effects of Low Earth Orbit Atomic Oxygen on the Properties of Polytetrafluoroethylene. *Acta Astronaut.* **2016**, *119*, 233–240.

(29) Rutledge, S. K.; Banks, B. A.; Forkapa, M.; Stueber, T.; Sechkar, E.; Malinowski, K. Atomic Oxygen Treatment as a Method of Recovering Smoke-Damaged Paintings. *J. Am. Inst. Conserv.* **2000**, *39* (1), 65–74.

(30) Brady-Boyd, A.; O'Connor, R.; Armini, S.; Selvaraju, V.; Hughes, G.; Bogan, J. On the Use of (3-Trimethoxysilylpropyl) Diethylenetriamine Self-Assembled Monolayers as Seed Layers for the Growth of Mn Based Copper Diffusion Barrier Layers. *Appl. Surf. Sci.* **2018**, *427*, 260–266.

(31) Wagner, A. J.; Wolfe, G. M.; Fairbrother, D. H. Atomic Oxygen Reactions with Semifluorinated and n -Alkanethiolate Self-Assembled Monolayers. *J. Chem. Phys.* **2004**, *120* (8), 3799–3810.

(32) Miller, D. J.; Biesinger, M. C.; McIntyre, N. S. Interactions of CO_2 and CO at Fractional Atmosphere Pressures with Iron and Iron Oxide Surfaces: One Possible Mechanism for Surface Contamination? *Surf. Interface Anal.* **2002**,

33 (4), 299–305.

(33) Aureau, D.; Morscheidt, W.; Etcheberry, A.; Vigneron, J.; Ozanam, F.; Allongue, P.; Chazalviel, J. N. Controlled Oxidation of Alkyl Monolayers Grafted onto Flat Si(111) in an Oxygen Plasma of Low Power Density. *J. Phys. Chem. C* **2009**, *113* (32), 14418–14428.

(34) Konstadinidis, K.; Zhang, P.; Opila, R. L.; Allara, D. L. An In-Situ X-Ray Photoelectron Study of the Interaction between Vapor-Deposited Ti Atoms and Functional Groups at the Surfaces of Self-Assembled Monolayers. *Surf. Sci.* **1995**, *338* (1–3), 300–312.

(35) Laibinis, P. E.; Whitesides, G. M. Self-Assembled Monolayers of n-Alkanethiolates on Copper Are Barrier Films That Protect the Metal against Oxidation by Air. *J. Am. Chem. Soc.* **1992**, *114*, 9022–9028.

(36) Torres, J.; Perry, C. C.; Bransfield, S. J.; Fairbrother, D. H. Radical Reactions with Organic Thin Films: Chemical Interaction of Atomic Oxygen with an X-Ray Modified Self-Assembled Monolayer. *J. Phys. Chem. B* **2002**, *106* (24), 6265–6272.

(37) Chen, S. Te; Cheng, Y. S.; Chang, Y. H.; Yang, T. M.; Lee, J. T.; Chen, G. S. Activation of Amino-Based Monolayers for Electroless Metallization of High-Aspect-Ratio through-Silicon Vias by Using a Simple Ultrasonic-Assisted Plating Solution. *Appl. Surf. Sci.* **2018**, *440*, 209–216.

(38) Yuan, H.; Gibson, K. D.; Li, W.; Sibener, S. J. Modification of Alkanethiolate Monolayers by O(^{3}P) Atomic Oxygen: Effect of Chain Length and Surface Temperature. *J. Phys. Chem. B* **2013**, *117* (16), 4381–4389.

(39) Scardamaglia, M.; Susi, T.; Struzzi, C.; Snyders, R.; Di Santo, G.; Petaccia, L.; Bittencourt, C. Spectroscopic Observation of Oxygen Dissociation on Nitrogen-Doped Graphene. *Sci. Rep.* **2017**, *7* (1), 1–11.

(40) Gupta, B.; Kumar, N.; Panda, K.; Kanan, V.; Joshi, S.; Visoly-Fisher, I. Role of Oxygen Functional Groups in Reduced Graphene Oxide for Lubrication. *Sci. Rep.* **2017**, *7*, 1–14.

(41) Yang, Z.; Xu, M.; Liu, Y.; He, F.; Gao, F.; Su, Y.; Wei, H.; Zhang, Y. Nitrogen-Doped, Carbon-Rich, Highly Photoluminescent Carbon Dots from Ammonium Citrate. *Nanoscale* **2014**, *6* (3), 1890–1895.

(42) Liu, S.; Tian, J.; Wang, L.; Zhang, Y.; Qin, X.; Luo, Y.; Asiri, A. M.; Al-Youbi, A. O.; Sun, X. Hydrothermal Treatment of Grass: A Low-Cost, Green Route to Nitrogen-Doped, Carbon-Rich, Photoluminescent Polymer Nanodots as an Effective Fluorescent Sensing Platform for Label-Free Detection of Cu(II) Ions. *Adv. Mater.* **2012**, *24* (15), 2037–2041.

(43) Gorham, J.; Smith, B.; Fairbrother, D. H. Modification of Alkanethiolate Self-Assembled Monolayers by Atomic Hydrogen: Influence of Alkyl Chain Length. *J. Phys. Chem. C* **2007**, *111* (1), 374–382.

Chapter 6

6 Characterisation of Electroless Deposited Cobalt by Hard and Soft X-ray Photoemission Spectroscopy

This chapter investigates electroless deposited (ELD) cobalt films which are currently being used to replace traditional copper interconnects. The ELD films are characterised using HAXPES measurements taken in Diamond Light Source Synchrotron outside Oxford. This facility is capable of making both soft and hard X-rays measurements simultaneously, ensuring that both surface and bulk properties are explored. HAXPES measurements were employed firstly to establish the chemical uniformity of the deposited Co film and secondly to investigate the buried Si-Co interface ~20 nm below the surface.

6.1 Introduction

As scaling continues newer materials are required with the intent to replace copper as the interconnect metal of choice. In the newest 10 nm technology node cobalt has already replaced copper in the first three metal lines[1]. Cobalt is an attractive alternative to copper because although its bulk resistivity is larger than copper, on interconnect length scales its effective resistivity is less. The product of the bulk resistivity ρ_0, and the electron mean free path λ, is used to predict which metal has the highest conductivity (or in other words lowest resistivity) in narrow interconnect lines. The electron mean free path is an important parameter as it characterises the electron scattering in the wire. For cobalt this product has been shown to be in the range of 4.82 - 7.31 x 10^{-16} Ωm^2 depending on the crystal structure, whereas copper is 6.70 x 10^{-16} Ωm^2.[2] By depositing high quality cobalt films of a certain crystal structure, the resistance could very well be decreased. Cobalt's electron mean free path and its ability to form large grains would also limit the number of scattering events which in turn would keep the resistance to a minimum[2]. In traditional copper interconnects as the lines decrease in size, the rise in resistivity is mainly due to scattering events at grain boundaries and interfaces [3–5].

An ELD process is attractive due to the fact it can be used to deposit on metals and insulators, it can achieve very uniform thin films, and it is a relatively low-cost process as described in Chapter 1. ELD cobalt is a strong candidate to fully replace copper as the via prefill or interconnect. Jiang *et al.*[6] and Van der Veen *et al.*[7] have both shown that using cobalt as the via metal, the cobalt can outperform copper with feature sizes below 28 nm and 15 nm, respectively, in terms of lower resistance and electromigration resistance. In this method there is no barrier required for dense low-*k* dielectrics, so the cobalt is free to take up the full area of the via. Mont *et al.* have looked at cobalt as the interconnect metal for the 7 nm technology node by assessing how easily it could be integrated into the fabrication process[8]. ELD CoWB and CoWP have also attracted attention as capping layers, barriers and seed layers[9–15].

The ELD process requires a seed layer or catalyst to activate the surface, in order to deposit high quality metal films on the insulator. For an ELD Co film Pd is usually the metal of choice for a catalyst. The traditional TaN barrier is not a suitable surface for the Pd catalyst as the Pd tends to agglomerate into large islands ranging in size from ~10–100 nm leading to nonconformal thin cobalt layers[9]. To improve the quality of the film the cobalt must be >20 nm but this is not compatible with future interconnect thickness constraints. The Pd nano-islands need to be much smaller <10 nm to facilitate the nucleation and growth of thin cobalt films[16]. In this study the DETA SAM is employed as an adhesion promoter for the Pd seed layer deposition. The Pd adheres to the amino terminal group of the SAM and forms a seed layer (~1 nm) for the ELD Co[11,17]. Malki *et al.* used two different SAMs, APTMS and N-(3trimethoxysilylpropyl) diethylenetriamine or TPDA, to form a gold catalyst layer for ELD of a CoWP film. TPDA differs from APTMS as it has a longer hydrocarbon chain and more amine moieties[18]. Malki observed how the different SAMs affected the surface coverage and size of the Au islands which in turn affected the growth of the CoWP film.

Chen *et al.* describe the formation of a Co silicide following the insertion of an ELD Co-B barrier between a SiO_2 substrate and a Cu film which received thermal annealing[9]. They viewed this silicide formation as a negative effect since it might allow the diffusion of copper into the dielectric. Metal silicides however, are of interest to the semiconductor industry due to their metallic properties, thermal stability, low resistance and process compatibility and are already used in devices[19,20].

In this study the ability of electroless deposition to deposit a metallic Co film is investigated. With HAXPES the effective sampling depth is such that the full 20 nm thick films deposited by colleagues in IMEC can be characterised. This is done in terms of the chemical oxidation state that the cobalt exists in and the presence of chemical impurities resulting from the deposition process.

6.2 Experimental Methods

The sample under investigation was a layered stack, as shown in Figure 6.1(a) and was prepared in IMEC immediately before the HAXPES measurement time at Diamond Light Source. The DETA SAM was deposited using the same process, described in Chapter 3, on a UV-ozone treated native oxide surface. The substrates were then immersed in a $PdCl_2$ acidic solution, with a pH of 2, for 2 minutes and then rinsed for 2 minutes with deionised (DI) water. Co was deposited by ELD to a thickness of 20 nm from a solution of $CoSO_4$, NH_4Cl and water with a dimethyl ammonium borane (DMAB) reducing agent. Following Co deposition, the samples were annealed in a forming gas atmosphere at 420°C for 15 minutes.

HAXPES and XPS measurements were both performed at Diamond Light Source in the UK on the same surface location. Five different positions across the sample were explored, as shown in Figure 6.1(b), to establish the uniformity of the film. These positions were approximately 2 mm apart giving a good spatial variation. Due to the high photon energy employed in HAXPES, buried interfaces up to ~20 nm below the surface are easily accessible compared to ~7-8 nm sampling depth in conventional XPS measurements. At this particular beamline, one can illuminate a precise location on the sample under consideration using both soft and hard X-rays simultaneously.

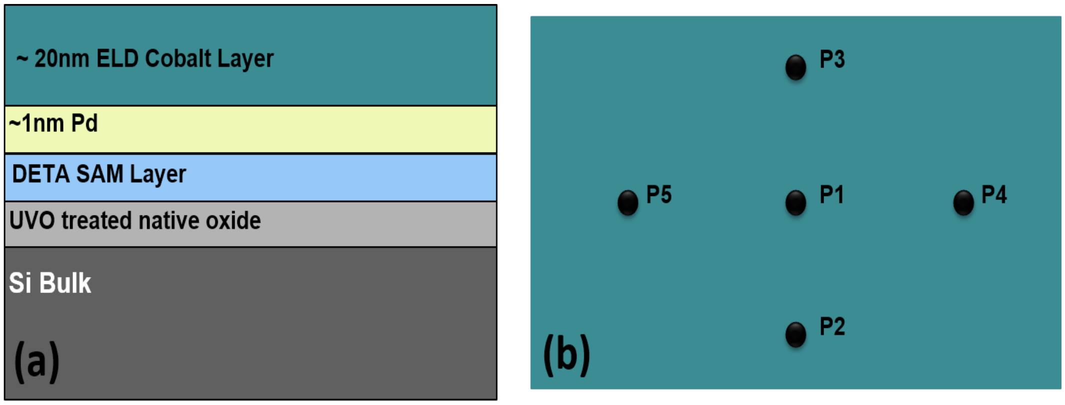

Figure 6.1 (a) Schematic displaying the different layers in the sample stack. In (b) the location of the five positions

This gives the unique advantage of simultaneously recording surface and bulk properties during each experimental step. The soft X-ray incident photon energy was 1,200 eV, which is comparable to X-rays generated from a conventional Mg anode (1253.6 eV). While the hard X-ray incident photon energy was 5,906 eV. A VG Scientia EW4000 HAXPES energy analyser was used to record the spectra. The sample was placed in the ultra-high vacuum chamber at a base pressure of approximately 5 x 10^{-10} mbar. The sample received three anneals, 300°C, 400°C and 500°C in-vacuo and photoemission spectra were acquired after each anneal. The sample was held at temperature for one hour.

Peak fitting analysis was carried out using AAnalyzer software[21]. As synchrotron radiation was used the resolution was better than conventional XPS. In addition to cobalt the following elements were identified in the spectra in both the soft and hard X-rays: silicon, oxygen, carbon, nitrogen, palladium and boron. The HAXPES B 1s, C 1s, N 1s, O 1s and Si 1s spectra were all fitted with Voigt profiles. The Co 2p peak profile was used to distinguish between the metallic and oxide states of the element. All peak fitting parameters are listed in Table 6.1. The parameters for the Si 1s are given and described in detail later in this chapter.

Table 6.1 Peak fitting parameters for B 1s, C 1s, O 1s, and N 1s.

Peak Fitting Parameters					
B 1s	**FWHM (eV)**	**Lorentzian (eV)**	**C 1s**	**FWHM (eV)**	**Lorentzian (eV)**
CoB	0.5	0.15	**C-C**	1.3 - 1.4	0.2
B-C	1.25	0.15	**C-O / C-N-O**	1.5	0.2
BN / B-O	1	0.15	**C=O**	1.3	0.2
B_2O_3	1.5	0.15	**CO_3**	1.1	0.2
O 1s			**N 1s**		
CoO	1.25	0.21	**BN**	1.5	0.21
CO_3	1.45	0.21	**N-O**	1.5	0.21
B-O	1.5	0.21			0.21
B_2O_3	1.6	0.21			0.21

AFM images were acquired using a Veeco Dimension 3100 in tapping mode as described in Chapter 4. The images were analysed by Gwyddion software version

2.39[22] also described in Chapter 4. Scanning electron microscope (SEM) images were acquired using a Hitachi S5500 Field Emission SEM operating at an accelerating voltage of 1 kV to optimise the surface region. For both AFM and SEM images two samples were investigated. The first was an as-received sample from IMEC and the second was a sample which had received a 500°C vacuum anneal inside the XPS chamber in DCU.

6.3 Results & Discussion

6.3.1 Sample Overview

To investigate the homogeneity of the chemical composition of the samples under investigation, five different positions across the surface were scanned with both hard and soft x-rays with a beam spot size of 100 μm. Figure 6.2 shows a HAXPES wide energy scan window acquired at 5.9 keV going from 40 eV up to 170 eV which records both the Co 3s and 3p along with the Si 2s. This 130 eV wide window scan showing the raw intensity demonstrates how homogenous the sample is with spectra for every position measured overlaying perfectly.

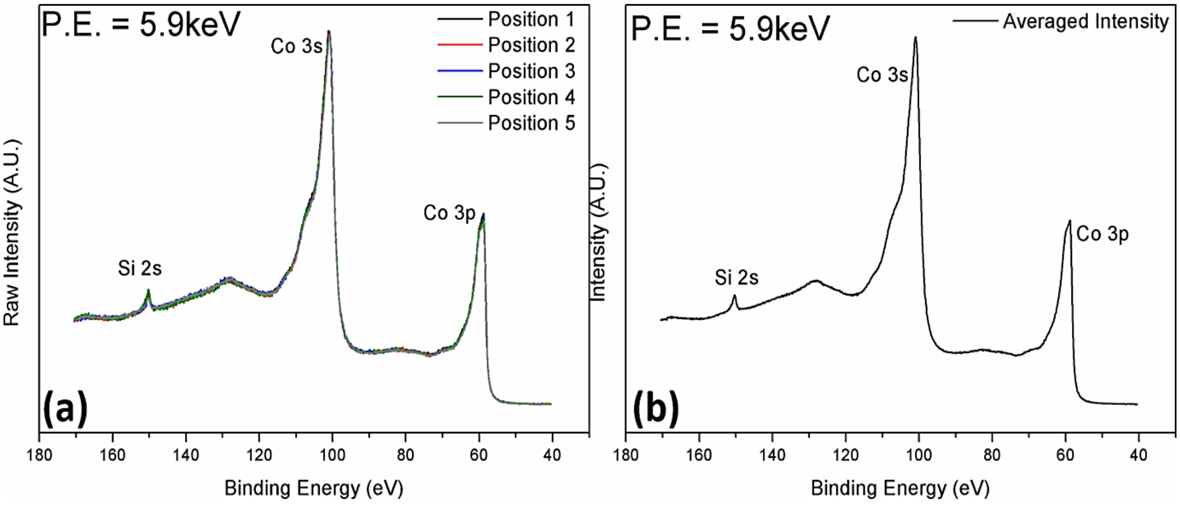

Figure 6.2 (a) Shows the raw intensity of the five positions overlaid on the surface. In (b) the positions have been averaged.

It also gives great confidence in the reproducibility of the measurement across the sample. This reproducibility is observed for nearly all the elemental peaks at each experimental step recorded at both photon energies. Therefore, these peaks were averaged. There are only two exceptions the Si 1s recorded with hard X-rays and the Co 2p recorded with soft X-rays which will be discussed later in this chapter.

From survey spectra taken in both the soft (Figure 6.3) and hard X-ray (Figure 6.4) regimes it is possible to identify the elements present within the different sampling depths of the two photon energies used and deduce from this information, the physical location of the different elements perpendicular to the surface. From the cobalt ELD deposition, nitrogen, carbon and boron have become incorporated into the film with the carbon and nitrogen concentrations decreasing with thermal annealing. This is observed in both soft and hard X-ray spectra. In initial scans of the as-received sample there is no Pd detected at either energy since the Pd does not form a continuous film but instead forms nano-islands across the surface. However, with thermal annealing from 400°C and 500°C a Pd signal is detected and is assumed to originate from the diffusion of the Pd towards the surface of the Co film. As the Pd starts to diffuse it becomes more evenly distributed throughout the Co film and is thus, more easily observed. The intensity of the Pd 3d peak is very small compared to the other peaks and is just about evident in the survey scan following the 400°C anneal.

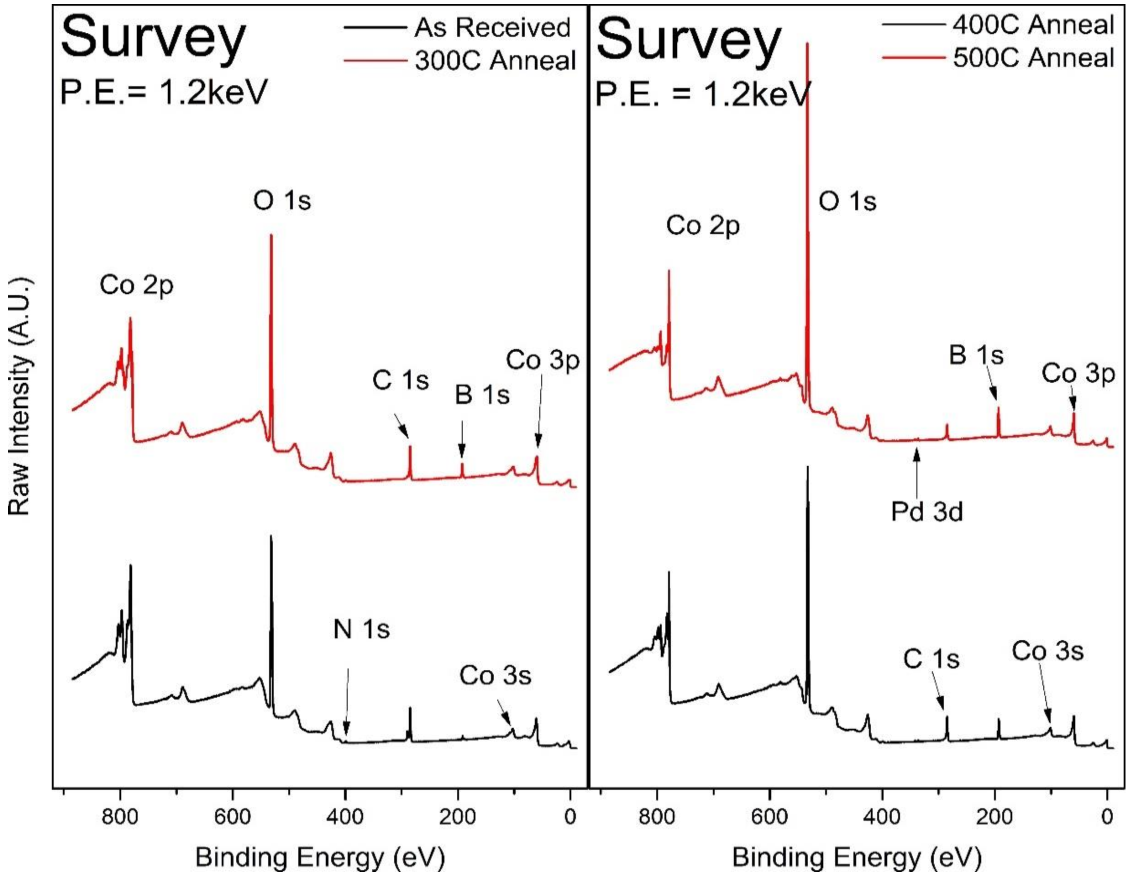

Figure 6.3 Soft X-ray survey scans of the ELD cobalt film which show a very strong o 1s peak.

Soft X-ray survey spectra are dominated by the O 1s which would suggest that the sample surface is oxidised. The oxygen signal is seen to increase with each anneal as does the B 1s. It is difficult to ascertain what changes occur in the cobalt peaks from the survey spectra. The absence of the Si 2s peak (~150 eV) confirms that this film is > 8 nm thick. In the HAXPES survey scans the Co 2p and Co 2s are the dominant features. One important point to note is that the Si 1s, at a binding energy of ~1839 eV, is visible in the HAXPES scans in Figure 6.4, this indicates that the entirety of the Co film (~20 nm) is accessible as the only source of Si is the underlying substrate. In both the soft and hard X-ray scans the presence of N 1s and C 1s peaks are observed. The intensity of the Co 2p peak in the HAXPES survey scans make it difficult to see the smaller peaks like the N 1s and C 1s however, they can readily be observed using narrow energy scans.

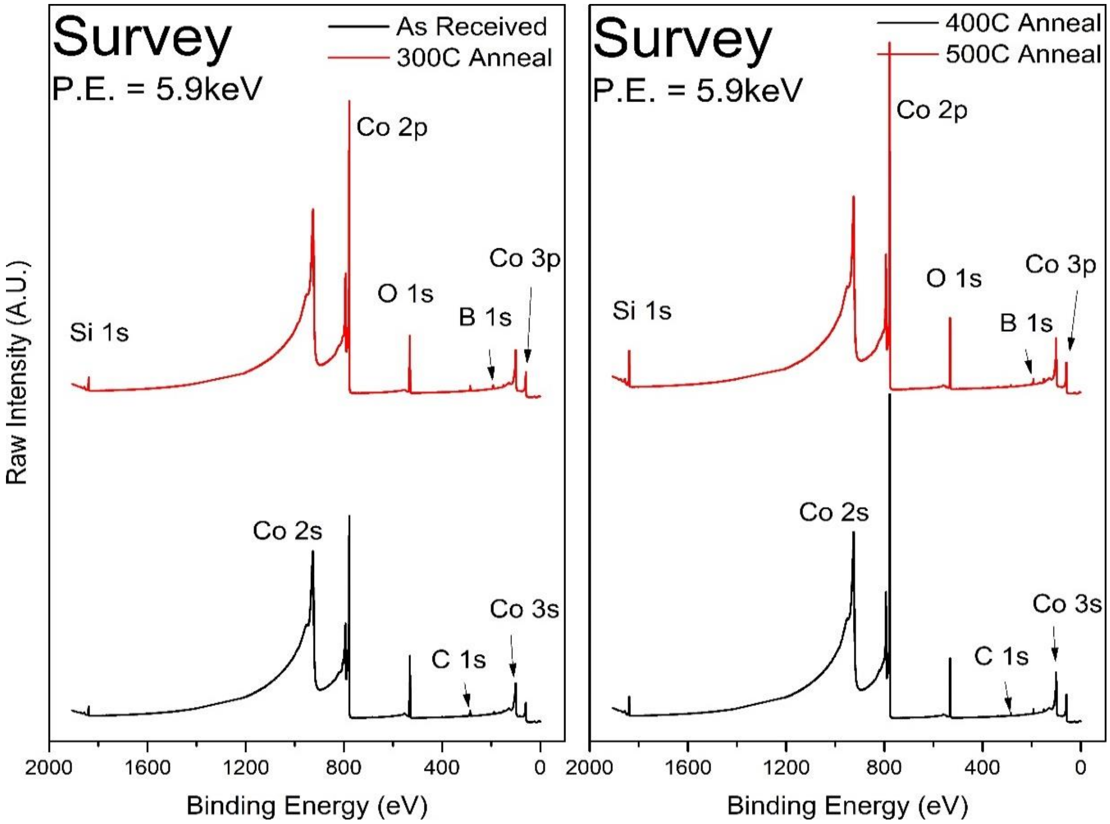

Figure 6.4 HAXPES survey scans of the ELD cobalt film shows the Co 2p peak dominating the spectra.

6.3.2 Characterisation of the ELD Co Film

The cobalt films appear to be mostly metallic in nature as seen from the high energy scans, with only a small oxide peak which decreases upon anneal, as shown in Figure 6.5(a). The main component peak has a binding energy position of 778.1 eV which is in the correct position for Co metal[23,24] with the oxide component coming in at a binding energy of 781.1 eV which is consistent with cobalt oxide species[24–26]. As the oxide peak on the higher binding energy side of the metallic component peak is not very pronounced, it suggests that the oxide is surface localised. After the 300°C anneal the oxide signal decreases while the metallic signal increases. This trend is seen for the following two anneals until it is almost completely removed by the 500°C anneal, which is more easily seen in Figure 6.5 (b).

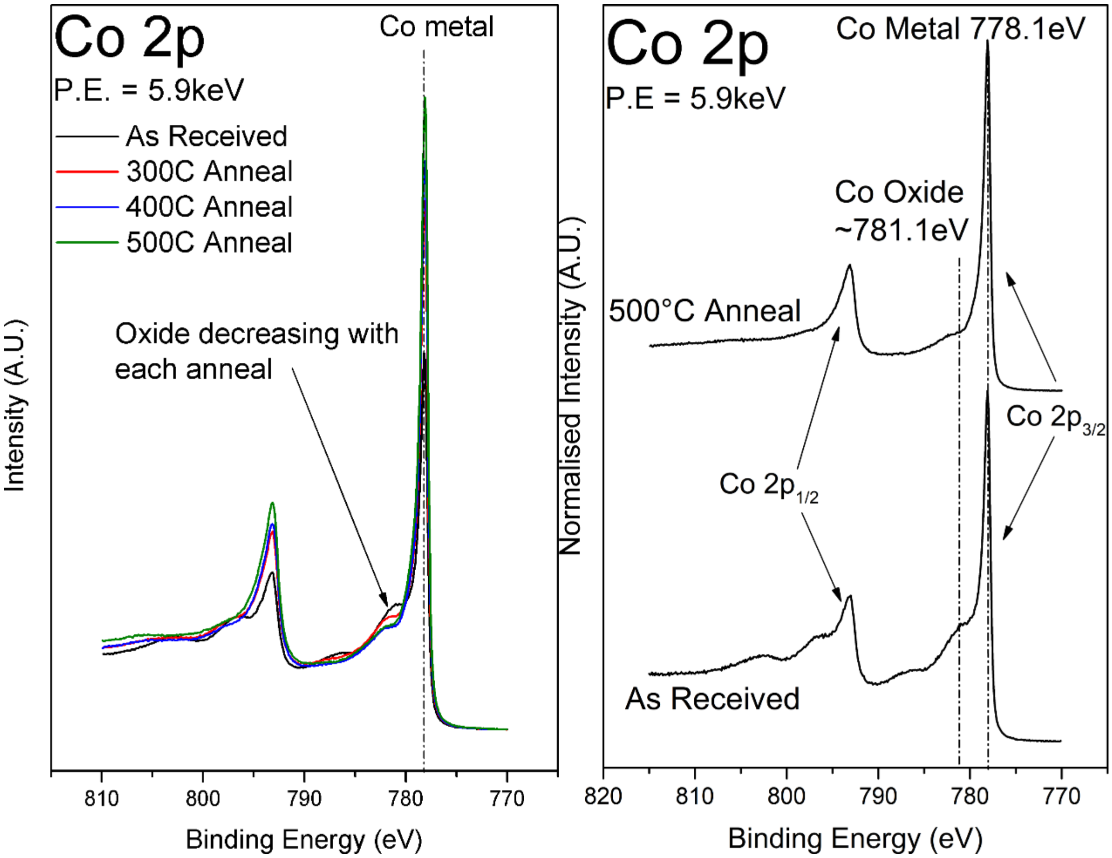

Figure 6.5 High energy Co 2p (a) All experimental steps are overlaid to demonstrate the decomposition of the oxide component and the increase in intensity of the metal component (b) The difference between the first and last steps with binding energy positions.

It can therefore be deduced that the ELD process was successful in depositing a mostly metallic cobalt film. To confirm that the cobalt oxide is surface localised, the soft X-ray scan of the Co 2p were analysed. Upon loading, the Co 2p peak appears to be homogenous at each position. Concentrating on position 5 in Figure 6.6, upon loading, the sample appears completely oxidised at a binding energy of 781.1 eV, which is the same as for the hard X-ray spectra. With the first anneal at 300°C a metallic shoulder starts to emerge at 778.1 eV on the lower binding energy side of the oxide peak. This again is consistent with the high energy spectra. With each subsequent anneal the cobalt becomes more metallic as the oxide is decomposed. The metal component peak grows until the oxide peak is almost completely removed.

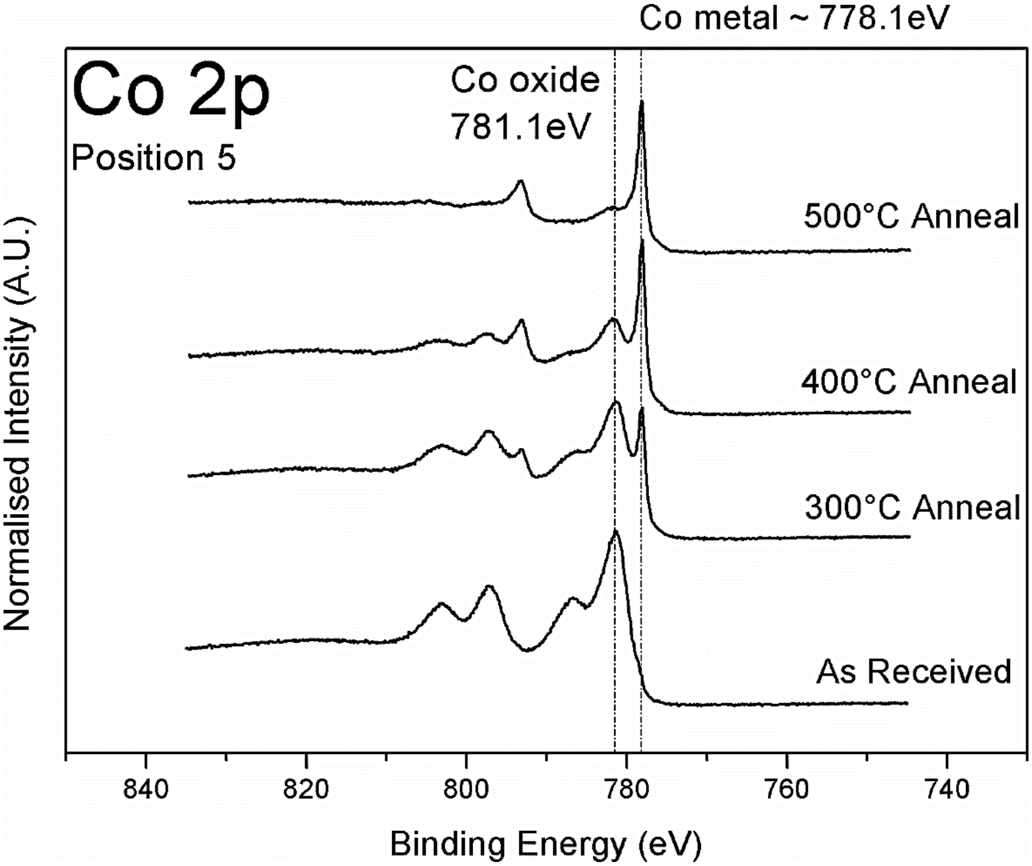

Figure 6.6 Co 2p spectra taken from position 5 on the sample showing the surface is almost completely oxidised until annealing leads to oxide decomposition and the increase in the metallic Co signal.

The sample appears to be the same at each position upon loading but after annealing there are variations across the sample where the oxide is seen to decrease but does so differently at each position. This can be seen in Figure 6.7(a) where each position is overlaid as-received and in Figure 6.7(b) following the 500°C anneal. The apparent difference between positions has been attributed to temperature variations across the sample during annealing. The sample plate that the sample was mounted to, had a circular section removed for radiative heating.

This meant that certain parts of the sample were in the line of sight of the heating filament while others were not. It is thought that the heating was not completely uniform across the sample as a result of this, hence the slight difference in oxide thickness following the anneals.

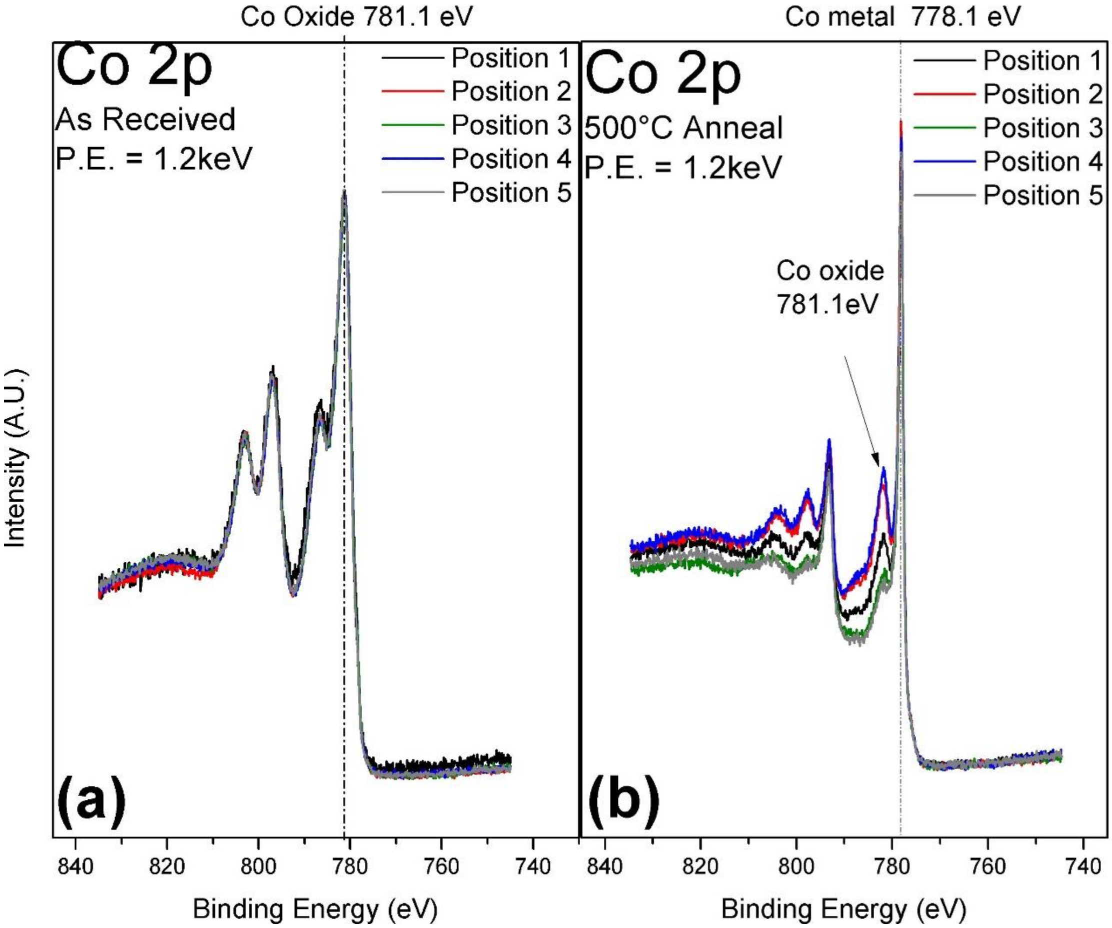

Figure 6.7 Soft X-ray scans of the Co 2p taken at each position showing the variation in the decomposition of the oxide.

The ability to convert this thick surface oxide, which is approximately equal to the sampling depth of this photon energy (~6-7 nm), to a metal is of great importance because there now exists a ~20 nm thick metallic Co film which aids electron transport in the line.

From the initial scans there was no evidence of the palladium catalyst in either the hard or soft X-ray spectra in any of the 5 positions measured. It is only following the 400°C anneal that the Pd can be seen to emerge with the signal increasing further after the 500°C anneal. Figure 6.8 illustrates the Pd 2p peak profile acquired at a photon energy of 5.9 keV. Hedman *et al.* previously reported a binding energy position for the metallic Pd 2p using laboratory based XPS containing a Cr anode which has a photon energy of 5417 eV [27]. The peak in the current study appears to be in a metallic state with the $2p_{3/2}$ at binding energy of 3174.3 eV, the $2p_{1/2}$ at a binding energy of 3331.3 eV and a possible oxide shoulder on the higher binding energy side of both peaks. This was determined by analysis of the Pd 3d which has a binding energy of 335.4 eV and is consistent with literature values for a metallic Pd sample[28–30].

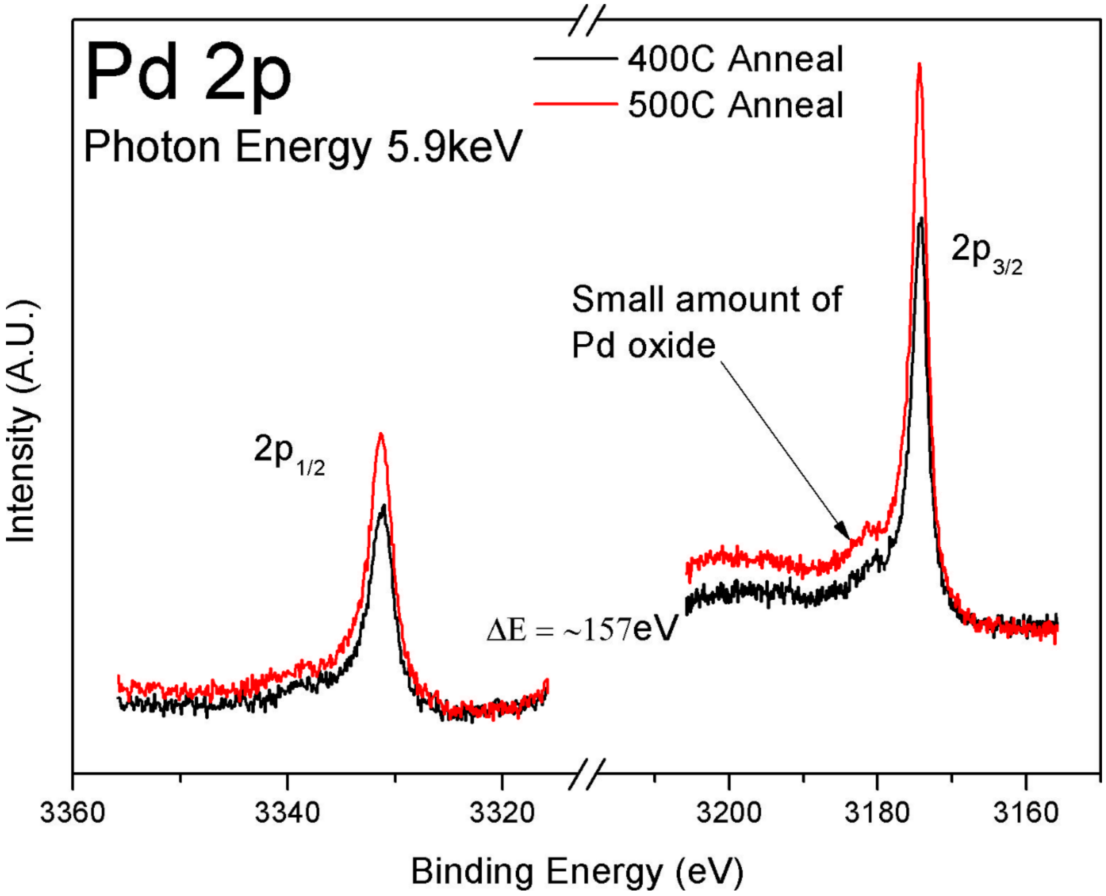

Figure 6.8 Pd 2p spectrum showing a metallic profile with the presence of a small oxide signal.

As the Pd is known to form small nanoclusters or islands on the SAMs and is thought to have a surface coverage of ~10 %, it is difficult to detect in the initial scans, even with HAXPES measurements[16,31]. It is only after annealing, that the Pd can diffuse through the Co hence becoming more uniformly distributed throughout the film, that it becomes detectable.

To ascertain if there was any evidence of the DETA SAM the high energy spectra of the C 1s and N 1s were examined. Looking at the C 1s spectra displayed in Figure 6.9, initially there are two main peaks with several component peaks visible in the spectra. A peak at lower binding energy which is attributed to C-C bonds and adventitious carbon from atmospheric exposure, and a peak at higher binding energy which has been attributed to a cobalt carbonate. The N 1s spectra displayed in Figure 6.10 have just one broad peak which can be deconvoluted into two component peaks.

The deconvoluted spectra in Figure 6.9 show the evolution of the C 1s over the course of the experiment. The as-received sample shows evidence of four component peaks: C-C, C-O / C-N-O, C=O bonds and CO_3 at 284.8 eV, ~286 eV, ~288.4 eV and 289.8 eV respectively. The peak at 289.8 eV is in the correct position for a carbonate species which are commonly formed in the ELD process[32,33] and is consistent with the literature for a cobalt carbonate[34,35]. The subsequent 300°C anneal sees a dramatic decrease in the carbonate peak to around one quarter of its original intensity. The intensity of the main peak is also decreased. A small peak at a binding energy of ~283.4 eV is also seen after the 300°C anneal which could be the formation of a cobalt carbide. However, this peak disappears following the 400°C anneal. The intensity of all component peaks continues to decrease for the subsequent 400°C and 500°C anneals. At this point the carbonate has been removed and the C-C peak is at approximately half of its original intensity. From these spectra it appears as though the peak at 284.8 eV is not just adventitious carbon but is carbon that has been incorporated into the film during the ELD process.

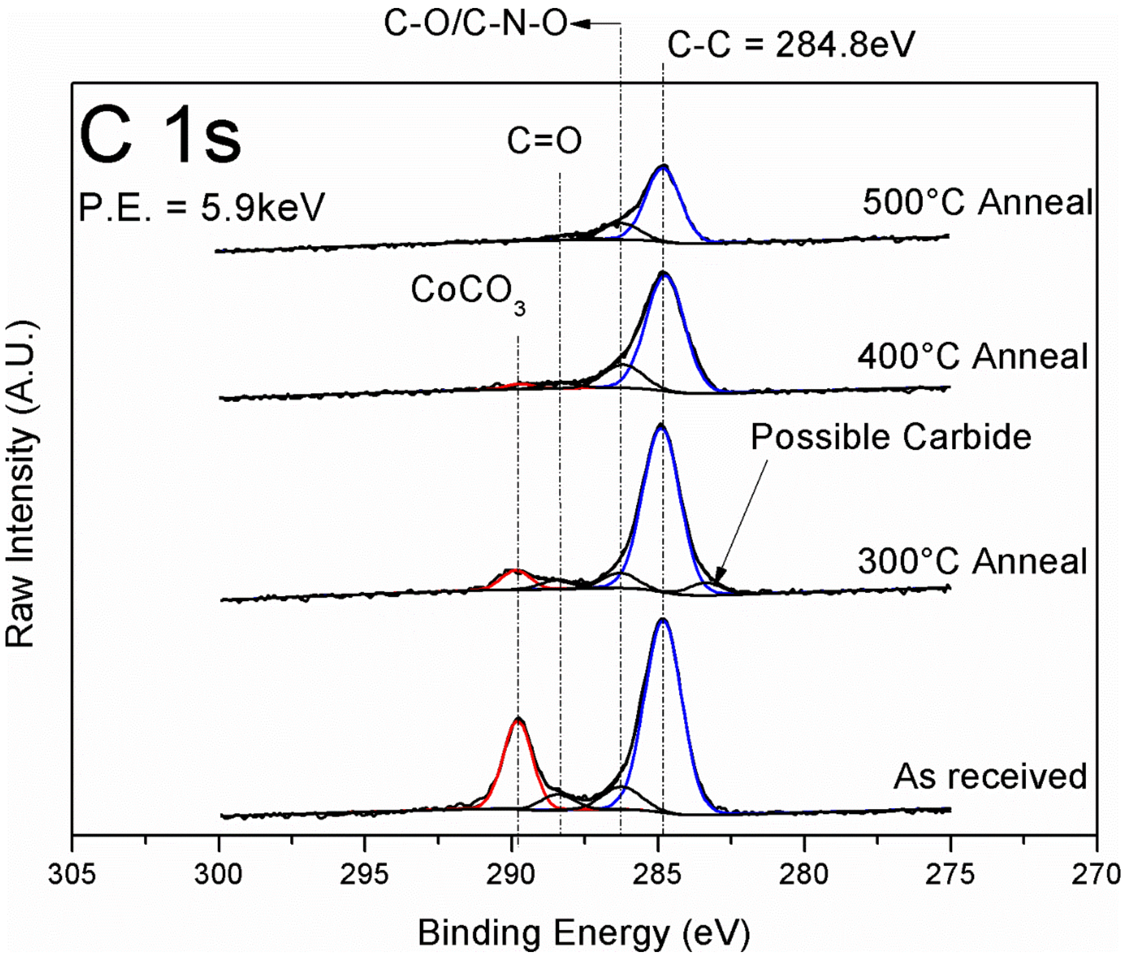

Figure 6.9 High energy C 1s spectrum showing a decomposition of all component peaks with increasing anneal temperature.

Examination of the N 1s HAXPES spectra in Figure 6.10 reveals a broad peak that consists of two component peaks. One is attributed to N-C-O bonds at 399.35 eV and the other is attributed to boron nitride (BN) at 398.1 eV[36–38]. The source of boron comes from the reducing agents used during the electroless deposition and will be discussed later in this chapter. The signal to noise ratio is poorer for the nitrogen than the other spectra due to the small quantity of nitrogen in the film. Just like the carbon, the nitrogen appears to have been introduced during the ELD process from the solution and so is uniformly distributed throughout the film. Subsequent annealing steps lead to a reduction in the intensity of these peaks, however both components remain throughout the annealing cycle.

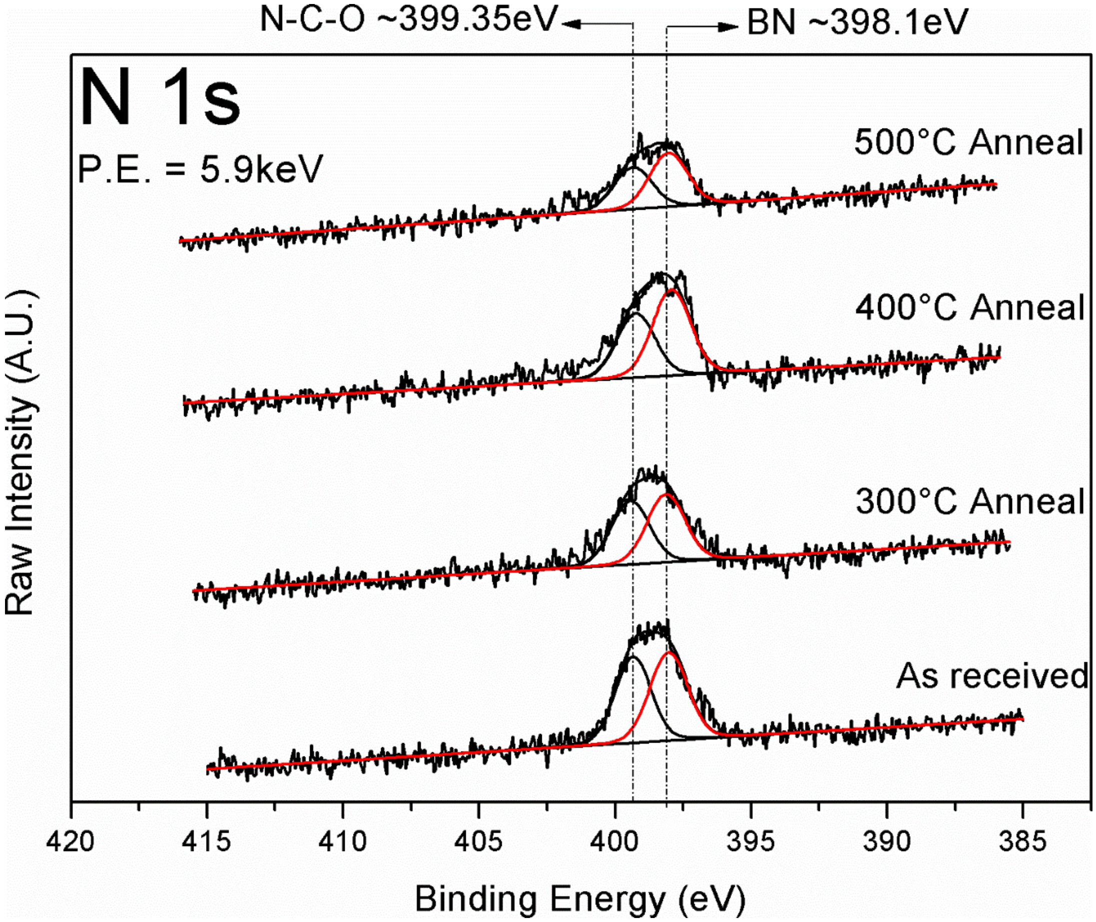

Figure 6.10 N 1s spectra shows bad signal to noise ratio but peak fitting shows two component peaks are present.

Due to the fact that carbon has been introduced into the film, from the deposition process and from atmospheric exposure, it is not possible to unambiguously distinguish the carbon signal originating from the DETA SAM. Likewise with the nitrogen, although the DETA should be the only source of nitrogen in the sample. However, it is clear that some nitrogen has been integrated into the film via the ELD process, hence it is not possible to distinguish the DETA SAM.

The soft X-ray scans of both the C 1s and N 1s core levels, in Figure 6.11(a) and (b) respectively, appear to mirror the hard X-ray scans. The initial C 1s shows the main C-C peak has a higher intensity due to it being more surface localised and being more sensitive to the adventitious carbon. However, following anneal these components decrease in intensity until the carbonate is removed and the C-C is at half its original height. The N 1s again appears to have two component peaks, both of which decrease in intensity upon thermal anneal. The presence of the Co LMM Auger peak appears to broaden the nitrogen peak making it more difficult to deconvolute the spectrum.

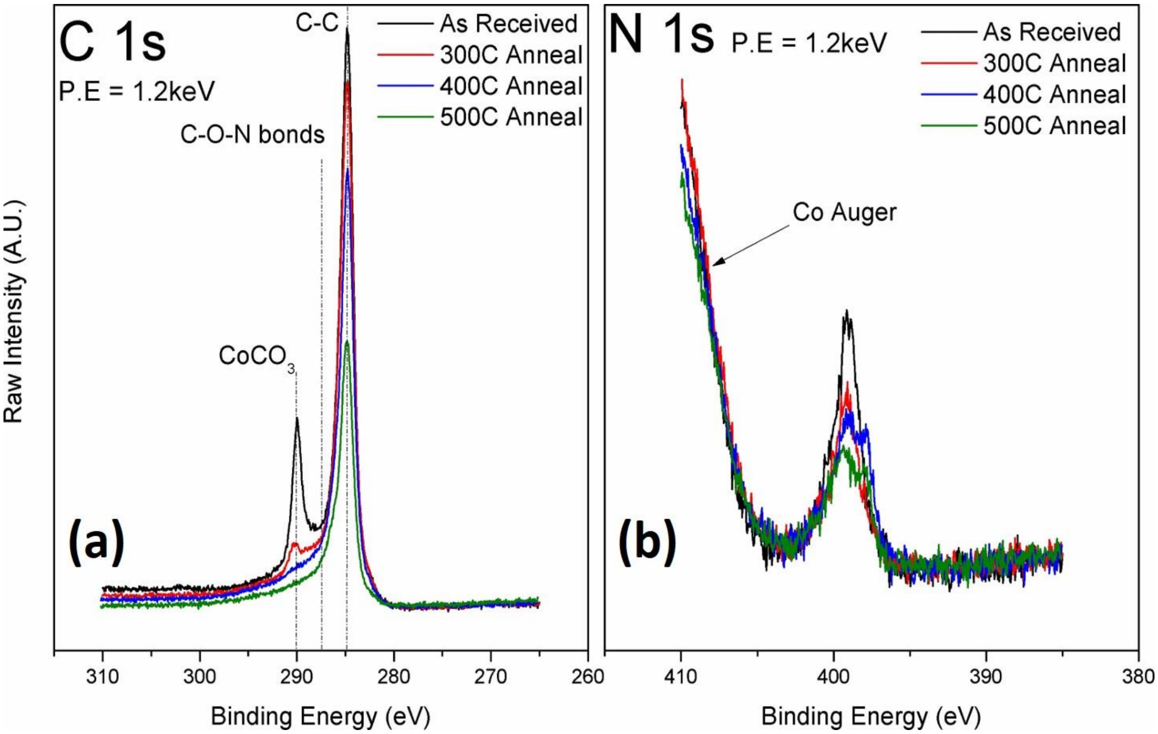

Figure 6.11 Soft X-ray scans of the (a) C 1s and (b) N 1s.

Figure 6.12 illustrates the high energy O 1s spectra along with the B 1s spectra. Two interesting things to note in these spectra are (i) the oxygen signal is not decreasing even though the cobalt oxide and carbonate are seen to decompose and (ii) it appears that boron from the reducing agent has become incorporated into the cobalt film.

Peak fitting analysis of the as-received O 1s scan reveals three component peaks are present, the first is cobalt oxide at a binding energy of 529.9 eV[23–25], the second is the carbonate at 531.4 eV[34,35,39] and finally B-O bonds at 532.3 eV[37]. After the 300°C anneal there is a decrease in the carbonate and a sharp reduction in the cobalt oxide. The B-O component peak grows significantly and also shifts to a higher binding energy. Following the 400°C anneal the cobalt oxide component has mostly decomposed and is no longer visible in the O 1s peak profile. By the 500°C anneal the oxygen has almost fully converted to a B_2O_3 with just a small amount of C-O bonds. With each anneal the peak shifts to a higher binding energy until it is at a binding energy of 532.9 eV which is in the correct position for B_2O_3 [37,40].

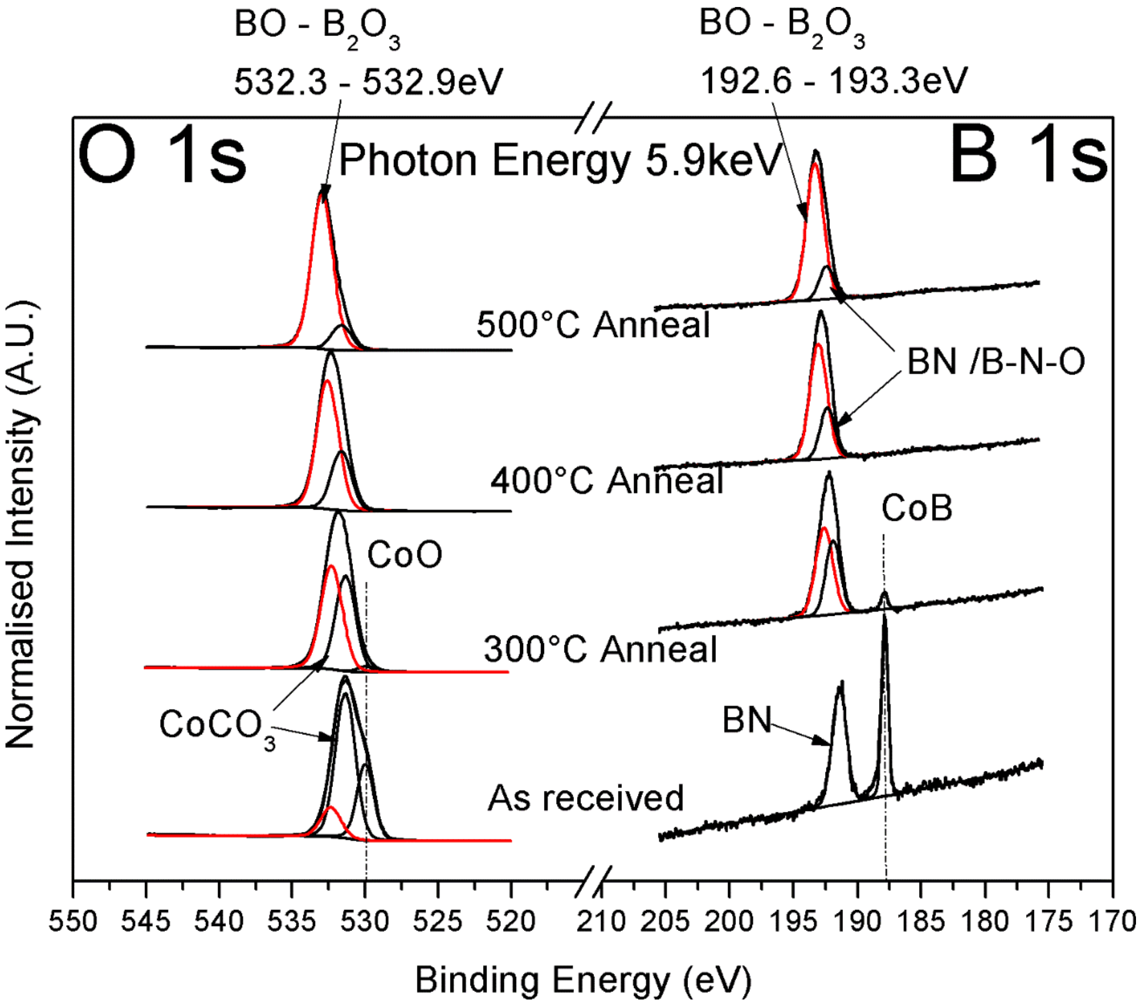

Figure 6.12 High energy peak fitted O 1s and B 1s spectra for the as-received sample and as a function of thermal anneal.

In the initial B 1s spectra there are three component peaks which have been attributed to cobalt boride (CoB) at 187.8 eV[41], B–C bonds at 188.4 eV[37] and BN / B-O bonds at 191.4 eV[36–38]. At first the boron bonds to the cobalt to form a cobalt boride and to any available nitrogen to form boron nitride. There is also evidence for B-C bonds. Following the 300°C anneal some oxygen is released from the cobalt oxide and the carbonate and proceeds to oxidise the boron. The boride decreases significantly, and a new oxide peak begins to emerge at a binding energy of 192.6 eV. With the 400°C anneal this CoB peak has decomposed, the boron is becoming increasingly oxidised and is shifting to a higher binding energy. After the 500°C anneal the peak has again shifted to a higher binding energy of 193.3 eV and is in the correct position for B_2O_3 [42–45].

Boron chemically reacts very readily with oxygen, so it appears that as the oxygen is being released from the cobalt oxide and the carbonate, it does not desorb from the film but bonds to the boron instead. The shift in binding energy position is seen in both the boron and the oxygen spectra and has also been noted in previous studies[40,43]. Due to oxygen's higher electronegativity, the boron transfers charge to the oxygen resulting in a chemical shift to higher binding energy.

Soft X-ray spectra of the O 1s and B 1s peaks in Figure 6.13(a) and (b) respectively, show very similar trends to the hard X-ray spectra. The O 1s shows evidence of a CoO, a carbonate and some B-O bonds when first loaded. With each anneal the oxide and carbonate decompose and the B-O component peak grows. There is also an increase in intensity of the oxygen signal and a shift to higher binding energy with each anneal. This is due to the diffusion of the boron oxide to the surface of the Co film. By the 500°C anneal the O 1s has converted to B_2O_3 just like in the hard X-ray spectra. In the B 1s initially there is the cobalt boride and boron nitride. The intensity of the boride is considerably smaller in the soft X-ray scans due to the surface sensitivity of the measurement. After the 300°C anneal the boride has decomposed and the nitride is starting to oxidise and shift to higher binding energy. After the 500°C anneal the main component is B_2O_3 with some BN /B-N-O bonds still visible on the lower binding energy side of the peak. As both signals are seen to increase it is surmised that the B_2O_3 is diffusing to the top interface.

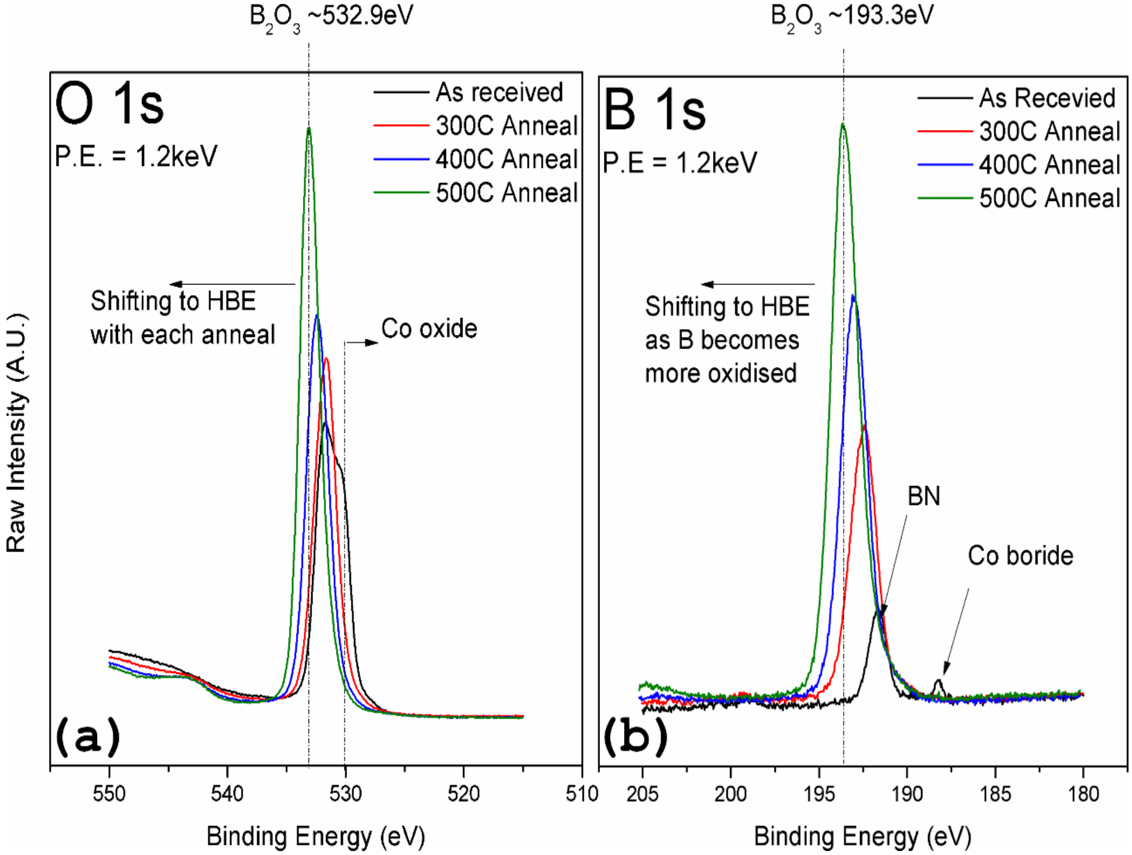

Figure 6.13 Soft X-ray scans of (a) O 1s and (b) B 1s spectra for the as-received sample and as a function of thermal anneal. (HBE: Higher binding energy)

The AFM images displayed in Figure 6.14, show that the morphology of the samples changed very little before and after the vacuum thermal annealing. The similarity of both samples demonstrates that the electroless deposition process is very conformal and uniform. There is no observable change in the R_{rms} which was found to be 1.1 nm in both the as-received sample and the annealed sample. The grain size of the film also remains constant with an average grain diameter of 38.3 nm for the as-received sample and an average grain diameter of 38.2 nm for the sample annealed at 500°C. Likewise, SEM images (Figure 6.15) of the same samples reveal little change in the surface morphology before and after anneal.

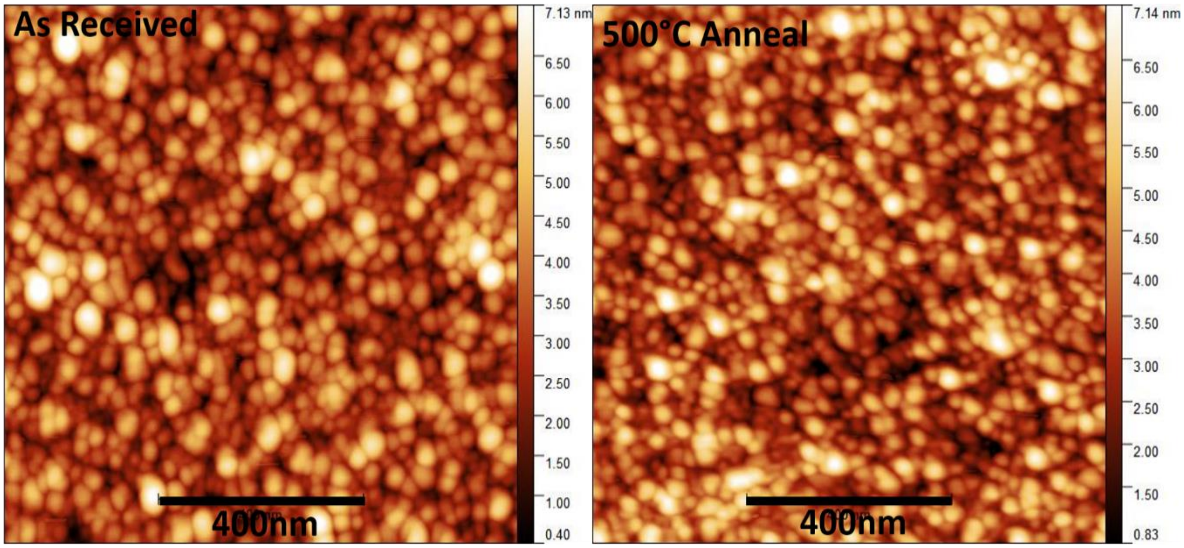

Figure 6.14 AFM images taken before and after thermal annealing show very little change in the surface morphology of the ELD Co films.

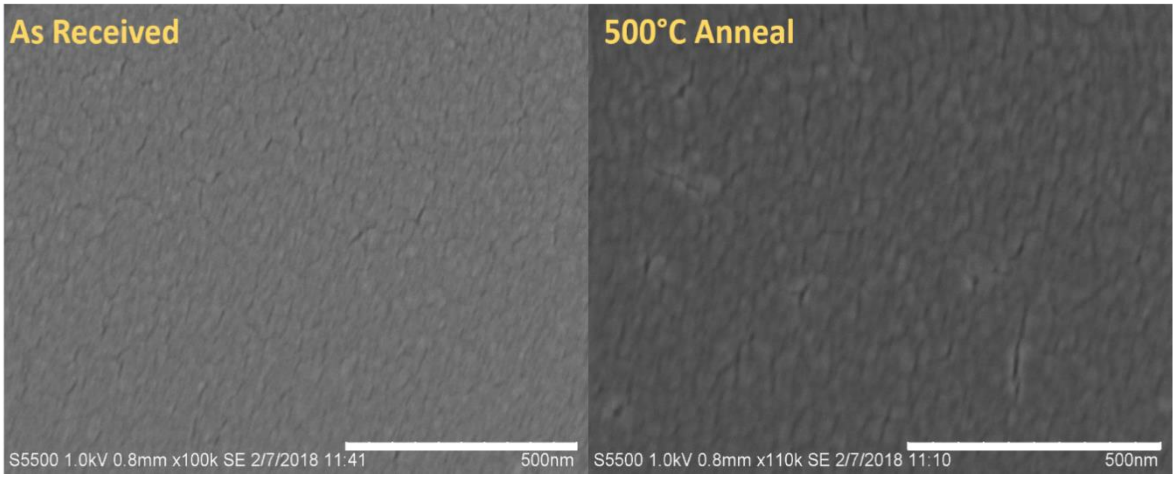

Figure 6.15 SEM images also show little to no change in surface morphology between the two samples.

6.3.3 The Si-Co Interface

The interaction of a deposited thin film of Co with the underlying Si is very difficult to investigate with conventional XPS, given that the Co 3s and the Si 2p peaks overlap. With films thicker than the sampling depth of XPS the Si-Co interface is inaccessible to this measurement method. HAXPES measurements have been used here to access this interface by observing the Si 1s. From Figure 6.2 it is seen that the Si 2s is not a viable option as its intensity is quite small.

Initial observations of the Si 1s at each position show significant variation across the sample as illustrated in Figure 6.16 (a). It can clearly be seen that the interface has been dramatically altered during the ELD process with every position looking considerably different. The SiO_2 appears to have decomposed to form the sub oxide states.

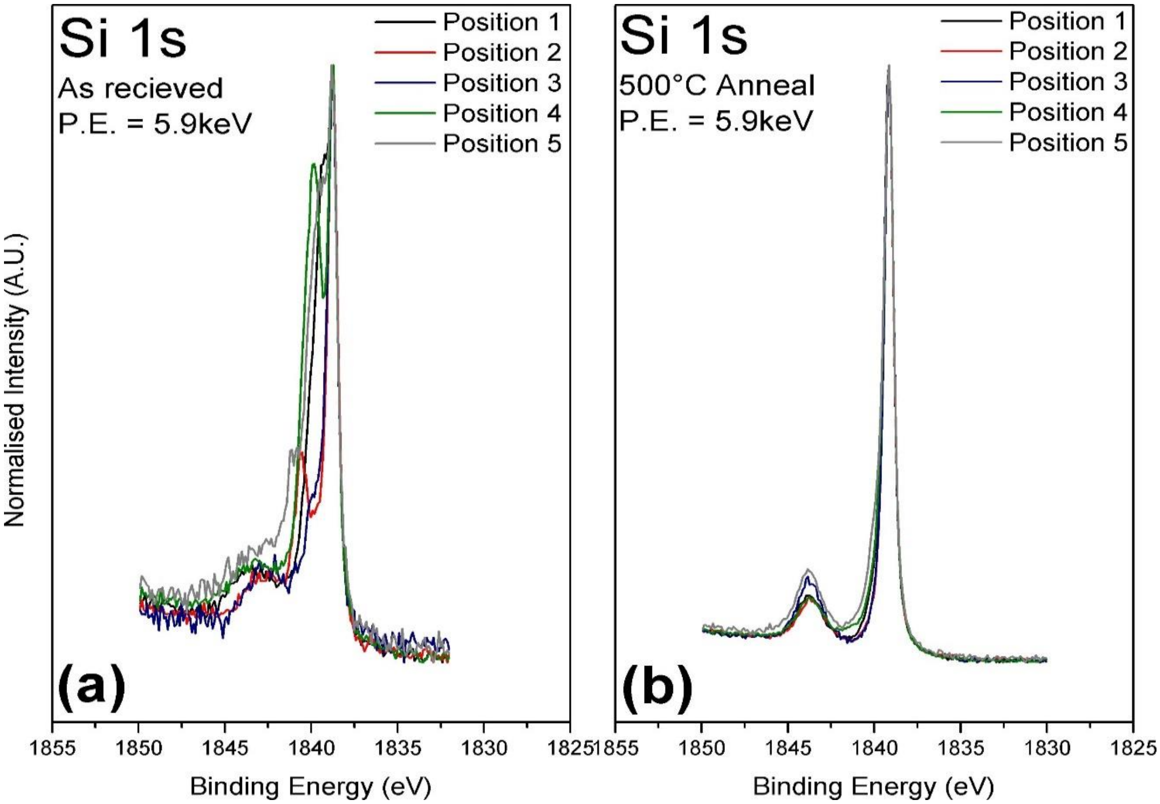

Figure 6.16 (a) The Si 1s spectrum showing the variation of the interface across the sample after electroless deposition, (b) following the 500°C anneal the Si appears much more uniform across the film.

It also looks as if there is more than one peak around the same binding energy as the Si bulk which would indicate the presence of cobalt silicide. As each position looks so different initially, the positions have not been averaged. A detailed analysis of position 1 will be presented. However, the overall trends are the same for each position and following the 500°C anneal all positions are very similar in profile as seen in Figure 6.16 (b).

The fitted spectrum of position 1 as-received is shown in Figure 6.17. There are nine peaks visible and a consistent approach was taken to fit the spectrum. The bulk silicon with a binding energy position of 1839.1 eV was found to agree very well with the literature[46–48]. On either side of the bulk peak there is the presence of two other peaks which have been assigned to cobalt silicide phases. These two silicide peaks have the same Gaussian value (0.55 eV) as the Si bulk and both peaks are situated ~0.4 eV from the bulk.

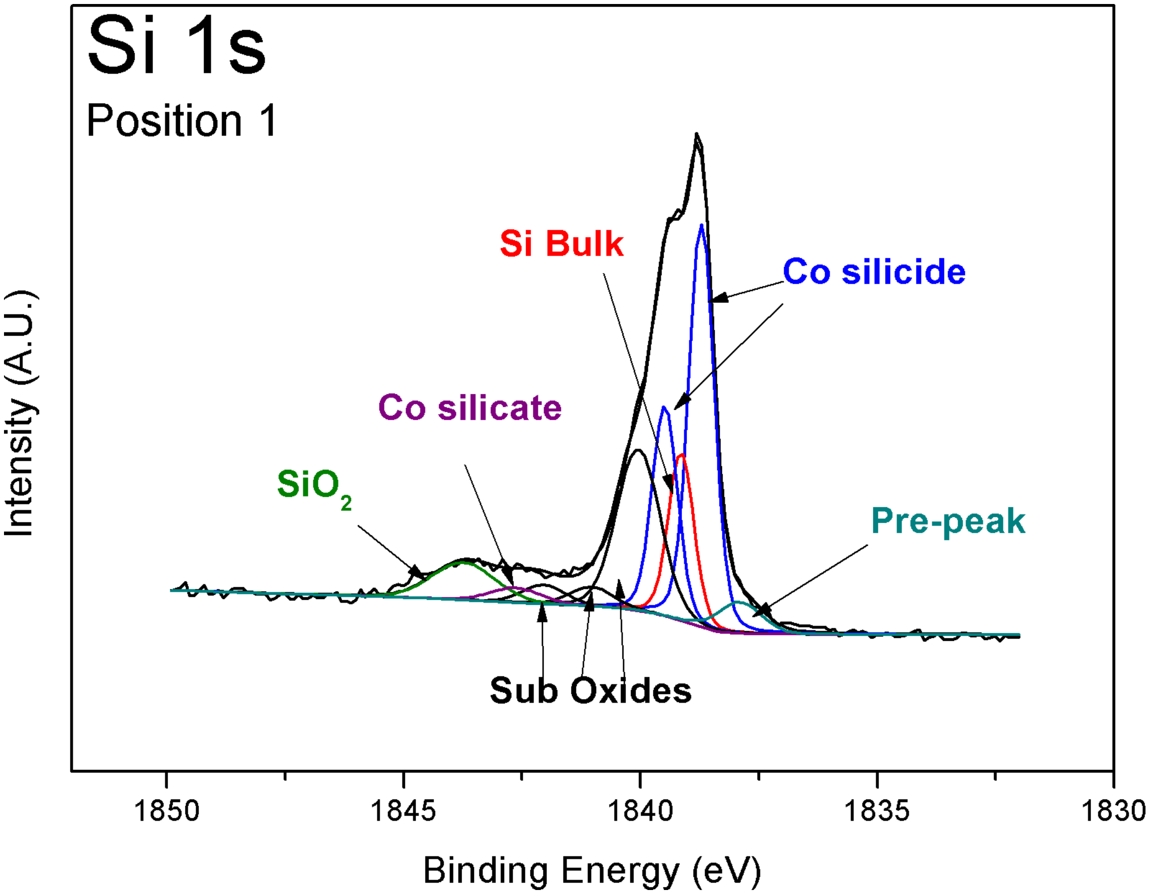

Figure 6.17 Fitted Si 1s spectra as-received showing all possible peak assignments.

Assigning the correct stoichiometry to these peaks is difficult as although cobalt silicides are well studied this is the first instance in which the Si 1s has been analysed for the presence of cobalt silicide. Previous studies of the Si 2p will be used as references to facilitate correct assignment of these silicide phases. Also, the Co 2p will be of little assistance as the metal signal is so strong it will saturate out other smaller components. Figure 6.5 illustrates how even the surface oxide which is ~5-8 nm thick is quite a small feature in the spectrum.

It is suggested that there are at least two stable silicide phases present, CoSi on the higher binding energy side at 1839.5 eV and what could be either $CoSi_2$ or Co_2Si on the lower binding energy side at 1838.7 eV. There are very conflicting reports in the literature as to the location of these silicide peaks. Gomoyunova *et al.* have consistently stated in several papers, that the CoSi phase appears at a higher binding energy than either the Si bulk or the other silicide phases with respect to the Si 2p[49,50]. Hwang *et al.* have reported on the growth of a CoSi phase following anneal of an ultra-thin cobalt film on a silicon substrate. This phase is at a binding energy ~0.4 eV higher than the bulk peak in the Si 2p which is consistent with the findings presented here for the Si 1s [51]. Pan *et al.* have also used electronic structure calculations to state that the expected shift in the Si 1s due to CoSi would be ~0.36 eV which again is consistent with the findings here[52].

The silicide on the lower binding energy side is harder to establish. $CoSi_2$ and Co_2Si are both considered to be at a lower binding energy to CoSi[49]. $CoSi_2$ has a lattice structure very similar to Si with only a 1.1 % mismatch[52–54]. Again, using electronic structure calculations from Pan *et al.* there should be no observable shift in binding energy from the Si bulk position for $CoSi_2$ [52]. However, some groups have found $CoSi_2$ to have a lower binding energy than the bulk silicon[51]. While others have found it to have a higher binding energy than the bulk silicon[55]. Co_2Si has been reported to have a lower binding energy[49,56,57]. The cobalt rich Co_2Si is thought to form first and only be stable up to ~400°C[58,59] but could exist in both a high temperature and low temperature form[60]. It is also known to exist with the CoSi state[58,61]. It is suggested that in this case it is the cobalt rich Co_2Si phase that is present as it has formed upon deposition and it is seen to decompose at higher temperatures whereas $CoSi_2$ is stable up to much higher temperatures.

In the Si 2p the binding energy of the SiO_2 peak is known to depend on the oxide thickness. Eickhoff *et al.* have shown that in the Si 1s, the difference between the Si bulk and SiO_2 is a 0.62 eV higher energy shift than in the Si 2p[47]. Therefore, the peak at 1843.7 eV which is +4.6 eV from the Si bulk peak has been assigned to SiO_2. The sub oxide states of silicon Si^{1+}, Si^{2+} and Si^{3+} are also included. Caspers *et al.* investigated the Si 1s peak at a Europium oxide (EuO)-Si interface where the silicon has been passivated with Eu[62]. Here the growth of sub oxide states is observed. Although the binding energy positions for these sub oxides is not explicitly stated it can be deduced from the graphs that they are in agreement with the sub oxide positions present here. Also based on Eickhoff's analysis the sub oxide states should be in a very similar position as in the Si 2p[47].

Since the electroless deposition process has “churned up” the silicon interface, it seems reasonable to assume that the cobalt has not only bonded with the silicon but with oxygen being released from the reducing agents to form a silicate. Therefore, a peak at 1842.7 eV has been attributed to the formation of a cobalt silicate. The formation of a cobalt silicate is thermodynamically possible but usually requires a lot of heat(> 1000°C)[63–65]. The proximity of this peak to the SiO_2 peak also puts it in the correct energy range for a silicate.

The origin of the final peak on the lower binding energy side of the Si bulk at ~1838 eV is unknown but one paper in the literature has been found where it has been attributed to a “pre-peak”. This pre-peak was observed by Badia-Romano *et al.* in a HAXPES spectra of an iron silicide where the peak was observed in both the Si 1s and the Fe 1s. It is believed that this peak is due to iron suboxides at the sample surface due to defects[46]. As the binding energy of the Co 1s is ~7709 eV it was not possible to observe this peak.

Figure 6.18 displays the deconvoluted Si 1s at each experimental step. It is clear from the as received spectra that the Si interface has come into contact with the ELD Co solution. The Pd layer cannot function as a protective barrier for the Si as it is not a continuous layer. Likewise, the SAM layer did not appear to offer any protection to the Si interface for this sample. As the DETA SAM is indistinguishable from other sources of carbon and nitrogen in the spectrum, it is unclear if the ELD Co solution etched away the SAMs or if it just diffused through the SAMs. The possible Co_2Si phase appears more prominent than the CoSi phase and bulk Si. The first sub oxide also takes up a large area of the peak.

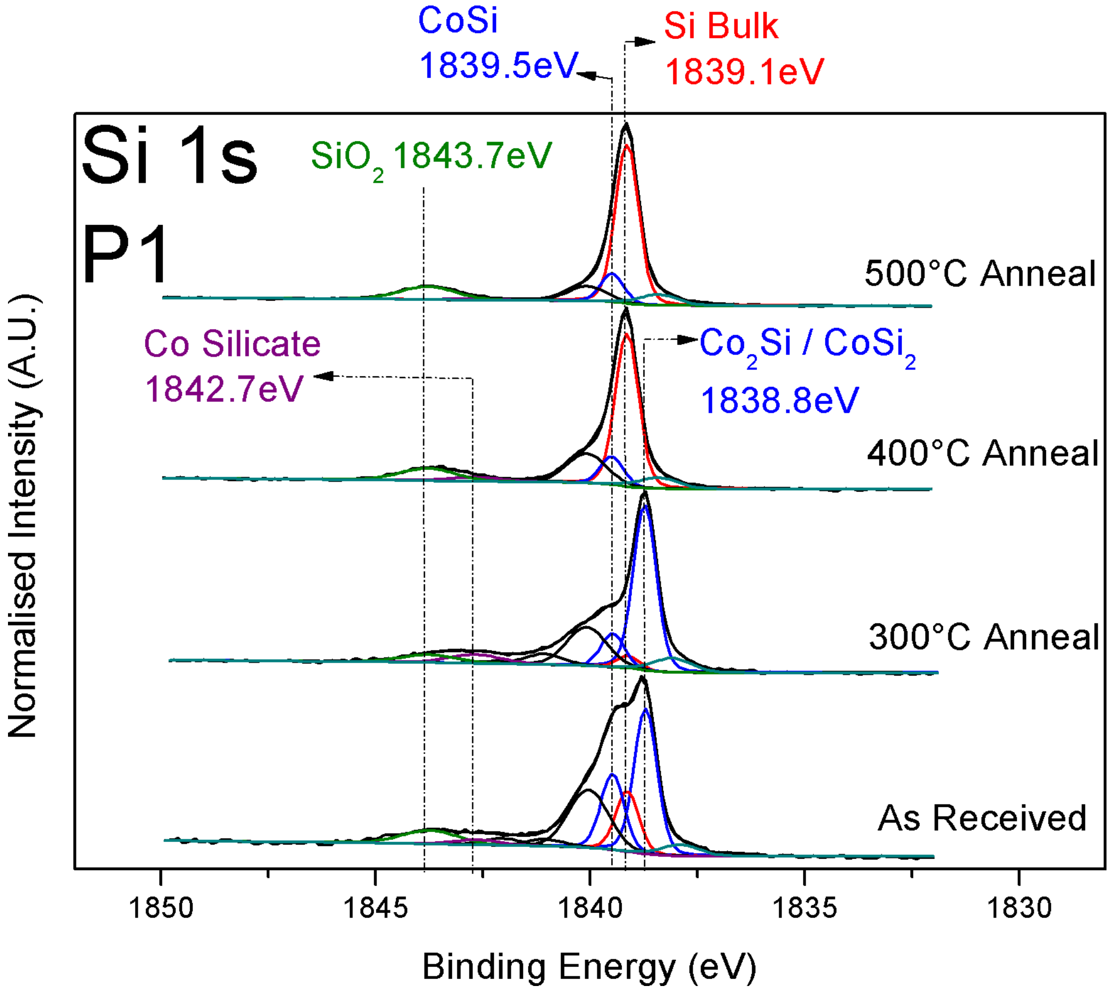

Figure 6.18 Peak fitted Si 1s spectra showing the churned-up interface with silicide present as-received which becomes more SiO2 like following sequential anneals.

Following the 300°C anneal the Co_2Si phase grows significantly while the bulk Si component peak reduces as it is consumed to form more silicide. The 400°C anneal sees the breakdown of this phase as the silicon bulk increases. The silicate, Si^{2+} and Si^{3+} have almost completely decomposed and released enough oxygen to breakdown this cobalt rich phase with the CoSi phase being more stable remains. The first sub oxide has also decreased in intensity. By the 500°C anneal the bulk Si, CoSi and SiO_2 peaks have become stable and have not changed appreciably since the last anneal. The Si^{2+} and Si^{3+} have decomposed completely while the cobalt silicate is almost gone. The Si^{1+} is still quite large but it is expected with a higher annealing temperature that this oxide phase would decompose.

Peak fitting parameters for the Si 1s are displayed in Table 6.2. The Lorentzian value used for all peaks was 0.12 eV which was obtained from fitting a reference silicon sample. The Gaussian value for the bulk silicon and SiO_2 components were also found from the reference silicon sample. The silicides were given the same Gaussian as the bulk silicon peak. The binding energy positions of all peaks were fixed along with the Gaussian and Lorentzian values. This ensured that any change in the overall profile was due to a real change in one of the component peaks and not just from varying the parameters. The pre-peak was the only peak that did not have a fixed position.

Table 6.2 Peak fitting parameters for the Si 1s over the course of the experiment.

Si 1s	Co_2Si/ $CoSi_2$	Si Bulk	CoSi	Si^{1+}	Si^{2+}	Si^{3+}	Silicate	SiO_2	Pre-Peak
Gaussian (eV)	0.55	0.55	0.55	1	1	1	1.4	1.48	1
Binding Energy (eV)	1838.7	1839.1	1839.5	1840.0	1841.0	1842.0	1842.6	1843.7	1837.89 – 1838.4

6.4 Conclusions

From this study it can be seen that this ELD Co film is indeed very homogenous at all the positions measured. The SAMs have been successful in trapping the Pd which in turn was successful in promoting the reaction for the electroless deposition. It cannot be confirmed if the DETA SAM has survived the ELD process or if it has been etched away. This is due to the carbon and nitrogen in the DETA being indistinguishable from the carbon and nitrogen introduced during the ELD process. The high energy scans show that the Co film is a superior quality, metallic film with a small amount of surface oxide present which can be eliminated by thermal annealing. The quality of the metal film is of the upmost importance for devices as any oxide can decrease the conductivity. It is clear that boron has become incorporated into the film and bonds with the released oxygen to form B_2O_3. The carbon and nitrogen introduced from the deposition, reduce with each thermal anneal. It has been shown that the ELD process forms two cobalt silicide phases at the Si-Co interface which are unstable at high temperatures. It is thought that the ELD process has "churned up" the Si-Co interface and consequentially formed cobalt silicide. The silicide is shown to be unstable and decomposes upon thermal annealing. It is proposed that in the cobalt metallisation scheme that the formation of this silicide will not impact negatively on the resistance of the line nor will it induce cobalt diffusion into the dielectric due to the metallic properties of the Co silicide.

6.5 References

(1) Auth, C.; Aliyarukunju, A.; Asoro, M.; Bergstrom, D.; Bhagwat, V.; Birdsall, J.; Bisnik, N.; Buehler, M.; Chikarmane, V.; Ding, G.; Fu, Q.; Gomez, H.; Han, W.; Hanken, D.; Haran, M.; Hattendorf, M.; Heussner, R.; Hiramatsu, H.; Ho, B.; Jaloviar, S.; Jin, I.; Joshi, S.; Kirby, S.; Kosaraju, S.; Kothari, H.; Leatherman, G.; Lee, K.; Leib, J.; Madhavan, A.; Marla, K.; Meyer, H.; Mule, T.; Parker, C.; Parthasarathy, S.; Pelto, C.; Pipes, L.; Post, I.; Prince, M.; Rahman, A.; Rajamani, S.; Saha, A.; Santos, J. D.; Sharma, M.; Sharma, V.; Shin, J.; Sinha, P.; Smith, P.; Sprinkle, M.; Amour, A. St.; Staus, C.; Suri, R.; Towner, D.; Tripathi, A.; Tura, A.; Ward, C.; Yeoh, A. A 10nm High Performance and Low-Power CMOS Technology Featuring 3rd Generation FinFET Transistors, Self-Aligned Quad Patterning, Contact over Active Gate and Cobalt Local Interconnects. *2017 IEEE Int. Electron Devices Meet.* **2017**, 29.1.1-29.1.4.

(2) Gall, D. Electron Mean Free Path in Elemental Metals. *J. Appl. Phys.* **2016**, *119* (8), 1–5.

(3) Moors, K.; Sorée, B.; Magnus, W. Resistivity Scaling in Metallic Thin Films and Nanowires Due to Grain Boundary and Surface Roughness Scattering. *Microelectron. Eng.* **2017**, *167*, 37–41.

(4) Liu, H. D.; Zhao, Y. P.; Ramanath, G.; Murarka, S. P.; Wang, G. C. Thickness Dependent Electrical Resistivity of Ultrathin (<40 nm) Cu Films. *Thin Solid Films* **2001**, *384* (1), 151–156.

(5) Mallikarjunan, A.; Sharma, S.; Murarka, S. P. Resistivity of Copper Films at Thicknesses Near the Mean Free Path of Electrons in Copper. *Electrochem. Solid-State Lett.* **2000**, *3* (9), 437–438.

(6) Yu Jiang; Nalla, P.; Matsushita, Y.; Harm, G.; Jingyan Wang; Kolics, A.; Zhao, L.; Mountsier, T.; Besser, P.; Hui-Jung Wu. Development of Electroless Co Via-Prefill to Enable Advanced BEOL Metallization and via Resistance

Reduction. In *2016 IEEE International Interconnect Technology Conference / Advanced Metallization Conference (IITC/AMC)*; IEEE, 2016; pp 111–113.

(7) Van Der Veen, M. H.; Vandersmissen, K.; Dictus, D.; Demuynck, S.; Liu, R.; Bin, X.; Nalla, P.; Lesniewska, A.; Hall, L.; Croes, K.; Zhao, L.; Bömmels, J.; Kolics, A.; Tökei, Z. Cobalt Bottom-up Contact and via Prefill Enabling Advanced Logic and DRAM Technologies. In *2015 IEEE International Interconnect Technology Conference and 2015 IEEE Materials for Advanced Metallization Conference, IITC/MAM 2015*; 2015; pp 25–27.

(8) Mont, F. W.; Zhang, X.; Wang, W.; Kelly, J. J.; Standaert, T. E.; Quon, R.; Todd, E. Cobalt Interconnect on Same Copper Barrier Process Integration at the 7nm Node. In *IITC 2017 - 2017 IEEE International Interconnect Technology Conference*; 2017; pp 7–9.

(9) Chen, G. S.; Tang, Y. S.; Chen, S. T.; Yang, T. J. Electroless Deposition of Ultrathin Co-B Based Barriers for Cu Metallization Using an Innovative Seeding Technique. *Electrochem. Solid-State Lett.* **2006**, *9* (8), C141.

(10) Liu, W. L.; Hsieh, S. H.; Tsai, T. K.; Chen, W. J. Growth Kinetics of Electroless Cobalt Deposition by TEM. *J. Electrochem. Soc.* **2004**, *151*, C680.

(11) Nakano, H.; Itabashi, T.; Akahoshi, H. Electroless Deposited Cobalt-Tungsten-Boron Capping Barrier Metal on Damascene Copper Interconnection. *J. Electrochem. Soc.* **2005**, *152* (3), C163.

(12) Osaka, T.; Aramaki, H.; Yoshino, M.; Ueno, K.; Matsuda, I.; Shacham-Diamand, Y. Fabrication of Electroless CoWP/NiB Diffusion Barrier Layer on SiO_2 for ULSI Devices. *J. Electrochem. Soc.* **2009**, *156* (9), H707–H710.

(13) Hauschildt, M.; Hintze, B.; Gall, M.; Koschinsky, F.; Preusse, A.; Bolom, T.; Nopper, M.; Beyer, A.; Aubel, O.; Talut, G.; Zschech, E. Advanced Metallization Concepts and Impact on Reliability. *Jpn. J. Appl. Phys.* **2014**, *53* (5S2), 05GA11.

(14) Chen, S. Te; Liu, Y. Y.; Chen, G. S. Ultrathin Cobalt-Alloyed Barrier Layers for Copper Metallization by a New Seeding and Electroless-Deposition Process. *Appl. Surf. Sci.* **2015**, *354*, 144–147.

(15) Kohn, A.; Eizenberg, M.; Shacham-Diamand, Y.; Israel, B.; Sverdlov, Y. Evaluation of Electroless Deposited Co(W,P) Thin Films as Diffusion Barriers for Copper Metallization. *Microelectron. Eng.* **2001**, *55* (1–4), 297–303.

(16) Kind, H.; Bittner, A. M.; Cavalleri, O.; Kern, K.; Greber, T. Electroless Deposition of Metal Nanoislands on Aminothiolate-Functionalized Au(111) Electrodes. *J. Phys. Chem. B* **1998**, *102* (39), 7582–7589.

(17) Osaka, T.; Yoshino, M. New Formation Process of Plating Thin Films on Several Substrates by Means of Self-Assembled Monolayer (SAM) Process. *Electrochim. Acta* **2007**, *53* (2), 271–277.

(18) Malki, M.; Rozenblat-raz, A.; Duhin, A.; Inberg, A.; Horvitz, D.; Shacham-diamand, Y. Surface & Coatings Technology Thin Electroless Co (W, P) Film Growth on Titanium – Nitride Layer Modified by Self-Assembled Monolayer. **2014**, *252*, 1–7.

(19) Kittl, J. A.; Opsomer, K.; Torregiani, C.; Demeurisse, C.; Mertens, S.; Brunco, D. P.; Van Dal, M. J. H.; Lauwers, A. Silicides and Germanides for Nano-CMOS Applications. *Mater. Sci. Eng. B Solid-State Mater. Adv. Technol.* **2008**, *154–155* (1–3), 144–154.

(20) Lavoie, C.; D'Heurle, F. M.; Detavernier, C.; Cabral, C. Towards Implementation of a Nickel Silicide Process for CMOS Technologies. *Microelectron. Eng.* **2003**, *70* (2–4), 144–157.

(21) Orozco, P. AAnalyzer http://rdataa.com/aanalyzer/aanaHome.htm.

(22) Nečas, D.; Klapetek, P. Gwyddion: An Open-Source Software for SPM Data Analysis. *Cent. Eur. J. Phys.* **2012**, *10* (1), 181–188.

(23) Biesinger, M. C.; Payne, B. P.; Grosvenor, A. P.; Lau, L. W. M.; Gerson, A. R.; Smart, R. S. C. Resolving Surface Chemical States in XPS Analysis of First Row Transition Metals, Oxides and Hydroxides: Cr, Mn, Fe, Co and Ni. *Appl. Surf. Sci.* **2011**, *257* (7), 2717–2730.

(24) Mclntyre, N. S.; Cook, M. G. X-Ray Photoelectron Studies on Some Oxides and Hydroxides of Cobalt, Nickel, and Copper. *Anal. Chem.* **1975**, *47* (13), 2208–2213.

(25) Dupin, J.-C.; Gonbeau, D.; Vinatier, P.; Levasseur, A. Systematic XPS Studies of Metal Oxides, Hydroxides and Peroxides. *Phys. Chem. Chem. Phys.* **2000**, *2* (6), 1319–1324.

(26) Oku, M.; Hirokawa, K. X-Ray Photoelectoron Spectrosopy of Co_3O_4. *J. Electron Spectrosc. Relared Phenom.* **1976**, *8*, 475–481.

(27) Hedman, J.; Klasson, M.; Nilsson, R.; Nordling, C. The Electronic Structure of Some Palladium Alloys Studied by ESCA and X-Ray Spectroscopy. *Phys. Scr.* **1971**, *4*, 195–201.

(28) Grunthaner, P. J.; Grunthaner, F. J.; Madhukar, A. Chemical Bonding and Charge Redistribution: Valence Band and Core Level Correlations for the Ni/Si, Pd/Si, and Pt/Si Systems. *J. Vac. Sci. Technol.* **1982**, *20* (3), 680–683.

(29) Singh, R. K.; Rahul, R.; Neergat, M. Stability Issues in Pd-Based Catalysts: The Role of Surface Pt in Improving the Stability and Oxygen Reduction Reaction (ORR) Activity. *Phys. Chem. Chem. Phys.* **2013**, *15* (31), 13044.

(30) Ye, X.-R.; Lin, Y.; Wang, C.; Engelhard, M. H.; Wang, Y.; Wai, C. M. Supercritical Fluid Synthesis and Characterization of Catalytic Metal Nanoparticles on Carbon Nanotubes. *J. Mater. Chem.* **2004**, *14* (5), 908.

(31) Olivier, S.; Decorps, T.; Calvo-Muñoz, M. L.; Da Silva, S.; Cayron, C.; Haumesser, P. H.; Passemard, G. Inhomogeneous Nucleation and Growth of

Palladium and Alloyed Cobalt during Self-Aligned Capping of Advanced Copper Interconnects. *Thin Solid Films* **2010**, *518* (17), 4773–4778.

(32) Moulder, J. Handbook of X Ray Photoelectron Spectroscopy: A Reference Book of Standard Spectra for Identification and Interpretation of XPS Data, 2nd ed.; Chastin, J., Ed.; Perkin-Elmer Corporation: USA, 1992.

(33) Christie, A.; Sutherland, I.; Walls, J. An XPS Study of Ion-Induced Dissociation on Metal Carbonate Surfaces. *Vacuum* **1981**, *31* (10–12), 513–517.

(34) Yang, J.; Cheng, H.; Frost, R. L. Synthesis and Characterisation of Cobalt Hydroxy Carbonate $Co_2CO_3(OH)_2$ nanomaterials. *Spectrochim. Acta - Part A Mol. Biomol. Spectrosc.* **2011**, *78* (1), 420–428.

(35) Bazylewski, P.; Boukhvalov, D. W.; Kukharenko, A. I.; Kurmaev, E. Z.; Hunt, A.; Moewes, A.; Lee, Y. H.; Cholakh, S. O.; Chang, G. S. The Characterization of Co-Nanoparticles Supported on Graphene. *RSC Adv.* **2015**, *5* (92), 75600–75606.

(36) Guimon, C.; Gonbeau, D.; Pfister-Guillouzo, G.; Dugne, O.; Guette, A.; Naslain, R.; Lahaye, M. XPS Study of BN Thin Films Deposited by CVD on SiC Plane Substrates. *Surf. Interface Anal.* **1990**, *16* (1–12), 440–445.

(37) Matsoso, B. J.; Ranganathan, K.; Mutuma, B. K.; Lerotholi, T.; Jones, G.; Coville, N. J. Synthesis and Characterization of Boron Carbon Oxynitride Films with Tunable Composition Using Methane, Boric Acid and Ammonia. *New J. Chem.* **2017**, *41* (17), 9497–9504.

(38) Li, L.; Li, L. H.; Chen, Y.; Dai, X. J.; Xing, T.; Petravic, M.; Liu, X. Mechanically Activated Catalyst Mixing for High-Yield Boron Nitride Nanotube Growth. *Nanoscale Res. Lett.* **2012**, *7*, 1–8.

(39) Stoch, J.; Gablankowska-Kukucz, J. The Effect of Carbonate Contaminations on the XPS O 1s Band Structure in Metal Oxides. *Surf. Interface Anal.* **1991**, *17*

(3), 165–167.

(40) Pan, Z.; Yang, Y.; Huang, J.; Ren, B.; Yu, H.; Xu, R.; Ji, H.; Wang, L.; Wang, L. Study on the Preparation of Boron-Rich Film by Magnetron Sputtering in Oxygen Atmosphere. *Appl. Surf. Sci.* **2016**, *388*, 392–395.

(41) Paladini, M.; Godinho, V.; Arzac, G. M.; Jiménez de Haro, M. C.; Beltrán, A. M.; Fernández, A. Tailor-Made Preparation of Co–C, Co–B, and Co Catalytic Thin Films Using Magnetron Sputtering: Insights into Structure–composition and Activation Effects for Catalyzed $NaBH_4$ Hydrolysis. *RSC Adv.* **2016**, *6* (110), 108611–108620.

(42) Schild, D.; Ulrich, S.; Ye, J.; Stüber, M. XPS Investigations of Thick, Oxygen-Containing Cubic Boron Nitride Coatings. *Solid State Sci.* **2010**, *12* (11), 1903–1906.

(43) Wang, Y.; Trenary, M. Surface Chemistry of Boron Oxidation. 2. The Reactions of B_2O_2 and B_2O_3 with Boron Films Grown on Ta(110). *Chem. Mater* **1993**, *5* (364), 199–205.

(44) Kolel-Veetil, M. K.; Gamache, R. M.; Bernstein, N.; Goswami, R.; Qadri, S. B.; Fears, K. P.; Miller, J. B.; Glaser, E. R.; Keller, T. M. Substitution of Silicon within the Rhombohedral Boron Carbide (B_4C) Crystal Lattice through High-Energy Ball-Milling. *J. Mater. Chem. C* **2015**, *3* (44), 11705–11716.

(45) Ong, C. W.; Huang, H.; Zheng, B.; Kwok, R. W. M.; Hui, Y. Y.; Lau, W. M. X-Ray Photoemission Spectroscopy of Nonmetallic Materials: Electronic Structures of Boron and B_xO_y. *J. Appl. Phys.* **2004**, *95* (7), 3527–3534.

(46) Badía-Romano, L.; Rubín, J.; Bartolomé, F.; Magén, C.; Bartolomé, J.; Varnakov, S. N.; Ovchinnikov, S. G.; Rubio-Zuazo, J.; Castro, G. R. Morphology of the Asymmetric Iron-Silicon Interfaces. *J. Alloys Compd.* **2015**, *627*, 136–145.

(47) Eickhoff, T.; Medicherla, V.; Drube, W. Final State Contribution to the Si 2p Binding Energy Shift in SiO_2/Si(100). *J. Electron Spectros. Relat. Phenomena* **2004**, *137–140* (SPEC. ISS.), 85–88.

(48) Nichau, A.; Schnee, M.; Schubert, J.; Besmehn, A.; Rubio-Zuazo, J.; Breuer, U.; Bernardy, P.; Holländer, B.; Mücklich, A.; Castro, G. R.; Von Borany, J.; Buca, D.; Mantl, S. Photoemission Spectroscopy Study of the Lanthanum Lutetium Oxide/Silicon Interface. *J. Chem. Phys.* **2013**, *138* (15), 154709.

(49) Gomoyunova, M. V.; Grebenyuk, G. S.; Pronin, I. I. Binding Energies of Si 2p and Co 3p Electrons in Cobalt Silicides. *Tech. Phys. Lett.* **2011**, *37* (12), 1124–1126.

(50) Gomoyunova, M. V; Grebenyuk, G. S.; Pronin, I. I.; Solov'ev, S. M.; Vilkov, O. Y.; Vyalykh, D. V. Formation and Magnetic Properties of the Silicon-Cobalt Interface. *Phys. Solid State* **2013**, *55* (2), 437–442.

(51) Hwang, I. Y.; Kim, J. H.; Oh, S. K.; Kang, H. J.; Lee, Y. S. Ultrathin Cobalt Silicide Film Formation on Si(100). *Surf. Interface Anal.* **2003**, *35* (2), 184–187.

(52) Pan, J. S.; Liu, R. S.; Zhang, Z.; Poon, S. W.; Ong, W. J.; Tok, E. S. Co Growth on Si(001) and Si(111) Surfaces: Interfacial Interaction and Growth Dynamics. *Surf. Sci.* **2006**, *600* (6), 1308–1318.

(53) Zeng, F.; Xiong, X.; Huang, B. Cobalt Silicide Formations and Magnetic Properties of Laser Ablated Co(Cr) Thin Films. *Intermetallics* **2010**, *18* (3), 306–311.

(54) Chen, L. J.; Mayer, J. W.; Tu, K. N.; Sheng, T. T. Lattice Imaging of Silicide-Silicon Interfaces. *Thin Solid Films* **1982**, *93* (1–2), 91–97.

(55) Boscherini, F.; Joyce, J. J.; Ruckman, M. W.; Weaver, J. H. High-Resolution Photoemission Study of Co/Si(111) Interface Formation. *Phys. Rev. B* **1987**, *35* (9), 4216–4220.

(56) Vilkov, O.; Fedorov, A.; Usachov, D.; Yashina, L. V.; Generalov, A. V.; Borygina, K.; Verbitskiy, N. I.; Grüneis, A.; Vyalikh, D. V. Controlled Assembly of Graphene-Capped Nickel, Cobalt and Iron Silicides. *Sci. Rep.* **2013**, *3*, 1–7.

(57) Usachov, D. Y.; Fedorov, A. V.; Vilkov, O. Y.; Erofeevskaya, A. V.; Vopilov, A. S.; Adamchuk, V. K.; Vyalikh, D. V. Formation and Lithium Doping of Graphene on the Surface of Cobalt Silicide. *Phys. Solid State* **2015**, *57* (5), 1040–1047.

(58) Murarka, S. P. Silicide Thin Films and Their Applications in Microelectronics. *Intermetallics* **1995**, *3* (3), 173–186.

(59) Van Bockstael, C.; De Keyser, K.; Demeulemeester, J.; Vantomme, A.; Van Meirhaeghe, R. L.; Detavernier, C.; Jordan-Sweet, J. L.; Lavoie, C. In Situ Study of the Formation of Silicide Phases in Amorphous Co-Si Mixed Layers. *Microelectron. Eng.* **2010**, *87* (3), 282–285.

(60) Zhang, L.; Du, Y.; Xu, H.; Pan, Z. Experimental Investigation and Thermodynamic Description of the Co-Si System. *Calphad Comput. Coupling Phase Diagrams Thermochem.* **2006**, *30* (4), 470–481.

(61) Zhao, J.; Ballast, L. K.; Hossain, T. Z.; Trostel, R. E.; Bridgman, W. C. Effect of Rapid Thermal Annealing Temperature on the Formation of CoSi Studied by X-Ray Photoelectron Spectroscopy and Micro-Raman Spectroscopy. *J. Vac. Sci. Technol. A Vacuum, Surfaces, Film.* **2000**, *18* (4), 1690.

(62) Caspers, C.; Gloskovskii, A.; Gorgoi, M.; Besson, C.; Luysberg, M.; Rushchanskii, K. Z.; Ležaić, M.; Fadley, C. S.; Drube, W.; Müller, M. Interface Engineering to Create a Strong Spin Filter Contact to Silicon. *Sci. Rep.* **2016**, *6* (1), 22912.

(63) Koirala, R.; Safonova, O. V; Pratsinis, S. E.; Baiker, A. Effect of Cobalt Loading on Structure and Catalytic Behavior of CoO_x/SiO_2 in CO_2-Assisted

Dehydrogenation of Ethane. *Appl. Catal. A Gen.* **2018**, *552* (December 2017), 77–85.

(64) Mihailova, I.; Mehandjiev, D. Catalytic Activity of Co-Åkermanite and Co-Pyroxene in Oxidation Reactions. *Can. J. Chem.* **2011**, *89* (8), 939–947.

(65) Wagman, D. D.; Evans, W. H.; Parker, V. B.; Schumm, R. H.; Halow, I.; Bailey, S. M.; Churney, K. L.; Nuttall, R. L. The NBS Tables of Chemical Thermodynamic Properties. Selected Values for Inorganic and C1 and C2 Organic Substances in SI Units [J. Phys. Chem. Ref. Data 11, Suppl. 2 (1982)]. *J. Phys. Chem. Ref. Data* **1982**, *11* (2), 1807–1812.

Chapter 7

7 Conclusions and Future Work

7.1 Conclusions

The principle aim of this thesis was to investigate the use of self-assembled monolayers (SAMs) as a means of solving some of the main problems in the BEOL for the microelectronics industry. XPS was primarily used to examine the chemical interactions at the SAM-substrate interface and to study the interaction of the SAMs with subsequently deposited metals. Other techniques such as HAXPES, AFM and SEM were also employed to aid and enhance the study.

7.1.1 Interaction of Mn with the DETA SAM deposited on SiO_2 and SOG

Chapter 3 utilises XPS to investigate the interaction of a thin Mn film with the DETA SAM deposited on a native SiO_2 substrate and on a spin-on-glass substrate. Initial tests show the stability of the DETA SAM which was held in UHV for two days. Over layer thickness calculations performed on the SiO_2 component peak in the Si 2p spectra show an increase in thickness of the silicon dioxide from the reference SiO_2 to the DETA deposited on SiO_2. This demonstrates how the SAM covalently bonds to the substrate via its silane head group adding an additional monolayer of SiO_2.

Focusing on the DETA-on-SiO_2, following a thin mainly metallic Mn deposition in UHV there is evidence of the deposited metal interacting with the DETA SAM. This is seen in the formation of a Mn-carbide in the C 1s spectrum and a Mn-nitride in the N 1s. Following a post metallization anneal at 200°C, the carbide is seen to decompose due to residual oxygen in the chamber, the nitride however, remains. Also observed in the O 1s and Si 2p spectra following anneal is the emergence of a peak which corresponds to the formation of $MnSiO_3$. This signifies that the Mn has diffused through the SAM and interacted with the underlying substrate. With a higher temperature anneal at 400°C, the silicate peak is seen to grow.

Turning to the SAM-on-SOG, there are similarities to the SAM-on-SiO_2. Upon Mn deposition the formation of Mn-carbide and Mn-nitride can be seen. This time however, the carbide requires a higher temperature anneal to decompose. Unlike the SAM-on-SiO_2, with this sample there is evidence of silicate formation upon Mn deposition without any applied temperature. Subsequent annealing steps see the increase of the silicate peak in both the Si 2p and the O 1s core level spectra.

On both substrates it has been shown that the Mn can interact with the DETA SAM by forming Mn-carbide and Mn-nitride with the hydrocarbon chain and the amino terminal group respectively. It has also been shown that the Mn can diffuse through the SAM and form Mn-silicate at the DETA/substrate interface. These chemical interactions could be extremely beneficial for barrier layer and interconnect applications as $MnSiO_3$ has been shown to be an effective barrier to copper diffusion,[1,2] while Mn-nitride has been shown to improve the adhesion of copper to the ILD[3]. It is proposed that the formation of the $MnSiO_3$ layer creates a stable barrier on the substrate surface that could potentially seal the pores in a porous dielectric material.

7.1.2 The role of SAMs in Improving Nucleation and Adhesion

Chapter 4 investigates the use of a range of SAMs to improve nucleation and adhesion of copper to the underlying dielectric material. Two amino terminated SAMs, one with a short chain (APTMS) and one with a long chain (DETA), were investigated along with a short chain carbon terminated SAM (PTMS) with native

SiO_2 as a reference substrate. Through XPS analysis, the interaction of an ultra-thin copper film deposited *in-situ* on all four samples was examined.

It has been observed that the APTMS and the DETA SAMs, which contain the amino terminal group, pose substantial benefits in terms of both nucleation and adhesion to the deposited copper. While the DETA performs the best in terms of nucleation following a thermal anneal at 400°C, both the DETA and the APTMS retain approximately the same amount of copper. The SiO_2 reference sample performs the worst, although some copper is deposited on the surface, following the anneal the copper is almost completely removed from the surface. The PTMS does retain more of the deposited copper than the SiO_2 but displays inferior nucleation and adhesion than the amino-terminated SAMs.

Thick copper films were then deposited for adhesion tape testing, AFM and 4-point probe measurements. Tape testing performed on samples with and without a 400°C anneal demonstrate almost indistinguishable results for both the DETA and APTMS. The amino-terminated SAMs again outperform the SiO_2 and the carbon-terminated PTMS. Upon copper deposition the AFM shows that all samples are almost identical in terms of morphology, grain size and R_{rms}. The ensuing anneal sees a change in the morphology of all the samples. The grains appear to agglomerate and the R_{rms} increases for all samples. The DETA and APTMS seem to form a more homogenous film while the PTMS sees an increase in R_{rms} to 6.7 nm. From the 4-point probe measurements it can be seen that the insertion of a SAM layer does not appreciably affect the resistivity values of the copper films.

All of these results indicate that the amino-terminated SAMs display several advantages over the carbon-terminated SAM and the reference SiO_2. It is not clear however, if the chain length impacts the results. Although nucleation is better on the DETA for ultra-thin films, retention is roughly the same on the DETA and the APTMS following anneal. Thicker films suggest very similar results in terms of adhesion tape testing and morphology/surface roughness.

7.1.3 Effect of Atomic Oxygen on DETA and OTMS SAMs

For the first time, extremely controlled atomic oxygen exposures have been performed from small 100 L exposures, medium 500 L exposures to larger 1000 L exposures. The small exposures show a stepwise modification of the DETA SAM. A mechanism for the removal of the SAM is proposed whereby the atomic oxygen strips the hydrocarbon and terminal groups from the surface. The head group remains unaffected, as it has covalently bonded to the surface and inspection of the Si 2p shows no change in the SiO_2 peak over the course of the experiment. Since the carbon nitrogen ratio remains relatively constant throughout the study it appears as though the atomic oxygen plucks the hydrocarbon chain and the terminal group from the surface together as opposed to smaller moieties at a time. The long chain OTMS also shows a stepwise modification when exposed to 500 L of atomic oxygen. For this SAM, the etching process appears to incorporate the oxygen into the SAM layer before removing small moieties from the hydrocarbon chain.

It is seen that the decay of the DETA SAM photoemission signal is linear in nature and independent of the exposure size. While it is observed that the OTMS SAM has a different etch rate to the DETA and is seen to follow an exponential trend. It is suggested that the amino terminal groups of the DETA offers more protection against the atomic oxygen etching than the long chain OTMS, since the oxygen cannot penetrate the SAM layer as easily. These results suggest that the choice of SAM in an AS-ALD process is very important because if the SAM cannot withstand a large number of oxidation pulses during the ALD cycle it could potentially limit the thickness of the deposited film.

7.1.4 The use of DETA SAM in ELD of Cobalt

HAXPES measurements were used to access the entirety of a ~20 nm electroless deposited Co film and to investigate the underlying Si-Co interface. HAXPES characterisation of the ELD cobalt film showed a homogenous and high quality metallic film. A small amount of surface oxide was present which readily decomposed with a modest thermal anneal. The DETA SAM was successful in trapping the Pd which is used as the catalyst in initiating the reaction for the Co ELD process.

From the ELD process it is seen that carbon, nitrogen and boron have become incorporated into the film from the both the solution and the reducing agent used during the process. Since the carbon and nitrogen in the DETA cannot be distinguished from the incorporated carbon and nitrogen, it is difficult to ascertain if the DETA is still present at the end of the process or if it has been etched away. The boron is observed to bond with oxygen which is released by the decomposition of the surface cobalt oxide to form B_2O_3.

Through rigorous peak fitting of the Si 1s peak using strict constraints on the peak parameters, it has been possible to identify two Co silicide phases which form at the Si-Co interface. These silicides have been identified as CoSi at 1839.5 eV and Co_2Si at 1838.8 eV BE. These silicides are observed to be unstable with higher temperature annealing, where the Co_2Si phase is seen to decompose after a 400°C anneal and the CoSi phase decreases in intensity with each anneal.

7.2 Future Work

7.2.1 DETA SAMs as a Pore Sealant for Low-*k* Dielectrics

From the result in Chapter 3 it can be said that the Mn can interact with the different groups in the DETA SAM by forming three chemical interactions: a Mn-silicate with the head group, a Mn-carbide with the hydrocarbon chain and a Mn-nitride with the terminal group. Since it is known that $MnSiO_3$ forms a stable barrier it would be beneficial to deposit a thin copper film and investigate if the copper can penetrate this barrier and diffuse into the pores in a porous low-*k* dielectric. TEM analysis with elemental mapping would give a clear picture of how stable the barrier was and if there was any diffusion into the dielectric.

7.2.2 SAMs as an Adhesion Promoter for Copper

In Chapter 4, analysis of the four different starting samples reveal that the amino-terminated SAMs perform the best in terms of nucleation and adhesion of both ultra-thin and thick copper films. To gain a better understanding of the adhesion of the copper to the SAMs, 4-point bending tests could be performed. These tests could be performed to cause fractures in the sample which would occur at either the SiO_2/SAM interface or the SAM/Cu interface. XPS analysis could then be used to identify at which interface the fracture occurred[4]. If the amino-terminated SAM has bonded well to the copper film the fracture would be expected at the SiO_2/SAM interface. Using shadow masks (from Figure 4.3), metal-oxide-semiconductor (MOS) capacitor structures could be fabricated to assess the effectiveness of the SAM as a barrier layer by electrical characterisation using bias-temperature stress (BTS), capacitance-voltage (C-V) and current-voltage (I-V) measurements.

7.2.3 Further Investigation of the Effect of Atomic Oxygen on SAMs

Results obtained in Chapter 5 led to the proposal of a SAM etch mechanism. However, further investigation is needed to confirm this mechanism. Previous studies have compared atomic oxygen treatment of a carbon-terminated SAM cooled with liquid nitrogen and at room temperature[5]. This was to observe the mechanism behind the etching of the SAM. It is thought that this approach would also benefit the interpretation of the etching of the amino-terminated SAM. By cooling the SAM, it might be possible to decipher if the DETA is etched by the proposed mechanism or by first removing small moieties and then the full SAM chain. For the carbon-terminated OTMS SAM it would be useful to compare its decay to both shorter and longer chain SAMs. This would clarify if the exponential decay rate is due to the chain length. A previous study looking at various chain length SAMs and their etching when exposed to atomic hydrogen has found some differences in the removal process which is attributed to the hydrocarbon chain length[6].

7.2.4 Further Characterisation of ELD Cobalt Films

In Chapter 6 the properties of an ELD cobalt film were outlined. Since cobalt is not as well studied as copper as an interconnect material there are many studies which could be carried out. TEM and secondary ion mass spectroscopy (SIMS) could reinforce the HAXPES results showing a high quality metallic film with surface localised oxide which can be removed after thermal anneal. These techniques would also display any evidence of cobalt diffusion into the SiO_2. Fabricating several more ELD Co samples by the same process would reveal if the formation of the Co silicide is a common occurrence at the Si-Co interface. X-ray diffraction (XRD) could possibly identify the two cobalt silicide phases. MOS capacitors could be fabricated for electrical characterisation.

7.3 References

(1) Nguyen, M. P.; Sutou, Y.; Koike, J. Diffusion Barrier Property of $MnSi_xO_y$ Layer Formed by Chemical Vapor Deposition for Cu Advanced Interconnect Application. *Thin Solid Films* **2015**, *580*, 56–60.

(2) Byrne, C.; Brennan, B.; McCoy, A. P.; Bogan, J.; Brady, A.; Hughes, G. In Situ XPS Chemical Analysis of $MnSiO_3$ Copper Diffusion Barrier Layer Formation and Simultaneous Fabrication of Metal Oxide Semiconductor Electrical Test MOS Structures. *ACS Appl. Mater. Interfaces* **2016**, *8* (4), 2470–2477.

(3) Au, Y.; Lin, Y.; Gordon, R. G. Filling Narrow Trenches by Iodine-Catalyzed CVD of Copper and Manganese on Manganese Nitride Barrier/Adhesion Layers. *J. Electrochem. Soc.* **2011**, *158* (5), D248.

(4) Gandhi, D. D.; Lane, M.; Zhou, Y.; Singh, A. P.; Nayak, S.; Tisch, U.; Eizenberg, M.; Ramanath, G. Annealing-Induced Interfacial Toughening Using a Molecular Nanolayer. *Nature* **2007**, *447* (7142), 299–302.

(5) Yuan, H.; Gibson, K. D.; Li, W.; Sibener, S. J. Modification of Alkanethiolate Monolayers by $O(^3P)$ Atomic Oxygen: Effect of Chain Length and Surface Temperature. *J. Phys. Chem. B* **2013**, *117* (16), 4381–4389.

(6) Gorham, J.; Smith, B.; Fairbrother, D. H. Modification of Alkanethiolate Self-Assembled Monolayers by Atomic Hydrogen: Influence of Alkyl Chain Length. *J. Phys. Chem. C* **2007**, *111* (1), 374–382.